Ludwig-Maximilians-Universität München
Faculty of Physics

Fractional Chern Insulators in Hofstadter-Hubbard Models: New Probes and Routes Towards Cold Atom Quantum Simulation

Felix A. Palm

München, 2023

Fractional Chern Insulators in Hofstadter-Hubbard Models: New Probes and Routes Towards Cold Atom Quantum Simulation

Dissertation
an der Fakultät für Physik
der Ludwig-Maximilians-Universität München

vorgelegt von

Felix Alexander Palm

aus München

München, den 10. Mai 2023

Erstgutachter: Prof. Dr. Fabian Grusdt
Zweitgutachterin: Prof. Dr. Monika Aidelsburger
Abgabedatum: 10. Mai 2023
Datum der mündlichen Prüfung: 28. Juni 2023

Zusammenfassung

Seit der Entdeckung des integralen und des fraktionalen Quanten-Hall-Effekts in den 1980ern hat das Zusammenspiel topologischer Eigenschaften und starker Wechselwirkungen großes Interesse unter Physiker*innen der kondensierten Materie und Wissenschaftler*innen verwandter Felder erregt. Die darauf folgende Definition topologisch geordneter Zustände führte zu einer Fülle an Literatur zu diesem Thema. Die direkte Beobachtung nichtabelscher Anyonen, einer wesentlichen Signatur topologisch geordneter Systeme mit potentiellen Anwendungen für fehlertolerante Quantencomputer, blieb jedoch aus.

Um dieser Frage nachzugehen, untersucht diese Dissertation die Eigenschaften fraktionaler Quanten-Hall-Zustände auf einem Gitter mit einem Schwerpunkt auf dem Hofstadter-Modell, welches in Quantensimulatoren mit kalten Atomen simuliert werden kann. Durch theoretische Studien dieser Systeme versuchen wir, die notwendigen Bestandteile zu verstehen, um exotische Materiezustände in Experimenten mit beispielloser Kontrolle über die Teilchen und ihre Wechselwirkungen zu realisieren.

Unsere Arbeit untersucht zuerst bosonische Realisierungen fraktionaler Quanten-Hall-Zustände auf einem Gitter unter besonderer Berücksichtigung des Pfaffschen Zustands als einem paradigmatischen nichtabelschen Zustand. Anschließend schlagen wir längliche Systeme vor, um topologische Ordnung mittels der Zentralladung zu untersuchen, und präsentieren einen modularen Ansatz um ausgedehnte Laughlin Zustände zu wachsen. Außerdem studieren wir Quanten-Hall Ferromagnetismus im Hofstadter-Fermi-Hubbard-Modell, was eine direkte Beobachtung skyrmionischer Anregungen erlaubt. Schließlich verallgemeinern wir den Ansatz zusammengesetzter Fermionen auf Gittersysteme, um analytische Ansatzwellenfunktionen zu entwickeln.

Unsere Ergebnisse bereiten den Weg für Experimente mit kalten Atomen in naher Zukunft, um wechselwirkende topologische Zustände in einem Hofstadter-Hubbard-Modell zu realisieren.

Abstract

Since the discovery of the integer and fractional quantum Hall effects in the 1980's, the interplay of topological properties and strong interactions sparked great interest among condensed matter physicists and scientists of related fields. The subsequent definition of topologically ordered states has led to an abundance of literature on the subject. However, the direct observation of non-Abelian anyon braiding, a key signature of topologically ordered systems with potential applications for fault-tolerant topological quantum computation, has remained elusive.

To address this issue, this thesis explores the properties of fractional quantum Hall states on a lattice, with a focus on the Hofstadter-Hubbard model that can be simulated using cold atom quantum simulators. Through theoretical studies of these systems, we aim to understand the ingredients necessary to realize exotic states of matter in experiments with unprecedented control of the particles and their interactions.

Our work first investigates bosonic realizations of fractional quantum Hall states on a lattice, with a specific focus on the Pfaffian state as a paradigmatic non-Abelian state. Afterwards, we propose elongated systems to probe topological order using the central charge and present a modular approach to grow extended Laughlin states. Additionally, we study quantum Hall ferromagnetism in the Hofstadter-Fermi-Hubbard model, allowing for direct observations of skyrmion excitations. Finally, to develop analytical ansatz wave functions, we generalize the composite fermion approach to lattice systems.

Our findings pave the way for near-term cold atom experiments that realize interacting topological states in a Hofstadter-Hubbard model.

Acknowledgments

While I hope that this dissertation appropriately illustrates some of the physical insight I gained during my PhD, I will not even attempt to mention all those things I could learn which are not directly visible from this thesis. I am very grateful for this experience and appreciate the support and contribution of many people making this experience possible.

I would like to start by thanking Fabian Grusdt for being an amazing, ever supportive supervisor. Thank you for taking me in as your first graduate student and walking this road with me! I very much appreciate the many hours of our discussions and the freedom I had in choosing and pursuing interesting projects. I particularly appreciate the great advice and support not only related to physics but also regarding important decisions around the academic life. Last, but not least, getting a lot of helpful feedback on my manuscripts helped to improve my scientific writing significantly. Thank you for making this PhD an opportunity to learn many things - physics- and otherwise!

I would also like to thank Monika Aidelsburger for examining this thesis. More importantly, she was a wonderful co-supervisor, not only when it comes to bringing in an experimentalist's perspective, but also for her advice on academic life in general. I could not imagine a better team of supervisors than Fabian and Monika and I am very grateful for all the knowledge they shared with me.

I am grateful to Uli Schollwöck for the hospitality at his chair and his helpful advice whenever I could need his experience and insight.

I would also like to thank Dmitri Efetov for being the chair of the examination board, and Jan von Delft, Ilka Brunner, and Erwin Frey for being part of the board.

During my PhD I had the chance to stay abroad for research visits to two foreign universities. I would like to thank Mohammad Hafezi and his group at the University of Maryland for having me and making my stay an unforgettable experience. I would also like to thank Nathan Goldman and his group at the Université Libre de Bruxelles for their hospitality and the interesting discussions we had. I am looking forward to have more of those in the future.

I would like to thank all members of the Grusdt group, the Schollwöck chair and the von Delft chair. I enjoyed my many years on the fourth floor a lot and will miss the many chats we had. Cordula Weber provided extraordinary help whenever I struggled with administrative tasks.

I am grateful to the members of IMPRS-QST and DFG FOR2414 for fruitful discussions and making this a wonderful PhD experience even in times of a pandemic. Especially Rajah Nutakki, Isaac Tesfaye, Frederick del Pozo, Ephraim Bernhardt, Alexander Hesse, and Botao Wang were amazing companions during this time.

During my PhD I got the opportunity to collaborate with wonderful people. Special thanks to Max Buser who was a huge help in setting up my DMRG simulations and finding my way as a beginning PhD student. Julian Léonard, Annabelle Bohrdt, Thomas Köhler, and Cécile Repellin were great collaborators on very different projects and I could learn a lot from everyone of them. You helped me understand that physicists come in many flavors and that we achieve our best results when working together. Sebastian Paeckel and Sam Mardazad opened a whole new branch of physics for me in showing me the world of numerical methods. Collaborating with all of you was extraordinarily insightful and I learned a lot.

I am also indebted to Mert Kurttutan, Fabian Pauw, and Fabian Döschl who I had the opportunity to co-supervise and collaborate with, as well as the many enthusiastic attendees of various tutorials throughout my studies. Your comments and questions helped me gain more insight and intuition myself, had a significant impact on how I talk about physics, and helped me find my style of advising.

I would also like to thank Matjaž Kebrič, Henning Schlömer, Reja Wilke, Tizian Blatz, Mattia Moroder, and Lukas Homeier for countless hours of discussions and proof-reading parts of this thesis. A special thank you goes to Etienne Staub who not only was a wonderful friend during my entire studies, but also improved many of my manuscripts throughout my studies with his comments regarding both language and content.

Finally, I am grateful to my family for their support during all these years. Gisela and Ludger gave me the opportunity to get excited about science at an early age and always supported me during my studies. Natascha's support and understanding, especially on days when things did not go smoothly, were incredibly helpful during my entire studies. Me finishing my PhD is as much their accomplishment as it is my own.

Publications

In the following, the author's publications and preprints are listed. They contain large parts of the material presented here, partly with textual overlap. These publications are the result of collaborations of various authors, all of which contributed substantially to the work and to the preparation of the manuscripts. Specific contributions by the respective authors are indicated below.

Publications in peer-reviewed journals

- F. A. Palm, M. Buser, J. Léonard, M. Aidelsburger, U. Schollwöck, and F. Grusdt. Bosonic Pfaffian state in the Hofstadter-Bose-Hubbard model. *Physical Review B*, **103**(16), L161101, 2021

  FP performed the numerical DMRG calculations. MB helped with those DMRG calculations and with the interpretation of the results. FG performed the exact diagonalization studies. FG and US supervised the project. All authors contributed to the conceptual achievements of the work and the writing of the manuscript.
- F. A. Palm, S. Mardazad, A. Bohrdt, U. Schollwöck, and F. Grusdt. Snapshot-based detection of $\nu = \frac{1}{2}$ Laughlin states: Coupled chains and central charge. *Physical Review B*, **106**(8), L081108, 2022

  FP performed the numerical DMRG calculations. SM helped with those DMRG calculations. AB and FG came up with the snapshot protocol for the entanglement entropy. SM and AB helped with the interpretation of the results. FG and US supervised the project. All authors contributed to the conceptual achievements of the work and the writing of the manuscript.
- F. A. Palm, M. Kurttutan, A. Bohrdt, U. Schollwöck, and F. Grusdt. Ferromagnetism and skyrmions in the Hofstadter-Fermi-Hubbard model. *New Journal of Physics*, **25**, 023021, 2023

  FP performed the DMRG calculations. AB helped with the interpretation of the data. FG and US supervised the project. All authors contributed to the conceptual achievements of the work and the writing of the manuscript.

Publications submitted to peer-reviewed journals

- R. H. Wilke, T. Köhler, F. A. Palm, and S. Paeckel. Symmetry-protected Bose-Einstein condensation of interacting hardcore Bosons, arXiv:2110.15770, 2021

  SP proposed the mapping and the study of stabilizing mechanisms of the BEC phase in the system. RW carried out the analytic computations. TK performed the DMRG simulations. All authors contributed to the theoretical development of the mapping and the writing of the manuscript. [*not presented in this thesis*]

Manuscripts in preparation

The following manuscripts are currently in preparation and are derived from results presented in this thesis:

- F. A. Palm, C. Repellin, N. Goldman, and F. Grusdt. Interacting Topological States on Coupled Chains at Filling Factor $\nu = 1$. in preparation
- F. A. Palm, N. Goldman, and F. Grusdt. Growing Fractional Chern Insulators in a Quantum Gas Microscope. in preparation
- F. Pauw, F. A. Palm, A. Bohrdt, S. Paeckel, and F. Grusdt. Detecting Hidden Order in Fractional Chern Insulators. in preparation

[*not presented in this thesis*]

Contents

Introduction

> "Up to 1980 nobody expected that there exists an effect like the quantized Hall effect, which depends exclusively on fundamental constants and is not affected by irregularities in the semiconductor like impurities or interface effects."
>
> — *Klaus von Klitzing* [8]

This statement, made by Klaus von Klitzing in his Nobel Lecture after the prize had been awarded to him for "the discovery of the quantized Hall effect" [9], nicely captures the beauty of this by now well-established field in condensed matter physics. In the 1980's, the strikingly accurate quantization of the Hall conductivity came as a surprise to many of the experts in the field. Nowadays, the surprising robustness in the presence of imperfections of the samples is attributed to the topological origin of the phenomenon. Subsequent to its discovery [10], the quantum Hall effect was explained by its relation to a global invariant of the non-interacting bands, now known as the TKNN invariant introduced by Thouless, Kohmoto, Nightingale, and den Nijs [11]. This invariant is tightly connected to the mathematical field of topology. In particular, the TKNN invariant is the physical realization of the Chern number, which classifies certain vector bundles and sections thereof [12], which are physically realized by the quantum mechanical wave function. Since these days, the field of condensed matter physics got acquainted with various manifestations of topological features, especially employing concepts of low-dimensional topology and providing a playground for this fascinating topic.

Soon after the first observation of a non-interacting topological system, the discovery of the fractional quantum Hall (FQH) effect by Tsui, Stormer, and Gossard in 1982 sparked even further interest in the field [13]. This exotic state of matter clearly exhibited *some* kind of order, yet Ginzburg's and Landau's symmetry-breaking paradigm failed to characterize this order due to its absence of off-diagonal long-range order. New criteria were needed to classify various FQH states, and once again topology played its role in providing theorists with the necessary tools, resulting in the concept of "topological order" for this novel kind of quantum order. Most strikingly, the fractional value of the Hall conductivity could be explained using what is now known as the many-body Chern number [14], applying concepts of topology from the non-interacting to the (strongly) interacting case. Furthermore, features like the ground state degeneracy, chiral edge states, fractionalized quasiparticles and alike in FQH systems are deeply connected to global, topological properties of the system. Most importantly, FQH systems exhibit excitations known as anyons, i.e. particles evading a classification in bosons and fermions [15, 16]. A particularly interesting class are non-Abelian anyons, where the *order* of braiding operations affects the outcome of the process. Such non-Abelian anyons might prove useful in future topological quantum computation applications, whereby inherent fault tolerance could be achieved by exploiting the topological nature of these excitations [17].

Unfortunately, the direct observation of non-Abelian anyon braiding remained elusive so far.

However, novel experimental platforms allowing for unprecedented control might finally give access to this exotic behavior. The author believes that cold atoms in optical lattices provide a particularly promising route to achieve this goal and, more generally, realize exotic topologically ordered states, like FQH states or chiral quantum spin liquids. By now, several examples of cold atom realizations of topological states of matter exist [18, 19] and first steps towards addressing the FQH problem in such experiments were taken. In particular, the non-interacting Hofstadter model has been realized [20,21], and also the interacting regime has been reached [22]. Moreover, first bosonic Laughlin states were realized in the continuum [23], in a photonic system [24], and – more recently – also in an optical lattice [25].

In this thesis, we will follow the philosophy of this recent realization. We believe atoms in an optical lattice subject to an artificial magnetic field to be a promising platform for future investigations of topological states of matter in the near future. The studies presented in this thesis are inspired by the current capabilities of existing cold atom experiments and investigate potential directions accessible for such platforms. With these applications in mind, we perform variational studies of systems exhibiting lattice analogs of paradigmatic FQH states, also known as fractional Chern insulators (FCIs).

Outline

This thesis is structured as follows: In Chapter 1 we provide the reader with the necessary background on topological order and the quantum Hall effects. We also introduce key concepts of quantum simulation and discuss the numerical methods employed in this thesis.

Extensive numerical studies of bosonic systems are presented in Chapters 2-4. In particular, we focus on the Pfaffian state as a paradigmatic example of non-Abelian FQH states in Chapter 2, first reviewing important continuum results in Section 2.2 and commenting on the peculiarities of FQH states on thin cylinders in Section 2.3. In Section 2.4, we present evidence for the lattice Pfaffian state as the ground state of the Hofstadter-Bose-Hubbard model for suitable, experimentally realistic parameters, based on the results in Ref. [1].

In Chapter 3, we propose to study coupled chains to identify the topological order of putative FQH states using their edge states and the central charge. In Section 3.2 we review the continuum coupled wire construction as an approach to treat FQH systems analytically, before numerically studying discrete chains in Section 3.3. In particular, we investigate the $\nu = 1/2$-Laughlin state in Section 3.3.3 based on Ref. [2] and several interacting topological states at $\nu = 1$ in Section 3.3.4.

We conclude our numerical studies of bosonic quantum Hall states in Chapter 4 by investigating modular protocols to adiabatically prepare extended Laughlin states from small patches.

In Chapter 5, we study QH ferromagnetism in the fermionic Hofstadter-Hubbard model and discuss the accompanying skyrmion-like spin textures. After reviewing the physics of fermionic QH systems at $\nu = 1$ with an emphasis on interaction induced QH ferromagnetism in Section 5.2, we present numerical results of the lattice analog based on Ref. [3] in Section 5.3.

Finally, we present some analytical insights aiming for variational trial states in Chapter 6. In particular, we briefly present the ideas of the composite fermion approach to the FQH problem in Section 6.2 and generalize this approach to the lattice systems generally studied in this thesis in Section 6.3. We also derive (preliminary) trial states which might serve as a starting point for future analytical studies.

We conclude our discussion by summarizing the work presented in this thesis and putting it into a broader context in the field of quantum simulation of FQH systems. Furthermore, we provide an outlook briefly discussing future research directions opening up in connection with our results.

1 Theoretical Background

This thesis covers various different aspects of modern condensed matter physics, with a particular emphasis on topology and quantum simulation. While providing a complete overview of these exciting and broad fields is beyond the scope of this introductory chapter, we would like to equip the reader with a basic understanding of the most important concepts and results.

We start our discussion by defining topological order, before introducing some of its particularly prominent signatures in the context of quantum Hall physics, which are used in projects discussed later in this thesis. Equipped with this basic knowledge, we then turn to a brief review of the integer and fractional quantum Hall effects, mentioning in passing the celebrated TKNN formula explaining the quantization of the Hall response at integer filling factors. We also have a first encounter with the key subject of our studies, so called fractional Chern insulators.

After these two "physical" introductions, we review some methods relevant to the projects presented here, both on the experimental and the numerical side. The main goal of this dissertation is to propose realistic schemes to prepare and manipulate interacting quantum Hall states in cold atom quantum simulators utilizing optical lattices. We therefore provide the reader with a brief overview of existing and proposed quantum simulation platforms. Finally, we conclude this introductory chapter with a review of the numerical methods used in this thesis, with a special emphasis on their variational nature.

1.1. Topological Order and its Manifestations

Strongly interacting topological matter is characterized by a plethora of interesting effects. Among others, the interplay of interactions and topology can result in quantum number fractionalization [26] or fractional braiding statistics [15, 16]. While these phenomenological properties are probably the most useful ones for both the detection and future applications of topological states of matter, they do not necessarily provide a good starting point to classify and define topological order in the first place.

In this section, we will turn away from the phenomenological point of view and follow the approach taken by Chen, Gu and Wen [27] in their attempt to develop a precise notion of topological order. We will start our discussion with a definition of intrinsic topological order, before including a brief review of how symmetry protected topological (SPT) order and symmetry breaking order fit into this framework.

However, before including topology, we first need to define quantum phases in general. To this end, we consider a Hamilton operator $\hat{\mathcal{H}}(g)$ depending smoothly on a parameter g and its ground state $|\Psi(g)\rangle$. For a local operator $\hat{\mathcal{O}}$, we can evaluate its ground state expectation value $O(g) = \langle\Psi(g)|\, \hat{\mathcal{O}}\, |\Psi(g)\rangle$. Considering the thermodynamic limit, we say the system undergoes a quantum phase transition at g_c, if $O(g)$ has a singularity at g_c for some local operator $\hat{\mathcal{O}}$.

With this definition at hand, we can now define quantum phases as equivalence classes of ground states, also called *universality classes*:

> *Two ground states* $|\Psi(g_1)\rangle$ *and* $|\Psi(g_2)\rangle$ *are said to belong to the same universality class or quantum phase if and only if there exists a smooth family of local Hamiltonians* $\hat{\mathcal{H}}(g)$, $g \in [g_1, g_2]$, *such that there is no quantum phase transition along the path* $g \in [g_1, g_2]$.

Mathematically, this defines an equivalence relation for states, the equivalence classes of which are the quantum phases.

For gapped states $|\Psi(g_{1/2})\rangle$, i.e. such that in the thermodynamic limit all excited states above $|\Psi(g_{1/2})\rangle$ have a gap, we also give the following, equivalent characterization of states belonging to the same universality class:

> *Two gapped states* $|\Psi(g_{1/2})\rangle$ *belong to the same universality class if and only if there is a family of local Hamiltonians* $\hat{\mathcal{H}}(g)$, $g \in [g_1, g_2]$, *such that the energy gap above the ground state of* $\hat{\mathcal{H}}(g)$ *remains finite for all* $g \in [g_1, g_2]$. *This immediately implies that two states are in the same universality class if and only if they are adiabatically connected.*

While one implication of the above statement is useful in practice ("If one can find an adiabatic path connecting $|\Psi(g_1)\rangle$ and $|\Psi(g_2)\rangle$, then they are in the same universality class."), it is notoriously hard to decide whether *no* adiabatic path exists. To this end, Chen, Gu and Wen [27] provide an equivalent characterization of universality classes:

> *Two gapped states* $|\Psi(g_{1/2})\rangle$ *belong to the same universality class if and only if they are connected by a local unitary evolution.*

Here, a local unitary (LU) evolution is the time evolution under a local Hamiltonian for a finite time. It is important for the evolution to be possible in *finite* time, meaning in particular that it does not scale with the system size and remains finite in the thermodynamic limit.

The usefulness of the last characterization stems from the fact that for states belonging to the same phase the local unitary evolution can be constructed explicitly [28, 29].

1.1.1. Long-Range Entanglement and Topological Order

Having the definitions above at hand, the question arises what kinds of phases to expect. We start our further discussion by noting that there are broadly speaking two classes of states: *short-range entangled states* which can be transformed into a direct product state via a LU transformation, and *long-range entangled states* for which this is not possible. While there is only one phase of short-range entangled states,[1] there might be different long-range entangled phases of matter.

Short-range entangled states by definition are only governed by local properties of the system. In particular, they are not able to probe global, topological properties like the genus of the underlying manifold. Therefore, we say that *short-range entangled states have no topological order.*

In contrast, a non-trivial topological order is attributed to long-range entanglement:

> *The equivalence classes of local unitary transformation constitute distinct topological orders.*

This puts the colloquial statement that "distinct topologically ordered states cannot be transformed into each other without closing a gap" on rigorous grounds.

---

[1] This is true if we allow for transformations to break symmetries. If we require additional symmetries, the classification becomes richer, see below.

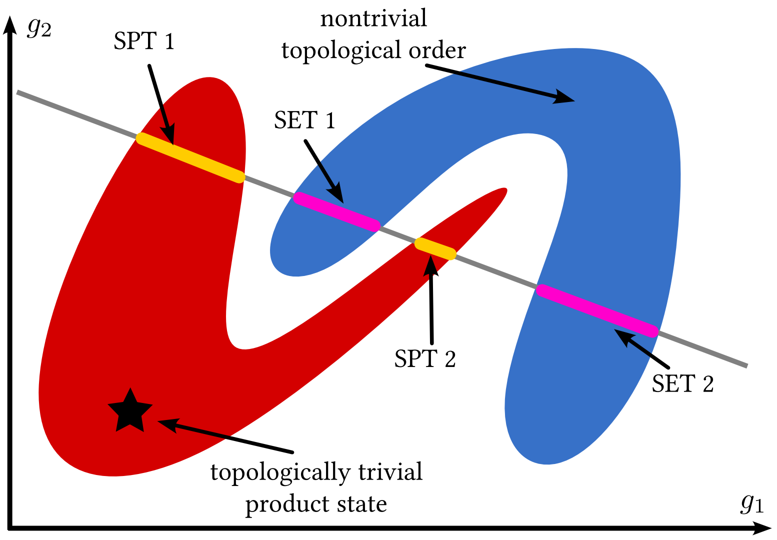

Fig. 1.1. Without relying on symmetries, topological universality classes indicated by the red and blue areas are defined as states which can be connected using a local unitary transformation. States in the red universality class can be connected to a product state (star) and are therefore topologically trivial. However, if we use a symmetry to constrain the allowed transformations to a subspace (gray line), we cannot connect certain states in the topologically trivial phase to each other (or the product state). The resulting phases are said to have symmetry protected topological (SPT) order. Similarly, enforcing a symmetry can lead to a finer classification of states with nontrivial topological order, called symmetry enriched topological (SET) orders. Figure adapted from Ref. [27] and [30].

In this thesis, we will discuss a particular example of topological order extensively. Quantum Hall states provide a prime example of topologically ordered states. In particular, they exhibit many of the characteristic features like quantum number fractionalization, chiral edge states and the famous topological ground state degeneracy. We will discuss these properties in more detail below as we develop our understanding of topological order further.

1.1.2. Symmetry Protected Topological (SPT) Phases

When defining short-range entanglement, we claimed all topologically trivial states to belong to the same phase. While this statement holds true in the absence of symmetries, requiring the LU transformations to obey certain symmetries enriches the picture significantly, see Fig. 1.1. In this case, not all states can be connected to the trivial product state while respecting the symmetries. Since the topological order in these states is protected by the symmetry at hand, such phases are called *symmetry protected topological (SPT) phases*. We emphasize again, that they are significantly different from phases with *intrinsic* topological order which does not require any symmetry.

Prominent examples of symmetries studied in the context of gapped, non-interacting systems are time-reversal (T), particle-hole (P), and chiral (C) symmetry [31]. For time-reversal T and particle-hole symmetry P, we distinguish three cases: the absence of the symmetry (denoted by 0) and - if present - whether the symmetry squares to $\pm\mathbb{1}$ (denoted by ± 1). In contrast, for the chiral symmetry C it is sufficient to distinguish whether the symmetry is present (1) or not (0). Using relations between these symmetries, it is possible to derive ten different combinations of them. We summarize the resulting ten universality classes in Tab. 1.1, where we also consider different dimensionalities d of the system. In this classification, generally known as the

				d							
Class	T	P	C	0	1	2	3	4	5	6	7
A	0	0	0	$\mathbb{Z}$		$\mathbb{Z}$		$\mathbb{Z}$		$\mathbb{Z}$	
AIII	0	0	1		$\mathbb{Z}$		$\mathbb{Z}$		$\mathbb{Z}$		$\mathbb{Z}$
AI	$+1$	0	0	$\mathbb{Z}$				$2\mathbb{Z}$		$\mathbb{Z}_2$	$\mathbb{Z}_2$
BDI	$+1$	$+1$	1	$\mathbb{Z}_2$	$\mathbb{Z}$				$2\mathbb{Z}$		$\mathbb{Z}_2$
D	0	$+1$	0	$\mathbb{Z}_2$	$\mathbb{Z}_2$	$\mathbb{Z}$				$2\mathbb{Z}$	
DIII	-1	$+1$	1		$\mathbb{Z}_2$	$\mathbb{Z}_2$	$\mathbb{Z}$				$2\mathbb{Z}$
AII	-1	0	0	$2\mathbb{Z}$		$\mathbb{Z}_2$	$\mathbb{Z}_2$	$\mathbb{Z}$			
CII	-1	-1	1		$2\mathbb{Z}$		$\mathbb{Z}_2$	$\mathbb{Z}_2$	$\mathbb{Z}$		
C	0	-1	0			$2\mathbb{Z}$		$\mathbb{Z}_2$	$\mathbb{Z}_2$	$\mathbb{Z}$	
CI	$+1$	-1	1				$2\mathbb{Z}$		$\mathbb{Z}_2$	$\mathbb{Z}_2$	$\mathbb{Z}$

Tab. 1.1. Altland-Zirnbauer classification of non-interacting topological phases. Here, d is the spatial dimension, T, P, and C denote the behavior of the Hamiltonian under time-reversal, particle-hole, and chiral transformations, respectively. The groups specify the possible values for the corresponding topological invariant, while an empty cell indicates the absence of (symmetry-protected) topological order in the corresponding system. The first row includes systems with intrinsic topological order, which is not protected by any symmetries. For $d = 2$ this class includes the integer quantum Hall states characterized by the Chern number. Adapted from Ref. [31].

"ten-fold way" or the "Altland-Zirnbauer" classification, states are identified by the values of a characteristic topological invariant. On general grounds, it turns out that such an invariant can only take values in $\mathbb{Z}$, $\mathbb{Z}_2$, or $2\mathbb{Z}$. Accordingly, an empty cell in the table indicates the absence of any (symmetry protected) topological order for the given set of symmetries and dimension. Furthermore, using general results, one can show that the pattern repeats upon an increase of dimensionality $d \to d + 8$, so that the table given here provides indeed a full classification of gapped, non-interacting topological orders.

Before turning to a more phenomenological perspective on topologically ordered phases, there are two more remarks:

When imposing symmetries, we can be even more ambitious. Starting from a phase with intrinsic topological order, we might again constrain the allowed LU transformation to obey certain symmetries. Similar to the case of SPT phases, this can lead to an additional fragmentation of the original topological universality class without symmetries. In this case, equivalence classes of the symmetry constrained transformations are called *symmetry enriched topological* (SET) phases, see Fig. 1.1.

Finally, one might wonder how this classification accounts for the ubiquitous symmetry breaking orders. In fact, such phases are topologically trivial and can be understood analogously to the SPT paradigm. However, in this case only a subset of states can be connected using LU transformations obeying the corresponding symmetry (the symmetric phase), while other states can only be reached by breaking the symmetry (the symmetry broken phase). In particular, different symmetry broken phases correspond to equivalence classes relying on LU transformations breaking different symmetries.

Using the classification of Chen, Gu, and Wen, we therefore end up with a whole zoo of possible phases:

- symmetry broken phases described by the Ginzburg-Landau paradigm,
- symmetry protected topological (SPT) phases,
- intrinsically topologically ordered phases, and
- symmetry enriched topological (SET) phases, refining an intrinsic topological order.

1.1.3. Detecting Topological Order

Our discussion of topological order so far focused on providing a formal definition. However, in physical applications the exotic properties of topological matter manifest themselves in certain characteristic phenomena. Before discussing a particular example of topological order in more detail in the next section, we will review some of the most striking properties here.

Topological Invariants

One of the hallmarks of topology in physics is the robust quantization of certain observables to integers or (simple) fractions. This quantization is often a consequence of the existence of a so-called topological invariant. Originating in algebraic topology, such invariants are understood as functors from the category of topological spaces (or manifolds) to the category of (Abelian) groups and are used to classify topological spaces and bundles [32]. Their calculation typically involves extensive use of algebraic relations and group theoretical results.

In contrast, in physics the group structure is rarely ever used and the value of an invariant is mainly used to characterize a topological phase of matter. However, the basic idea - finding a classification using a single number - carries over between fields. Most importantly, in both cases it requires a significant effort to change the value of a topological invariant: in topology this is often connected to cutting or gluing of spaces, whereas in physics a change typically indicates a topological phase transition (and therefore also a gap closing).

As we will encounter the Chern number at various points throughout this thesis, it seems appropriate to discuss this particular topological invariant in some more detail. Our discussion closely follows section II. of [33].

We start out by considering a Hamiltonian parametrized by a vector of parameters $\mathbf{g}$ with non-degenerate spectrum,

$$\hat{\mathcal{H}}(\mathbf{g}) \left|\psi_n(\mathbf{g})\right\rangle = E_n(\mathbf{g}) \left|\psi_n(\mathbf{g})\right\rangle . \tag{1.1}$$

Starting from an eigenstate $\left|\psi_n(\mathbf{g}(t=0))\right\rangle$, we consider a closed path $\mathbf{g}(t)$, $\mathbf{g}(t=0) = \mathbf{g}(t=1)$, in parameter space and adiabatically follow the instantaneous eigenstate $\left|\psi_n(\mathbf{g}(t))\right\rangle$. Upon returning to the initial parameters, the eigenstate has to return to the original state up to a phase factor,

$$\left|\psi_n(\mathbf{g}(t=0))\right\rangle = \mathrm{e}^{i\gamma_n} \left|\psi_n(\mathbf{g}(t=1))\right\rangle . \tag{1.2}$$

This phase contains a dynamical contribution,

$$\gamma_n^{(\mathrm{dyn})} = -\frac{1}{\hbar}\int_0^1 \mathrm{d}t\, E_n(\mathbf{g}(t)), \tag{1.3}$$

and a geometric contribution,

$$\gamma_n^{(\mathrm{geo})} = \oint \mathrm{d}\mathbf{g}\; i \left\langle \psi_n \middle| \nabla_{\mathbf{g}} \psi_n \right\rangle , \tag{1.4}$$

where the integrand of the geometric phase is the *Berry connection*[2] $\mathcal{A}^{(n)}(\mathbf{g}) = i \left\langle \psi_n \middle| \nabla_{\mathbf{g}} \psi_n \right\rangle$. For the case of more than one parameter we can define the *Berry curvature* as the exterior derivative of the Berry connection,

$$\mathcal{F}^{(n)}_{\mu\nu}(\mathbf{g}) = \partial_{g_\mu} \mathcal{A}^{(n)}_{\nu} - \partial_{g_\nu} \mathcal{A}^{(n)}_{\mu}. \tag{1.5}$$

While the Berry connection is a gauge dependent quantity under the gauge transformation $\left|\psi_n\right\rangle \to \mathrm{e}^{i\phi(\mathbf{g})} \left|\psi_n\right\rangle$, the Berry curvature does *not* depend on the gauge choice. Note that the

---

[2] This notion stems from the underlying geometric construction in which the Berry connection is indeed a connection on a certain $\mathrm{U}(1)$ fiber bundle. We will not elaborate on this further here, however, note the close analogy to the role of the $\mathrm{U}(1)$ gauge symmetry in electrodynamics.

Berry connection and curvature are both local, geometrical quantities. It is however possible to integrate the Berry curvature over a closed, two-dimensional submanifold $\mathcal{M}$ in parameter space to obtain a topological invariant known as the *(first) Chern number*,

$$C^{(n)} = \frac{1}{2\pi} \int_{\mathcal{M}} \mathrm{d}^2 g \, \mathcal{F}^{(n)}_{01}(\mathbf{g}), \tag{1.6}$$

where we denoted the components of the parameter space by $g_{0/1}$. It can be shown that the Chern number takes integer values [3] and therefore provides a useful topological invariant for two-dimensional systems. Furthermore, a similar construction using higher derivatives of the Berry connection allows for similar topological invariants in higher, even-dimensional parameter spaces.

For concreteness, we consider the case of Bloch bands in a two-dimensional lattice. In this case, the wave functions are the Bloch wave functions $|u^{(n)}_{\mathbf{q}}\rangle$ and the parameter space is given by the first Brillouin zone (BZ). Constructing the Berry connection and curvature as above, we can write the Chern number for the n-th single particle Bloch band as

$$C^{(n)} = \frac{1}{2\pi} \int_{\mathrm{BZ}} \mathrm{d}^2 q \; i\epsilon_{ij} \partial_{q_i} \langle u^{(n)}_{\mathbf{q}} | \partial_{q_j} u^{(n)}_{\mathbf{q}} \rangle = \frac{1}{2\pi} \int_{\mathrm{BZ}} \mathrm{d}^2 q \, \mathcal{F}^{(n)}(\mathbf{q}) \in \mathbb{Z}, \tag{1.7}$$

where we introduced the Berry flux $\mathcal{F}^{(n)}(\mathbf{q}) = \epsilon_{ij} \partial_{q_i} \mathcal{A}^{(n)}_j$.

Note that the Chern number can only take non-zero values if time-reversal symmetry is broken. Otherwise, the Bloch wave functions satisfy the relation $u^{(n)}_{\mathbf{q}}(\mathbf{r}) \propto u^{(n)}_{-\mathbf{q}}(\mathbf{r})^{\star}$ and therefore $\mathcal{F}^{(n)}(\mathbf{q}) = -\mathcal{F}^{(n)}(-\mathbf{q})$. The usual way to break time-reversal symmetry in solid state systems is the application of a magnetic field, while in cold atom systems for example shaking protocols can accomplish this.

Quantum Number Fractionalization & Anyons

While electrons and other elementary particles are considered indivisible, certain condensed matter systems exhibit a phenomenon known as quantum number fractionalization. An example for this are the charge carriers in fractional quantum Hall systems which for example for Laughlin states at $\nu = {}^{1}\!/_{m}$ were found to have charge $q = {}^{e}\!/_{m}$ [26, 35–37]. These charge carriers exhibit all properties of “usual” particles and are therefore considered quasiparticles of the system. However, since the underlying electrons are indeed not composed of sub-particles, single fractionalized quasiparticles can not be created locally, but are necessarily the result of a global operation. Note however, that not all topologically ordered systems exhibit fractionalized quasiparticles: the integer quantum Hall states provide a simple counterexample.

The fractionalized quasiparticles may not only carry a fraction of the elementary charge, but they might as well exhibit fractionalized braiding statistics [15, 16, 38]. In this case, adiabatically

---

[3] Using the more abstract language of differential forms, the Berry connection one-form is locally given by $A^{(n)} = \mathcal{A}^{(n)}_{\mu} \mathrm{d}g^{\mu}$, which however is in general not a *global* one-form but has to be defined on disjoint patches $\{\mathcal{M}_i\}_i$, the closure of which is covering all of $\mathcal{M}$. On the common boundaries of the patches the one-forms $A^{(n)}_i$ are connected by a gauge transformation, i.e. $A^{(n)}_1 - A^{(n)}_2 = \mathrm{d}f$ for a real-valued function f. Defining the Berry curvature two-form patch-wise by $F^{(n)}_i = \mathrm{d}A^{(n)}_i = \partial_{g^{\mu}} \mathcal{A}^{(n)}_{i;\nu} \mathrm{d}g^{\mu} \wedge \mathrm{d}g^{\nu}$, we can now define the Chern number as the integral $C^{(n)} = \frac{1}{2\pi} \sum_i \int_{\mathcal{M}_i} F^{(n)}_i$. For simplicity, we now assume that two patches $\mathcal{M}_1 \cup \mathcal{M}_2$ are sufficient to cover all of $\mathcal{M}$. We can now use Stokes’ theorem to rewritte the Chern number integral as $2\pi C^{(n)} = \int_{\mathcal{M}_1} F^{(n)}_1 + \int_{\mathcal{M}_2} F^{(n)}_2 = \int_{\mathcal{M}_1} \mathrm{d}A^{(n)}_1 + \int_{\mathcal{M}_2} \mathrm{d}A^{(n)}_2 = \oint_{\partial\mathcal{M}_1} A^{(n)}_1 + \oint_{\partial\mathcal{M}_2} A^{(n)}_2$. We note that the orientation of the boundaries $\partial\mathcal{M}_1$ and $\partial\mathcal{M}_2$ is opposite so that we can write $2\pi C^{(n)} = \oint_{\partial\mathcal{M}_1} \left(A^{(n)}_1 - A^{(n)}_2 \right) = \oint_{\partial\mathcal{M}_1} \mathrm{d}f$. This expression counts how often f winds by 2π along $\partial\mathcal{M}_1$ and hence always gives an integer multiple of 2π, so that the Chern number is quantized to be an integer. For more details, we refer the interested reader to Ref. [34].

exchanging two indistinguishable (quasi-)particles gives a phase $\mathrm{e}^{i\phi}$ in the wave function. (Fractionalized) Quasiparticles might result in a phase which is neither $\phi = 0$ (bosons), nor $\phi = \pi/2$ (fermions). As they can have any braiding statistics, they are also called *anyons*. Anyons can even exhibit non-Abelian braiding, where the order of the braiding operations involved plays a role and instead of a phase $\mathrm{e}^{i\phi} \in \mathrm{U}(1)$, a unitary matrix $\hat{U}$ is picked up by the many-body state. Non-Abelian braiding is considered as a possible route towards topological quantum computing [17].

The direct observation of anyonic braiding is one of the biggest experimental challenges in the context of topological systems. First experiments directly observed Abelian braiding in quantum Hall systems [39, 40], while non-Abelian braiding is still to be directly observed.

Topological Ground State Degeneracy

As already mentioned above, many topologically ordered states are able to "detect" the topology of the underlying manifold. A particularly striking instance of this is the ground state degeneracy of certain topologically ordered systems on a torus. More generally, for a surface of genus g the ground state degeneracy of many topological states can be seen to depend on g. Examples for this behavior are Kitaev's toric code [41] and Laughlin's fractional quantum Hall states [26, 42]. While this topological degeneracy is an important property of many topologically ordered states, it is again not necessary for a general topologically ordered phase. Once again, the integer quantum Hall states provide a simple counter example.

Edge States & Central Charge

As we discussed before, in the thermodynamic limit the invariant assigned to a gapped topological phase does not change as long as the excitation gap remains finite. This predicts a necessary gap closing at the interface between parts of distinct topological invariants.

A realization of this are gapless edge modes in topological systems, where the invariant necessarily has to change at the edge from a finite value in the system to zero in the ambient vacuum. Their existence is deeply connected to bulk properties of the system, a fact known as the *bulk-edge correspondence* [43, 44]. While we will not go into further detail regarding this correspondence, we mention that for quantum Hall systems the emergence of gapless edge modes is well understood [45–48]. Furthermore, we note that in this case the gapless modes even exhibit a well-defined chirality and are robust to perturbations of the system. In fact, they are the origin of the perfect transport along a Hall edge.

As the edge of a Hall system is described by a gapless, $(1+1)$-dimensional[4] theory, there is hope to model it using a conformal field theory (CFT). In particular, the edge theory of the system can be characterized (partially) by the central charge of the model. For our purposes, the central charge counts the number of gapless, chiral modes at the edge.

To understand the entanglement structure of the edge, we divide the system into two spatial subsystems A and $\bar{A}$ and construct the reduced density matrix $\hat{\rho}_A$ by taking the partial trace of the density matrix $\hat{\rho}$ over $\bar{A}$, i.e. $\hat{\rho}_A = \mathrm{tr}_{\bar{A}}\hat{\rho}$. Calculating the von Neumann entropy $S_A = \mathrm{tr}_A \hat{\rho}_A \log \hat{\rho}_A$ we obtain the *bipartite entanglement entropy*. For a gapless, finite, one-dimensional system of length L it was found [49] that the entanglement entropy for a subsystem of length ℓ scales as

$$S_A(\ell) = \frac{c}{6} \log\left(\frac{2L}{\pi a} \sin\left(\frac{\pi \ell}{L}\right)\right) + \text{const.}, \tag{1.8}$$

where c is the central charge and the constant term contains a non-universal contribution. Certain numerical methods, in particular those based on matrix product states, allow for a simple cal-

---

[4] Here, we explicitly included the time dependence of the theory.

culation of this entanglement entropy and are therefore well suited to extract the central charge of gapless quantum Hall edges without additional numerical effort.

Entanglement Entropy & Entanglement Spectra

Based on our definition of topologically ordered states using the notion of long-range entanglement, it seems natural to use the entanglement of the state itself to characterize topological order. By now, entanglement properties are a standard tool in identifying topologically ordered states in various different systems.

While in the last section we focused on a spatial bipartition of the system, also other bipartitions are possible. For a general bipartition, the state $|\psi\rangle$ can be written using the Schmidt decomposition

$$|\psi\rangle = \sum_k \mathrm{e}^{-\lambda_k/2} \, |\phi_A^k\rangle \, |\phi_{\bar{A}}^k\rangle \,, \tag{1.9}$$

where the $|\phi_\Omega^k\rangle$ are orthonormal in the k-index and are defined on the respective part Ω of the system. The Schmidt values λ_k can be used to calculate the entanglement entropy $S_A = \sum_k \lambda_k \mathrm{e}^{-\lambda_k}$ discussed above.

Furthermore, the full set of Schmidt values constitutes the *entanglement spectrum* of the state. This entanglement spectrum was found to be a unique “fingerprint” of certain topologically ordered states. For a spatial partition it proves particularly useful to study the edge theory of the system [50]. In particular, resolving the momentum or angular momentum associated with certain Schmidt values allows for fundamental insights into the nature of the edge. In contrast, a bipartition in particle number space gives a characterization of the quasiholes of the system [51–53].

Finally, topologically ordered systems exhibit a special form of spatial entanglement. In particular, gapped systems exhibit an area law scaling of the entanglement entropy of the form

$$S = \alpha L - \gamma + \ldots, \tag{1.10}$$

where L is the length of the boundary between two spatial subparts and the terms included in ... vanish as $1/L$ when $L \to \infty$. The coefficient $-\gamma$ of the $\mathcal{O}(L^0)$ contribution has been shown to be universal and is called the *topological entanglement entropy* (TEE). The TEE is related to the anyon content of the topological order and therefore can serve as an indicator for topological order [54, 55].

1.2. Quantum Hall Effects and (Fractional) Chern Insulators

In 1980, von Klitzing, Dorda, and Pepper made a ground breaking discovery. While studying a two-dimensional electron gas (2DEG) in a silicon MOSFET (metal-oxide-semiconductor field-effect transistor), they found a “new, potentially high-accuracy method for determining the fine-structure constant” [10]. However, their discovery became famous with a significantly different interpretation. Nowadays, the phenomenon is generally known as the *integer quantum Hall effect.*

From a theoretical point of view, the model describing their effect is strikingly simple. Electrons confined to a two-dimensional plane with a (strong) perpendicular magnetic field are described by the first-quantized Hamiltonian

$$\hat{\mathcal{H}} = \sum_i \frac{1}{2m_b} \left(\hat{\mathbf{p}}_i + \frac{e}{c} \mathbf{A}(\hat{\mathbf{r}}_i) \right)^2 + \sum_i U(\hat{\mathbf{r}}_i) + \frac{e^2}{\epsilon} \sum_{i<j} \frac{1}{|\hat{\mathbf{r}}_i - \hat{\mathbf{r}}_j|} + g\mu \sum_i \mathbf{B} \cdot \hat{\mathbf{S}}_i. \tag{1.11}$$

The first two terms describe the single-particle contributions, where m_b is the band mass of the electrons, $U(\hat{\mathbf{r}})$ is some external potential and $\mathbf{A}$ is the vector potential describing the external magnetic field $\mathbf{B} = \mathrm{rot}\mathbf{A}$. The third term describes the Coulomb repulsion between electrons, while the last term gives the Zeeman energy due to the external magnetic field.

Assuming a strong magnetic field and finite Landé factor $g \neq 0$, the ground state will be spin polarized so that the last term gives a constant contribution and therefore can be ignored. Diagonalizing the non-interacting model first, one finds largely degenerate Landau levels, which are separated by the cyclotron frequency $\omega_c = \frac{eB}{m_b c}$. As it turns out, each of these Landau levels can be assigned a Chern number $C = \pm 1$ which in turn is related to the transverse Hall response of the system [11].

1.2.1. Linear Response Theory: The TKNN Formula

Assuming a band insulating system, this result can be obtained in linear response theory, where the current response to an external electric field $\mathbf{E}(\omega)$ can be written as $\left\langle \hat{\mathbf{j}} \right\rangle (\omega) = \underline{\underline{\sigma}}(\omega)\mathbf{E}(\omega)$. Using the Kubo formula, we can derive an expression for the transverse Hall conductance $\sigma_H = \sigma_{xy}$ in the limit of a static external field, $\omega \to 0$,

$$\sigma_H = -\frac{i\hbar}{A_0 Z} \sum_{\gamma,\delta} \frac{\mathrm{e}^{-\beta E_\gamma} - \mathrm{e}^{-\beta E_\delta}}{(E_\gamma - E_\delta)^2} \langle \gamma | \hat{j}_x | \delta \rangle \langle \delta | \hat{j}_y | \gamma \rangle \,, \tag{1.12}$$

where γ, δ label the energy eigenstates, A_0 is the area of the Hall sample, Z is the partition sum, and $\beta = {}^1\!/_{k_\mathrm{B}T}$ is the inverse temperature. We expand the wave functions in terms of Bloch states $|u_\mathbf{k}^{(n)}\rangle$ and note that in this case the current operator can be written as the derivative of the Hamiltonian, $\hat{\mathbf{j}} = \frac{e}{\hbar}\nabla_\mathbf{k}\hat{\mathcal{H}}$. Thus, we find an expression for the Hall conductance in terms of the Bloch states,

$$\sigma_H = -\frac{ie^2}{A_0\hbar} \sum_{\mathbf{k},\mathbf{q},m,n} \frac{n_F(\varepsilon_\mathbf{k}^{(n)}) - n_F(\varepsilon_\mathbf{q}^{(m)})}{\left(\varepsilon_\mathbf{k}^{(m)} - \varepsilon_\mathbf{q}^{(n)}\right)^2} \langle u_\mathbf{k}^{(n)} | \frac{\partial \hat{\mathcal{H}}}{\partial k_x} | u_\mathbf{q}^{(m)} \rangle \langle u_\mathbf{q}^{(m)} | \frac{\partial \hat{\mathcal{H}}}{\partial k_y} | u_\mathbf{k}^{(n)} \rangle \,, \tag{1.13}$$

We rewrite the matrix elements as

$$\langle u_\mathbf{k}^{(n)} | \frac{\partial \hat{\mathcal{H}}}{\partial k_x} | u_\mathbf{q}^{(m)} \rangle = \left(\varepsilon_\mathbf{k}^{(n)} - \varepsilon_\mathbf{q}^{(m)}\right) \langle \partial_{k_x} u_\mathbf{k}^{(n)} | u_\mathbf{q}^{(m)} \rangle \tag{1.14}$$

and thus obtain

$$\begin{aligned} \sigma_H &= \frac{ie^2}{A_0\hbar} \sum_{\mathbf{k},\mathbf{q},m,n} n_F(\varepsilon_\mathbf{k}^{(n)}) \left(\langle \partial_{k_x} u_\mathbf{k}^{(n)} | u_\mathbf{q}^{(m)} \rangle \langle u_\mathbf{q}^{(m)} | \partial_{k_y} u_\mathbf{k}^{(n)} \rangle - (x \leftrightarrow y) \right) \\ &= \frac{e^2}{A_0\hbar} \sum_{\mathbf{k},n} n_F(\varepsilon_\mathbf{k}^{(n)}) i\epsilon_{ij} \langle \partial_{k_i} u_\mathbf{k}^{(n)} | \partial_{k_j} u_\mathbf{k}^{(n)} \rangle \\ &= \frac{e^2}{(2\pi)^2\hbar} \sum_n \int_\mathrm{BZ} \mathrm{d}^2k \, n_F(\varepsilon_\mathbf{k}^{(n)}) \, i\epsilon_{ij} \partial_{k_i} \langle u_\mathbf{k}^{(n)} | \partial_{k_j} u_\mathbf{k}^{(n)} \rangle \,. \end{aligned} \tag{1.15}$$

In the low temperature regime the Fermi-Dirac distribution trivializes to $n_F(\varepsilon_\mathbf{k}^{(n)}) = 1 \ (0)$ for completely filled (empty) Bloch bands. Therefore, we can rewrite the last integral expression as

$$\sigma_H = \frac{e^2}{h} \sum_{n \text{ filled}} \frac{1}{2\pi} \int_\mathrm{BZ} \mathrm{d}^2k \, \mathcal{F}^{(n)}(\mathbf{k}) = \frac{e^2}{h} \sum_{n \text{ filled}} C^{(n)}, \tag{1.16}$$

where we used the definition of the Chern number (Eq. (1.7)) in the last step.

This celebrated result is known as the *TKNN formula* named after Thouless, Khomoto, Nightingale, and den Nijs [11] and states that completely filled Bloch bands can exhibit a quantized Hall response if the bands are topologically non-trivial, $C^{(n)} \neq 0$. This result was also generalized to interacting and disordered systems by Niu, Thouless, and Wu [14] and lies at the heart of the topological understanding of the quantum Hall effect.

1.2.2. Integer Quantum Hall Effect

By tuning the magnetic flux density B or the electron density ρ, the magnetic filling factor $\nu = \frac{\rho}{B/\phi_0}$ of the system can be changed. Here, we measure the magnetic flux in units of the flux quantum $\phi_0 = \frac{h}{ce}$. Close to integer filling factors $\nu = n \in \mathbb{N}$, the Hall resistance $R_\mathrm{H} = \frac{1}{\sigma_\mathrm{H}}$ of systems with weak disorder develops characteristic plateaus at

$$R_\mathrm{H} = \frac{h}{ne^2} = \frac{R_\mathrm{K}}{n}, \qquad n \in \mathbb{N}, \tag{1.17}$$

where we defined the von Klitzing constant $R_\mathrm{K} = {}^{h}\!/\!{}_{e^2}$. This quantization is exactly the discovery by von Klitzing *et al.* and can be understood using a purely non-interacting picture. In particular, the ground state of the system is unique for the case of completely filled Landau levels, $\nu \in \mathbb{N}$.

A proper theory of the origin of extended Hall plateaus necessarily includes the role of disorder in realistic systems. In this case, the longitudinal super-current is carried by extended edge states alone, while in the bulk disorder leads to finite width Hall plateaus around $\nu \in \mathbb{N}$. We do not discuss this in further detail but refer the interested reader to the existing literature [56, 57].

1.2.3. Fractional Quantum Hall Effect

The physics of the 2DEG changes drastically if we consider partially filled Landau levels. From the non-interacting picture we expect an extensive ground state degeneracy and by no means any plateaus in the Hall resistance. However, interactions (for example the Coulomb interaction in electronic systems) can lift this degeneracy and might still favor an (incompressible) unique ground state for certain values of the filling factor.

In fact, Tsui, Stormer, and Gossard observed a quantized plateau at filling factor $\nu = {}^{1}\!/\!{}_{3}$ in 1982 [13], introducing the fractional quantum Hall (FQH) effect. Soon after, many other plateaus at fractional filling factors were found, almost exclusively at odd denominator fractions. Up to this day, precision experiments identify new fractions and the list of Hall plateaus continues to grow, see Fig. 1.2.

While many details of the Hall problem depend on the specific form of the interaction and the number of filled Landau levels[5], some variational results are known.

Probably the most prominent variational trial state is the celebrated wave function which earned Laughlin his share of the 1998 Nobel prize in physics [26]. Starting from the so-called plasma analogy, he derived a wave function which matches the energy and other observables obtained in exact diagonalization studies almost perfectly. The Laughlin wave function at filling factor $\nu = {}^{1}\!/\!{}_{m}$,

$$\Psi_\mathrm{LN}^{(m)}(z_1, \ldots, z_N) \propto \left(\prod_{i<j} (z_i - z_j)^m \right) \mathrm{e}^{-\frac{1}{4}\sum_k |z_k|^2}, \tag{1.18}$$

---

[5] Projecting the potential to the lowest partially-filled Landau level and treating the other Landau levels as inert typically gives good results. However, this is a subtle question as can be seen in the context of the absence of a Hall plateau at $\nu = {}^{1}\!/\!{}_{2}$ [59].

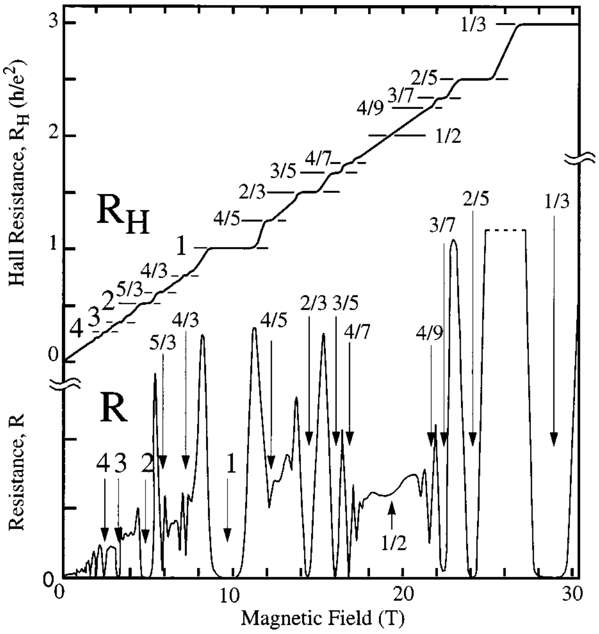

Fig. 1.2. The "fractional quantum Hall skyline" around the time when the Nobel prize in physics was awarded to Laughlin, Stormer, and Tsui for their work on the phenomenon. The Hall resistance R_H exhibits clear plateaus at various integer and fractional values of the filling factor, where the longitudinal resistance R drops to zero. This figure was taken from Ref. [58].

can be written down for fermions (odd m) as well as for bosons (even m). Here, we introduced the convention to write the two-dimensional coordinates using a complex coordinate $z = x + iy$ and in units of the magnetic length $\ell_B = \sqrt{\hbar c/eB}$. The first term is called the Jastrow factor and plays a crucial role in the understanding of the short-range correlations of the Laughlin state. In particular, we see that the two-particle correlations $g^{(2)}(z, z') = \langle : \hat{\rho}(z)\hat{\rho}(z') : \rangle$ decay polynomially as $z \to z'$, where $\hat{\rho}$ is the local density operator and $: \ldots :$ denotes normal ordering.

Building upon Laughlin's trial wave function and hierarchy states derived from it, Jain proposed the idea of weakly interacting composite fermions (CFs) as appropriate quasiparticles for the quantum Hall problem [60]. In this picture, each constituent particle forms a bound state with a given number of magnetic flux quanta, see Fig. 1.3. Thus, the CFs experience a reduced magnetic field forming Landau level-like Λ *levels*. Neglecting interactions between CFs, we might again consider completely filled Λ levels and a resulting integer quantum Hall effect for CFs. However, because of the flux attachment, the filling factor with respect to the external magnetic field can now take fractional values as observed.

The CF picture provides an intuition for the even richer physics of the interacting quantum Hall problem. In particular, allowing interactions between composite fermions one might arrive at a full hierarchy of fractional quantum Hall states [61] and even paired states [62]. We will discuss some of these states in more detail in this thesis.

Before concluding our brief introduction to the fractional quantum Hall effect, we would like to have a brief look at the related topological invariant. While in the non-interacting case an expansion in Bloch wave functions provides a simple connection between the Hall response and the Chern number as an integral over the Brillouin zone, this simple argument does not apply to interacting systems. However, introducing so called twisted-boundary conditions where additional phases are acquired as a particle encircles the holes of a torus, Niu, Thouless, and Wu defined a many-body Chern number, which even accounts for the ground state degeneracy on

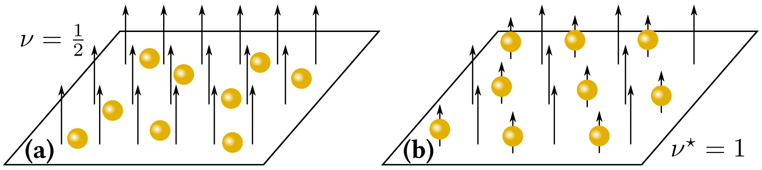

Fig. 1.3. **(a)** Bosons (visualized as yellow spheres) experiencing a strong magnetic field at magnetic filling factor $\nu = 1/2$. Upon attaching one flux quantum to each boson, composite fermions (CFs) are formed **(b)**. The CFs experience a reduced magnetic field and hence an increased magnetic filling factor $\nu^\star = 1$ of effective Λ levels. The resulting integer quantum Hall state of CFs can give physical intuition for the fractional quantum Hall state of the original bosons. A very similar construction is possible for fermions or more attached flux quanta per particle. Figure adapted from Ref. [57].

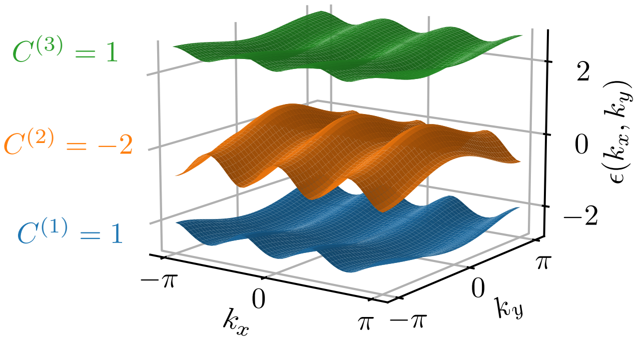

Fig. 1.4. Band structure for a Hofstadter model at $\alpha = 1/3$ flux quanta per plaquette on a torus. Note the finite Chern number $C^{(n)} \neq 0$ of all Hofstadter bands.

the torus. In particular, they generalized the TKNN formula to the interacting case and therefore provided a topological explanation of the fractional quantum Hall effect [14].

1.2.4. (Fractional) Chern Insulators

The attempt to discretize the quantum Hall problem seems a natural step both from a theoretical point of view as well as from the perspective of cold atom experiments in optical lattices. In some sense, this fundamental problem was first addressed by Hofstadter when discussing the problem of Bloch electrons in a magnetic field [63]. While the Hofstadter model explicitly assumes non-interacting particles it already contains the necessary topological band structure to exhibit quantum Hall-like physics. In fact, completely filled Hofstadter bands can be understood as an immediate analog of the integer quantum Hall system and their Hall response can be explained noting the non-zero Chern number of Hofstadter bands, see Fig. 1.4. As the ground state for a completely filled Chern band is an insulator, the lattice analogs of integer quantum Hall states are also called *Chern insulators*.

However, adding interactions was found to enrich the zoo of quantum Hall states enormously. This problem was first addressed by Kol and Read starting from a FQH state in the presence of a periodic potential [64]. Hofstadter-Hubbard models are natural candidates for rich ground state phase diagrams discretizing the fractional quantum Hall problem on the Hamiltonian side. This is even more true as the lattice introduces an additional, competing length scale to the problem and therefore lattice effects might result in interesting new physics. Today, the lattice analogs (and generalizations as we shall see below) of FQH states are known as *fractional Chern insulators* (FCIs).

The vanilla Hofstadter-Bose-Hubbard model was first studied by Sørensen, Demler, and Lukin in a cold atom context [65]. They found an analog of the Laughlin state at $\nu = 1/2$ to be robust to lattice effects, a finding which was discussed further by the same authors together with Hafezi [66]. Further numerical studies explored the phase diagram of the Hofstadter-Hubbard model for bosons [1, 2, 67–74] and fermions [3, 71, 75] in more detail. Also preparation schemes were proposed to realize ground states of said models in optical lattices [1, 76–81] and proposals for their detection exist [82–94]. The non-interacting Hofstadter model was realized with ultracold atoms [20, 21], as well as its interacting analog [22]. Recently, also a first atomic Laughlin state in a Hofstadter-Bose-Hubbard model was realized [25].

Note that all non-trivial Chern bands discussed in this thesis so far required some kind of (artificial) magnetic field to break time-reversal symmetry. However, Haldane noticed already in his seminal work in 1988 that it is also possible to break time-reversal symmetry without a net magnetic field [95]. In a simple tight-binding model this can be achieved by introducing complex hopping amplitudes. This idea stimulated new interest in this direction and lead to a plethora of FCI states without net magnetic field in recent years. By now, there exist various proposals for their realization in different experimental platforms. For a review of this exciting field of research we refer the reader to Ref. [96].

In this thesis, we will not discuss the rich physics of FCIs in the absence of a net magnetic field, but will restrict ourselves to the study of lattice analogs of FQH states. However, already this subclass provides interesting challenges for both theory and experiments as we will discuss below.

1.3. Quantum Simulation of Quantum Hall Systems

While historically the FQH effect was discovered and first studied in solids, these experiments typically do not allow for direct local insight into the correlated nature of the state. However, such insight is highly desirable if one tries to understand and ultimately manipulate the microscopic structure of interesting states of matter. Quantum simulators, which use one quantum system to simulate another one, may provide an opportunity to address this need. One particular hope of FQH physicsts with respect to quantum simulation is the creation, manipulation and observation of non-Abelian excitations. As this goal is also one of the major motivations for this thesis, we next review state-of-the-art quantum simulation platforms with a special emphasis on cold atom systems.

1.3.1. Cold Atoms in the Continuum

Approaches to simulate continuum quantum Hall physics in cold atomic gases used rapidly rotating harmonic traps to mimic the effect of a magnetic fields [97–100]. In the rotating frame the Hamiltonian is formally equivalent to the FQH problem if the rotation frequency Ω approaches the harmonic oscillator frequency ω. It was shown theoretically that even upon replacing the Coulomb interaction by an on-site repulsion the system can exhibit interesting FQH states [101–104]. Furthermore, protocols to prepare such states and even their anyonic excitations were developed [105–107]. Although reaching the quantum degenerate regime turned out to be challenging, Gemelke, Sarajlic, and Chu observed signatures of a bosonic Laughlin state at $\nu = 1/2$ in rotating microtraps [23].

For a review of rapidly rotating quantum gases we refer the interested reader to Ref. [108] and references therein. We remark that a similar approach has recently seen revived interest, for example in an experiment in Zwierlein's group [99, 100].

1.3.2. Cold Atoms in Optical Lattices

Over the last two decades, cold atoms in optical lattices have provided an alternative approach to quantum simulation. A high degree of control and versatility along with advanced single-site quantum gas microscopy [109–112] make this platform particularly promising to study novel states of matter. Experimental measurements of multi-point correlation functions give highly desirable insights into the microscopic correlated nature of such states. Furthermore, interferometric probes of topological invariants in such systems were already demonstrated [113, 114] and extensions of such methods to anyons are possible [39, 84].

Here, we briefly provide some theoretical background on the models used to describe these systems. We restrict this discussion to spinless, bosonic systems, however most of these concepts can easily be generalized to spinful particles and in particular fermions, at least on the theoretical side.[6] From a theory point of view, spinless bosons in an optical square lattice are accurately described by the Bose-Hubbard model:

$$\hat{\mathcal{H}}_{\mathrm{BH}} = -t \sum_{\langle \mathbf{i},\mathbf{j} \rangle} \left(\hat{a}_{\mathbf{i}}^{\dagger} \hat{a}_{\mathbf{j}} + \mathrm{H.c.} \right) + \frac{U}{2} \sum_{\mathbf{i}} \hat{n}_{\mathbf{i}} \left(\hat{n}_{\mathbf{i}} - 1 \right). \tag{1.19}$$

Here, $\hat{a}_{\mathbf{i}}^{(\dagger)}$ are the bosonic annihilation (creation) operators, t is the hopping amplitude between neighboring lattice sites $\langle \mathbf{i}, \mathbf{j} \rangle$, and U is the strength of the on-site Hubbard interaction.

To study the effect of a magnetic field piercing the system, we include so-called Peierls phases in the hopping terms, $t \to t \exp\left[i\varphi_{\langle \mathbf{i},\mathbf{j} \rangle} \right]$. Using these phases, we can define the flux per plaquette α via

$$\sum_{\lambda \in \partial p} \varphi_{\lambda} = 2\pi\alpha, \tag{1.20}$$

where p is a given plaquette with boundary links ∂p. Similar to the usual quantum Hall problem we assume the magnetic field to be static, so that we treat the phases as fixed, external parameters of the model. We will use the gauge redundancy of the vector potential, which is also present in the Peierls phases, to choose a specific gauge in our studies.

Including magnetic fields into the Bose-Hubbard model, we finally end up with the *Hofstadter-Bose-Hubbard model* described by the Hamiltonian

$$\hat{\mathcal{H}}_{\mathrm{HBH}} = -t \sum_{\langle \mathbf{i},\mathbf{j} \rangle} \left(\mathrm{e}^{i\varphi_{\langle \mathbf{i},\mathbf{j} \rangle}} \, \hat{a}_{\mathbf{i}}^{\dagger} \hat{a}_{\mathbf{j}} + \mathrm{H.c.} \right) + \frac{U}{2} \sum_{\mathbf{i}} \hat{n}_{\mathbf{i}} \left(\hat{n}_{\mathbf{i}} - 1 \right). \tag{1.21}$$

The Hofstadter-Bose-Hubbard model is a natural discretization of the problem of an interacting two-dimensional system in a strong perpendicular magnetic field, i.e. the fractional quantum Hall problem. As already mentioned in our discussion of fractional Chern insulators, numerical studies of the Hofstadter-Bose-Hubbard model found various FQH states in this model.

Over the last decade, cold atom experiments using optical lattices became capable of implementing non-interacting [20, 21, 115, 116] and interacting [22] Hofstadter models using cold atoms. These experiments culminated in the recent realization of the first atomic Laughlin state in a lattice system in Greiner's group [25].

1.3.3. Other Quantum Simulation Platforms

While the projects in this thesis are mainly inspired by and tailored to the needs of cold atom experiments, we briefly mention alternative platforms useful for quantum simulations of

---

[6] Experiments with cold fermions have their very own challenges, which we will not discuss further here.

fractional quantum Hall physics. We note however, that many of these platforms follow a slightly different approach than the cold atom quantum simulators discussed above: While the latter try to realize FQH states as ground states of a Hamiltonian inspired by the electronic Hall problem, an alternative approach tries to realize the corresponding states without referring to a certain Hamiltonian. Consequently, while such platforms allow for more flexibility in realizing the target state itself, they might be less suited for studying excitations and dynamics of FQH systems.

In this context we especially emphasize photonic systems which create interesting states of matter from individual photons. As one result of these efforts, a Laughlin state of two photons was realized in Simon's group in 2020 [24]. Furthermore, photonic systems might even be capable of realizing models reminiscent of the Hall problem [117–125]. For a more systematic review of the capabilities of photonic platforms, we refer the interested reader to Ref. [126].

Yet another platform are Rydberg atoms, which are closely related to other cold atom setups but somewhat different in spirit with respect to Hall physics. Again, there exist proposals to realize FQH states on their own without referring to the Hall problem per se [127]. Recently, also a realization of a bosonic Laughlin state in a Rydberg system starting from a Hofstadter-Hubbard-type Hamiltonian was proposed [128, 129].

Finally, we would like to mention that spin systems may also provide a possibility to study FQH physics. This seems reasonable given the existing connection between FQH states and certain quantum spin liquids discussed already in the early days of the field [130]. Whether this analogy could be exploited for quantum simulation platforms remains unclear, however the vast existing technology to simulate spin systems using for example trapped ions or superconducting qubits might prove useful here.

In summary, the quantum simulation of fractional quantum Hall systems provides a new way to study and manipulate interacting phases of matter. Furthermore, the extraordinary flexibility of these platforms compared to usual solid state devices provides an exciting playground also for theorists. Nevertheless, observables to identify and characterize topological phases are needed, as well as realistic preparation schemes for large systems. The scope of this thesis is to address these questions with more complicated states in mind. In particular, an unambiguous direct observation of non-Abelian braiding might be addressed using quantum simulators. Not surprisingly, a significant part of this thesis explores the question whether the Pfaffian state, a "simple" state exhibiting non-Abelian excitations, can be realized and detected in cold atom experiments.

1.4. Numerical Methods

Before concluding this introductory discussion of the background of this thesis, we briefly introduce the numerical methods used. While the emphasis of this thesis lies on physical insight instead of developing numerical methods, such methods are heavily used here to tackle challenging quantum many-body problems. We restrict our discussion to the mere minimum necessary to understand and appreciate the methods used and the results obtained here. In particular, the presentation here by no means claims to be a complete review of any technical details. For more detailed discussions we refer the interested reader to the existing literature where appropriate.

1.4.1. Variational Principle

The variational principle is without doubt one of the corner stones for finding approximate solutions to complicated quantum mechanical problems. As most of the numerical methods used in this thesis rely on this result, we will briefly review it in an abstract setting.

Consider a quantum mechanical problem described by a Hamiltonian $\hat{\mathcal{H}}$, where we do not specify whether the system is interacting or not. We denote the (unknown and most likely complicated) eigenstates of the Hamiltonian by $|\varphi_\alpha\rangle$, which form a complete, orthonormal eigenbasis of the underlying Hilbert space. Therefore, we can expand an arbitrary state $|\psi\rangle$ in this basis:

$$|\psi\rangle = \sum_\alpha |\varphi_\alpha\rangle \langle\varphi_\alpha|\psi\rangle =: \sum_\alpha c_\alpha |\varphi_\alpha\rangle . \tag{1.22}$$

Accordingly, we can write the expectation value of the Hamiltonian for this state as

$$\langle\psi|\hat{\mathcal{H}}|\psi\rangle = \sum_{\alpha,\beta} \overline{c_\alpha} c_\beta \langle\varphi_\alpha|\hat{\mathcal{H}}|\varphi_\beta\rangle = \sum_\alpha E_\alpha |c_\alpha|^2. \tag{1.23}$$

For reasonable physical models the Hamiltonian is bounded from below so that there is a minimal eigenenergy E_0 associated with the ground state $|\varphi_0\rangle$ of the model. Therefore, we can estimate the expectation value of $\hat{\mathcal{H}}$ for the state $|\psi\rangle$ to be

$$\langle\psi|\hat{\mathcal{H}}|\psi\rangle \geq E_0 \sum_\alpha |c_\alpha|^2 = E_0 \langle\psi|\psi\rangle , \tag{1.24}$$

with equality for the (possibly degenerate) ground state $|\psi\rangle = |\varphi_0\rangle$. Equivalently, we can obtain the ground state energy E_0 by minimizing over all allowed states:

$$E_0 = \min_{|\psi\rangle} \frac{\langle\psi|\hat{\mathcal{H}}|\psi\rangle}{\langle\psi|\psi\rangle}. \tag{1.25}$$

If we restrict the states $|\psi\rangle$ to a subspace $\mathscr{H}_\text{var}$ of the physical Hilbert space, we can still perform this minimization, however now the equality does not hold necessarily, as the ground state might lie outside of $\mathscr{H}_\text{var}$. Nevertheless, we can find a variational upper bound to the ground state energy:

$$E_0 \leq \inf_{|\psi\rangle \in \mathscr{H}_\text{var}} \frac{\langle\psi|\hat{\mathcal{H}}|\psi\rangle}{\langle\psi|\psi\rangle}. \tag{1.26}$$

This result is known as the famous *variational principle*.

The variational principle is particularly useful for interacting many-body systems, where the true ground state is in many cases very hard to find or completely unknown. However, in many cases certain *variational ansätze*, i.e. parametrizations of the subspace $\mathscr{H}_\text{var}$, can be chosen based on physical intuition or numerical capabilities. Famous examples are Laughlin's wave functions for FQH states [26] on the analytical side and for example variational Monte Carlo methods on the numerical side [131]. In recent years, also more complicated ansatz classes like artificial neural networks [132] or various tensor network ansätze have become popular in the numerical community. In this thesis, we will mainly use matrix product states, one particular tensor network ansatz. Therefore, we will next introduce these concepts.

1.4.2. Matrix Product States and Density Matrix Renormalization Group

As discussed above, approximate solutions of correlated quantum many-body systems can be found using a suitable parametrization of the many-body state by a variational ansatz. One particularly successful ansatz class are tensor network states, which we will briefly introduce in an abstract way before turning to a specific subclass used extensively in this thesis.

Consider a lattice model of L sites with a local d-dimensional Hilbert space $\mathscr{H}_i = \text{span}\,\{|\sigma_i\rangle\}$ at each site i. A general quantum state $|\Psi\rangle$ in the full Hilbert space $\mathscr{H} = \bigotimes_{i=1,\dots,L} \mathscr{H}_i$ can then be written as

$$|\Psi\rangle = \sum_{\sigma_1,\dots,\sigma_L} c_{\sigma_1,\dots,\sigma_L} |\sigma_1,\dots,\sigma_L\rangle , \qquad \text{with } c_{\sigma_1,\dots,\sigma_L} \in \mathbb{C}. \tag{1.27}$$

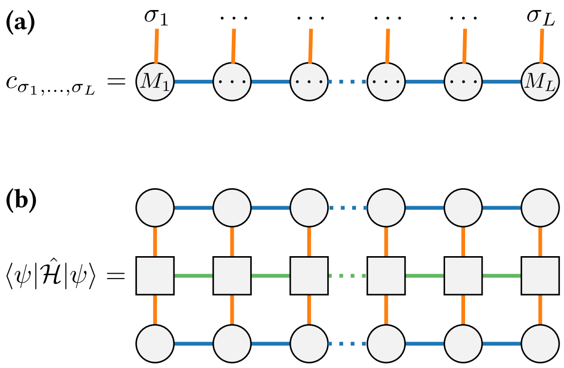

Fig. 1.5. Graphical representation of tensor networks used in matrix product states and operators. Internal legs of the MPS (MPO) are indicated in blue (green), while physical legs are indicated in orange. Rank-3 MPS tensors are depicted as circles, whereas squares represent rank-4 MPO tensors. **(a)** Partially contracted tensor network representing a typical coefficient of a generic many-body state. **(b)** Fully contracted tensor network representing the expectation value of the Hamilton operator $\hat{\mathcal{H}}$.

In this form, we have to calculate and store $\mathcal{O}\left(d^L\right)$ coefficients to represent the state. Even if symmetries or other constraints can reduce the number of distinct, non-zero coefficients, this becomes hardly tractable for a classical computer for already tens of sites, especially for bosonic systems, where the local Hilbert space is a priori infinite-dimensional.

A more efficient way of representing a quantum state uses local tensors $\underline{\underline{T}}_i^{\sigma_i}$ of rank n [133]. In an abstract form, we can then rewrite the coefficients of our quantum state as

$$c_{\sigma_1,\ldots,\sigma_L} = \mathrm{Tr}\left(\prod_{i=1}^{L} \underline{\underline{T}}_i^{\sigma_i}\right), \tag{1.28}$$

where internal indices of the tensors have been contracted and are therefore suppressed in our notation. This representation has the advantage that instead of storing and manipulating the $\mathcal{O}(d^L)$ coefficients of the full quantum state, we instead approximate the state using $\mathcal{O}(dL\chi^N)$ parameters, where χ is the dimension of the internal indices, also called the bond dimension, and N is typically a small number for tensor networks of practical use. In particular, by restricting the bond dimension, one can obtain (controlled) approximations of the true quantum state. Especially if there is an efficient method to optimize the tensors of the tensor network variationally, then increasing the bond dimension can provide more and more accurate approximate solutions.

Note that not all tensor networks are equally useful for our purposes for various (sometimes subtle) reasons [133, 134]. In fact, different tensor network topologies were used and tailored for specific physical applications and we do not go into further detail here. On the contrary, we will restrict our discussion to an especially well-behaved class of tensor network states known as *matrix product states* (MPS).

Matrix Product States

As the name suggests, matrix product states use matrices $\underline{\underline{M}}_i^{\sigma_i}$ (i.e. tensors of rank 3, one physical index and two internal indices) as local tensors, see Fig. 1.5**(a)**. In this case, the contraction of internal indices corresponds to the usual matrix multiplication and we can rewrite the coefficients of an arbitrary quantum state $|\Psi\rangle$ as

$$c_{\sigma_1,\ldots,\sigma_L} = \prod_{i=1}^{L} \underline{\underline{M}}_i^{\sigma_i}. \tag{1.29}$$

Here, the matrices have dimensions $(\chi_i, \chi_i + 1)$, where in particular $\chi_1 = \chi_{L+1} = 1$ so that we do not need to take the trace explicitly. As alluded to before, we introduce the over all bond dimension $\chi = \max_i \chi_i$. For applications it is crucial to find a good approximation of the many-body state $|\Psi\rangle$ using a finite bond dimension χ. In fact, such a truncation can be found based on the entanglement spectrum of the state, however we will not go into further detail, but refer the interested reader to the literature [135]. For a finite bond dimension we are left with $\mathcal{O}(dL\chi^2)$ matrix entries which have to be optimized and stored. Again, symmetries and other constraints can reduce this number significantly, which makes MPS a celebrated variational ansatz class.

The aforementioned truncation of the MPS at a finite bond dimensions obviously limits the quantum states which can be accurately represented by an MPS. In particular, the orbital entanglement of an MPS is bounded by $S \leq \log \chi$. However, states with reasonably weak entanglement can be accurately represented by MPS already at intermediate bond dimensions. In particular, ground states of gapped, locally interacting Hamiltonians exhibit area law entanglement and therefore can be studied using MPS in particular in one dimension, where $S \sim$ const.. Also for gapless one-dimensional systems the entanglement entropy scales as $S \sim \log L$, where L is the length of the system.

Similarly, many topologically ordered states in two dimensions exhibit weak entanglement, which then again encodes the complex entanglement *structure*. While this requires larger bond dimensions than non-critical systems in 1D, there is still a chance to represent ground states of topological systems in 2D using MPS of finite bond dimension. In fact, we will exploit this and use MPS in many of the numerical studies in this thesis.

Density Matrix Renormalization Group

As already mentioned before, MPS are a useful ansatz for a variational approximation of interacting many-body ground states. In particular, the density matrix renormalization group (DMRG) introduced by White [136] provides an efficient algorithm to optimize an MPS to represent the ground state of low-dimensional systems [135, 137]. Where the DMRG algorithm is employed in this thesis, we use the existing SyTen toolkit [138]. Therefore we restrict our discussion of the DMRG to a minimum, focusing on those aspects particularly important to understand our simulations. In particular, we discuss the single-site variant [139] without going into further details about the advantages and disadvantages of this particular approach. The interested reader is refered to Ref. [135] for a review of the DMRG algorithm.

Having introduced matrix product *states* in the previous section, we note that also quantum mechanical operators can be represented using local low-rank tensors. This way, we translate abstract operators to *matrix product operators* (MPOs) which can then be used to perform tensor network operations like contractions and alike. In this case, evaluating the expectation value of an operator with respect to a certain state translates to contracting the corresponding tensor network as visualized in Fig. 1.5**(b)**.

Inspired by the variational principle, we want to optimize the matrices of our MPS such that the energy is minimized. To this end, we note that Eq. (1.26) can be rewritten as

$$0 \leq \inf_{|\psi\rangle \in \mathscr{H}_{\mathrm{MPS}}} \left(\langle\psi|\hat{\mathcal{H}}|\psi\rangle - E_0 \langle\psi|\psi\rangle \right) . \tag{1.30}$$

Next, we perform an iterative *sweep*, where we keep all matrices fixed except for those at one active site k. Thus, we reduce the problem from an extremely challenging nonlinear optimization to a significantly easier linear optimization problem. In particular, the problem can be cast in the form of a generalized eigenvalue problem visualized in Fig. 1.6 After optimizing the active site k the algorithm continues in the same manner for the next site $k + 1$. Iterating this scheme on all sites we sweep through the system. During each optimization the bond dimension of the active

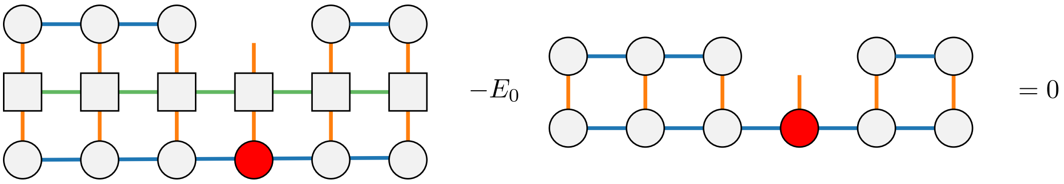

Fig. 1.6. Intermediate step of the (single-site) DMRG algorithm. The generalized eigenvalue problem visualized here is used to optimize the active site of the MPS highlighted in red.

site matrix is truncated to χ according to a Schmidt decomposition such that an efficient and tractable representation of the ground state can be found. In particular, performing more sweeps at successively increasing bond dimension the accuracy of the variational ansatz can iteratively be increased.

The simple single-site variant of the DMRG algorithm presented here tends to get stuck in local minima. While there exist also other approaches, here we overcome this problem by admixing weak perturbations to the optimized tensors, resulting in the strictly single-site DMRG (DMRG3S) [139], which we will not discuss further.

We briefly comment on DMRG's capability to also find excited states of a given Hamiltonian. To this end, recall that any excited state $|\Psi_1\rangle$ necessarily has to be orthogonal to the ground state $|\Psi_0\rangle$. Therefore, restricting the search for the first excited state corresponds to a ground state search in the Hilbert space orthogonal to $|\Psi_0\rangle$. In applications, this can be implemented by adding a Lagrange multiplier to the Hamiltonian, ending up with

$$\hat{\mathcal{H}}^{(1)} = \hat{\mathcal{H}} + \lambda \left|\Psi_0\right\rangle \left\langle\Psi_0\right| , \tag{1.31}$$

where $\lambda \gg E_0, E_1$. Now, the DMRG algorithm can be applied using the new Hamiltonian $\hat{\mathcal{H}}^{(1)}$ to approximate the first excited state. In principle, this protocol can also be applied to find higher states, however, it is numerically costly and does in general not exploit the entanglement structure sufficiently well to be of practical use [134].

1.4.3. Metropolis-Hastings Monte Carlo Sampling

In this thesis we will encounter situations, where a wave function is either known exactly or can be obtained from an ansatz by a projection which is difficult to perform analytically. In both cases, sampling snapshots of the wave function can prove useful to determine expectation values of observables. We will briefly discuss this approach here, emphasizing aspects particularly important to this thesis. We note that the general approach has applications far beyond the scope of the discussion here, in particular in the context of variational Monte Carlo methods.

Consider a complete basis $\{|\alpha\rangle\}$ of the Hilbert space for which we can calculate overlaps $\langle\alpha|\Psi\rangle$ with a known state $|\Psi\rangle$ efficiently. Assume further that also the matrix elements $\langle\alpha|\hat{\mathcal{O}}|\beta\rangle$ of some observable $\hat{\mathcal{O}}$ can be evaluated efficiently. Then we can write the expectation value of $\hat{\mathcal{O}}$ as

$$\langle\Psi|\hat{\mathcal{O}}|\Psi\rangle = \sum_{\alpha,\beta} \frac{\langle\Psi|\alpha\rangle \langle\alpha|\hat{\mathcal{O}}|\beta\rangle \langle\beta|\Psi\rangle}{\langle\Psi|\Psi\rangle} . \tag{1.32}$$

Evaluating the sum over all states $|\alpha\rangle , |\beta\rangle$ is not feasible in most relevant cases so that we turn to a stochastic approach. To this end, we first rewrite the expectation value as

$$\begin{aligned}\langle\Psi|\hat{\mathcal{O}}|\Psi\rangle &= \sum_\beta \frac{|\langle\beta|\Psi\rangle|^2}{\langle\Psi|\Psi\rangle}\left(\sum_\alpha \langle\alpha|\hat{\mathcal{O}}|\beta\rangle \frac{\langle\Psi|\alpha\rangle}{\langle\Psi|\beta\rangle}\right) \\ &= \sum_\beta p(\beta)o(\beta),\end{aligned} \tag{1.33}$$

where we defined the probability distribution $p(\beta) = {}^{|\langle\beta|\Psi\rangle|^2}/_{\langle\Psi|\Psi\rangle}$ and the observable-dependent quantity $o(\beta) = \sum_\alpha \langle\alpha|\hat{\mathcal{O}}|\beta\rangle \frac{\langle\Psi|\alpha\rangle}{\langle\Psi|\beta\rangle}$. In many applications the observables of interest are sparse in the computational basis, i.e. $\left|\left\{|\alpha\rangle \mid \langle\alpha|\hat{\mathcal{O}}|\beta\rangle \neq 0\right\}\right| \leq \mathcal{O}(L)$ for all β. In this case, only a few summands contribute to the sum in $o(\beta)$ and hence we can efficiently apply a Markov Chain Monte Carlo method to evaluate the expectation value [140].

We generate a set of snapshots drawn from the basis states $\{|\alpha\rangle\}$ according to the probability distribution $p(\alpha)$ using the Metropolis-Hastings algorithm [141,142]. After having generated the snapshots, we can now approximate the true expectation value by

$$\begin{aligned}\langle\Psi|\hat{\mathcal{O}}|\Psi\rangle \approx \mathbb{E}\left[\hat{\mathcal{O}}\right] &:= \frac{1}{N_{\text{snapshot}}} \sum_{|\text{snapshot}\rangle} o(|\text{snapshot}\rangle) \\ &= \frac{1}{N_{\text{snapshots}}} \sum_{|\text{snapshot}\rangle} \left(\sum_\beta \langle\alpha|\hat{\mathcal{O}}|\text{snapshot}\rangle \frac{\langle\Psi|\alpha\rangle}{\langle\Psi|\text{snapshot}\rangle}\right),\end{aligned} \tag{1.34}$$

where N_{snapshot} is the number of snapshots. Assuming that the snapshots are indeed independent, we can use the estimate of the standard deviation of $\hat{\mathcal{O}}$ to approximate the uncertainty of our sampling procedure:

$$\sigma(\hat{\mathcal{O}}) \approx \mathbb{E}\left[\sigma(\hat{\mathcal{O}})\right] = \sqrt{\frac{1}{N_{\text{snapshots}}(N_{\text{snapshots}}-1)} \sum_{|\text{snapshots}\rangle} \left(\mathbb{E}\left[\hat{\mathcal{O}}\right] - o(|\text{snapshot}\rangle)\right)^2}. \tag{1.35}$$

However, the assumption of independent snapshots is typically hard to guarantee in applications. Keeping only Monte Carlo snapshots which are separated along the Markov chain helps a lot, but care has to be taken by including the autocorrelation time. Furthermore, methods like data binning can improve the accuracy of the estimate of the expectation value $\mathbb{E}\left[\hat{O}\right]$ significantly [143].

2 Non-Abelian FCIs in Optical Lattices: The Bosonic Pfaffian State

2.1. Introduction and Outline

Arguably, the most prominent feature of topologically ordered phases of matter is the nontrivial braiding statistics of its anyonic quasiparticle excitations. While the elementary particles (leptons, quarks, gauge bosons and the Higgs particle) fall into the two categories of fermions and bosons, topologically ordered systems may exhibit anyons being neither fermions nor bosons. Apart from providing an exciting playground for physicists, these anyons might be used in future applications, for example in the context of quantum computing. In particular, so-called non-Abelian anyons, where the outcome of the braiding procedure depends on the order of operations, are a promising building block for future topological quantum computers [17, 144].

However, any technological application of topological quasiparticles requires means to create, manipulate and detect such particles in a controllable environment. Not surprisingly, the direct demonstration of non-Abelian braiding [145–147] in extended systems [148] has become one of the biggest challenges of modern experimental physics.

A particularly promising class of systems believed to host non-Abelian anyonic excitations are fractional quantum Hall (FQH) systems. Accordingly, it seems meaningful to quantum simulate related systems using ultracold atoms in optical lattices. However, finding a clear route to realize non-Abelian quantum Hall states in these systems remains challenging and any attempt to detect anyonic excitations first requires the identification and realization of a suitable Hamiltonian as well as preparation schemes to reach the desired ground state.

In this chapter, we present density matrix renormalization group (DMRG) studies of the Hofstadter-Bose-Hubbard model at $\alpha = 1/6$ magnetic flux quanta per plaquette. In particular, we study the model on a square lattice on extended cylinders close to the continuum limit, i.e. in the dilute limit and at small flux per plaquette. We find strong indications that the ground state at magnetic filling factor $\nu = 1$ is a lattice analog of the continuum non-Abelian Pfaffian state, one of the first microscopic states found to possess non-Abelian anyons [62]. Two- and three-particle correlation functions and the incompressibility of the ground state characterize the Pfaffian state both in the continuum and in our lattice systems. On the thin cylinders studied here, the topologically ordered Pfaffian state evolves into a charge density wave (CDW) from which adiabatic preparation of the Pfaffian state might be possible in extended systems.

The signatures discussed here are accessible in current cold atom experiments and we propose a direct adiabatic pathway into the Pfaffian state for small systems of a few bosons. We conclude that the Pfaffian state at $\nu = 1$ is readily realizable in small lattice systems and offers rich physics.

This chapter is based on the results from Ref. [1], the text and figures of which were rearranged, adapted, and supplemented here. It is structured as follows: in Sec. 2.2 non-Abelian FQH states are introduced and Moore and Read's Pfaffian state is discussed as an example in both

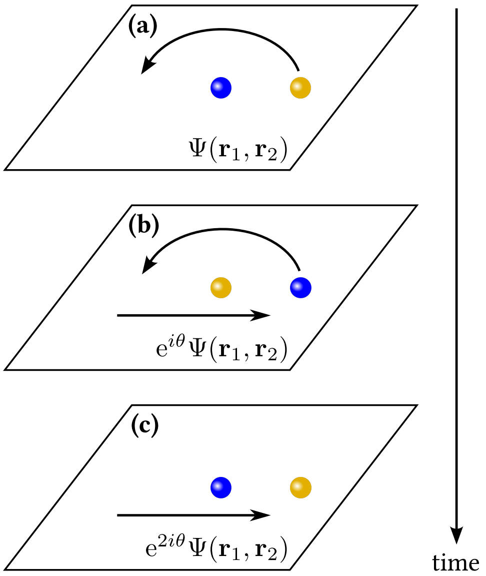

Fig. 2.1. (a) Starting from two particles in two dimensions at positions $\mathbf{r}_1$ and $\mathbf{r}_2$ described by the wave function $\Psi(\mathbf{r}_1,\mathbf{r}_2)$, we move one of them past the other and shift the pair to the original positions **(b)**. Thus, the wave function of the new state is $e^{i\theta}\Psi(\mathbf{r}_1,\mathbf{r}_2)$. **(c)** Repeating the same procedure, we end up with the original configuration described by the wave function $e^{2i\theta}\Psi(\mathbf{r}_1,\mathbf{r}_2)$. This corresponds to winding one particle around the other, for which the graph on the right visualizes the according braid.

fermionic and bosonic Hall systems. Specifics of the cylinder geometry important for our discussion are presented in Sec. 2.3. Finally, we discuss signatures of the lattice Pfaffian state in the Hofstadter-Bose-Hubbard model in Sec. 2.4, before concluding with summarizing remarks and an outlook in Sec. 2.5.

2.2. Non-Abelian Fractional Quantum Hall States

As mentioned in the introductory chapter, topologically ordered systems can exhibit novel quasiparticles obeying exotic braiding properties. In this section, we review the concepts of braiding statistics and non-Abelian braiding in more detail before providing an example for a potential realization in FQH systems. We note that while these concepts may seem rather abstract and mathematical at first, they are in fact of enormous practical relevance in the context of topological quantum computing.

2.2.1. Braiding Statistics and (Non-Abelian) Anyons

We start our discussion by introducing the concept of particle braiding and follow the line of thoughts presented in Ref. [144]. The basic insights covered here go back to the literature of the late 70's [149] and early 80's [150].

Consider two identical, indistinguishable, impenetrable particles described by the wave function $\Psi(\mathbf{r}_1,\mathbf{r}_2)$. In an adiabatic process, we move one of the particles past the other as visualized in Fig. 2.1**(a)** and shift the pair to the original positions **(b)**. This results in an effective exchange of the two particles and the wave function can pick up an arbitrary phase θ so that the new state is $e^{i\theta}\Psi(\mathbf{r}_1,\mathbf{r}_2)$. Repeating this process, we effectively moved the first particle around the other one along a closed loop and end up with the final state $e^{2i\theta}\Psi(\mathbf{r}_1,\mathbf{r}_2)$ **(c)**.

In $d \geq 3$ spatial dimensions, this process is physically equivalent to doing nothing, as closed loops in $\mathbb{R}^3 \setminus \{\mathbf{0}\}$ can always be contracted into a point. Correspondingly, the phase θ_{3D} has to be such that the initial state and the final state coincide:

$$\Psi_{\mathrm{3D}}(\mathbf{r}_1, \mathbf{r}_2) = \mathrm{e}^{2i\theta_{\mathrm{3D}}} \Psi_{\mathrm{3D}}(\mathbf{r}_1, \mathbf{r}_2) \qquad \Rightarrow \qquad \theta_{\mathrm{3D}} = 0, \pi. \tag{2.1}$$

The two solutions for θ correspond to the familiar bosons ($\theta_{\mathrm{3D}} = 0$) and fermions ($\theta_{\mathrm{3D}} = \pi$).

In contrast, in two spatial dimensions, not all closed loops are contractible. Therefore, the braiding process which we performed here carries an actual physical meaning and the initial and final states do not have to be the same. Accordingly, there is no constraint on the phase θ_{2D}, which is often called the statistical angle. As this angle can take *any* value, the corresponding particles are called *anyons*.

For a generalization of this concept to the case of $N \geq 2$ identical, indistinguishable particles it turns out to be useful to introduce some mathematical notions [151]. Consider N particles located on a manifold $\mathcal{M}$ of dimension $d \geq 2$. It is natural to define the *ordered configuration space* of these impenetrable particles as

$$\tilde{\mathcal{C}}_N\left(\mathcal{M}\right) := \left\{ (\mathbf{r}_1, \dots \mathbf{r}_N) \in \mathcal{M}^N \;\middle|\; \mathbf{r}_i \neq \mathbf{r}_j \text{ for } i \neq j \right\}. \tag{2.2}$$

For identical, indistinguishable particles it is necessary to symmetrize this space, i.e. to identify configurations which are related via a permutation of particles. Thus, we end up with the *(unordered) configuration space*

$$\mathcal{C}_N\left(\mathcal{M}\right) := \tilde{\mathcal{C}}_N\left(\mathcal{M}\right) / S_N, \tag{2.3}$$

where S_N denotes the symmetric group on N elements. The fundamental group of $\mathcal{C}_N\left(\mathcal{M}\right)$ is called the *braid group* of $\mathcal{M}$ on N strands, $\mathcal{B}_N(\mathcal{M}) = \pi_1\left(\mathcal{C}_N\left(\mathcal{M}\right)\right)$. Here, we will exclusively deal with the case $\mathcal{M} = \mathbb{R}^2$, i.e. particles on a two-dimensional plane, so that we introduce the notation $\mathcal{B}_N := \mathcal{B}_N(\mathbb{R}^2)$.

Physically speaking, the elements of $\mathcal{B}_N$ can be understood as the topologically distinct classes of trajectories taking N particles from some initial positions $\{\mathbf{r}_1, \dots, \mathbf{r}_N\}$ to the same positions.[1] As usual when dealing with quantum mechanics in the presence of symmetries, we have to understand how the braid group acts on quantum states, i.e. study the representation theory of the braid group.

The simplest possible representations of the braid group are one-dimensional, corresponding to multiplication by a phase factor $\mathrm{e}^{i\theta}$. We already encountered this behavior in the case of two particles, which can easily be generalized to the many-body case, $N > 2$. Anyons corresponding to such a one-dimensional representation of $\mathcal{B}_N$ are called *Abelian anyons*, as the order of braiding does not play any role in the final phase.

More interestingly, it is possible to study *non-Abelian anyons* associated with higher-dimensional representations of the braid group. To this end, consider the case of a g-fold degenerate ground state ψ_α, $\alpha = 1, \dots, g$. In this case, an element σ of the braid group acts on the state ψ_α as a unitary $g \times g$-matrix $\rho(\sigma)$, i.e.

$$\psi_\alpha \to \rho(\sigma)_{\alpha\beta} \psi_\beta, \tag{2.4}$$

which can in general result in a non-Abelian braiding procedure:

$$\rho(\sigma_1)\rho(\sigma_2) \neq \rho(\sigma_2)\rho(\sigma_1) \qquad \text{for some } \sigma_1, \sigma_2 \in \mathcal{B}_N(\mathbb{R}^2). \tag{2.5}$$

---

[1] By "topologically distinct" we mean trajectories which cannot be connected by a smooth deformation.

In particular, braiding non-Abelian anyons will give rise to non-trivial rotations in the degenerate ground state Hilbert space.

The degenerate quasiparticle states could be used to encode quantum information, thus realizing topological qubits [17]. Quantum gates could be implemented by braiding quasiparticles, thus changing the state of the system. As long as temperatures are much lower than the excitation gap, such states are robust against the accidental creation of anyons. Also errors due to an accidental braiding of quasiparticles are negligible as only the topology of the braid matters, but not its local geometry.

Any attempt to realize topological quantum computing using non-Abelian anyons needs to begin with the realization of the anyons themselves. The FQH state studied in the remainder of this chapter turns out to be insufficient for universal quantum computation, i.e. it is not possible to realize *all* unitary gates using only braiding operations, but additional unprotected operations are needed [144]. Nevertheless, understanding the difficulties in realizing this "simplest" non-Abelian anyon is believed to be a fruitful endeavor. So far, direct evidence of non-Abelian anyon braiding is still lacking and cold atom quantum simulators may provide a useful platform to accomplish this milestone.

2.2.2. The Fermionic Pfaffian State

While the Hall resistance in electronic samples exhibits many plateaus at odd-denominator fractions, only very few plateaus were observed at even denominators. From a theory point of view this can be attributed to the fact that the particularly robust fermionic Laughlin state can only emerge at fillings $\nu = 1/m$ for odd integers m. Furthermore, hierarchy states derived from the Laughlin states also exhibit odd-denominator filling fractions [15, 61].

Nevertheless, some plateaus were found at even denominators. Most prominently, Willett *et al.* observed a plateau at $\nu = 5/2$ which was confirmed in further experiments along with other even-denominator fractions [152–154]. By now, it is settled that the plateau at $\nu = 5/2$ is a fully developed FQH plateau and the question arises whether it can be described by a simple trial state. One of the earliest proposals was to interpret the state as a paired state at $\nu_{\text{eff}} = 1/2$ on top of a completely filled Landau level contributing a Landau level filling of 2 because of the electron's spin [155, 156]. A promising candidate for such a state at $\nu_{\text{eff}} = 1/2$ was proposed by Moore and Read in 1999 [62] and is commonly known as the *Pfaffian state* described by the wave function

$$\Psi_{\text{Pf}}^{1/2}(z_1, \ldots, z_N) \propto \left(\text{Pf}\left(\frac{1}{z_i - z_j}\right) \prod_{i<j} (z_i - z_j)^2 \right) \mathrm{e}^{-\frac{1}{4}\sum_k |z_k|^2}, \tag{2.6}$$

where the Pfaffian $\text{Pf}(M)$ of an antisymmetric matrix M_{ij} is defined as

$$\text{Pf}(M) = \mathcal{A}\left(M_{12} M_{34} \ldots M_{N-1,N}\right) \tag{2.7}$$

with the antisymmetrization operator $\mathcal{A}$. As this wave function is very similar to that of a p-wave superconductor of spin polarized electrons, the Pfaffian wave function is frequently interpreted as a p-wave paired state of composite fermions (CFs). While the Pfaffian state arises as a trial state for the FQH problem, related lattice versions of the Pfaffian were found in spin systems [157], which lead to the proposal of a parent Hamiltonian [158], and in the Haldane model [159].

One of the most exciting properties of the Pfaffian are its derived quasiparticle and quasihole states. Surprisingly for a state at $\nu_{\text{eff}} = 1/2$, the elementary quasiparticles/-holes carry charge $\pm 1/4$. Furthermore, they exhibit non-Abelian braiding statistics introduced above [62]. While the anyons are exact eigenstates for a parent Hamiltonian including only three-body repulsion, their role in the FQH state realized at $\nu = 5/2$ in the presence of the electronic Coulomb repulsion is less clear.

This already hints towards a discussion in the literature around the plateau at $\nu = 5/2$. While the Pfaffian state is an interesting candidate, there exist also alternative proposals for the ground states' nature and, accordingly, for the low-lying excitations. In fact, there has been a long and still ongoing debate on what the underlying microscopic state of the $\nu = 5/2$ plateau is [160–163]. We do not go into further detail here, but instead propose to study a closely related bosonic system using atomic quantum simulators.

Before diving into the physics of the bosonic Pfaffian state, we conclude our brief discussion of the electronic FQH at even-denominator fractions by a comment on another fraction. In fact, the first interesting feature of Hall systems at $\nu = 1/2$ is the *absence* of a Hall plateau in electronic samples. While this seems surprising at first, given the emergence of a plateau at $\nu = 2 + 1/2$, this can be understood by taking into account the effect of higher Landau level projection of the Coulomb potential. It was shown by Scarola, Park, and Jain [59] that at $\nu = 1/2$ the interaction between the CFs forming a Fermi sea is repulsive, while at $\nu = 5/2$ this interaction is in fact attractive. Therefore, the paired Pfaffian state at $\nu = 5/2$ can be interpreted as a consequence of the Cooper instability due to the Coulomb interaction projected to the second Landau level. In contrast, the CF Fermi sea at $\nu = 1/2$ does not exhibit said Cooper instability and hence the CFs remain unpaired.

2.2.3. The Bosonic Pfaffian State

Similar to the fermionic Pfaffian wave function at certain even-denominator filling factors, it is possible to construct a bosonic Pfaffian at $\nu = 1$ [62],

$$\Psi^{1}_{\mathrm{Pf}}\left(z_1, \dots, z_N\right) \propto \left(\mathrm{Pf}\left(\frac{1}{z_i - z_j}\right) \prod_{i<j} (z_i - z_j) \right) \mathrm{e}^{-\frac{1}{4}\sum_k |z_k|^2}. \tag{2.8}$$

Again, in analogy with the fermionic case, this wave function describes a paired state of CFs. This pairing can be seen in the behavior of on-site two- and three-particle correlations, which exhibit the characteristic behavior

$$g^{(2)}(0) \neq 0, \qquad g^{(3)}(0) = 0. \tag{2.9}$$

Consequently, while the CFs experience an effective two-body attraction, ultimately resulting in the pairing of CFs, the three-body interactions are screened. This also explains the nature of the parent Hamiltonian with only three-body repulsion in the lowest Landau level.

We remark that, as for the fermionic state, the elementary excitations carry charge $\pm\nu/2$, i.e. $\pm 1/2$ [62]. Therefore, even though we are considering a state at $\nu = 1$, the excitations exhibit charge fractionalization and (non-Abelian) braiding behavior.

Interestingly enough, numerical studies involving only two-body contact interactions in the lowest Landau level found the bosonic Pfaffian to be the ground state of the continuum model at filling $\nu = 1$ [103,104,164]. Furthermore, exact diagonalization studies of the discrete Hofstadter-Bose-Hubbard model on small, toroidal systems have found indication for a lattice analog of the Pfaffian [165]. However the robustness of the state with respect to strong two-particle interactions in larger systems remained unclear. Part of our goal is to clarify this behavior and understand under which conditions the Pfaffian could be realized in cold atom experiments.

2.3. Quantum Hall Physics on Thin Cylinders: Tao-Thouless States

Realizing the Hall problem on a cylinder places the continuum FQH states close to topological CDW states in the quasi-one-dimensional limit while the topologically ordered FQH states are restored in the 2D limit [166]. Previous studies of the continuum Pfaffian on thin cylinders showed that this state is closely related to the so-called Tao-Thouless states [167, 168]. In particular, there is a state which consists of an alternation of doubly-occupied and unoccupied Landau level orbitals, $|\ldots 2020 \ldots\rangle$. As we will interpret our DMRG results on the lattice in terms of this Tao-Thouless state, we will now discuss some of its prominent features.

Assuming an infinite cylinder ($l_x = \infty$) and using the Landau gauge, $\mathbf{A} = xB\hat{\mathbf{y}}$, the wave functions of the Landau level orbitals take the form

$$\psi_{k,m}(x, y) = \mathrm{e}^{iky}\mathrm{e}^{-(x+k\ell_B)^2/2\ell_B^2}\,\mathrm{H}_m(x + k\ell_B^2), \tag{2.10}$$

where k is the eigenvalue of the momentum in y-direction, H_m are the Hermite polynomials and $\ell_B = \sqrt{1/B}$ is the magnetic length, where we used natural units where $\hbar = c = e = 1$. Here, m denotes the Landau level, where $m = 0$ is the lowest Landau level (LLL) we consider here. For the LLL orbitals, the Hermite polynomials are constant, $\mathrm{H}_0(x + k\ell_B^2) = 1$, and therefore do not contribute to the structure of the orbitals. These eigenstates are extended around the cylinder and localized in x-direction around $-k\ell_B^2$, where k is quantized as $k_n = \frac{2\pi}{l_y}n, n \in \mathbb{Z}$ with l_y the circumference of the cylinder. Accordingly, we can determine the centers of the Landau level orbitals to be at

$$x_n = -\ell_B^2 k_n = -\frac{2\pi\ell_B^2}{l_y}\cdot n, \quad n \in \mathbb{Z}. \tag{2.11}$$

For a system of N particles the CDW related to the Pfaffian state has $N/2$ maxima corresponding to the occupied Landau level orbitals of the $|\mathrm{TT}_{20}\rangle = |\ldots 2020 \ldots\rangle$ Tao-Thouless state in the limit $l_y \to 0$. Accordingly, the CDW wavelength is given by $\lambda_{\mathrm{TT}} = |x_2 - x_0| = 4\pi\ell_B^2/l_y$, where x_n denotes the center of the n-th LLL orbital. Equivalently, we expect the wave vector of a simple sinusoidal fit to be

$$k_{\mathrm{TT}}^{\mathrm{Pf}} = \frac{2\pi}{\lambda_{\mathrm{TT}}} = \frac{l_y}{2\ell_B^2}. \tag{2.12}$$

In continuous FQH systems on cylinders, the Laughlin states in the 2D limit ($l_y \to \infty$) are adiabatically connected to symmetry-breaking Tao-Thouless states in the limit of thin cylinders ($l_y \to 0$) [166]. For the bosonic case at $\nu = 1$ studied here, the interplay of the CDW and the Pfaffian was discussed in the continuum by Seidel *et al.* [168] and Bergholtz *et al.* [167].

2.4. Hofstadter-Bose-Hubbard Model at $\nu = 1$: Lattice Pfaffian State

Aiming for an accessible model to realize the bosonic Pfaffian state in cold atom experiments, we study the Hofstadter-Bose-Hubbard model. In particular, we consider bosons on a $L_x \times L_y$-square lattice with lattice constant a assuming periodic boundary conditions in the short y-direction, thus realizing the square lattice on a thin cylinder (see Fig. 2.2). The lattice is subject to a perpendicular magnetic field with flux α per plaquette in units of the magnetic flux quantum. The resulting Hamiltonian in the Landau gauge reads

$$\hat{\mathcal{H}} = -t\sum_{x,y}\left(\hat{a}_{x+1,y}^\dagger\hat{a}_{x,y} + \mathrm{e}^{2\pi i\alpha x}\hat{a}_{x,y+1}^\dagger\hat{a}_{x,y} + \mathrm{H.c.}\right) + \frac{U}{2}\sum_{x,y}\hat{n}_{x,y}\left(\hat{n}_{x,y} - 1\right), \tag{2.13}$$

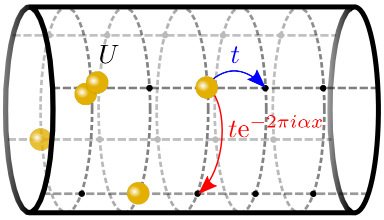

Fig. 2.2. Sketch of the Hofstadter-Bose-Hubbard model on a cylinder, see Eq. (2.13). The bosons can hop with hopping amplitude t and pick up a phase of $2\pi i\alpha$ upon hopping around a plaquette, mimicking the effect of a magnetic field. Furthermore, they experience an onsite Hubbard repulsion of strength U/t.

where $\hat{a}_{x,y}^{(\dagger)}$ annihilates (creates) a boson at site $\mathbf{i} = (x, y \mod L_y)$ and $\hat{n}_{x,y} = \hat{a}_{x,y}^{\dagger}\hat{a}_{x,y}$ is the boson number operator. The first term of the Hamiltonian describes hopping with amplitude t between neighboring sites, and the last term describes repulsive ($^{U}/_{t} > 0$) on-site interactions.

For periodic boundary conditions in the y-direction, the total number of flux quanta is given by $N_\phi = \alpha\,(L_x - 1)\,L_y$, where we restrict our analysis to the case $\alpha = {}^{1}/_{6}$. Furthermore, for most of our study we consider dilute systems of N bosons close to filling factor $\nu = {}^{N}/_{N_\phi} = 1$. Dilute systems at small flux per plaquette connect the model to the continuum limit, so that we are able to relate our findings to earlier results for bosonic FQH systems [65, 101, 102, 161].

Numerical Method

Using the single-site variant [139] of the DMRG method [135–137], we calculate the canonical ground state of the Hofstadter-Bose-Hubbard Hamiltonian. We exploit the $\mathrm{U}(1)$ symmetry associated with the particle-number conservation and truncate the local Hilbert space to at most $N_{\max} = 3$ bosons per site. We ensure convergence of our simulations by comparing the energy expectation value $\langle\hat{\mathcal{H}}\rangle$, the corresponding variance $\langle\hat{\mathcal{H}}^2\rangle - \langle\hat{\mathcal{H}}\rangle^2$, the local particle density $\langle\hat{n}_{x,y}\rangle$, and the local currents,

$$\langle\hat{j}^{x}_{x,y}\rangle = it\langle\hat{a}^{\dagger}_{x+1,y}\hat{a}_{x,y}\rangle + \text{H.c.}, \qquad \langle\hat{j}^{y}_{x,y}\rangle = ite^{2\pi i\alpha x}\langle\hat{a}^{\dagger}_{x,y+1}\hat{a}_{x,y}\rangle + \text{H.c.}, \tag{2.14}$$

for different bond dimensions up to $\chi = 3000$.

We consider finite systems of varying size and consider different two-particle interaction strengths, $^{U}/_{t} = 2, 5, \infty$. Here, the limit of hard-core bosons ($^{U}/_{t} = \infty$) is achieved by truncating the local Hilbert space to at most $N_{\max} = 1$ boson per site.

Screened Interactions

In the continuum limit, the ground state of $\hat{\mathcal{H}}$ at $\nu = 1$ is well described by the Pfaffian trial state [164]. As discussed above, the Pfaffian is the exact zero-energy ground state of the repulsive three-body parent Hamiltonian [155]

$$\hat{\mathcal{H}}^{(3)} \propto \sum_{i,j,k} \delta(z_i - z_j)\delta(z_j - z_k) \tag{2.15}$$

acting on the lowest Landau level. This Hamiltonian allows for two particles at the same location but penalizes three particles at the same point in space. Similar to the way the $\nu = {}^{1}/_{2}$ Laughlin state fully screens local two-body interactions, the $\nu = 1$ Pfaffian has vanishing energy with respect to this three-body parent Hamiltonian [60, 101].

As mentioned above, this can be understood in the CF picture. The $\nu = {}^{1}/_{2}$ Laughlin state can be described using non-interacting CFs with one flux quantum attached to each boson. In

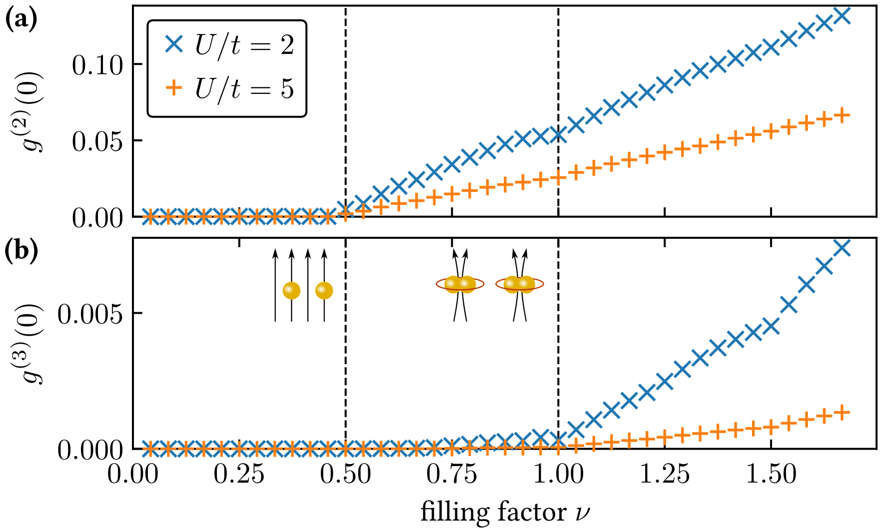

Fig. 2.3. **(a)** Two-particle and **(b)** three-particle on-site correlations as a function of the filling factor ν for fixed flux $\alpha = 1/6$, different two-particle interaction strengths U, at most $N_{\max} = 3$ particles per site, $L_y = 4$, and $L_x = 37$. The sudden increase of correlations at $\nu = 1/2$ and 1 indicates the existence of the Laughlin and Pfaffian state, respectively. In the corresponding regions, the screened composite particles are illustrated.

the $\nu = 1$ Pfaffian state the same CFs form pairs which experience a screened interaction among each other [59], thus resulting in a vanishing three-boson interaction energy.

To see whether we can find similar screening effects in our lattice systems, we calculate the ground state's two- and three-particle on-site correlations,

$$g^{(2)}(0) = \sum_{\mathbf{i}} \frac{\langle \hat{n}_{\mathbf{i}} (\hat{n}_{\mathbf{i}} - 1) \rangle}{\langle \hat{n}_{\mathbf{i}} \rangle^2}, \qquad g^{(3)}(0) = \sum_{\mathbf{i}} \frac{\langle \hat{n}_{\mathbf{i}} (\hat{n}_{\mathbf{i}} - 1)(\hat{n}_{\mathbf{i}} - 2) \rangle}{\langle \hat{n}_{\mathbf{i}} \rangle^3}, \tag{2.16}$$

for a broad range of filling factors. We consider systems of $L_x \times L_y = 37 \times 4$ sites and finite interaction strength $U/t = 2, 5$.

We find that the on-site two-particle correlations $g^{(2)}(0)$ essentially vanish below $\nu = 1/2$, see Fig. 2.3**(a)**. We understand this as a key signature for the $1/2$ Laughlin state. Similarly, we observe the three-particle correlations $g^{(3)}(0)$ to be strongly suppressed for filling factors up to $\nu = 1$, see Fig. 2.3**(b)**. We interpret this suppression as a hallmark of the Pfaffian related to the screened three-particle interactions in its parent Hamiltonian.

To confirm that these findings are not mere finite size effects, we also determine the on-site correlations for $L_y = 4, L_x = 25$ and $L_x = 37$. For both system sizes they are in very good agreement, see Fig. 2.4. While this does not necessarily imply that the same holds true in the thermodynamic limit, it provides a meaningful first indication of interesting FQH states in experimentally relevant lattice systems.

Before continuing our discussion by providing further evidence for the lattice analog of the Pfaffian at $\nu = 1$, we would like to point out another kink in the three-particle on-site correlations at $\nu = 3/2$. Similar to the Pfaffian as a two-body bound state of CFs, there exists a three-body bound state of CFs which is expected to be of interest at $\nu = 3/2$, the simplest so-called parafermion state [169]. Additional studies are needed to see whether the $\nu = 3/2$ kink of the three-particle correlations observed here is indeed related to this parafermion state. We do not explore this in more detail here, but instead return to our discussion of the $\nu = 1$ Pfaffian state.

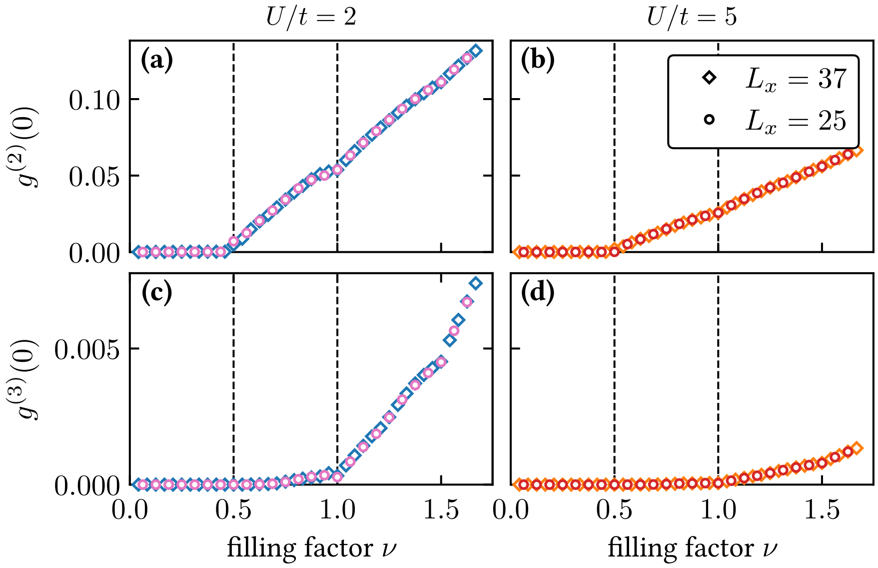

Fig. 2.4. Two- and three-particle on-site correlations for $U/t = 2$ [**(a)** and **(c)**] and $U/t = 5$ [**(b)** and **(d)**], for $L_y = 4$ and both $L_x = 25$ and 37.

Charge Gap and Incompressibility

While the suppressed three-particle on-site correlations at $\nu = 1$ provide an experimentally accessible indicator for the presence of a ground state related to the Pfaffian, they do not reveal further insight into the microscopic nature of the state.

As mentioned above, the continuum Pfaffian is an incompressible state with a charge gap in the bulk [169]. To investigate this property in the lattice systems at hand, we study the dependence of the grand-canonical ground state on the chemical potential μ.

To this end, we first find the canonical ground states for varying particle number N using DMRG. We denote the energy of such an N-particle state by E_N. Introducing the chemical potential μ, the grand-canonical ground state energy is then given by

$$E^{\text{grand}}(\mu) = \min_N (E_N - \mu N) . \tag{2.17}$$

From this, we determine the particle number, or equivalently the filling factor ν, of the grand-canonical ground state as a function of the chemical potential μ. This method allows for a very precise calculation of the charge gap Δ given by the width of the plateau of $\nu(\mu)$ at $\nu = 1$.[2] [3] We find that strong interactions stabilize an incompressible phase and result in a large charge gap, $\Delta \sim 0.1\, t$, see Fig. 2.5**(a)**.

To see whether this behavior carries over to larger systems, we perform a finite-size extrap-

---

[2] The charge gap can also be obtained directly from the canonical ground state energies using

$$\Delta = E_{N+1} + E_{N-1} - 2E_N .$$

However, this formula is not sensitive to jumps of the grand-canonical ground state by more than one particle. Therefore, we stick to the slightly more complicated method discussed in the text, which does not need more numerical effort than an estimation of the charge gap using the formula above, but yields slightly more reliable results.

[3] We estimate the error of the charge gap at $\nu = 1$ by the ground state variance of the Hamiltonian, $\text{var}(\hat{\mathcal{H}}) = \langle\hat{\mathcal{H}}^2\rangle - \langle\hat{\mathcal{H}}\rangle^2$. As we also use the variance to check the convergence of our calculations, this error is negligibly small ($\text{var}(\hat{\mathcal{H}}) \lesssim 10^{-5} t^2$) compared to the size of the charge gap.

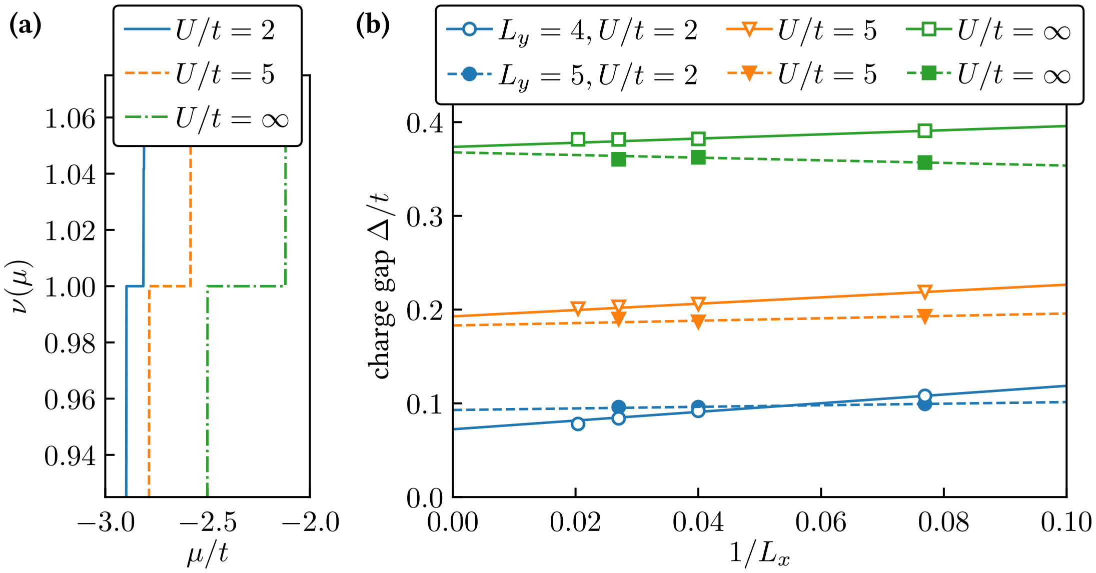

Fig. 2.5. **(a)** Filling factor ν of the grand-canonical ground state as function of the chemical potential μ for $L_y = 4, L_x = 37$. **(b)** Charge gap Δ for different system sizes (L_x, L_y) and interaction strengths $^U/_t$ at $\nu = 1$ with at most $N_{\text{max}} = 3$ bosons per site. The size of the gap on infinite cylinders is estimated from a linear fit and depends on both the interaction strength $^U/_t$ and the circumference L_y of the cylinder.

$^U/_t$	$^\Delta/_t$		n_1	
	$L_y = 4$	$L_y = 5$	$L_y = 4$	$L_y = 5$
2	0.072(3)	0.093(5)	0.055(2)	0.051(1)
5	0.193(2)	0.183(9)	0.0528(7)	0.0420(7)
∞	0.3736(6)	0.368(2)	0.0382(5)	0.021(1)

Tab. 2.1. Extrapolated charge gap Δ and CDW order parameter n_1 for an infinite cylinder as obtained by a linear fit of the finite-size results shown in Figs. 2.5 and 2.7.

olation of the charge gap in the cylinder length L_x. In particular, we use a linear fit of the form

$$\Delta(L_x) = \Delta + \frac{A}{L_x}, \tag{2.18}$$

where Δ is the estimate for the charge gap on an infinite cylinder ($L_x \to \infty$) and A is a non-universal fit parameter. The extrapolation to $L_x \to \infty$ gives rise to an additional error from the least-square fit which is the dominant contribution to the overall uncertainty of the extrapolated charge gap.

The obtained gap extrapolates well to the thermodynamic limit, $^1/_{L_x} \to 0$, see Fig. 2.5**(b)**, and the extrapolated charge gaps are given in Tab. 2.1. We observe a general trend of stronger interactions resulting in larger charge gaps. Because the circumference $L_y = 4, 5$ of the cylinder is comparatively short, on the order of the magnetic length, gapless edge states at the ends of the cylinder cannot be resolved yet.

Charge Density Wave

The local particle density is one of the first observables coming to mind in the context of quantum gas microscopy. In particular, site resolved measurements are by now routinely accessible in optical lattice experiments [109–112]. Therefore, finding probes for interesting many-body states based on such measurements is one of the main goals of our study.

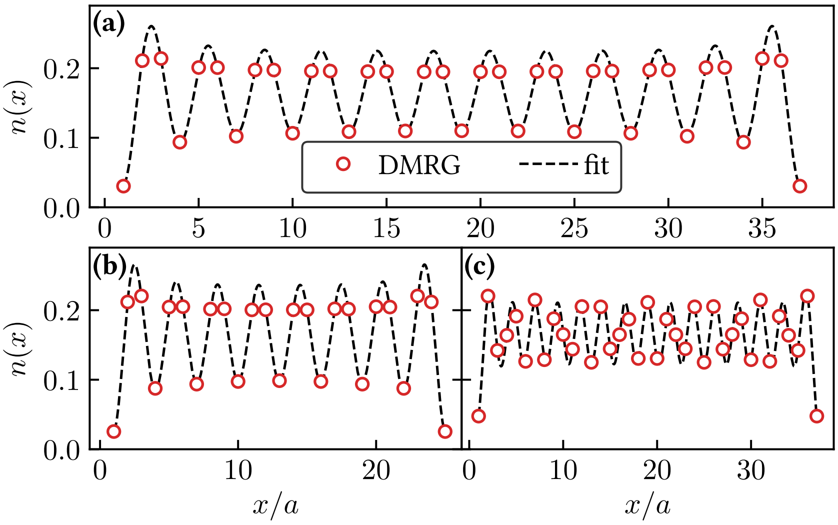

Fig. 2.6. Density profile and CDW fit for **(a)** $L_x \times L_y = 37 \times 4, {}^{U}\!/t = 5$, **(b)** $L_x \times L_y = 25 \times 4, {}^{U}\!/t = 2$ and **(c)** $L_x \times L_y = 37 \times 5, {}^{U}\!/t = 5$ with at most $N_{\text{max}} = 3$ bosons per site at $\nu = 1$. The maxima correspond to the occupied Landau level orbitals of the $|\ldots 2020 \ldots\rangle$ Tao-Thouless state. We fitted the function in Eq. (2.20) to the numerical data using all parameters. The wave vectors of the fitted curve are $ak_{\text{CDW}} = 2.0976(5), 2.1018(9), 2.6203(9)$, respectively, while the predicted values are **(a,b)** $ak_{\text{CDW}}^{\text{pred}} = 2.0944$ and **(c)** 2.6180 in the continuum.

We find that the local density

$$n(x) = \sum_y \langle \hat{n}_{x,y} \rangle / L_y \tag{2.19}$$

develops a pronounced charge density wave (CDW) for all considered parameters, see Fig. 2.6. The rapid decay of enhanced density modulations at the edges shows that the remaining oscillations are indeed a bulk property and not an edge effect. While the 2D FQH system is topologically ordered, we attribute the symmetry-breaking ground state found here to the finite system size and in particular the thin cylinders, favoring Tao-Thouless states even in the continuum.

Building upon our DMRG results, we fit the density distribution by

$$n(x) = n_0 + n_1 \sin(kx + \phi_0) \left(1 + \eta(x, A, \xi)\right), \tag{2.20}$$

with $\eta(x, A, \xi) = A/2(\exp[-x/\xi] + \exp[-(L_x - 1 - x)/\xi])$ capturing the decay at the edges. We extract the CDW order parameter n_1 from the fit and extrapolate the finite size results to the limit $L_x \to \infty$ as shown in Fig. 2.7. The extrapolated order parameter for the $L_y = 4$ cylinder is larger than for the wider $L_y = 5$ cylinder, independently of the interaction strength, in agreement with the continuum results [167, 168]. Moreover, the wave vectors obtained from our fits are in agreement with the expected wave vectors for the Tao-Thouless state.

Two- and Three-Particle Correlations

One of the key signatures of the continuum Pfaffian state is its paired nature, which is built into the trial wave function. To see whether this is also true for our state under study, we compare the two- and three-particle correlations of our lattice system to well-known continuum results.

To this end, we use Monte Carlo sampling to generate snapshots of the continuum Pfaffian wave function centered around the point $\mathbf{r} = (0, 0)$. Afterwards, we calculate the density profile

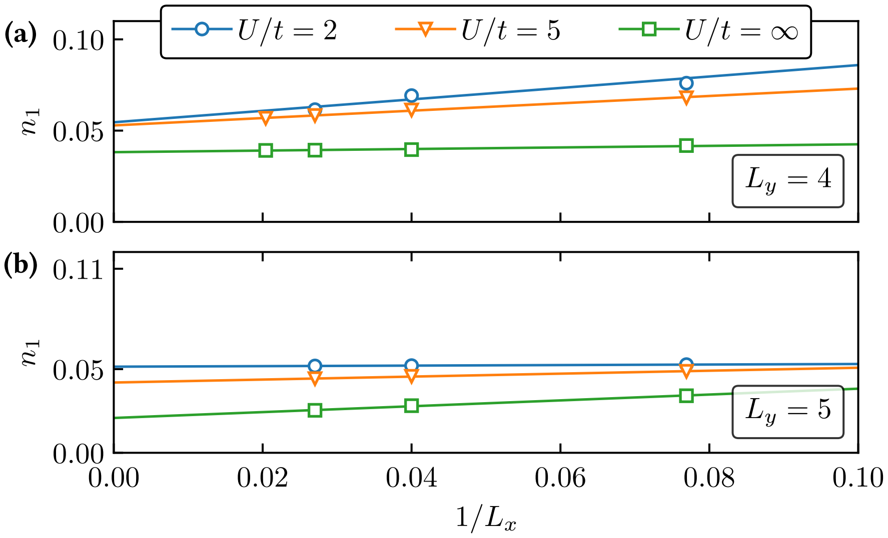

Fig. 2.7. CDW order parameter for **(a)** $L_y = 4$ and **(b)** $L_y = 5$ with at most $N_{\max} = 3$ bosons per site. The limit of infinite cylinders is extrapolated by a linear fit at $\nu = 1$. As compared to $L_y = 4$, for $L_y = 5$ the order parameter is smaller at all interaction strengths.

using concentric rings R_m of width δr, i.e.

$$\hat{n}_m = \int_{\mathbf{r}\in R_m} \mathrm{d}^2 r \; \hat{\rho}(\mathbf{r}), \tag{2.21}$$

where $R_m = \left\{\mathbf{r} \in \mathbb{R}^2 \mid r_m \leq |\mathbf{r}| < r_{m+1}\right\}$ with $r_m = m\delta r$, $m \in \mathbb{N}_0$. Starting from this density, we can now write the density-density correlations as

$$\begin{aligned} \langle : \hat{n}_0 \hat{n}_m : \rangle &= \int_{\mathbf{r}\in R_1} \mathrm{d}^2 r \int_{\mathbf{r}'\in R_m} \mathrm{d}^2 r' \;\langle : \hat{\rho}(\mathbf{r})\hat{\rho}(\mathbf{r}') : \rangle \\ &\approx \int_{\mathbf{r}\in R_1} \mathrm{d}^2 r \int_{\mathbf{r}'\in R_m} \mathrm{d}^2 r' \;\langle : \hat{\rho}(\mathbf{0})\hat{\rho}(\mathbf{r}') : \rangle \\ &= \pi r_1^2 \int_{\mathbf{r}'\in R_m} \mathrm{d}^2 r' \;\langle : \hat{\rho}(\mathbf{0})\hat{\rho}(\mathbf{r}') : \rangle \,. \end{aligned} \tag{2.22}$$

Using the spatial isotropy of the density distribution, we can approximate the expectation value as $\langle : \hat{\rho}(\mathbf{0})\hat{\rho}(\mathbf{r}') : \rangle \approx \langle : \hat{\rho}(\mathbf{0})\hat{\rho}(r'\hat{\mathbf{e}_x}) : \rangle = \langle \rho(\mathbf{0}) \rangle \langle \rho(\mathbf{r}') \rangle \, g^{(2)}(r')$ and find

$$\begin{aligned} \langle : \hat{n}_0 \hat{n}_m : \rangle &\approx \pi r_1^2 \int_{\mathbf{r}'\in R_m} \mathrm{d}^2 r' \;\langle \rho(\mathbf{0}) \rangle \langle \rho(\mathbf{r}') \rangle \, g^{(2)}(r') \\ &\approx \pi r_1^2 \pi \left(r_{m+1}^2 - r_m^2\right) n_1 n_m g^{(2)}(r_m) \\ &= \pi^2 \delta r^4 \left(2m+1\right) n_1 n_m g^{(2)}(r_m), \end{aligned} \tag{2.23}$$

where $n_k = \langle \hat{n}_k \rangle$. Thus, we conclude that - for a fine enough resolution δr - the two-point correlation function can be approximated by

$$g^{(2)}(r_m) \approx \frac{\langle : \hat{n}_0 \hat{n}_m : \rangle}{\pi^2 \delta r^4 \left(2m+1\right) n_1 n_m}, \tag{2.24}$$

where the expectation value can be evaluated using the Monte Carlo sampled snapshots. Similarly, we find for the three-point correlation function

$$g^{(3)}(r') \coloneqq \langle : \hat{\rho}(\mathbf{0})\hat{\rho}(\mathbf{0})\hat{\rho}(r'\hat{\mathbf{e}_x}) : \rangle / [\langle \rho(\mathbf{0}) \rangle^2 \langle \rho(\mathbf{r}') \rangle] \tag{2.25}$$

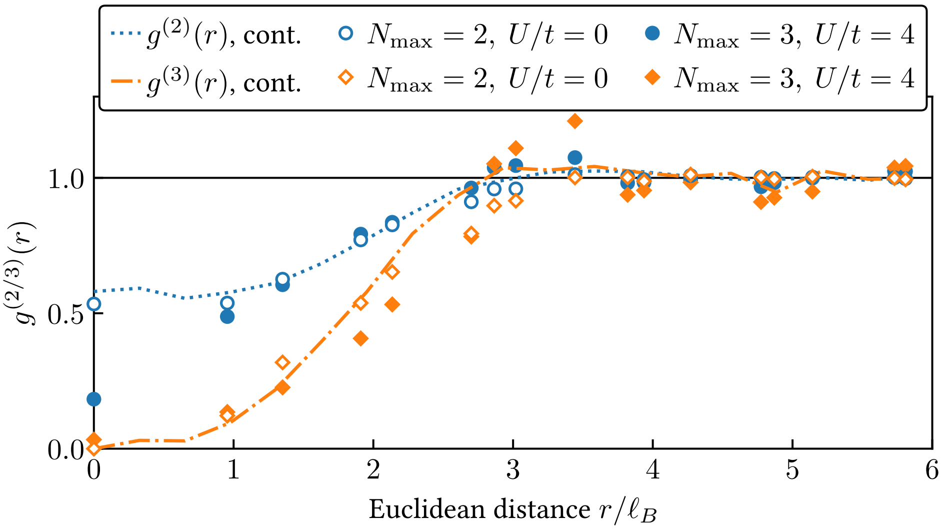

Fig. 2.8. Two- and three-particle correlations as function of the Euclidean distance in units of the magnetic length $\ell_B = a/\sqrt{2\pi\alpha}$ for $\alpha = 1/6$, $L_x = 37$, and $L_y = 4$. At short distances, the $g^{(2)}$-function stays finite whereas the $g^{(3)}$-function drops to zero as expected for the continuum Pfaffian (dotted lines). For $U/t = 0$ and 4 we used $N_{\max} = 2$ and 3, respectively.

the approximate expression

$$g^{(3)}(r_m) \approx \frac{\langle : \hat{n}_0 \hat{n}_0 \hat{n}_m : \rangle}{\pi^3 \delta r^6 \,(2m+1)\, n_1^2 n_m}. \tag{2.26}$$

In two dimensions, the Pfaffian exhibits strongly suppressed three-particle on-site correlations, $g^{(3)}(r \to 0) \to 0$, while the two-particle on-site correlations remain finite, $g^{(2)}(0) \neq 0$ (dotted lines in Fig. 2.8).

To compare our lattice system to the continuum result, we start by calculating the ground state of the three-body parent Hamiltonian $\hat{\mathcal{H}}^{(3)}$ in Eq. (2.15) on the lattice by setting $U/t = 0$, $N_{\max} = 2$. Determining the two- and three-particle correlation functions,

$$\begin{aligned} g^{(2)}_{\mathbf{i},\mathbf{j}} &= \frac{\left\langle \hat{a}^\dagger_{\mathbf{i}} \hat{a}^\dagger_{\mathbf{j}} \hat{a}_{\mathbf{i}} \hat{a}_{\mathbf{j}} \right\rangle}{\left\langle \hat{n}_{\mathbf{i}} \right\rangle \left\langle \hat{n}_{\mathbf{j}} \right\rangle} = \frac{\left\langle \hat{n}_{\mathbf{i}} \left(\hat{n}_{\mathbf{j}} - \delta_{\mathbf{ij}} \right) \right\rangle}{\left\langle \hat{n}_{\mathbf{i}} \right\rangle \left\langle \hat{n}_{\mathbf{j}} \right\rangle}, \\ g^{(3)}_{\mathbf{i},\mathbf{j}} &= \frac{\left\langle \hat{a}^\dagger_{\mathbf{i}} \hat{a}^\dagger_{\mathbf{i}} \hat{a}^\dagger_{\mathbf{j}} \hat{a}_{\mathbf{i}} \hat{a}_{\mathbf{i}} \hat{a}_{\mathbf{j}} \right\rangle}{\left\langle \hat{n}_{\mathbf{i}} \right\rangle^2 \left\langle \hat{n}_{\mathbf{j}} \right\rangle} = \frac{\left\langle \hat{n}_{\mathbf{i}} \left(\hat{n}_{\mathbf{i}} - 1 \right) \left(\hat{n}_{\mathbf{j}} - 2\delta_{\mathbf{ij}} \right) \right\rangle}{\left\langle \hat{n}_{\mathbf{i}} \right\rangle^2 \left\langle \hat{n}_{\mathbf{j}} \right\rangle}, \end{aligned} \tag{2.27}$$

with respect to a fixed test site $\mathbf{i}$ for varying site $\mathbf{j}$, we plot $g^{(2)}(r)$ and $g^{(3)}(r)$ as functions of the (Euclidean) distance $r = |\mathbf{i} - \mathbf{j}|$. We average over all available test sites in the bulk region of the cylinder. The close agreement of the parent Hamiltonian's ground state (open symbols in Fig. 2.8) with the continuum result suggests that pairing is also present in this state on the lattice.

Finally, the experimentally relevant case $U/t = 4$, $N_{\max} = 3$ (solid symbols in Fig. 2.8) shows qualitatively similar correlations, in particular for $g^{(3)}(r)$. Only the on-site $g^{(2)}(0)$ is modified, indicating that the microscopic structure of the bosonic bound state has changed slightly on the smallest length scales.

Adiabatic State Preparation

In cold atom experiments, adiabatic preparation schemes connecting an easily realizable initial state to the desired target state present one of the main routes towards realizing exotic states of matter. Here, our goal is to propose possible paths for an adiabatic preparation of the bosonic Pfaffian state. Roughly speaking, a suitable path avoids regions in parameter space where the many-body excitation gap becomes small or closes completely. By definition, in the thermodynamic limit a path connecting states with different topological orders will always encounter a gapless point. In experimentally accessible systems, however, finite-size effects will in general result in a finite gap, allowing for adiabatic paths connecting different topological universality classes.

For small systems ($L_x = L_y = 6, N = N_{\text{max}} = 4$) exact diagonalization (ED) is a suitable method to study not only the ground state but also the excitation gap. In particular, we consider an array of 1D chains with tunable interchain hopping t_y and a 2D plane with open boundary conditions and tunable hopping t_{pbc} across the boundaries, ultimately resulting in a torus for $t_{\text{pbc}} = t_y = t_x$. The key signatures of the Pfaffian discussed earlier are also visible in these systems, see Fig. 2.9.

In the 2D regime we find a finite-size excitation gap closely related to the charge gap observed in our DMRG calculations. Furthermore, the sharp drop of the three-particle on-site correlations $g^{(3)}(0)$ as a function of α or, equivalently, the filling factor $\nu = N/[\alpha L_x L_y]$ both on a plane and a torus shows the expected suppression of three-body correlations in the lattice system, see Fig. 2.9**(c)**. Also the excitation gap (see Fig. 2.9**(a)**) and the two-particle correlations $g^{(2)}(0)$ (see Fig. 2.9**(b)**) for varying periodic hopping t_{pbc}/t_x confirm our earlier understanding.

Various adiabatic preparation schemes for other FQH states have been proposed in recent years [76,78–80,170,171]. Making use of the large excitation gap found in ED, a path like the one proposed by He *et al.* [79] (indicated by the blue lines in Fig. 2.9) provides a promising candidate, where the minimal gap is of the order $\sim 0.05 t_x$. Another possibility could be the preparation of the Pfaffian starting from the closely related CDW and slowly turning on 2D couplings [80].

The exact filling factor and hence the flux per plaquette at which we expect the Pfaffian and the Laughlin state depend on the choice of boundary conditions and are significantly affected by very small system sizes. For periodic boundary conditions the flux per plaquette is given by $\alpha_{\text{pbc}} = N/[\nu L_x L_y]$, while for open boundary conditions we have $\alpha_{\text{obc}} = N/[\nu(L_x - 1)(L_y - 1)]$. Thus, we expect the $\nu = 1$ Pfaffian ($\nu = 1/2$ Laughlin) state for periodic boundary conditions at $\alpha_{\text{Pf,pbc}} = N/[L_x L_y]$ and $\alpha_{\text{LN,pbc}} = 2N/[L_x L_y]$, respectively. These values are indicated by white lines in Fig. 2.9. In addition we included the one- and two-quasiparticle and -quasihole excitations of the Laughlin state, obtained by removing/adding one or two flux quanta, respectively. We observe signatures of these states in both the excitation gap and the two-particle on-site correlation.

For open boundary conditions, the filling factors of the Pfaffian and the Laughlin state are shifted to $\nu_{\text{Pf}} = N/[N-1]$ and $\nu_{\text{LN}} = N/[2N-1]$, respectively, as can be derived from their exact wave functions in a disk geometry. Again, we indicated the corresponding values for α by white lines. From the ED results for the gap, Fig. 2.9**(a)**, we conclude that the states on the torus and in the plane can be continuously connected.

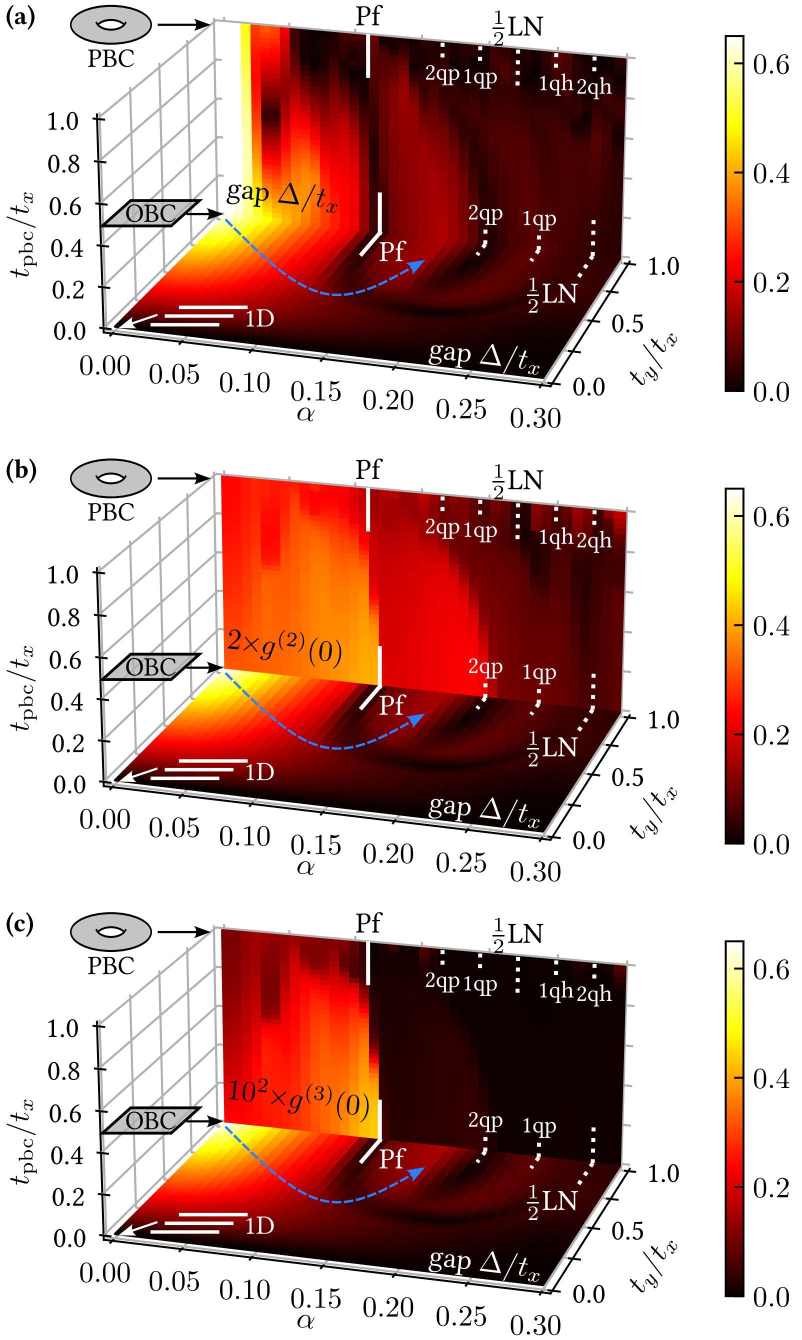

Fig. 2.9. Exact diagonalization of the Hofstadter-Bose-Hubbard Hamiltonian for $L_x = L_y = 6, N = 4, U/t_x = 4$ for varying flux α per plaquette. We tune between 1D chains and open boundary conditions (OBC) using t_y/t_x, and between open (OBC) and periodic boundary conditions (PBC) using t_{pbc}/t_x. The plane shows the excitation gap Δ in all panels, while the wall shows the gap in **(a)**, the rescaled two-particle on-site correlations $2g^{(2)}(0)$ in **(b)**, and the rescaled three-particle on-site correlations $10^2 g^{(3)}(0)$ in **(c)**. The blue dotted line indicates a possible path we propose for adiabatic preparation of the ground state, starting from a trivial superfluid state. "Pf" and "$\frac{1}{2}$LN" denote the Pfaffian and the Laughlin state respectively, "qp" and "qh" refer to quasiparticle and quasihole excitations of the Laughlin state.

2.5. Summary and Outlook

Concluding our discussion of the Hofstadter-Bose-Hubbard model at $\nu = 1$, we have found a close connection between its ground state and the Pfaffian trial wave function in the continuum. The most striking feature of the lattice Pfaffian is the associated suppression of on-site three-body correlations. As discussed above, state-of-the-art techniques [109–112] allow for measurements of n-particle correlation functions in cold atom experiments providing a direct insight into the correlated nature of a state.

Regarding the experimental realization, we emphasize that two-body interactions are sufficient to stabilize the Pfaffian in a Hofstadter-Hubbard type of model. While this is not too surprising based on earlier continuum results [101, 102], it is definitely good news for experimentalists, as such models can be readily realized with existing techniques. To this end, we have proposed a realistic preparation scheme for small systems, and the closely related CDW in the quasi-1D-limit may provide a way to adiabatically prepare larger ground states.

Our work paves the way for future studies of excitations or the Hall response [82,83,87,172] in the Pfaffian. Furthermore it raises interesting new questions about the realizability of the Pfaffian state in even more accessible setups, like systems with open boundaries. We will address this question in the next chapter after first providing new insights into the Laughlin state at $\nu = 1/2$.

3 Coupled Chains: Central Charge and Snapshot-Based Detection

3.1. Introduction and Outline

While solid state realizations of FQH states are restricted to essentially isotropic systems, spatial anisotropies are an interesting subject for various reasons. Analytically, coupled quantum wires can give additional insight into the formation of topologically ordered states as a result of inter-chain couplings and interactions [173–175]. A prime example is the emergence of Laughlin, hierarchy, and Read-Rezayi states at their respective filling factors. Coupled wires also allow for an intuitive understanding of the edge theory as well as the quasiparticle content.

On a different note, ultracold atoms in optical lattices allow for quantum simulations of systems with anisotropic hopping. Here, approaches starting from decoupled, one-dimensional chains provide a promising route for the adiabatic preparation of topologically ordered states [79, 176]. However, viable experimental schemes for elucidating the topological nature of the states remain scarce, while it seems reasonable that these systems might exhibit an even richer zoo of topological phases.

Therefore, the generalization of the coupled wire approach to discrete chains provides a promising way to construct exotic quantum phases in an experimentally accessible setup and motivates the numerical studies presented in this chapter.

In particular, we present density matrix renormalization group (DMRG) simulations of interacting bosons on coupled chains subject to a magnetic field, where we consider systems at magnetic filling factors of $\nu = 1/2$ and 1. Tuning the inter-chain hopping, we find transitions from trivial quasi-one-dimensional states to topologically ordered states. While finite-size and lattice effects affect microscopic properties of the wave function, we identify the state using universal properties which are robust to such effects.

We mainly resolve the transitions using the central charge as extracted from the entanglement entropy of spatial bipartitions. Addressing the need for experimentally accessible observables, we propose a scheme to estimate the central charge from Fock basis snapshots. In particular, we show that the central charge can be estimated in current cold atom experiments using the number entropy as a proxy for the entanglement entropy.

We also discuss signatures of the topological phase in experimentally more established observables like the on-site density-density correlations and the momentum distribution and bulk correlations along the chains. Finally, we exemplify the topological nature of the ground state by calculating the many-body Chern number as function of the inter-chain hopping strength.

The model studied here is experimentally realizable with existing cold atom techniques and the proposed observables pave the way for the detection and classification of a larger class of interacting topological states of matter.

This chapter is structured as follows: In Sec. 3.2 we briefly review the coupled wire construction in the continuum, before presenting our results for discrete chains in Sec. 3.3. In particular, we discuss systems at filling factor $\nu = 1/2$ hosting the Laughlin state in Sec. 3.3.3, which is based on the results of Ref. [2], the text and figures of which were rearranged, adapted, and supplemented here. Furthermore, we present results at $\nu = 1$ in Sec. 3.3.4, which are yet to be published [5]. We conclude our discussion by summarizing our findings and giving an outlook for future studies in Sec. 3.4.

3.2. Coupled Wire Construction in the Continuum

One-dimensional quantum systems are a prominent example for interacting many-body systems allowing for analytical insights. In particular, bosonization techniques building on field-theoretical methods and scaling arguments proved useful for a broad class of (quasi) one-dimensional problems [177]. In order to apply such methods to the study of two-dimensional, topologically ordered systems, a "coupled wire approach" can be used. Such an approach starts from an array of one-dimensional quantum wires subject to a perpendicular magnetic field. Upon introducing specific inter- and intra-wire coupling terms, the system exhibits various phases, among which we are mainly interested in topological phases mimicking the familiar FQH states in the two-dimensional limit.

In this section, we sketch the construction originally introduced by Kane, Mukhopadhyay, and Lubensky in Ref. [173] and developed further by Teo and Kane in Ref. [174]. We closely follow the arguments of Ref. [174], but focus on particularly simple cases relevant to state-of-the-art cold atom experiments. Nevertheless, we find various interesting topological states which might be realized in anisotropically coupled Hofstadter-Hubbard models. Note however, that the analytical results presented here make use of continuous quantum wires instead of discretized chains. We will turn to the latter case below in the context of our numerical studies.

3.2.1. General Approach of the Bosonic Construction

Consider an array of uncoupled spinless bosonic one-dimensional quantum wires, which are parametrized by a single coordinate x and a wire index j. The single-particle dispersion of the bosons is given by $\epsilon(k_x) = \frac{k_x^2}{2m}$, where m is the mass of the particles. Next, the system is subjected to a perpendicular magnetic field of strength B described by the Landau gauge vector potential $\mathbf{A} = -By\hat{\mathbf{e}}_x$. The magnetic field shifts the momentum in each wire, $k_x \to k_x + yB = k_x + jaB$,

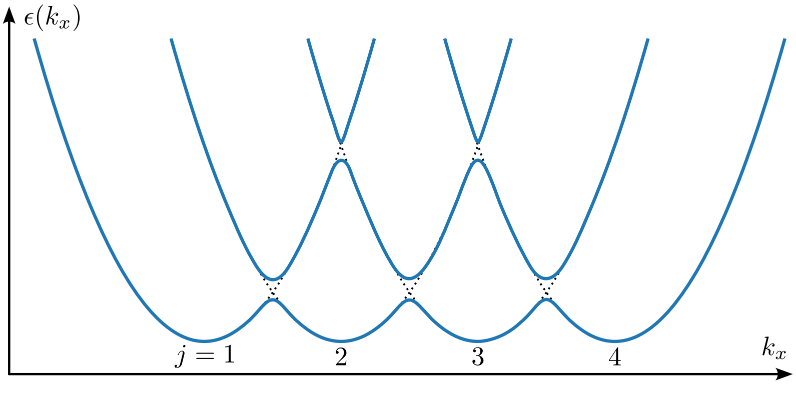

Fig. 3.1. Single-particle dispersion relation $\epsilon(k_x)$ for an array of four coupled wires. Note the emergence of relatively flat Landau level-like bands emerging upon coupling the initial free-particle parabolae (dotted lines). Figure adapted from Ref. [174]

where a is the spacing between different wires.[1] Coupling the wires lifts the degeneracies at the band crossing points and results in Landau level-like single particle bands, see Fig. 3.1.

Following Ref. [174] in "bosonizing the bosons", the Hamiltonian for coupled bosonic wires takes the form

$$\mathcal{H}^0 = \sum_{j,j'} \int \mathrm{d}x \; (\partial_x\varphi_j, \partial_x\theta_j)\, \underline{\underline{M}}_{jj'} \begin{pmatrix} \partial_x\varphi_{j'} \\ \partial_x\theta_{j'} \end{pmatrix}, \qquad \underline{\underline{M}}_{jj'} = \underline{\underline{\mathbb{1}}}\delta_{jj'}\frac{v_F}{2\pi} + \underline{\underline{U}}_{jj'}, \tag{3.1}$$

where φ and θ are the new bosonic variables and $\underline{\underline{U}}_{jj'}$ contains the forward scattering interactions. This Hamiltonian describes a gapless phase of coupled Luttinger liquids.

Next, we discuss additional inter-wire scattering terms, which can open gaps and hence give rise to new many-body phases. The most general term takes the form

$$\begin{aligned} V^{\{m_l,n_l\}} &= \sum_j \int \mathrm{d}x \, \left(v^{\{m_l,n_l\}} \mathcal{O}_j^{\{m_l,n_l\}}(x) + \text{H.c.} \right), \\ \mathcal{O}_j^{\{m_l,n_l\}} &= \mathrm{e}^{i\sum_l (aBn_l + k_F m_l)x} \mathrm{e}^{i\sum_l \left(n_l\varphi_{j+l} + m_l\theta_{j+l}\right)}. \end{aligned} \tag{3.2}$$

Here, we defined the "Fermi momentum" of the one-dimensional bosons $k_F = \pi\bar{\rho}$, where $\bar{\rho}$ is the average one-dimensional boson density. Thus, we can write the magnetic filling factor as $\nu = {}^{2k_F}\!/_{aB}$.

The allowed values for m_l and n_l are restricted by charge conservation,

$$\sum_l n_l = 0, \tag{3.3}$$

and momentum conservation,

$$\sum_l (aBn_l + k_F m_l) = 0, \tag{3.4}$$

as well as the constraint

$$m_l \equiv 0 \mod 2 \tag{3.5}$$

arising during the bosonization procedure. While this significantly restricts the allowed interaction terms, a full analytical study of the problem has to be done perturbatively using for example a renormalization group (RG) analysis. An alternative approach is to explore the phase diagram under the *assumption* that certain operators are RG-relevant. Here, we will follow the latter approach to discuss various FQH-like states in some detail.

3.2.2. Laughlin State from Coupled Wires

Consider tunneling between neighboring wires j and $j+1$ described by the operator

$$\mathcal{O}_\ell \propto \mathrm{e}^{i(\varphi_j - \varphi_{j+1} + m(\theta_j + \theta_{j+1}))}, \tag{3.6}$$

where we introduced the index ℓ for the link between wires j and $j+1$. Using momentum conservation, it can be seen that the magnetic filling factor is given by

$$\nu = -2\frac{\sum_l l n_l}{\sum_l m_l} = -2\,\frac{0 \times 1 - 1 \times 1}{m + m} = \frac{1}{m} \tag{3.7}$$

and hence the operator $\mathcal{O}_\ell$ is allowed at $\nu = {}^{1}\!/_{m}$.

---

[1] We use natural units where $\hbar = c = e = 1$.

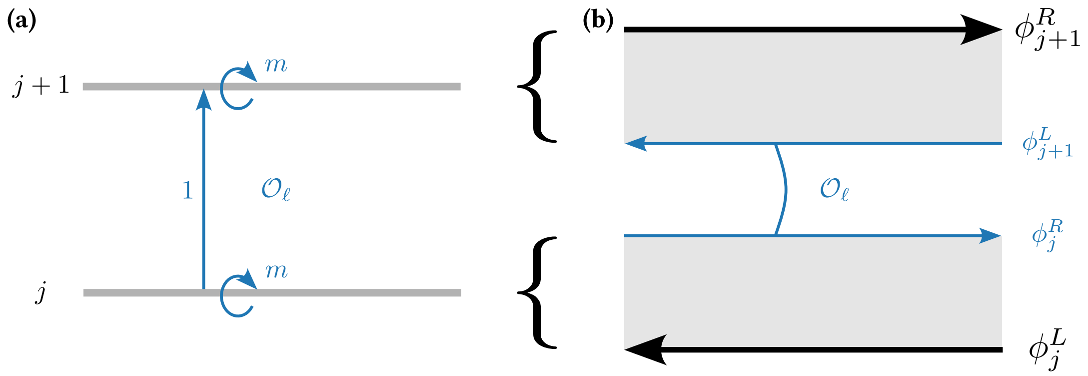

Fig. 3.2. **(a)** Scattering processes leading to the Laughlin state at $\nu = {}^1\!/_m$ in the coupled wire construction. The circular arrow indicates backscattering within a wire ($m\left(\theta_j + \theta_{j+1}\right)$), while the vertical arrow represents hopping between neighboring wires ($\varphi_j - \varphi_{j+1}$). **(b)** As $\mathcal{O}_\ell$ becomes RG-relevant, counter-propagating modes (indicated by the arrows) in neighboring wires pair up and are gapped out (blue). For a finite system, one bosonic chiral edge mode (black) remains, resulting in central charge $c = 1$ as expected for a Laughlin state. Figure adapted from Ref. [174].

Using the commutativity of the interaction terms, $\left[\mathcal{O}_{j-1/2}, \mathcal{O}_{j+1/2}\right] = 0$, we can simplify the problem by introducing left- and right-moving modes in the wires,

$$\phi^R_j = \varphi_j + m\theta_j \qquad \text{and} \qquad \phi^L_j = \varphi_j - m\theta_j, \tag{3.8}$$

as well as density $\tilde{\theta}_\ell$ and phase variables $\tilde{\phi}_\ell$ defined on the links ℓ,

$$\begin{aligned} \tilde{\theta}_\ell &= \left(\phi^R_j - \phi^L_{j+1}\right)/2 = \left(\varphi_j - \varphi_{j+1} + m\left(\theta_j + \theta_{j+1}\right)\right)/2 \\ \tilde{\varphi}_\ell &= \left(\phi^R_j + \phi^L_{j+1}\right)/2 = \left(\varphi_j + \varphi_{j+1} + m\left(\theta_j - \theta_{j+1}\right)\right)/2. \end{aligned} \tag{3.9}$$

With these new degrees of freedom the tunneling operator $\mathcal{O}_\ell$ can be rewritten as $\mathcal{O}_\ell \propto \mathrm{e}^{2i\tilde{\theta}_\ell}$, thus ending up with the Hamiltonian

$$\mathcal{H} = \tilde{\mathcal{H}}^0 + v\sum_\ell \int \mathrm{d}x\; \cos 2\tilde{\theta}_\ell(x), \tag{3.10}$$

where $\tilde{\mathcal{H}}^0$ is the earlier coupled Luttinger liquid Hamiltonian, Eq. (3.1), in terms of the new degrees of freedom. Using scaling arguments, it can be shown that this perturbation can indeed become relevant in the RG sense for certain choices of the forward scattering interactions in $\tilde{\mathcal{H}}^0$ [174]. In this case, the field $\tilde{\theta}_\ell$ is constrained to the minimum of the cosine potential, hence resulting in a gapped phase.

We note that a kink $\tilde{\theta}_\ell(x) \to \tilde{\theta}_\ell(x) + \pi$ can be understood as a low energy excitation of the system. The charge density can be written as $\tilde{\rho}_\ell(x) = \partial_x\tilde{\theta}_\ell/(m\pi)$ so that such a kink can be interpreted as a (localized) quasiparticle of charge $q = {}^1\!/_m$. By extending this formalism further and defining quasiparticle operators, it can be shown that the quasiparticles corresponding to kinks in $\tilde{\theta}_\ell$ carry also the right statistical charge, i.e. the obey the familiar anyonic braiding statistics with statistical angle ${}^\pi\!/_m$.

The operator $\mathcal{O}_\ell$ induces a pairing of left- and right-moving bosonic modes in neighboring wires, see Fig. 3.2. In the case of a finite number of wires, there naturally emerge chiral edge modes from the unpaired modes in the outermost wires. Furthermore, it can be concluded from the bosonized theory that these edge modes obey the chiral Luttinger liquid form for $\nu = {}^1\!/_m$ FQH edges [178].

Based on these analogies with the familiar Laughlin state at $\nu = 1/m$ we identify the emergent coupled wire state with the corresponding FQH state. In concluding, we briefly remark that the coupled wire construction can also give rise to various other phases not directly related to FQH states, in particular superconducting states, CDW states and other crystalline states [173]. Which state forms the actual ground state for a given set of microscopic parameters depends on the specific operators which become relevant in the RG sense. However, as the microscopic details of the low-energy theory are typically not known, the question which operators are present or become relevant cannot be answered in general, but (numerical) studies starting from a microscopic model have to be performed.

Our DMRG studies below can be understood as an approach avoiding RG arguments by numerically finding microscopic parameters of an anisotropic Hofstadter-Hubbard model which stabilize the Laughlin state at $\nu = 1/2$. At the same time, our work extends the original coupled wire construction to discretized chains, thus connecting analytical insights from field theory methods to an experimentally relevant lattice model.

3.2.3. Coupled Wires at $\nu = 1$

Having understood the behavior of coupled wires at $\nu = 1/2$ and, in particular, how they can host the Laughlin state, we now increase the filling factor and study the same problem at $\nu = 1$. Following the discussion of Ref. [174], we consider this setup as a two-component boson system where each bosonic species has a density such that $\nu^\star = 1/2$. Alternatively, this system can be viewed as a bilayer system. We introduce an additional index $a = 1, 2$ labeling the bosonic species and again write the Hamiltonian as

$$\mathcal{H} = \mathcal{H}^0 + V, \tag{3.11}$$

where $\mathcal{H}^0$ is defined analogously to the single-component case and V includes the tunneling and backscattering processes.

Here, we consider three such processes included in V,

$$V = \sum_j \int \mathrm{d}x \, \left(\sum_{a,b=1}^{2} t_{ab} \mathcal{O}^t_{j;ab} + u\mathcal{O}^u_j + v\mathcal{O}^v_j \right) + \text{H.c.}, \tag{3.12}$$

which are visualized in Fig. 3.3. The first term couples neighboring wires, potentially mixing the channels in those wires (if $t_{12}, t_{21} \neq 0$):

$$\mathcal{O}^t_{j;ab} = \mathrm{e}^{i\left(\varphi_{j;a} - \varphi_{j+1;b} + 2(\theta_{j;a} + \theta_{j+1;b})\right)}, \tag{3.13}$$

where the prefactor of 2 in the exponential is fixed by the filling factor. For a system with $t_{ab} = t\delta_{ab}$ this term is of exactly the same form which generated the Laughlin state at $\nu = 1/2$ above.

The remaining terms in V couple the two components in the same wire and are only meaningful in this two-component context. In particular, the second term introduces a coupling of the phase variables $\varphi_{j;a}$,

$$\mathcal{O}^u_j = \mathrm{e}^{i(\varphi_{j;1} - \varphi_{j;2})}, \tag{3.14}$$

whereas the third term locks the densities $\theta_{j;a}$

$$\mathcal{O}^v_j = \mathrm{e}^{i(2\theta_{j;1} - 2\theta_{j;2})}. \tag{3.15}$$

All other allowed terms at $\nu = 1$ would include coupling between further-neighbor wires and are neglected here for simplicity.

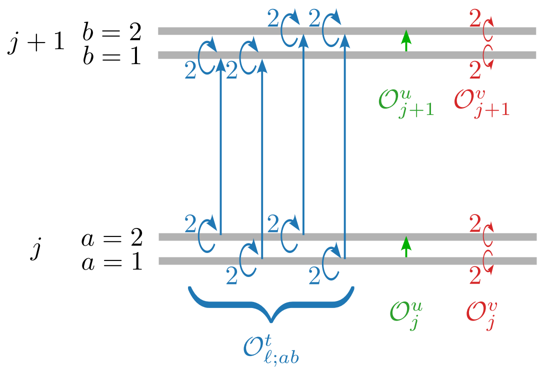

Fig. 3.3. Scattering processes at $\nu = 1$ in the coupled wire construction using two bosonic species $a = 1, 2$. The circular arrow indicates backscattering within a wire, while the vertical arrow represents hopping between neighboring wires j and $j+1$. The three types of processes depicted here are the only ones allowed by momentum and charge conservation which connect at most nearest-neighboring wires. Note the occurrence of inter-species processes described by $\mathcal{O}_j^{u/v}$, which were absent for the Laughlin state at $\nu = 1/m$. The prefactors of 2 in the exponent of the operators $\mathcal{O}_j^{t,u,v}$ are a consequence of the filling factor $\nu^\star = 1/2$ for each of the bosonic species. Figure adapted from Ref. [174].

As for the case of the Laughlin state above, we introduce left- and right-moving bosonic fields

$$\phi^R_{j;a} = \varphi_{j;a} + 2\theta_{j;a} \qquad \text{and} \qquad \phi^L_{j;a} = \varphi_{j;a} - 2\theta_{j;a}. \tag{3.16}$$

Furthermore, we define "charge" and "spin" fields

$$\phi^{R/L}_{j;\rho} = \left(\phi^{R/L}_{j;1} + \phi^{R/L}_{j;2}\right)/2 \qquad \text{and} \qquad \phi^{R/L}_{j;\sigma} = \left(\phi^{R/L}_{j;1} - \phi^{R/L}_{j;2}\right)/2. \tag{3.17}$$

Using these new degrees of freedom, we can now rewrite the interaction terms in V.

Isotropic coupling $t_{ab} = t$

For the moment we assume for simplicity that $t_{ab} = t$, i.e. that the tunneling process in $\mathcal{O}^t$ is independent of the bosonic species, and that $t, u, v \in \mathbb{R}$. We will return to the more general case below. Under these assumptions, we can write the three operators as

$$\begin{gathered}\sum_{a,b} t_{ab}\mathcal{O}^t_{j;ab} + \text{H.c.} = 8t\cos\left(\phi^R_{j;\rho} - \phi^L_{j+1;\rho}\right)\cos\phi^R_{j;\sigma}\cos\phi^L_{j+1;\sigma}, \\ u\mathcal{O}^u_j + \text{H.c.} = 2u\cos\left(\phi^R_{j;\sigma} + \phi^L_{j;\sigma}\right), \qquad \text{and} \qquad v\mathcal{O}^v_j + \text{H.c.} = 2v\cos\left(\phi^R_{j;\sigma} - \phi^L_{j;\sigma}\right).\end{gathered} \tag{3.18}$$

In contrast to the Laughlin case above, the terms in V do not commute and the analysis is more involved for the general case. However, a significant simplification applies for the case where the forward scattering terms in $\mathcal{H}^0$ are such that the charge $\phi^{R/L}_{j;\rho}$ and spin fields $\phi^{R/L}_{j;\sigma}$ decouple and the spin degrees of freedom are non-interacting [174]. In this case, we can fermionize the spin field using the identity

$$\frac{\kappa_{j,\sigma}}{\sqrt{2\pi x_c}}\mathrm{e}^{i\phi^{R/L}_{j;\sigma}} = \xi^{R/L}_{j;\sigma} + i\eta^{R/L}_{j;\sigma}, \tag{3.19}$$

where $\kappa_{j,\sigma}$ are the Klein factors necessary to ensure anticommutativity of the fermionic operators, x_c is a short-distance cutoff, and $\xi^{R/L}_{j;\sigma}$ and $\eta^{R/L}_{j;\sigma}$ are Majorana fermions. For the charge field we introduce new degrees of freedom analogously to the Laughlin case,

$$\tilde{\theta}_{\ell;\rho} = \left(\phi^R_{j;\rho} - \phi^L_{j+1;\rho}\right)/2 \qquad \text{and} \qquad \tilde{\varphi}_{\ell;\rho} = \left(\phi^R_{j;\rho} + \phi^L_{j+1;\rho}\right)/2. \tag{3.20}$$

Finally, the Hamiltonian can now be decomposed as

$$\begin{aligned}\mathcal{H} &= \mathcal{H}^0\left[\tilde{\theta}_{\ell;\rho}, \tilde{\varphi}_{\ell;\rho}\right] + \mathcal{H}^0_{\mathrm{M}}[\xi_\sigma] + \mathcal{H}^0_{\mathrm{M}}[\eta_\sigma] + V,\\ \mathcal{H}^0_{\mathrm{M}}[\xi_\sigma] &= \sum_j \int \mathrm{d}x\, i\left(\xi^R_{j;\sigma}\partial_x\xi^R_{j;\sigma} - \xi^L_{j;\sigma}\partial_x\xi^L_{j;\sigma}\right),\\ V &= \sum_j \int \mathrm{d}x\, \left[\tilde{t}\cos\left(2\tilde{\theta}_{\ell;\rho}\right) i\xi^R_{j;\sigma}\xi^L_{j+1;\sigma} + (\tilde{u}-\tilde{v})\, i\xi^R_{j;\sigma}\xi^L_{j;\sigma} + (\tilde{u}+\tilde{v})\, i\eta^R_{j;\sigma}\eta^L_{j;\sigma}\right],\end{aligned} \tag{3.21}$$

where we introduced new, effective couplings $\tilde{t}$, $\tilde{u}$, and $\tilde{v}$ [174].

To understand the possible ground state phases, we again rely on RG arguments. To this end, we assume that $\mathcal{H}^0[\tilde{\theta}, \tilde{\varphi}]$ is such that the coupling $\tilde{t}$ is relevant, and $\tilde{\theta}_{\ell;\rho}$ is pinned to a minimum of the cosine potential. As a result, counter-propagating bosonic modes in neighboring wires are paired up and the two remaining bosonic modes in the outermost wires remain gapless and later on constitute a single bosonic chiral edge mode in the quantum Hall system.

For the fermionic sector, we conclude that $\mathcal{H}$ describes a system of two independent, free Majorana fermions ξ and η of differing masses given by the parameters $\tilde{t}$, $\tilde{u}$ and $\tilde{v}$. In particular, we find the dispersion relations

$$\epsilon_\xi(k_x, k_y) = \sqrt{v_{\mathrm{M}}^2 k_x^2 + \left|\tilde{t}\mathrm{e}^{ik_y} + \tilde{u} - \tilde{v}\right|^2} \qquad \text{and} \qquad \epsilon_\eta(k_x) = \sqrt{v_{\mathrm{M}}^2 k_x^2 + (\tilde{u}+\tilde{v})^2}. \tag{3.22}$$

From these expressions it becomes evident that for any non-zero $\tilde{u}+\tilde{v}$ the η-fermions are gapped, whereas the gap for the ξ-fermions closes for $\tilde{t} = \pm|\tilde{u} - \tilde{v}|$. Therefore, we find (at least) two possible phases depending on the parameters. In fact, the two regions with $\tilde{t} < |\tilde{u} - \tilde{v}|$ are equivalent, so that we indeed end up with exactly two phases.

Strongly paired phase The phase just mentioned can be identified with a strongly paired state. To see this, we consider the limit $\tilde{t} \ll |\tilde{u} - \tilde{v}|$, where the dominant interactions are given by the expression

$$V_{\mathrm{SP}} = \sum_j \int \mathrm{d}x\, \left[(\tilde{u}-\tilde{v})\, i\xi^R_{j;\sigma}\xi^L_{j;\sigma} + (\tilde{u}+\tilde{v})\, i\eta^R_{j;\sigma}\eta^L_{j;\sigma}\right]. \tag{3.23}$$

Consequently, the Majorana modes pair up within a single wire as indicated in Fig. 3.4**(a)**. Counter-propagating bosonic modes in neighboring wires are paired up and the only remaining gapless mode is a single bosonic mode resulting in central charge $c = c_{\mathrm{SP}} = 1$. For the bosons it is now energetically unfavorable to tunnel between the wires individually as this would excite the gapped ξ-modes. However, a pair of bosons can still tunnel without creating any excitations in the fermionic sector so that we end up with an effective pairing of bosons [174].

Pfaffian phase In the opposite limit, $\tilde{t} \geq |\tilde{u} - \tilde{v}|$, the state emerging from the coupled wire construction can be identified with the Pfaffian state. To see this, we concentrate on the case $\tilde{u} = \tilde{v}$ and note that in this case the interactions reduce to

$$V_{\mathrm{Pf}} = \sum_j \int \mathrm{d}x\, \left[\tilde{t}\cos\left(2\tilde{\theta}_{\ell;\rho}\right) i\xi^R_{j;\sigma}\xi^L_{j+1;\sigma} + (\tilde{u}+\tilde{v})\, i\eta^R_{j;\sigma}\eta^L_{j;\sigma}\right]. \tag{3.24}$$

Again, the η-Majorana modes pair up in the same wire as before. However, for the ξ-Majorana modes we find pairing of counter-propagating modes in neighboring wires similar to the bosonic mode, as illustrated in Fig. 3.4**(b)**. Accordingly, a chiral Majorana edge mode remains in this case

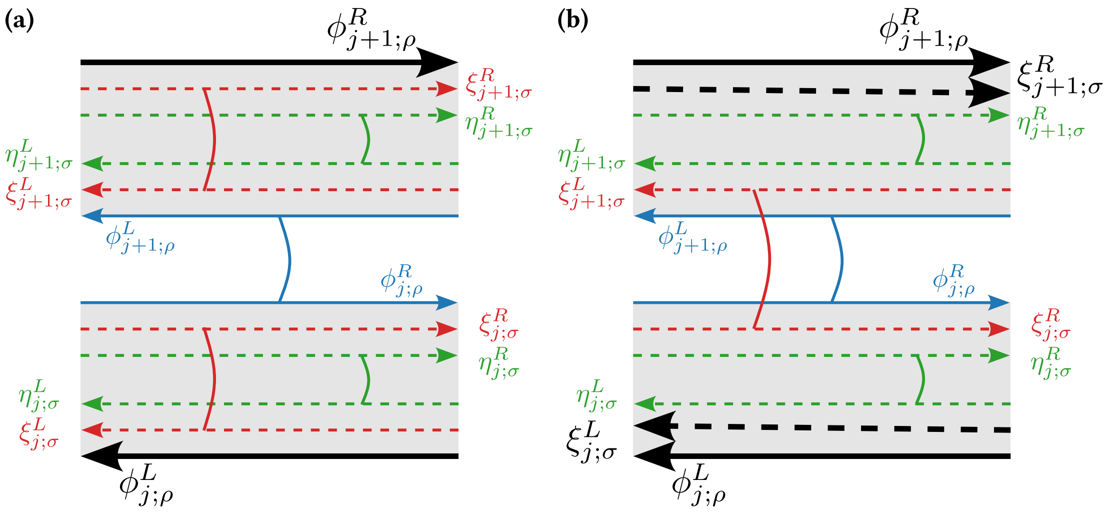

Strong pairing state: $c_{\text{SP}} = 1$

Pfaffian state: $c_{\text{Pf}} = {}^3\!/_2$

Fig. 3.4. Schematic diagrams visualizing the coupling of various edge modes in different parameter regimes. Solid lines represent bosonic charge modes $\phi^{R/L}_{j;\rho}$, whereas dashed lines indicate Majorana modes $\xi^{R/L}_{j;\sigma}$ and $\eta^{R/L}_{j;\sigma}$. Modes which are gapped out are indicated by the same color and an arc connecting them. **(a)** In the strong pairing state all Majorana modes and all bulk charge modes are gapped out, hence resulting in only one chiral bosonic edge mode with central charge $c_{\text{SP}} = 1$. **(b)** In contrast, the Pfaffian state exhibits central charge $c_{\text{Pf}} = {}^3\!/_2$ stemming from an additional unpaired Majorana mode ξ. Figure adapted from Ref. [174].

in addition to the bosonic mode discussed before. This edge theory coincides with that of Moore and Read's Pfaffian state [62] and exhibits central charge $c_{\text{Pf}} = {}^3\!/_2$.

We briefly discuss the charge of the Pfaffian's quasiparticles in the context of the coupled wire construction. Naively, we would expect that in close analogy to the Laughlin state the quasiparticles manifest themselves as kinks $\tilde\theta_{\ell;\rho} \to \tilde\theta_{\ell;\rho} + \pi$ and hence might carry charge e. This is, however, not the case! In fact, we find that we can "split up" this excitation by noting that already the transformation $\varphi_{j;1} \to \varphi_{j;1} + 2\pi$ acting on only one bosonic component, connects physically equivalent states. In turn, this transformation results in a π-shift of the chiral bosonic modes, $\phi^{R/L}_{j;\rho/\sigma} \to \phi^{R/L}_{j;\rho/\sigma} + \pi$, and hence $\left(\tilde\theta_{\ell;\rho}, \xi_{j;\sigma}, \eta_{j;\sigma}\right) \to \left(\tilde\theta_{\ell;\rho} + {}^\pi\!/_2, -\xi_{j;\sigma}, -\eta_{j;\sigma}\right)$. We therefore conclude that the elementary excitations of the Pfaffian state carry charge $q^\star_{\text{Pf}} = {}^e\!/_2$. Furthermore, the corresponding kink in the density field $\tilde\theta_{\ell;\rho}$ results in a change of sign in the mass term coupling the Majorana modes $\propto i\xi^R_{j;\sigma}\xi^L_{j+1;\sigma}$ and hence binds a zero-energy Majorana bound state.

Generic coupling t_{ab}

Before concluding our discussion of the coupled wire construction, we briefly return to some of the simplifications introduced above. In particular, we relax the assumption that $t_{ab} = t$ for all a, b and consider the general form of the corresponding term

$$\sum_{ab} t_{ab}\mathcal{O}^t_{j;ab} + \text{H.c.} = i\left(\xi^R_{j;\sigma}, \eta^R_{j;\sigma}\right) \underline{\underline{T}} \begin{pmatrix}\xi^L_{j+1;\sigma}\\ \eta^L_{j+1;\sigma}\end{pmatrix}, \qquad T_{kl} = \tilde t_{kl}\cos\left(2\tilde\theta_{\ell;\rho} + \beta_{kl}\right), \tag{3.25}$$

where β_{kl} and $\tilde t_{kl}$ depend on t_{ab}.

As before, we assume that the field $\tilde\theta_{\ell;\rho}$ is pinned at a minimum of the cosine potential and study the non-interacting Majorana fermion problem. In addition to the two phases discussed

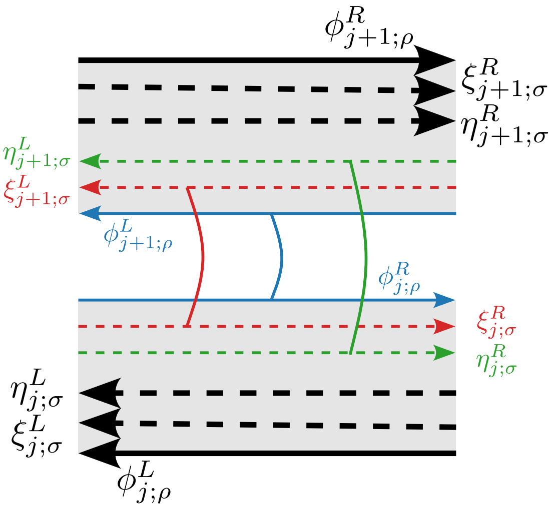

Bilayer state: $c_{\mathrm{B}} = 2$

Fig. 3.5. Schematic diagram visualizing the coupling of edge modes in the bilayer state. In this state both Majorana modes in the outermost wires remain gapless, hence resulting in central charge $c_{\mathrm{B}} = 2$. This state can also be interpreted as a close relative of two decoupled Laughlin states, which would equivalently have two chiral bosonic edge modes. Figure adapted from Ref. [174].

above, we find a third set of parameters exhibiting interesting physics. To see this, we consider the case $t_{ab} = t\delta_{ab}$ resulting in $\tilde{t}_{kl} = \tilde{t}\delta_{kl} \cos\left(2\tilde{\theta}_{\ell;\rho}\right)$ and hence the interaction term

$$\sum_j \int \mathrm{d}x \, \left[\tilde{t}\cos\left(2\tilde{\theta}_{\ell;\rho}\right) i\left(\xi^R_{j;\sigma}\xi^L_{j+1;\sigma} + \eta^R_{j;\sigma}\eta^L_{j+1;\sigma}\right) + (\tilde{u}-\tilde{v})\, i\xi^R_{j;\sigma}\xi^L_{j;\sigma} + (\tilde{u}+\tilde{v})\, i\eta^R_{j;\sigma}\eta^L_{j;\sigma}\right]. \tag{3.26}$$

The effect of the twofold competition between $\tilde{t}$ and $\tilde{u} \pm \tilde{v}$ can be seen most easily for the point $\tilde{u} = \tilde{v}$, where the ξ-fermions are gapped out by the $\tilde{t}$-term, whereas the η-fermions experience the competition between $\tilde{t}$ and $\tilde{u} + \tilde{v}$.

For $\tilde{t} \ll \tilde{u} + \tilde{v}$ we recover the Pfaffian state discussed above with one bosonic and one Majorana edge mode. In contrast, for $\tilde{t} > \tilde{u} + \tilde{v}$ the dominant contribution is of the form

$$V_{\mathrm{B}} = \sum_j \int \mathrm{d}x \, \tilde{t}\cos\left(2\tilde{\theta}_{\ell;\rho}\right) i\left(\xi^R_{j;\sigma}\xi^L_{j+1;\sigma} + \eta^R_{j;\sigma}\eta^L_{j+1;\sigma}\right), \tag{3.27}$$

hence leading to a pairing of the both Majorana modes between neighboring wires, see Fig. 3.5. In turn, we are left with the bosonic charge mode and two Majorana edge modes or, equivalently, with two bosonic edge modes in total. Consequently, this state, which we call the bilayer state, is characterized by central charge $c_{\mathrm{B}} = 2$. This can also be understood in the limit $\tilde{u} = \tilde{v} = 0$, where the model reduces to two independent copies of the Laughlin state at $\nu = 1/2$ exhibiting one bosonic edge mode each.

We conclude our discussion by remarking that all the phases above are potential ground state candidates of the fractional quantum Hall problem at $\nu = 1$. As already mentioned before, the question, which ground state is realized for a given set of microscopic parameters, is best answered using numerical methods. We will address this point below when studying the Hofstadter-Bose-Hubbard model in some detail.

3.3. Fractional Chern Insulators on Coupled Chains

3.3.1. Relevance for Cold Atoms in Optical Lattices

Anisotropic hopping amplitudes can routinely be realized in state-of-the-art cold atom experiments with optical lattices by tuning the lattice depth. In particular, dynamically tuning such hoppings can be accomplished with standard techniques. Combined with excellent local control in the preparation of one-dimensional states, this gives rise to the possibility to prepare extended two-dimensional systems from arrays of one-dimensional wires. In fact, such an approach is one of the key steps in the first realization of an atomic Laughlin state by Léonard *et al.* [25]. Also theoretical proposals have been developed in recent years to exploit similar approaches to adiabatically prepare extended FQH states in optical lattices [79, 176]. In particular, the adiabatic connection of FQH states to Tao-Thouless-like CDW states in the quasi-one-dimensional regime makes such approaches a particularly promising route towards FQH states of many atoms.

The controlled interpolation between one and two dimensions also allows for novel insights into the entangled nature of exotic many-body states. Connecting the quasi-one-dimensional chiral Luttinger liquid regime for decoupled chains to two-dimensional topological states is clearly not possible without changing the entangled nature significantly. As discussed before, various initially gapless modes are gapped out in the continuous coupled wire construction and we believe a similar result to hold true in the case of discrete chains. While numerically such a change of the gapless modes can be seen from a scaling of the bipartite entanglement entropy, this is less trivial in quantum gas experiments.

However, we will see below that in certain regimes essential features of the entanglement entropy can be approximated sufficiently well using the so called *number entropy* to resolve the transition from the topologically trivial regime to the FQH regime. In particular, the number entropy can be calculated from Fock basis snapshots of the system which are routinely available in experiments employing site-resolved quantum gas microscopy. Therefore, a direct measurement of the central charge in experiments is now within reach and might open new directions in identifying and characterizing topological states of matter.

3.3.2. Anisotropic Hofstadter-Bose-Hubbard Model

As discussed before, the Hofstadter-Bose-Hubbard model is a natural lattice analog of the bosonic fractional quantum Hall problem. Again, we study bosons on a square lattice of size $L_x \times L_y$, where we work in the regime $L_x \gg L_y$, ultimately aiming for the quasi-1D thermodynamic limit $L_x \to \infty$. Allowing for anisotropic hopping, the Hamiltonian in Landau gauge reads

$$\begin{aligned}\hat{\mathcal{H}} = &- t_x \sum_{x=1}^{L_x-1} \sum_{y=1}^{L_y} \left(\hat{a}^\dagger_{x+1,y} \hat{a}_{x,y} + \text{H.c.} \right) - t_y \sum_{x=1}^{L_x} \sum_{y=1}^{L_y-1} \left(\mathrm{e}^{2\pi i \alpha x} \hat{a}^\dagger_{x,y+1} \hat{a}_{x,y} + \text{H.c.} \right) \\ &+ \frac{U}{2} \sum_{x,y} \hat{n}_{x,y} \left(\hat{n}_{x,y} - 1 \right). \end{aligned} \tag{3.28}$$

Here, $\hat{a}^{(\dagger)}_{x,y}$ are bosonic annihilation (creation) operators and $\hat{n}_{x,y} = \hat{a}^\dagger_{x,y} \hat{a}_{x,y}$ are the boson number operators at site (x, y). The terms in the first line describe (potentially anisotropic) hopping with amplitude t_x and t_y between neighboring sites in x and y direction, respectively, while the second line describes repulsive ($U/t_x > 0$) on-site interactions. For most of this chapter we consider open boundary conditions in both directions, thus realizing the model on an array of coupled chains, similar to the one considered in the continuum coupled wire construction discussed above.

Numerical Method

We perform DMRG simulations [135–137] using the SyTen toolkit [138] and its implementation of the single-site variant [139]. We exploit the U(1)-symmetry associated with particle number conservation to determine the variational ground state of the Hofstadter-Bose-Hubbard model for a specified number of particles. Furthermore, we consider different truncations of the local Hilbert space by restricting the maximum number of bosons per site. Convergence of the simulations is ensured by comparing the ground state energy $\langle\hat{\mathcal{H}}\rangle$ and the corresponding variance $\langle\hat{\mathcal{H}}^2\rangle - \langle\hat{\mathcal{H}}\rangle^2$ for different bond dimensions up to $\chi = 6000$.

3.3.3. Laughlin State at $\nu = 1/2$ on Discrete Chains

We start our study by considering the system at magnetic filling factor $\nu = N/N_\phi = 1/2$ and fix the Hubbard interaction strength to $U/t_x = 5$, which is large compared to the band width of the lowest band and also the band gap of the single-particle model. For our studies at $\nu = 1/2$, we truncate the local Hilbert space to at most $N_{\max} = 3$ bosons per site, which is justified by the large value of U/t_x. Compared to a hard-core constraint, our truncation avoids an artificial enhancement of Laughlin physics.

We restrict ourselves to a magnetic flux per plaquette of

$$\alpha = N_\phi / \left[(L_x - 1)\,(L_y - 1)\right] = 1/4, \tag{3.29}$$

so that in the isotropic case, $t_y/t_x = 1$, continuum limit analogies of earlier studies apply [65]. Thus, at the magnetic filling factor $\nu = 1/2$ studied here, we expect the ground state in the isotropic limit to be closely related to the topologically ordered $1/2$-Laughlin state [26]. We will see that this behavior is to some extent robust to tuning the inter-chain hopping strength.

Bipartite Entanglement Entropy and Central Charge

As discussed before, the central charge provides a quantitative way to characterize the edge theory of a two-dimensional topologically ordered system. In particular, the number (and nature) of chiral gapless modes can be extracted from it. Therefore, it provides a prime quantity to identify FQH states with chiral edge modes.

For the Laughlin state at filling factor $\nu = 1/2$, the central charge is predicted to be $c_{\text{LN}} = 1$, stemming from a single chiral bosonic edge mode. In our studies, the size of the system along both directions is substantially larger than the magnetic length so that we expect this prediction to manifest in our numerical studies. Therefore, we expect the central charge to approach unity close to the isotropic limit, $t_y/t_x \approx 1$.

In contrast, in the weakly coupled regime, $t_y/t_x \approx 0$, the system can be considered a collection of L_y independent one-dimensional Luttinger liquids, each of which contributes a value of $c_{\text{LL}} = 1$ to the total central charge, thus adding up to $c = L_y$.

In order to determine the central charge numerically, we make use of a prediction from conformal field theory (CFT) for finite systems with open boundary conditions relating the central charge c to the bipartite entanglement entropy $S(x)$, namely

$$S_{\text{CFT}}(x) = \frac{c}{6}\log\left(\frac{2L_x}{\pi}\sin\left(\frac{\pi x}{L_x}\right)\right) + g, \tag{3.30}$$

where g is some non-universal constant and L_x is the length of the system [49].

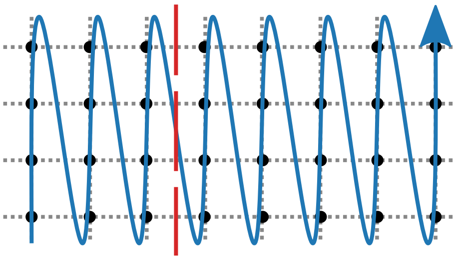

Fig. 3.6. Given the lattice sites of the two-dimensional square lattice (black dots), the MPS chain (blue line) is chosen such that neighboring sites in y-direction are also neighboring sites in the MPS chain. Thus, a cut perpendicular to the chains in x-direction (red dashed line) can be realized by cutting a single bond in the MPS chain, giving immediate access to the bipartite entanglement entropy as function of the cut's position.

Matrix product states (MPS) allow for a particularly simple extraction of the entanglement entropy. By appropriately choosing the MPS chain (see Fig. 3.6), the bipartite entanglement entropy between the two parts of the system is entirely carried by a single MPS bond. Therefore, upon cutting this bond denoted by ℓ we obtain a bipartition of the underlying lattice along the x-direction.

In our finite-size calculations, the bipartite entanglement entropy $S(\ell)$ as well as the particle density show significant oscillations in some cases, closely related to the CDW in the quasi-one-dimensional limit. We account for these oscillations in the entanglement entropy, in particular in small systems, by normalizing the entanglement entropy in a given bond ℓ by the local densities at the neighboring sites $x = \ell \pm 1/2$. Defining the density $n(x) = \sum_{y=1}^{L_y} \langle \hat{n}_{x,y} \rangle / L_y$ and the average density $\bar{n} = \sum_{x=1}^{L_x} n(x)/L_x$, we define the rescaled entanglement entropy

$$\tilde{S}(\ell) = \frac{2\bar{n}}{\left(n(\ell - \frac{1}{2}) + n(\ell + \frac{1}{2})\right)} S(\ell). \tag{3.31}$$

In addition, to reduce the effect of the truncation at a finite bond dimensions χ, we extrapolate the rescaled entanglement entropies $\tilde{S}(\ell; \chi)$ to infinite bond dimensions as

$$\tilde{S}(\ell; \chi) = \tilde{S}(\ell; \chi \to \infty) + A \log\left(1 + {}^{1}\!/\!{}_{\chi}\right). \tag{3.32}$$

Next, the extrapolated entanglement entropies $\tilde{S}(\ell; \chi \to \infty)$ are fitted using the CFT prediction in Eq. (3.30). Finally, we extrapolate the finite-size values for the central charge to infinite systems by a first-order extrapolation in ${}^{1}\!/\!{}_{L_x}$,

$$c(L_x) = c(L_x \to \infty) + {}^{B}\!/\!{}_{L_x}. \tag{3.33}$$

Examples for this extrapolation are given in Fig. 3.7.

For $L_y \geq 3$-leg systems, we find the value of the central charge to change drastically around $t_y/t_x \approx 0.6$, see Fig. 3.8. In particular, at large t_y/t_x we observe that the numerical central charge almost perfectly matches the theoretical prediction of $c_{\mathrm{LN}} = 1$. In the weakly coupled regime convergence of the DMRG calculations is difficult to achieve because of the small tunneling element t_y/t_x. Accordingly, the numerical values for the central charge do not coincide with the predicted values to the same degree of accuracy. Nevertheless, a clear change of behavior is visible in all the systems with $L_y = 3, \ldots, 6$ chains studied here, see Fig. 3.9.

Given the robustness of the transition with respect to the number of chains, we believe this feature to carry over to the thermodynamic limit and consider it striking evidence for the emergence of a Laughlin phase around $t_y/t_x \approx 1$.

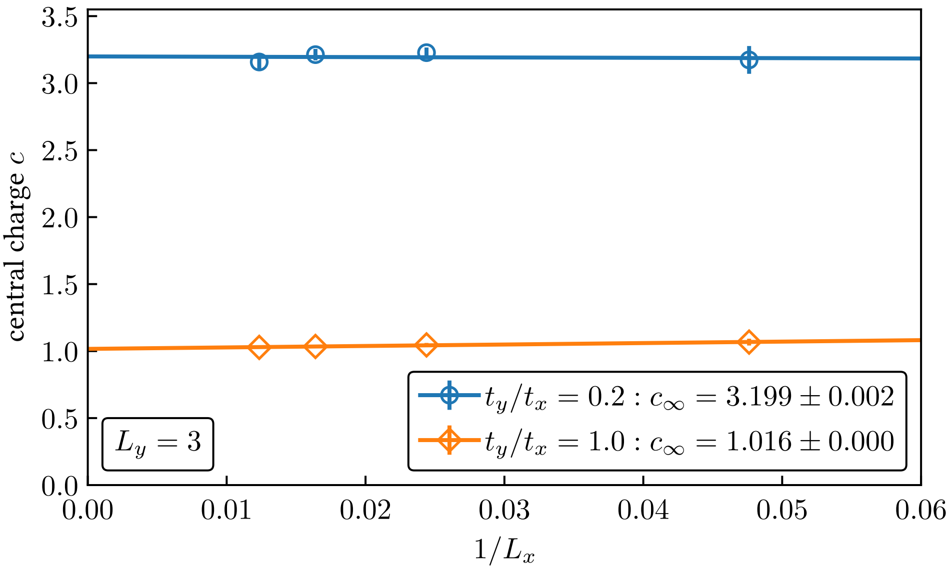

Fig. 3.7. Extrapolation of the central charge from finite L_x to $L_x \to \infty$ for $t_y/t_x = 0.2$ and $t_y/t_x = 1.0$. The error bars of the single data points indicate the uncertainty of the fit with the CFT formula.

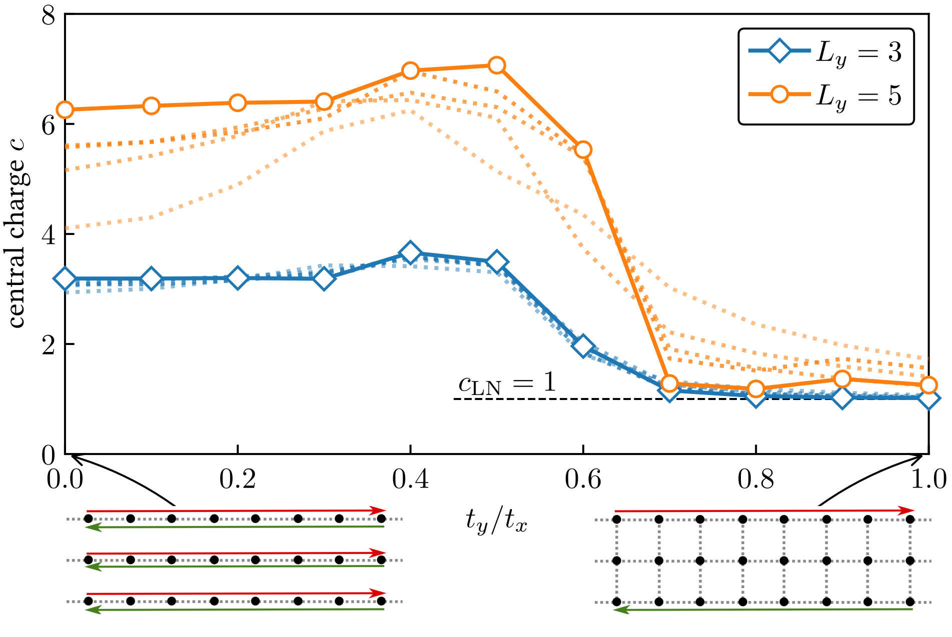

Fig. 3.8. Central charge as obtained from the bipartite entanglement entropy $S(x)$ for different system sizes after extrapolation to $L_x \to \infty$ for $L_y = 3$ (blue diamonds) and 5 (orange circles). Faded dotted lines indicate values for finite L_x with longer systems being less faded. We find a clear change of behavior around $t_y/t_x \approx 0.6$. Above this critical value, the central charge is in agreement with the prediction $c_{\mathrm{LN}} = 1$ for the Laughlin state. The sketches below the main panel illustrate the origin of the different behavior in the decoupled ($t_y/t_x = 0$) and the isotropic ($t_y/t_x = 1$) limit by only showing gapless chiral modes.

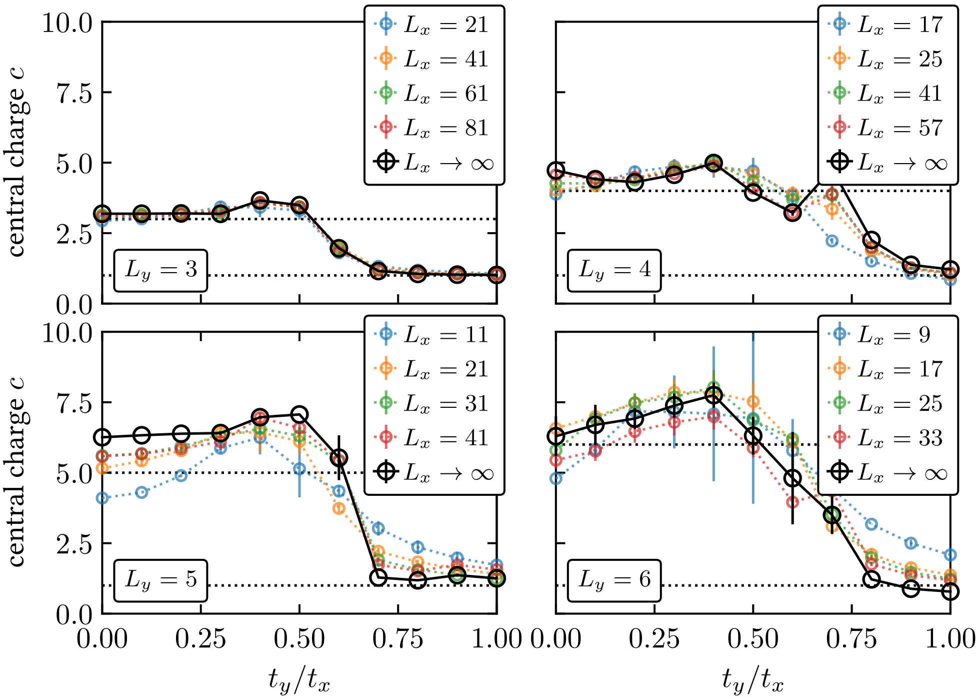

Fig. 3.9. Central charge as obtained from the rescaled and χ-extrapolated bipartite entanglement entropy for different system sizes ($L_y = 3, \ldots, 6$) and the extrapolated value in the limit $L_x \to \infty$. The dotted lines indicate $c = 1, L_y$ respectively.

Remarkably, our DMRG simulations rule out a Laughlin-like state in $L_y = 2$-leg systems, where we observe $c = 2$ throughout, as will be discussed below in more detail. However, additional nearest-neighbor repulsion has been argued to reintroduce Laughlin-like states [179–182].

Measuring the Central Charge Using Snapshots

To our knowledge, the central charge has so far eluded direct experimental measurements. We propose a protocol to measure the central charge in state-of-the-art quantum simulation platforms such as quantum gas microscopes. The typical outcome of these experiments are projective measurements in the Fock basis resulting in site resolved snapshots of the local particle number. Efficient methods to generate accurate snapshots from MPS have been developed [183] and proved useful for sampling realistic experimental outcomes in models similar to ours [184].

In order to extract the entanglement entropy $S(\ell)$ experimentally, we propose to use the particle number entropy $S_\mathrm{n}(\ell)$ as a meaningful proxy in certain regimes. A similar approach has proven useful in the context of many-body localization [185], and also theoretical attempts to study the entanglement entropy using particle number fluctuations have been undertaken earlier [186]. Here, we exemplify the use of snapshots and their number entropy to determine the central charge of the topologically non-trivial $1/2$-Laughlin state.

The main advantage of the number entropy is that it can be directly extracted from a given set of snapshots. To this end, each snapshot is split into two disjoint subsystems A and $\bar{A}$ and the probability p_{N_A} to observe N_A particles in subsystem A is determined. Then, the particle number entropy $S_\mathrm{n} = \sum_{N_A} p_{N_A} \log(p_{N_A})$ can be calculated. Repeating this scheme for different partitions of the system similar to the case of the entanglement entropy S above, one obtains the number entropy $S_\mathrm{n}(\ell)$ as function of the cut position.

In the isotropic limit, $t_y/t_x = 1$, the number entropy provides a good estimate of the entanglement entropy for already 2000 snapshots, see Fig. 3.10**(b)**. This behavior carries over to the entire regime in which we have identified the 1/2-Laughlin state using the entanglement entropy. In Fig. 3.10**(c)** we find that close to the isotropic limit the prediction of the central charge based on snapshots agrees reasonably well with the prediction from the entanglement entropy. Thus we conclude that this method can indeed be used to estimate the central charge in the Laughlin phase.

In the decoupled limit, $t_y/t_x = 0$, the number entropy extracted from the full system is not additive in the number of legs, see Fig. 3.10**(a)**. In contrast, extracting the number entropy from each leg separately, we find that the central charge $c_{\mathrm{n}}^{(1)}$ in each leg is in agreement with the value from the entanglement entropy, so that multiplying $c_{\mathrm{n}}^{(1)}$ by the number of legs provides the correct overall central charge for the whole system. In the intermediate regime, we attribute discrepancies between the central charge c and the estimate c_{n} to a combination of the non-applicability of the CFT prediction and the non-additivity of the number entropy.

We emphasize that the proposed measurement of the central charge is solely based on snapshots in the Fock basis, which are routinely generated in experiments with quantum gas microscopes [109–112]. The number entropy and the estimated central charge discussed here can be extracted from these snapshots without further experimental efforts and are accessible to existing experiments.

Additional Experimental Observables

Now, we discuss further observables accessible to quantum gas microscopes. A well known signature of the 1/2-Laughlin state, reflecting the flux-attachment underlying the formation of composite fermions [60], is a strong suppression of on-site correlations,

$$g^{(2)}(0) = \frac{1}{2L_x L_y} \sum_{x,y} \langle \hat{n}_{x,y} \left(\hat{n}_{x,y} - 1 \right) \rangle . \tag{3.34}$$

By allowing up to three bosons per site in our numerics, we do not artificially stabilize the Laughlin state by imposing a hard-core constraint for the bosons, formally $U/t = \infty$. In contrast, given the small particle number densities, our simulations can be expected to properly describe the experimental situation of a finite two-body interaction.

In Fig. 3.11 we show $g^{(2)}(0)$ as a function of t_y/t_x. In particular, we find that in the weakly coupled limit $g^{(2)}(0)$ is very small, while it increases with increasing inter-chain hopping. $g^{(2)}(0)$ takes a global maximum around $t_y/t_x \approx 0.6$ before it decreases again in the strongly coupled regime.

In the isotropic limit, this drop is a key feature of the 1/2-Laughlin state, indicating the screened interactions of composite fermions [60]. In contrast, in the decoupled limit this is the result of a different, Jordan-Wigner-type fractionalization of the bosons [187–189]. In the intermediate regime, the bosons are not able to fermionize and therefore the residual two-particle correlations are significantly larger compared to both of the limits.

As another experimental observable, we consider the momentum distribution along x in a given wire,

$$n_y(k_x) = \frac{1}{L_x} \sum_{x,x'} \mathrm{e}^{-ik_x(x-x')} \left\langle \hat{a}^{\dagger}_{x,y} \hat{a}_{x',y} \right\rangle , \tag{3.35}$$

where $k_x = \frac{2\pi m}{L_x}$, $m = 0, \ldots, L_x - 1$. The momentum distribution in a specific wire is experimentally accessible in various cold atom experiments with current techniques, for example by time-of-flight measurements with expansions only along the one-dimensional tubes.

The numerical results in Fig. 3.12 indicate the occupation of a chiral mode with finite momentum $k_x \neq 0$ at the boundary for $t_y/t_x \gtrsim 0.6$, while in the bulk the distribution remains peaked

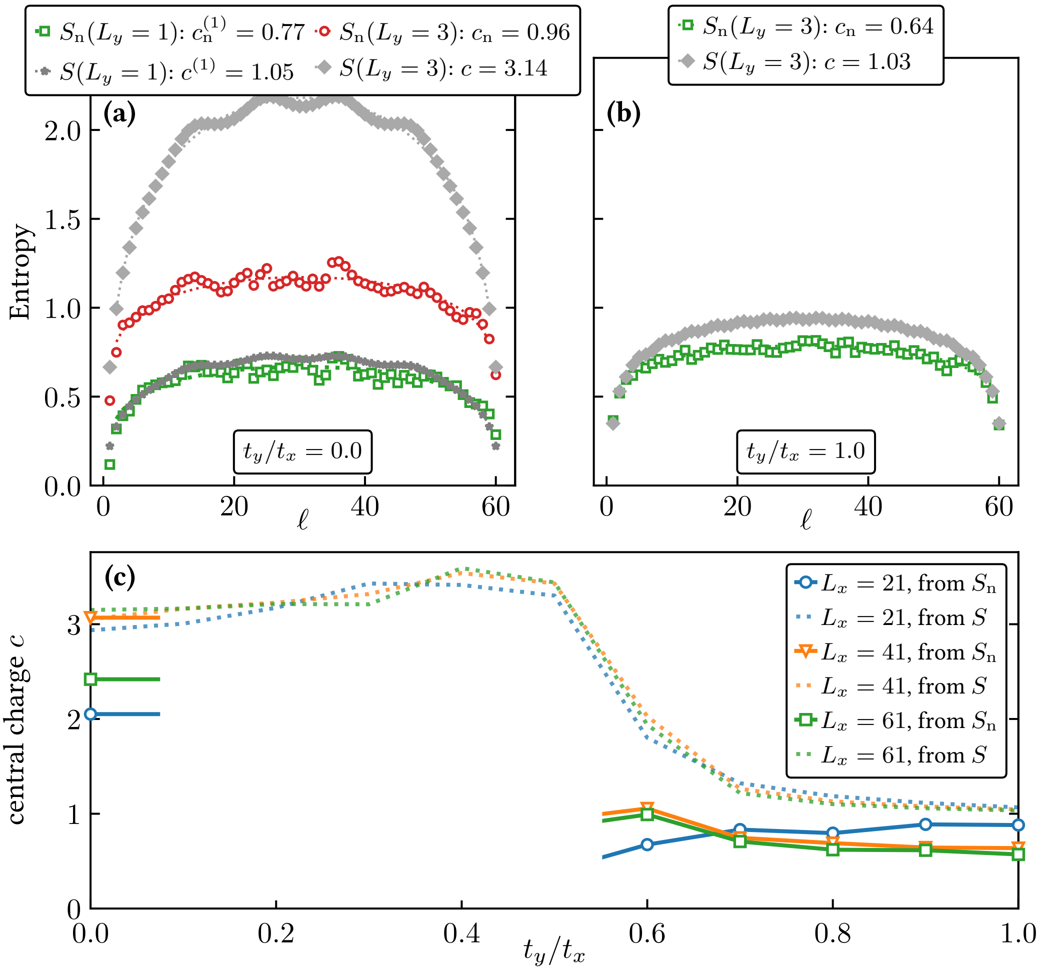

Fig. 3.10. **(a)** Number entropy $S_n(\ell)$ from 6000 (2000) snapshots of a single chain (three decoupled chains) of length $L_x = 61$. While the number entropy provides an accurate proxy for the entanglement entropy $S(L_y = 1)$ of a single chain, it is not additive in the number of chains. Therefore, we extract the central charge $c_n^{(1)}$ of a single chain to obtain the total central charge $c_n = L_y c_n^{(1)}$ in this limit. **(b)** In the isotropic limit, $t_y/t_x = 1$, the proxy $S_n(\ell)$ from 2000 snapshots of the 3-leg system is relatively accurate. **(c)** Central charges for 3-leg systems extracted from the number entropy $S_n(\ell)$ (solid lines) compared to the prediction from the entanglement entropy $S(\ell)$ (faded, dotted lines).

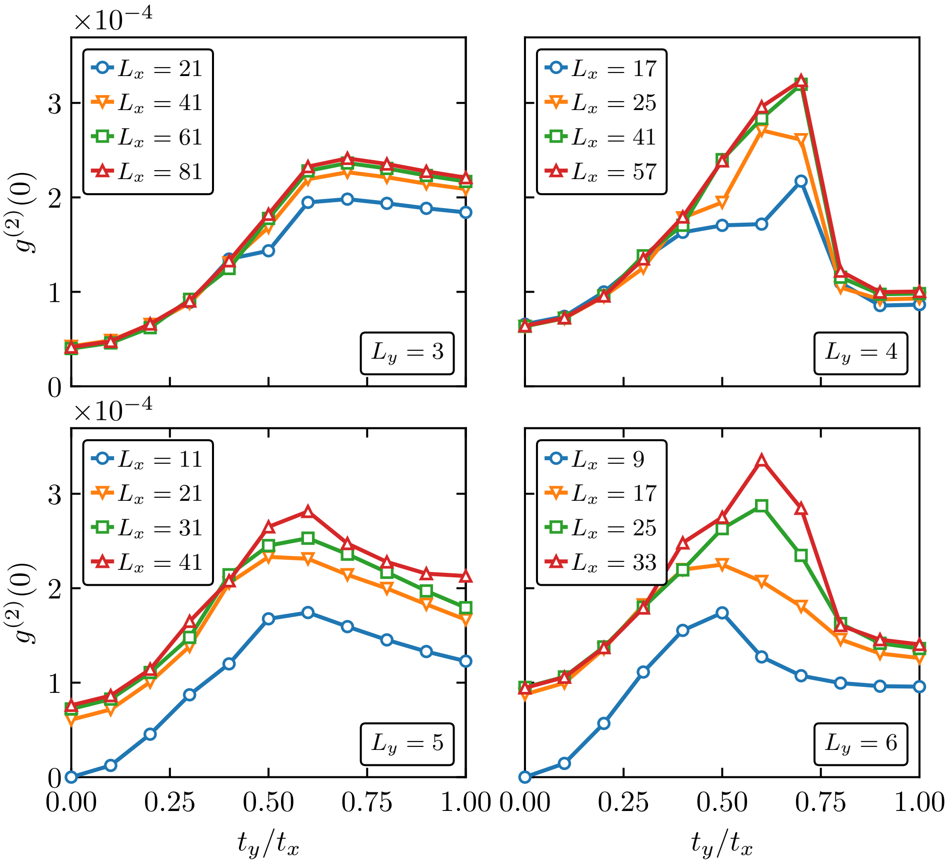

Fig. 3.11. On-site correlations $g^{(2)}(0)$ for $L_y = 3, \ldots, 6$ chains. The transition region at intermediate t_y/t_x is clearly visible by a maximum of $g^{(2)}(0)$.

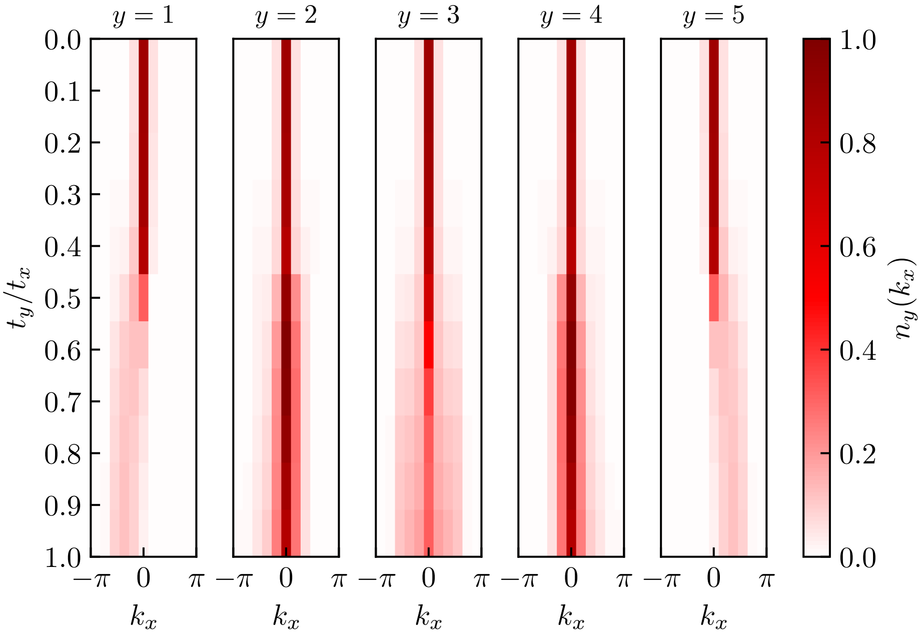

Fig. 3.12. Momentum distribution $n_y(k_x)$ for $L_y = 5, L_x = 11, U/t_x = 5.0$. We observe the emergence of a chiral mode in the outermost chains ($y = 1, 5$) around $t_y/t_x \approx 0.6$. In these chains, the momentum distribution is peaked around a finite momentum $k_x \neq 0$, whereas the remaining bulk chains exhibit a peak around $k_x = 0$ at all t_y/t_x.

around $k_x = 0$ even around $t_y/t_x \approx 1$. We interpret the sudden change around $t_y/t_x \approx 0.6$ as further evidence for the 1/2-Laughlin phase close to the isotropic limit indicated by the characteristic chiral edge mode.

This gapless edge mode also manifests itself in the presence of a chiral edge current. We define the currents in x- and y-direction as

$$\begin{aligned} j^x_{x,y} &= \left\langle \hat{j}^x_{x,y} \right\rangle = it_x \left\langle \hat{a}^\dagger_{x+1,y} \hat{a}_{x,y} \right\rangle + \text{c.c.}, \\ j^y_{x,y} &= \left\langle \hat{j}^y_{x,y} \right\rangle = it_y \mathrm{e}^{2\pi i \alpha x} \left\langle \hat{a}^\dagger_{x,y+1} \hat{a}_{x,y} \right\rangle + \text{c.c.}. \end{aligned} \tag{3.36}$$

In the regime of weakly coupled wires we expect no pronounced edge current, while in the Laughlin state the edge current should be far more prominent than the current fluctuations in the bulk.

Indeed, this is what we find in our numerical simulations. Typical current patterns are depicted in Fig. 3.13 for the weakly coupled, the transient, and the Laughlin regime. It is clearly visible that above some critical value of t_y/t_x a chiral edge current forms.

However, for systems with $L_y = 4$ chains we find some non-trivial vortex pattern in the current as visualized in Fig. 3.14.

Topological Classification: Many-Body Chern Number

In order to provide an unambiguous topological classification of the ground state, we determine the many-body Chern number [14, 34] as function of the anisotropic hopping strength. In particular, we use the method proposed by Dehghani *et al.* [190] to extract the many-body Chern number from a single ground state wave function. To this end, we perform DMRG calculations on cylinders of coupled chains with periodic boundary conditions in y-direction at bond dimensions up to $\chi = 3000$.

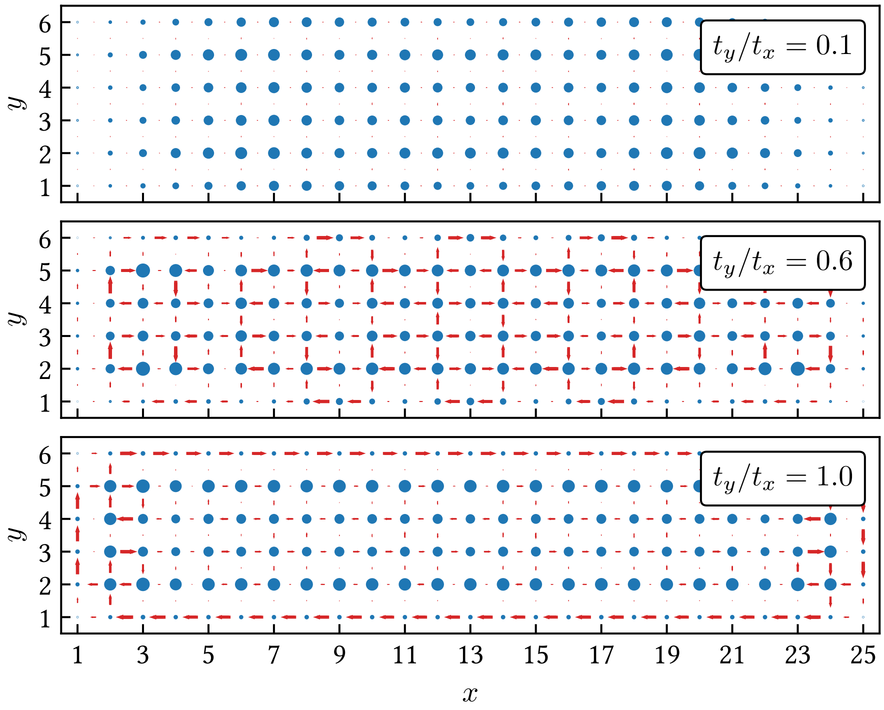

Fig. 3.13. Local currents for a system of size $L_x = 25, L_y = 6$ and $N = 15$ particles subject to $N_\phi = 30$ flux quanta. The length and width of the red arrows indicate the strength and direction of the current along a bond and the radii of the blue dots indicate the density at a given site. The hopping strength in the y-direction is increased from top to bottom, $t_y/t_x = 0.1, 0.6, 1.0$. In the isotropic limit we find the expected pronounced edge current.

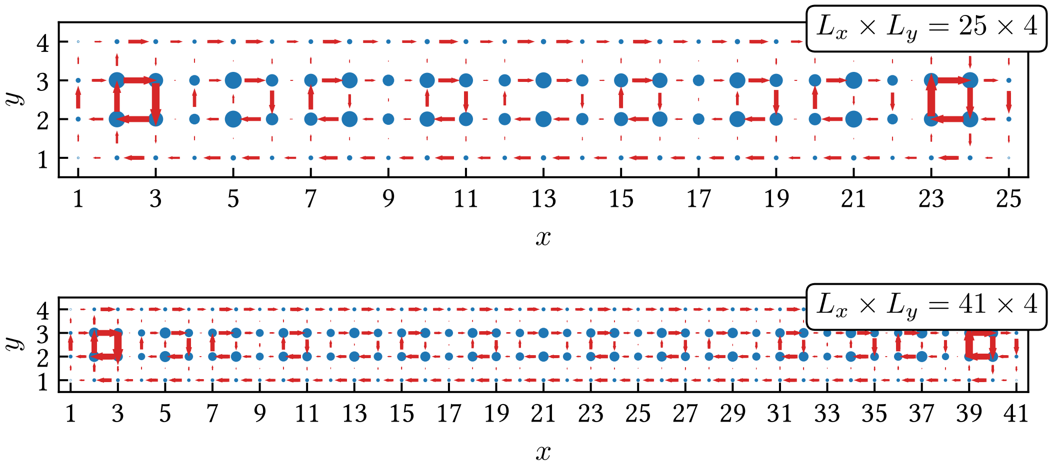

Fig. 3.14. Vortices in the current pattern for systems of $L_y = 4$ chains at $t_y/t_x = 1.0$.

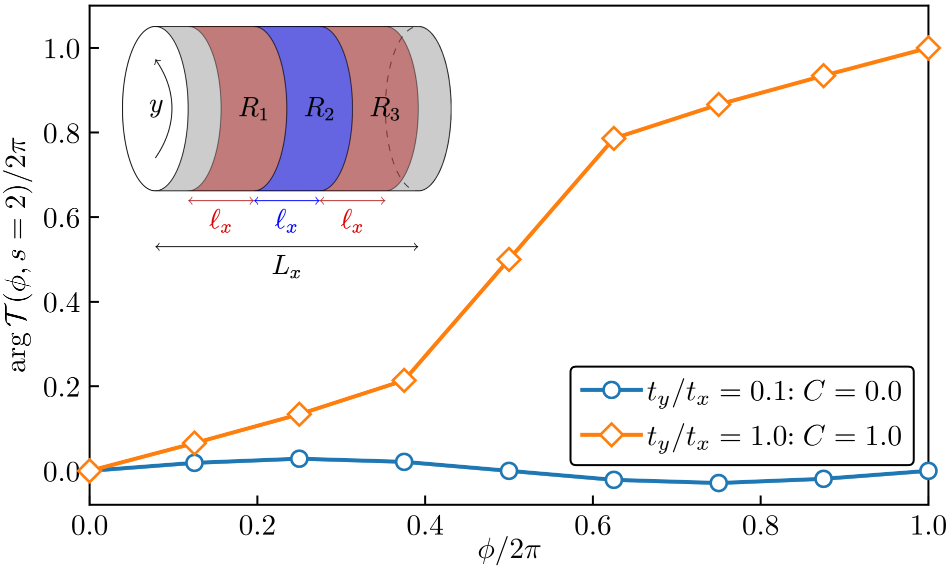

Fig. 3.15. Origin of different Chern numbers from the winding of $\mathcal{T}(\phi, s = 2)$ in the complex plane. The inset illustrates the regions used for the evaluation of the Chern number.

Following [190], we choose three cylindrical regions $R_{1,2,3}$ of length $\ell_x = \lfloor (L_x - 3)/3 \rfloor$ on the cylinder, where $\lfloor x \rfloor$ denotes the integer part of x, and define

$$\mathcal{T}(\phi, s) = \left\langle \hat{W}^\dagger_{R_1}(\phi) \hat{S}_{1,3} \hat{W}_{R_1}(\phi) \hat{V}^s_{R_1 \cup R_2} \right\rangle . \tag{3.37}$$

Here, $\hat{S}_{1,3}$ swaps the regions R_1 and R_3 and

$$\hat{W}_R(\phi) = \prod_{(x,y)\in R} \mathrm{e}^{i\hat{n}_{x,y}\phi} \qquad \text{and} \qquad \hat{V}_R = \prod_{(x,y)\in R} \mathrm{e}^{i\frac{2\pi y}{L_y}\hat{n}_{x,y}} \tag{3.38}$$

are defect operators.

During the application of the exponential operators we truncate the resulting MPS at bond dimension $\chi = 150$. The necessary SWAP operation is implemented on the level of an MPS overlap.

In our case, s is the ground state degeneracy on a torus, which for the 1/2-Laughlin state is known to be $s = 2$. Varying ϕ from 0 to 2π, we obtain the many-body Chern number as the winding number

$$C = \frac{1}{2\pi} \oint \mathrm{d}\phi \, \frac{\mathrm{d}}{\mathrm{d}\phi} \arg \mathcal{T}(\phi, s), \tag{3.39}$$

which is directly related to the Hall conductivity $\sigma_\mathrm{H} = \frac{C}{s}\frac{e^2}{h}$.

We exemplify the behavior of $\arg \mathcal{T}(\psi, s)$ for the two different regimes $t_y/t_x = 0.1$ and 1.0 in Fig. 3.15. Evaluating the winding number integral, we find that for weakly coupled chains the many-body Chern number vanishes, see Fig. 3.16, confirming our understanding of the topologically trivial phase in this regime. On the other hand, around $t_y/t_x \approx 1$ we find the many-body Chern number to be $C = 1$, hence resulting in the non-trivial Hall response $\sigma_\mathrm{H} = \frac{1}{2}\frac{e^2}{h}$ expected for the 1/2-Laughlin state. This is in agreement with the other observables discussed here and gives direct evidence for the topological nature of the ground state close to the isotropic limit.

This result also allows us to confirm our earlier assumption for the value of s by comparing the Hall conductivity σ_H obtained by this method to the Hall conductivity obtained from a charge

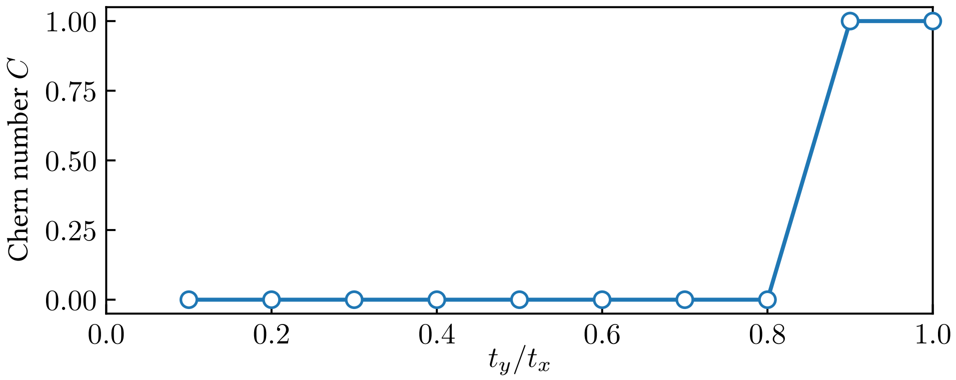

Fig. 3.16. Many-body Chern number as function of t_y/t_x for a cylinder of size $L_x \times L_y = 25 \times 3$. We find a transition towards a topologically non-trivial phase close to the isotropic limit.

pump procedure. To this end, we introduce a magnetic flux ϕ through the cylinder by modifying the Hamiltonian of the model to be

$$\begin{aligned}\hat{\mathcal{H}}\left(\phi\right) = &- t_x \sum_{x=1}^{L_x-1} \sum_{y=1}^{L_y} \left(\hat{a}^\dagger_{x+1,y}\hat{a}_{x,y} + \text{H.c.}\right) - t_y \sum_{x=1}^{L_x} \sum_{y=1}^{L_y-1} \left(\mathrm{e}^{2\pi i\alpha x \underline{+ i\phi x/L_y}}\, \hat{a}^\dagger_{x,y+1}\hat{a}_{x,y} + \text{H.c.}\right)\\ &+ \frac{U}{2}\sum_{x,y} \hat{n}_{x,y}\left(\hat{n}_{x,y} - 1\right).\end{aligned} \tag{3.40}$$

We perform DMRG ground state searches for slowly increasing values of ϕ with maximum bond dimension $\chi = 200$ to simulate an adiabatic flux insertion protocol. We cut the cylinder into two halves and track the particle number $n_L(\phi)$ in the left half as function of the inserted flux ϕ. Taking into account the unit charge of the bosons, we can define the pumped charge as

$$\delta Q(\phi) = n_L(\phi) - n_L(0). \tag{3.41}$$

We present the results of the charge pumping procedure in the different regimes in Fig. 3.17. In particular, we find that in the weakly coupled limit, $t_y/t_x = 0.1$, no significant charge is pumped and therefore no Hall response is observed. We attribute the small residual pumped charge to the difficult convergence in this challenging regime. In contrast, in the isotropic limit, $t_y/t_x = 1.0$, we find a pumped unit charge after inserting flux $\phi = 2 \times 2\pi$. This is consistent with a Hall conductivity of $\sigma_H^{\text{pump}} = \frac{1}{2}\frac{e^2}{h}$ after restoring units. This clearly shows that $s = 2$ is indeed the right ground state degeneracy in the topological regime and a similar approach can be used to obtain the correct factor also for more involved cases.

Limiting Case $L_y = 2$: Flux Ladders

As a limiting case we simulated two-leg ladders ($L_y = 2$) subject to a perpendicular magnetic field. Similar models were studied with various modifications in earlier studies [172, 179–182, 191–194]. We find that the physics in this regime is qualitatively different from the extended systems with $L_y \geq 3$ studied above. The extrapolated central charge for the ladder system is depicted in Fig. 3.18. Note, that we do not find a transition to the predicted $c_{\text{LN}} = 1$ for the Laughlin state, but instead find $c = 2$ independent of the inter-chain hopping. Nevertheless, the on-site correlations and the momentum distribution show some signatures reminiscent of larger systems, see Fig. 3.19. In particular, the suppression of the on-site correlations $g^{(2)}(0)$ close to the isotropic regime might hint towards a precursor of the Laughlin state.

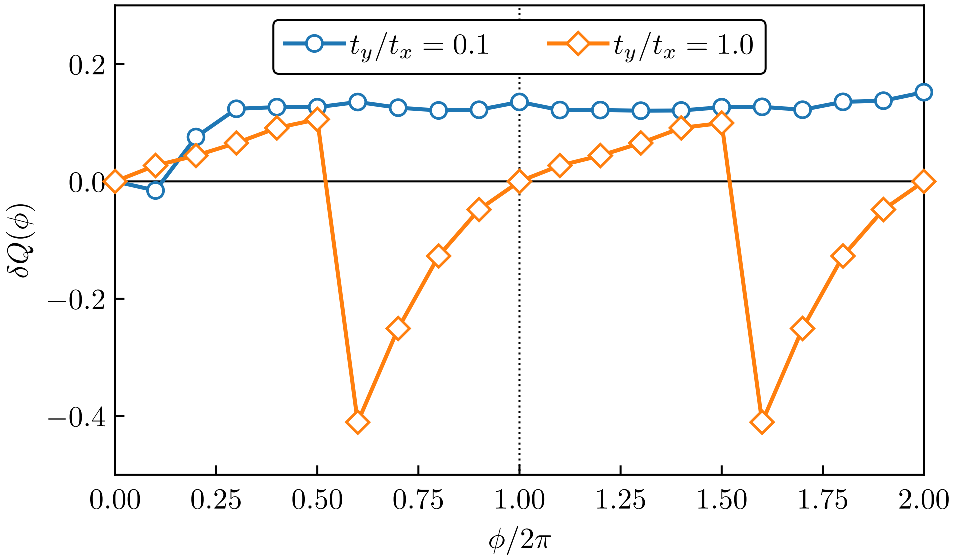

Fig. 3.17. Pumped charge as function of inserted flux for two different limits of the interchain coupling. In the weakly coupled limit, $t_y/t_x = 0.1$, only a small, non-significant amount of charge is pumped. We attribute the remaining pumped charge to convergence difficulties in this regime. In the isotropic limit, $t_y/t_x = 1.0$, an effective unit charge is pumped after the insertion of 4π flux. The jumps are due to the charge density wave forming on thin cylinders jumping to a competing configuration with occupied orbitals shifted by one.

However, we conclude that, in the model studied here, physics in the Laughlin universality class can only be achieved for systems of at least $L_y = 3$ chains. Nevertheless, this minimal setup already provides clear indication of the exciting topological nature of the ground state.

Conclusions

The bosonic $1/2$-Laughlin state can be realized in three or more coupled chains subject to a magnetic field close the isotropic limit. The transition from a topologically trivial phase to this topologically ordered phase as the inter-chain hopping strength is tuned can be seen from various observables. Most prominently, we have found the central charge to provide clear evidence in the strong-coupling phase by dropping to the expected value $c_{\mathrm{LN}} = 1$ for the Laughlin state. Furthermore, we have shown that in this regime, the number entropy S_{n} gives a good estimate for the central charge. The number entropy can be extracted from snapshots generated routinely by existing quantum gas microscopes. Other experimentally accessible observables like on-site correlations, the momentum distribution and chiral currents confirm the transition from the trivial to the Laughlin phase. Finally, we have identified the topological nature of the strong-coupling phase by extracting the many-body Chern number.

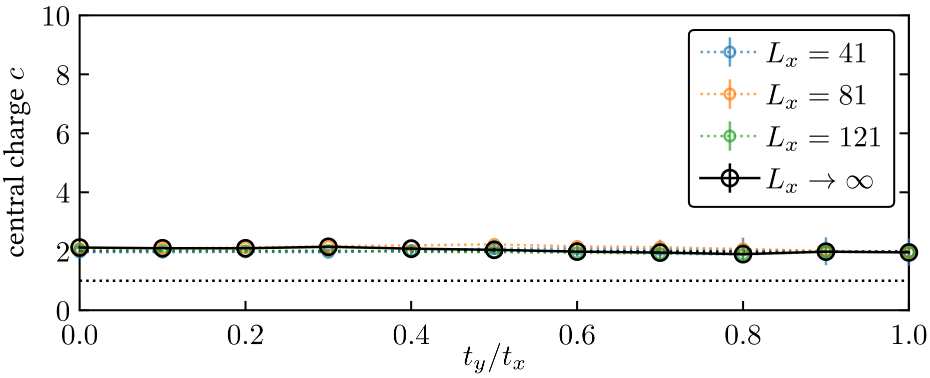

Fig. 3.18. Extracted central charge for ladder systems with $L_y = 2$. Note the qualitative difference from the extended systems discussed above, in particular the absence of a transition toward $c_{\text{LN}} = 1$ (indicated by the dotted line).

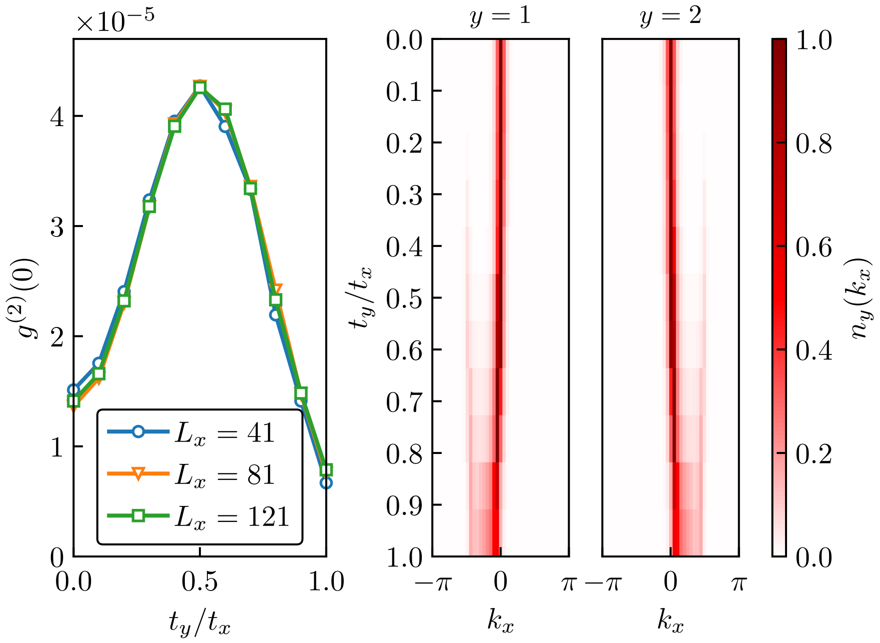

Fig. 3.19. On-site correlations (left) and momentum distribution in the two legs (right) for a ladder system.

3.3.4. Coupled Chains at $\nu = 1$

Given the existence of the Laughlin state at $\nu = 1/2$ on an array of coupled chains and the relevance of such systems to cold atom experiments, the natural question arises whether similar physics can also be observed at other magnetic filling factors ν. To study this, we now reduce the flux per plaquette to $\alpha = 1/6$ while at the same time increasing the particle number density such that we arrive at $\nu = 1$. We argued above that on a cylinder such a system exhibits a lattice analog of the celebrated Pfaffian state [1]. In this section we explore whether this is also the case for an array of coupled chains with open boundary conditions in both directions. As discussed above, the continuum coupled wire construction predicts the possible emergence of not only the Pfaffian state with central charge $c_{\mathrm{Pf}} = 3/2$, but also a strongly paired phase ($c_{\mathrm{SP}} = 1$) as well as the so-called bilayer phase ($c_{\mathrm{B}} = 2$).

In our numerical studies, we did not find evidence of the Pfaffian state in the anisotropic Hofstadter-Bose-Hubbard model on coupled chains for systems consisting of $L_y = 3, 4$, and 5 chains. However, for $L_y = 4$ chains close to the isotropic limit we find both the strongly paired phase ($c_{\mathrm{SP}} = 1$) as well as the bilayer phase ($c_{\mathrm{B}} = 2$). In particular, the strongly paired state at weak interactions is destroyed upon increasing the on-site two-body interactions in favor of the bilayer state. We have found first evidence for this phase transition being continuous.

If not mentioned otherwise, we truncate the local Hilbert space to at most $N_{\max} = 4$ bosons per site, justified by the dilute systems under consideration. Compared to a two- or three-particle hard-core constraint, our truncation avoids an artificial enhancement of the Pfaffian state and other competing (paired) states. Nevertheless, we used said hard-core three-body interactions ($N_{\max} = 2$) to see whether we can stabilize the Pfaffian state in a parent Hamiltonian-like system, which is not the case at the parameters studied here. In general, we find that this truncation of the local Hilbert space only negligibly affects the states studied here.

For $L_y = 3$ chains and hard-core three-body interactions, we find a state with central charge $c = 1$ independent of the remaining system parameters. Similarly, for $L_y = 5$ we only observe a state with central charge $c = 2$ in the isotropic regime. We were not able to resolve this behavior yet and further investigation is needed to understand whether this is indeed a physical feature of the system or a result of not fully converged numerics especially for the wider, and numerically more challenging, 5-leg system.

Before discussing our findings in detail, we would like to point out that the results presented in this section should still be considered preliminary. In particular, various questions, briefly mentioned at the end of this chapter, remained open at this point and will be addressed in the near future.

Spatial Bipartitions and Central Charge

As seen in the case of the Laughlin state at $\nu = 1/2$, the central charge allows for insights into the particle content of the edge theory of a two-dimensional system. In particular, it provides an important quantity in the classification of topological orders and is of key interest for the identification of FQH states and competing states with chiral edge modes.

For the bosonic Pfaffian state at filling factor $\nu = 1$, the central charge is predicted to be $c_{\mathrm{Pf}} = 3/2$ stemming from a bosonic ($c = 1$) and a Majorana ($c = 1/2$) edge mode. Other candidate states at $\nu = 1$ predicted by the coupled wire construction [174] are a strongly paired state with only the bosonic edge mode and hence central charge $c_{\mathrm{SP}} = 1$ and a bilayer state with one bosonic and two Majorana edge modes and central charge $c_{\mathrm{B}} = 2$.

We again perform MPS-based DMRG simulations to obtain the ground state for various system parameters, extract the entanglement entropy, and normalize the entanglement entropy carried by a given link ℓ by the local densities at the neighboring sites $x = \ell \pm 1/2$,

$$\tilde{S}(\ell) = \frac{2\bar{n}}{\left(n(\ell - \frac{1}{2}) + n(\ell + \frac{1}{2})\right)} S(\ell). \tag{3.42}$$

Furthermore, we extrapolate the entanglement entropy to infinite bond dimensions to account for truncation effects,

$$\tilde{S}(\ell; \chi) = \tilde{S}(\ell; \chi \to \infty) + A \log\left(1 + {}^{1}\!/\!{}_{\chi}\right). \tag{3.43}$$

In order to determine the central charge, we use the earlier CFT prediction relating the central charge c to the bipartite entanglement entropy $S(\ell)$, namely

$$S_{\mathrm{CFT}}(\ell) = \frac{c}{6} \log\left(\frac{2L_x}{\pi} \sin\left(\frac{\pi \ell}{L_x}\right)\right) + g, \tag{3.44}$$

where g is some non-universal constant and L_x is the length of the system [49]. This form can be rewritten as

$$S_{\mathrm{CFT}}(\lambda) = \frac{c}{6} \log\left(\sin\left(\pi\lambda\right)\right) + \mathrm{const.}, \tag{3.45}$$

where we introduced $\lambda = {}^{\ell}\!/\!{}_{L_x}$ and the non-constant part is independent of the system size so that we expect a scaling collapse to be applicable. We determine the entanglement entropy for systems of finite length $L_x = 25, 33, 41, 49$ and collapse them by shifting the numerical data such that

$$\tilde{S}(\lambda; \chi \to \infty) \to \tilde{S}(\lambda; \chi \to \infty) - \tilde{S}(\lambda = {}^{1}\!/\!{}_{2}; \chi \to \infty), \tag{3.46}$$

that is, we subtract the size-dependent constant shift in each data set and ensure that all curves go through $\tilde{S}(\lambda = {}^{1}\!/\!{}_{2}; \xi \to \infty) = 0$. We find a good collapse of the shifted entanglement entropy as visualized by exemplifying data points in Fig. 3.20. Encouraged by the successful scaling collapse, we extract the central charge from a fit of the CFT prediction $S_{\mathrm{CFT}}(\lambda)$ to the complete collapsed set.

The extracted values of the central charge for $L_y = 4$ are given in Fig. 3.21. For almost isotropic hopping $t_y \approx t_x$ and weak interactions, we find an extended phase exhibiting central charge $c \approx c_{\mathrm{SP}} = 1$, which we associate with the strongly paired phase in the coupled wire construction. Upon increasing the interaction strength, we find a transition to a phase with central charge $c \approx c_{\mathrm{B}} = 2$ consistent with the bilayer phase. Note that we do not find an extended regime with central charge $c_{\mathrm{Pf}} = {}^{3}\!/\!{}_{2}$ and therefore do not expect the Pfaffian state to be the ground state for the model under study using open boundary conditions in both directions.

The continuum Pfaffian state is known to be the exact ground state of hard-core three-body repulsive interactions in the lowest Landau level [155] and we found this behavior to carry over to lattice systems on cylinders [1]. Therefore, it might be possible to stabilize the Pfaffian state in our system by restricting the maximal local boson number to $N_{\max} = 2$, corresponding to a hard-core three-body repulsion. In particular in combination with weak and vanishing two-body interactions, $U/t_x \approx 0$, exact diagonalization on small tori found indication of the Pfaffian state in isotropic lattice systems [165]. However, extracting the central charge using the scaling approach discussed above we find essentially unchanged results in the limit of isotropic hopping, $t_y/t_x = 1$, see Fig. 3.22.

Additional Observables

While the entanglement entropy - and hence the central charge - are easily accessible in MPS-based numerical studies, they are notoriously hard to obtain experimentally. Despite first steps towards measurements of the central charge in quantum gas microscopy experiments, it is still

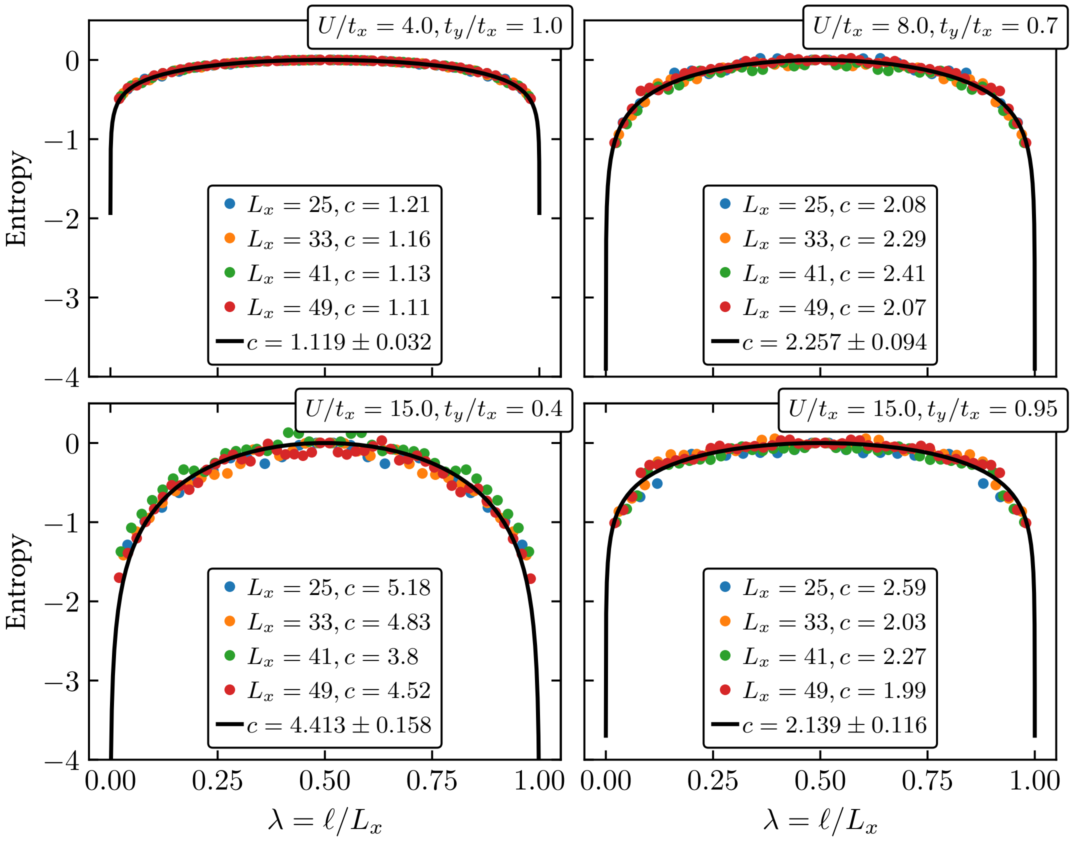

Fig. 3.20. Scaling collapse of the rescaled and shifted entanglement entropy extracted from MPS simulations for different parameters. The fit with the CFT prediction $S_{\mathrm{CFT}}(\lambda)$ (black solid line) is performed using all data points in the bulk, leaving out the outermost 2 data points for each system size on both ends of the chains.

favorable to detect and characterize interacting topological states by other means. Furthermore, such observables might allow for a refined and enhanced understanding of both the topological state under study itself and the quantum phase transitions between such states.

To this end, we next discuss experimentally accessible observables which are able to probe the correlated structure of the topological states under study. In particular, we study the decay of correlations $\langle \hat{a}^\dagger_{x,y} \hat{a}_{x',y} \rangle$ along the long x-direction of the system and the momentum distribution in the outermost leg, $y = 1$.

Correlations along the chains We start our discussion with the two-point correlations $\langle \hat{a}^\dagger_{x,y} \hat{a}_{x',y} \rangle$. In particular, we note that these correlations are expected to decay rapidly in the bulk of a topologically ordered system. Inspired by the explicit form of the decay for the Laughlin state [195], we expect a decay of the form

$$\frac{\left| \langle \hat{a}^\dagger_{x,y} \hat{a}_{x',y} \rangle \right|}{\sqrt{\langle \hat{n}_{x,y} \rangle \langle \hat{n}_{x',y} \rangle}} \propto \mathrm{e}^{-(x-x')^2/(4\xi^2)} + \mathrm{const.}, \tag{3.47}$$

where the constant contribution is added to account for finite-size effects. Using this prediction, we can perform a fit of the numerical data to extract the correlation length for different parameters. Examples of the fit are given in Fig. 3.23.

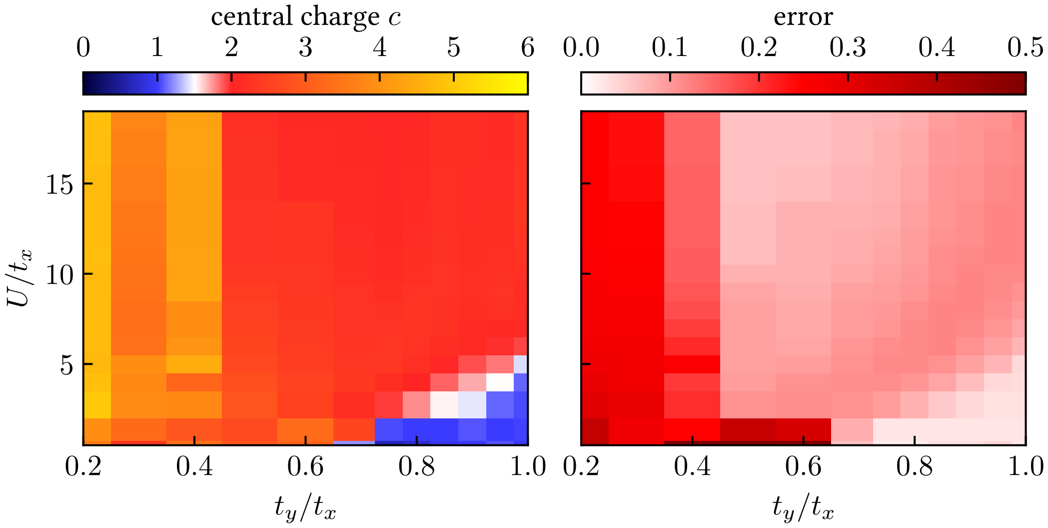

Fig. 3.21. Central charge c and its error as extracted from the bipartite entanglement entropy using a scaling collapse for $L_y = 4$. We find a regime with $c \approx c_{\mathrm{SP}} = 1$ for $t_y \approx t_x$ and weak interactions. Furthermore, we find an extended regime with $c \approx c_{\mathrm{B}} = 2$ for stronger interactions. At weak inter-chain coupling, $t_y/t_x \to 0$, we observe an increase of the central charge consistent with $c \approx L_y = 4$.

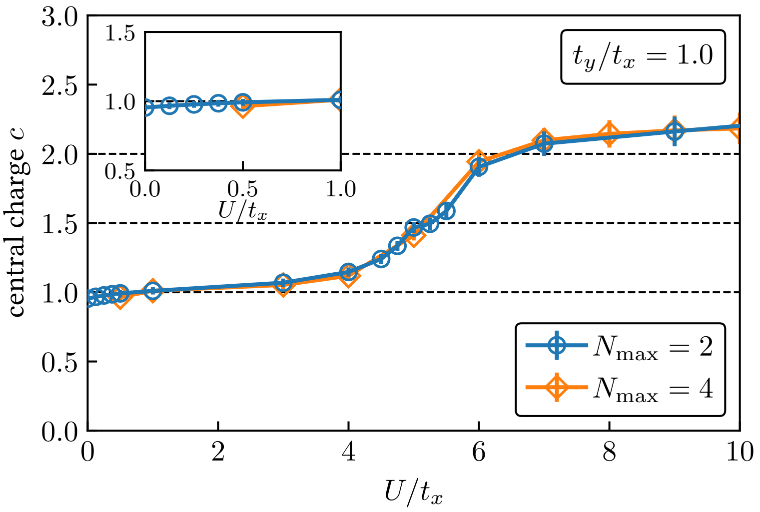

Fig. 3.22. Central charge c for an isotropic ($t_y/t_x = 1$) system with ($N_{\max} = 2$, blue circles) and without ($N_{\max} = 4$, orange diamonds) hard-core three-body repulsion. The results are essentially unchanged upon adding the additional constraint on the local particle number.

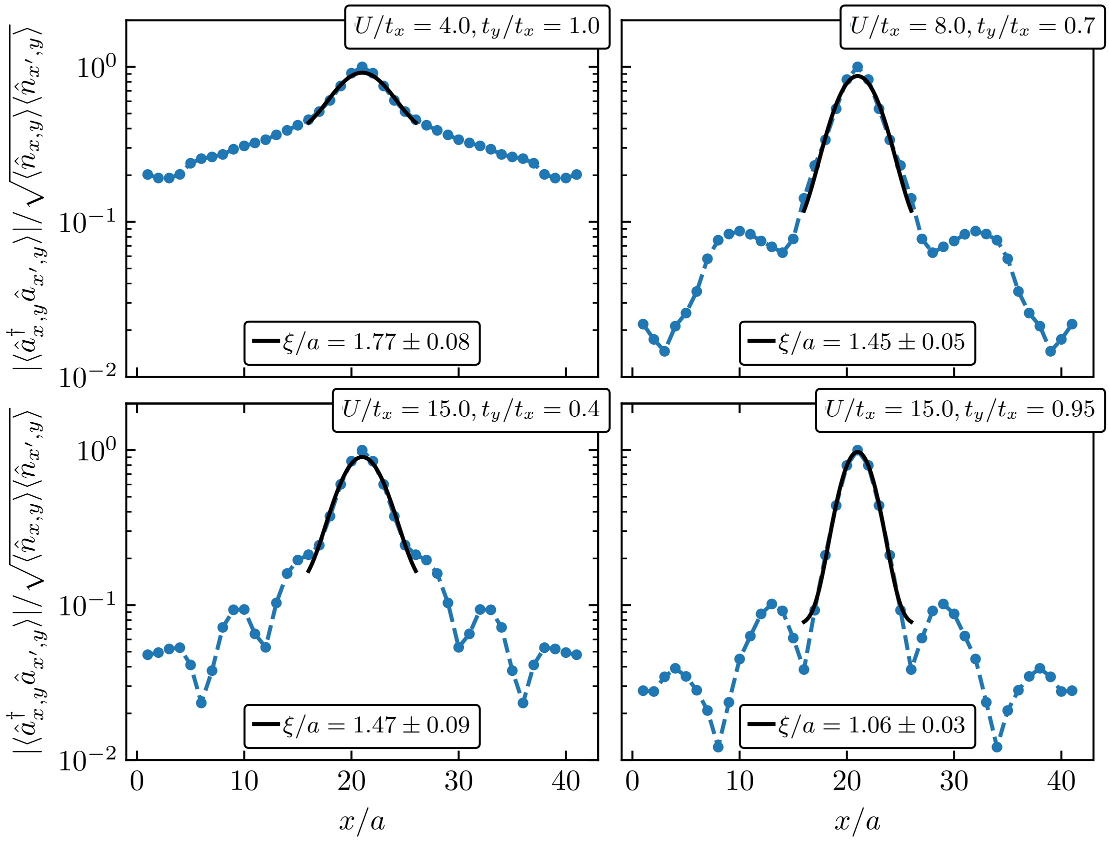

Fig. 3.23. Decay of the bulk correlations along the $y = 2$-leg of a $L_y = 4$-leg system for a fixed reference site $x' = 20$ and the data points shown in Fig. 3.20. The fit (black line) using $\exp[-{}^{(x-x')^2}/_{(4\xi^2)}] + \text{const.}$ works well close to the reference site in the middle of the system in all cases. A comprehensive overview of the extracted correlation length for the different phases is given in Fig. 3.24.

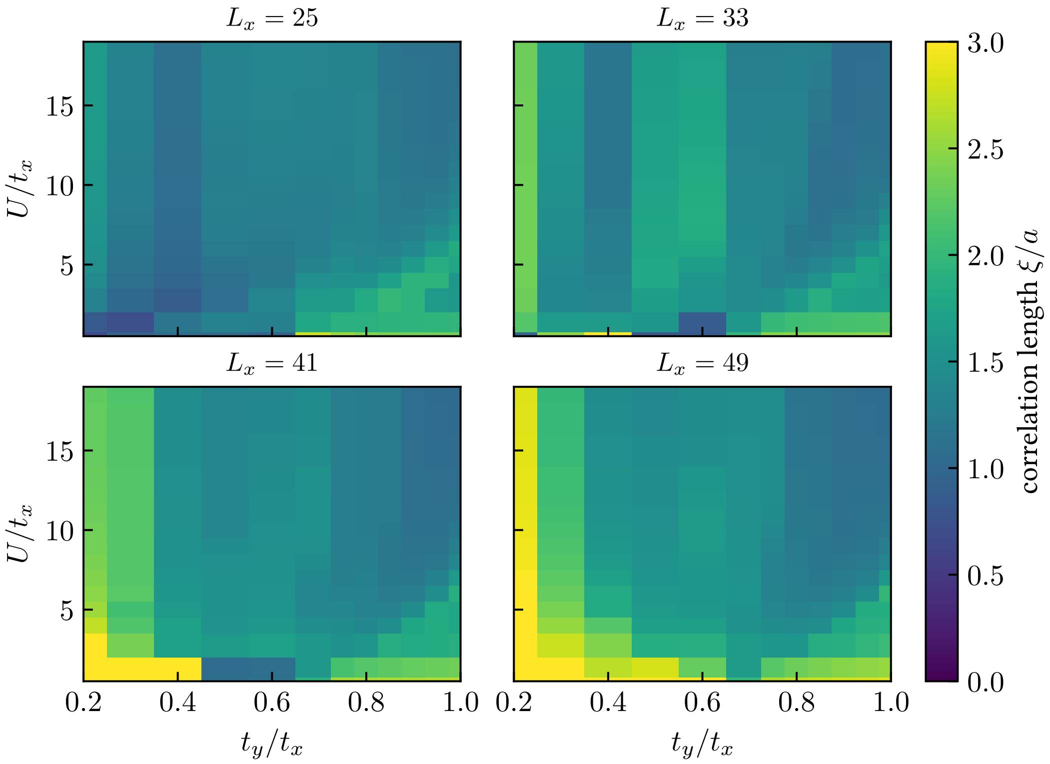

Fig. 3.24. Correlation length ξ of the normalized correlations $|\langle \hat{a}^{\dagger}_{x,y}\hat{a}_{x',y}\rangle|/\sqrt{\langle \hat{n}_{x,y}\rangle\langle \hat{n}_{x',y}\rangle}$ along the long direction of the chains for different chain lengths L_x. We find a characteristic change of behavior as the putative phase boundary between the strong pairing phase ($c_{\mathrm{SP}} = 1$) and the bilayer phase ($c_{\mathrm{B}} = 2$) is crossed. In particular, the correlation length in the bilayer phase is likely to be consistent with the correlation length $\xi_{\mathrm{LN}} = \ell_B \approx a$ of a Laughlin state at $\nu = 1/2$, see also Fig. 3.25.

We find that for all system sizes considered here the correlation length differs significantly between the regions where we found $c = 1$ and 2 respectively, see Fig. 3.24. In particular, we find the correlation length to change from $\xi_{\mathrm{SP}}/a \approx 2$ in the strong pairing phase ($c_{\mathrm{SP}} = 1$) to $\xi_{\mathrm{B}}/a \approx 1$ in the bilayer phase ($c_{\mathrm{B}} = 2$). Given the magnetic length $\ell_B = a/\sqrt{2\pi\alpha} \approx a$, it seems reasonable to (approximately) identify the correlation length ξ_{B} in the bilayer phase with the magnetic length. This is also in agreement with the interpretation of the bilayer phase as a two-fold copy of a Laughlin state at $\nu = 1/2$, which is also expected to exhibit $\xi_{\mathrm{LN}} \approx \ell_B$ [195].

We note in passing that for both phases discussed here the correlation length is significantly shorter than the system size L_x. Furthermore, upon systematically truncating the MPS at bond dimensions smaller than $\chi = 4000$ used above, we observe a light increase of the correlation length with increasing bond dimension, see Fig. 3.25. Additionally, we find a significant increase of ξ close to the critical interaction strength $U_c/t_x \approx 6$ possibly indicating a divergence of ξ in the thermodynamic limit. We interpret this as first indication for the phase transition being continuous. Before concluding our analysis of the correlation length, we would like to point out that for smaller t_y/t_x there is a change in the correlation length in the systems studied here. While the data obtained so far is not convincing enough on its own, this might be a first indication of the phase boundary of the bilayer phase as the inter-chain coupling is varied. Ultimately the system will undergo a phase transition to a state consisting of L_y decoupled Luttinger liquids, however the exact position of the phase transition - as well as whether there are additional phases at intermediate t_y/t_x - could not be resolved yet.

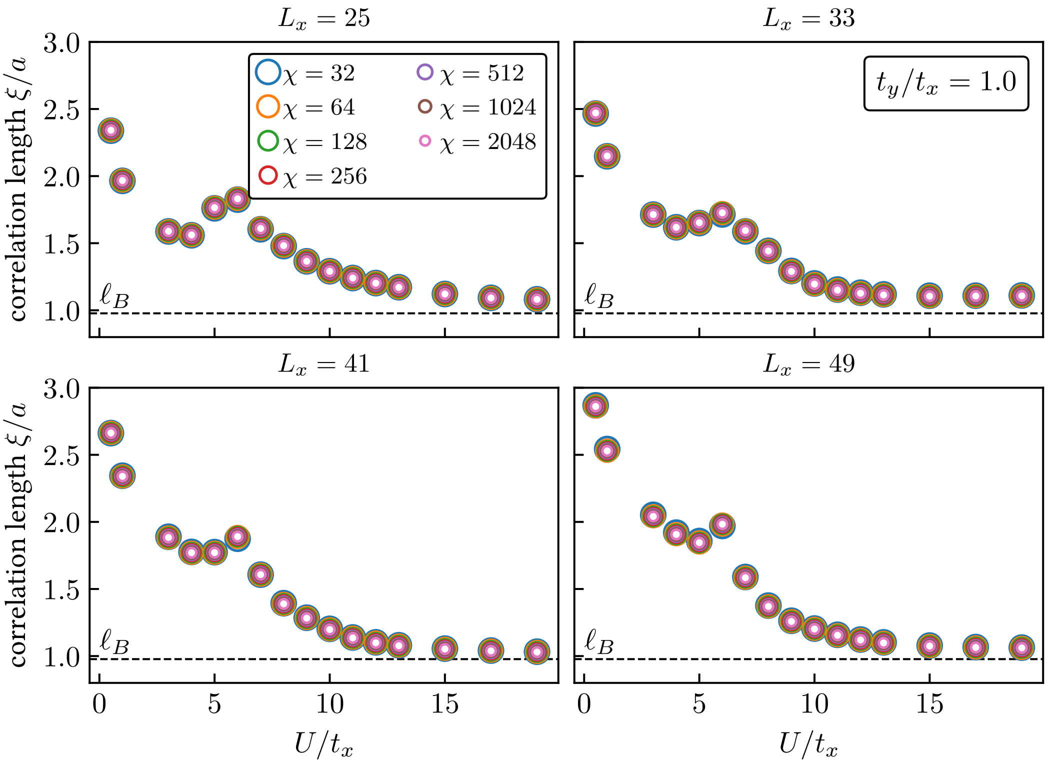

Fig. 3.25. Correlation length ξ in an isotropically coupled system as function of the interaction strength U/t_x. The symbols indicating different bond dimension truncations show first signs of a divergence as the bond dimension is increased close to the phase transition from between the strongly paired and the bilayer phase at $U_c/t_x \approx 6$. Close to this point also the correlation length itself is enhanced, which might be another indication of a true divergence in the thermodynamic limit.

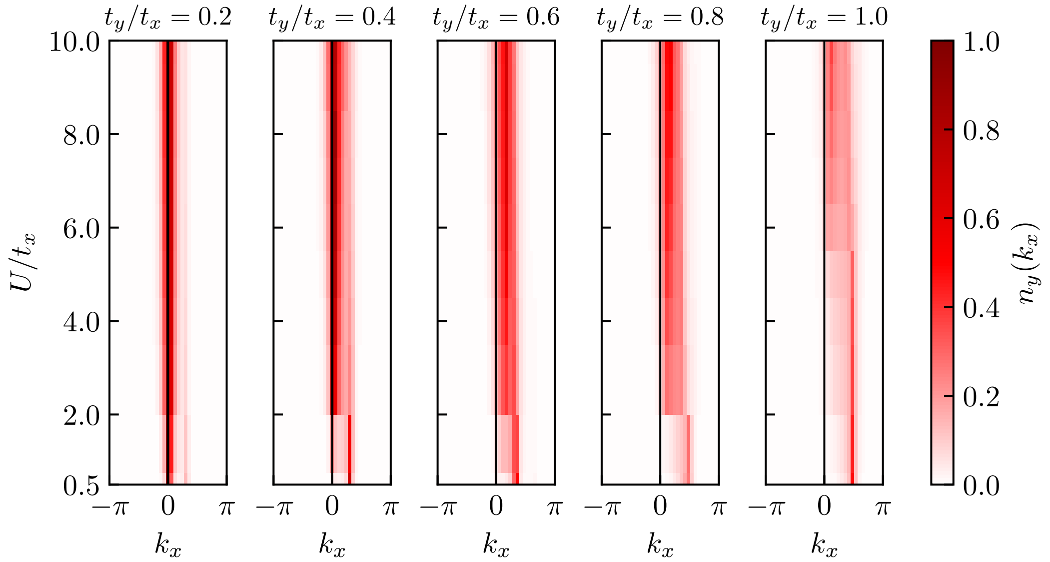

Fig. 3.26. Momentum distribution $n_{y=1}(k_x)$ on the edge ($y = 1$) as function of interaction strength U/t_x for selected values of the hopping anisotropy t_y/t_x for a system of $L_x = 33$ sites in the long direction. We observe different chiral edge modes at $k_x \neq 0$ for parameters consistent with the $c = 1$ and 2 phases discussed above.

Momentum distribution at the edge Having analyzed the bulk correlations we now turn to the edge of the system at hand. In particular, we calculate the momentum distribution at the edge given by

$$n_y(k_x) = \frac{1}{L_x}\sum_{x,x'} \mathrm{e}^{-ik_x(x-x')}\,\langle \hat{a}^\dagger_{x,y}\hat{a}_{x',y}\rangle\,, \quad \text{where} \quad k_x = \frac{2\pi m}{L_x}, \quad m = 0,\ldots,L_x-1. \tag{3.48}$$

Both the strongly paired state and the bilayer state exhibit chiral edge modes as was discussed in some detail for the continuum case and is also evident from the central charge. Therefore, we expect at least one peak in the momentum distribution $n_{y=1}(k_x)$ at the edge with finite k_x for both phases, potentially with different positions of the peak as we cross the phase transition.

Starting out in the limit of weakly coupled chains, $t_y/t_x = 0.2$, we find a peak of the momentum distribution at $k_x = 0$, see Figs. 3.26 and 3.27. In particular, this mode persists for all values of U/t_x in this limit. Upon increasing the inter-chain hopping, we observe a broadening and a shift of the peak towards some finite $k_x > 0$. We note, however, that while the broadening of the peak is visible for all U/t_x, a clear shift of the peak position is first observable in the limit of weak interactions. Furthermore, in the regime of sufficiently weak interaction for the $c = 1$ strongly paired phase to emerge, $U/t_x \leq 5$, we find a second shift of the peak position to even larger momenta upon increasing the inter-chain coupling t_y/t_x further. In particular, the position of this second shift coincides with the position of the phase transition as obtained from the central charge. While the momentum distribution in the strongly paired phase is surprisingly sharply peaked around $k_x^{\mathrm{SP}} \approx \frac{\pi}{2}$, in the bilayer phase the peak is less pronounced and at smaller momentum.

The position of the intermediate peak for sufficiently weak interactions at $t_y/t_x \leq 0.7$ does *not* coincide with the value for neither that one in the strongly paired phase nor the one in the bilayer phase. At this point, it remains open whether this regime is actually a distinct phase or a transition region arising due to finite size effects.

From these results it seems promising that the momentum distribution at the edge is not only

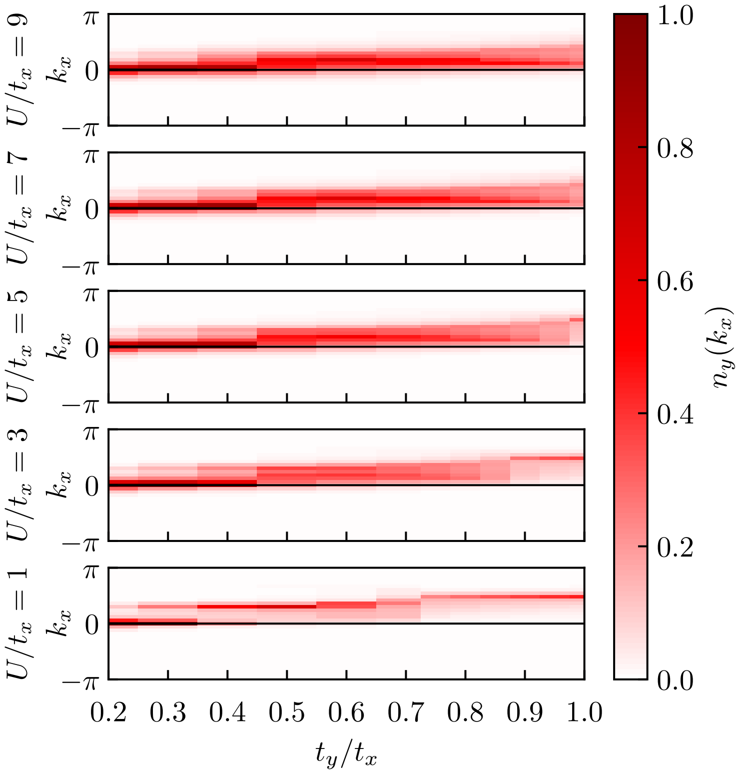

Fig. 3.27. Momentum distribution $n_{y=1}(k_x)$ on the edge ($y = 1$) as function of hopping anisotropy t_y/t_x for selected interaction strengths U/t_x for a system of $L_x = 33$ sites in the long direction. We see the emergence of different chiral edge modes at $k_x \neq 0$ as the system enters the topological phases with $c = 1$ and 2. Furthermore, we find a transient regime for small U where the momentum is peaked at yet another value.

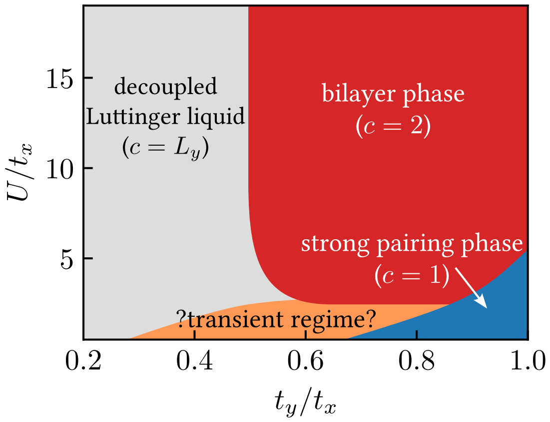

Fig. 3.28. Schematic phase diagram of the Hofstadter-Bose-Hubbard model on $L_y = 4$ coupled chains at $\alpha = 1/6$ and $\nu = 1$.

able to resolve the transition from topologically trivial Luttinger liquid states ($t_y/t_x \to 0$), but also to distinguish the emergent topological phases. To conclude our discussion of the $L_y = 4$-leg system, we found evidence for essentially four qualitatively different regions in the parameter regime studied here, summarized in our preliminary phase diagram in Fig. 3.28:

- A topologically trivial phase connected to the Luttinger liquid limit in the weakly coupled limit $t_y/t_x \to 0$. This state is characterized by the absence of a chiral edge mode and central charge $c \approx L_y$.
- The strong pairing phase with central charge $c = 1$ for weak interactions and strong inter-chain coupling. For this state we find a clearly visible chiral edge mode at $k_x^{\mathrm{SP}} \approx \frac{\pi}{2}$ and a correlation length of $\xi/a \approx 2$ for bulk correlations along x.
- The bilayer phase with $c = 2$ at stronger interactions and sufficiently strong inter-chain coupling, which is characterized by a fairly spread out momentum distribution along the edge which is weakly peaked at some finite $k_x^{\mathrm{B}} > 0$. This state also exhibits short-ranged bulk correlations with a correlation length of $\xi/a \approx \xi/\ell_B \approx 1$ which hints towards a close connection to the Laughlin state.
- A transient regime at weak interactions and intermediate inter-chain hopping, $t_y/t_x \in [0.4, 0.7]$, evident from the momentum distribution of the edge state. At this stage of our analysis it remains unclear whether this is yet another robust phase or a finite size effect in the transition region from the $c = L_y$ trivial phase to the strongly paired phase with $c = 1$. In this regime the central charge takes values consistent with $c \approx 3$, see Fig. 3.29, however with significant error bars, so that the exact nature of these features has yet to be investigated further.

Dependence on System Size

So far, we focused on systems of $L_y = 4$ chains. To see whether the behavior found there carries over to other system sizes, we now study arrays of $L_y = 3$ and 5 chains. As we observed earlier that truncating the local Hilbert space at $N_{\max} = 2$ does not affect the qualitative features of the ground states, we impose this truncation from now on for numerical convenience. Furthermore, we perform MPS simulations with bond dimensions up to $\chi = 4000$ which were sufficient to represent both the strongly paired and the bilayer state for $L_y = 4$.

Using again a data collapse for different system sizes ($L_x = 25, 37, 49, 61$ for $L_y = 3$ and $L_x = 19, 25, 31$ for $L_y = 5$), we can extract the central charge as function of t_y/t_x and U/t_x,

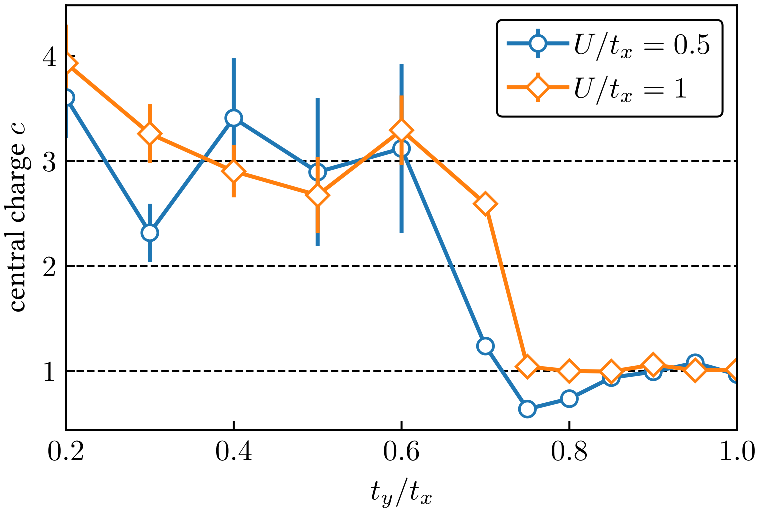

Fig. 3.29. Central charge as a function of t_y/t_x in the weakly interacting regime. We observe a transient regime at $t_y/t_x \in [0.4, 0.7]$ where the central charge takes values consistent with $c = 3$ before entering the strongly paired phase with $c_{\mathrm{SP}} = 1$.

see Fig. 3.30. We find a qualitatively different behavior for both system sizes $L_y = 3$ and 5, which do not only differ from $L_y = 4$ studied above, but also among each other. In particular, we find arrays of three chains to exhibit the strongly paired phase with $c = 1$ for most parameters considered here. The expected increase of the central charge at small t_y/t_x is first visible in strongly interacting systems.

In contrast, the 5-leg system exhibits not only a clear increase of the central charge below $t_y/t_x \lesssim 0.5$ close to the expected value $c(t_y = 0) = L_y = 5$, but also an almost constant central charge $c = 2$ close to the isotropic limit, $t_y/t_x \approx 1$, independent of U. Most interestingly, apart from minor variations of the numerical value, the central charge remains close to the value consistent with the bilayer phase even in the limit of weak interactions, where previously we found the strongly paired phase.

At this point, it is not entirely clear what causes this drastic change compared to the rich phase diagram on $L_y = 4$ chains. While we cannot completely exclude numerical uncertainties yet, we believe our results to be at least indicative of a qualitatively different physical behavior due to finite system sizes. We would like to remind the reader of the size-dependent behavior found during our analysis of a related problem at $\nu = 1/2$ presented above [2]. In particular, in that context systems of an even number of chains seemed to host current vortices at intermediate inter-chain coupling. While we did not examine the currents arising in the systems considered here, this will be an interesting starting point for future investigations.

We would like to point out the importance of our findings in small systems in view of current experimental capabilities. State-of-the-art cold atom experiments are capable of realizing fractional quantum Hall states of a few particles on small systems. In particular, a recent experiment by Léonard *et al.* [25] was able to realize a Laughlin state at $\nu = 1/2$ of two particles on 4×4 sites. Growing long systems of coupled chains from an array of such 4×4-patches might be a promising route towards the realization of systems comparable to those investigated above. While ultimately it is desirable to realize any given number of chains in cold atom quantum simulators, for now a starting point of four chains is not only in reach experimentally, but also hosts competing interacting topological phases. In any case, the question whether it might eventually be possible to realize other exotic states of matter, most prominently the Pfaffian state, in larger systems remains open at this stage and further clarification is needed.

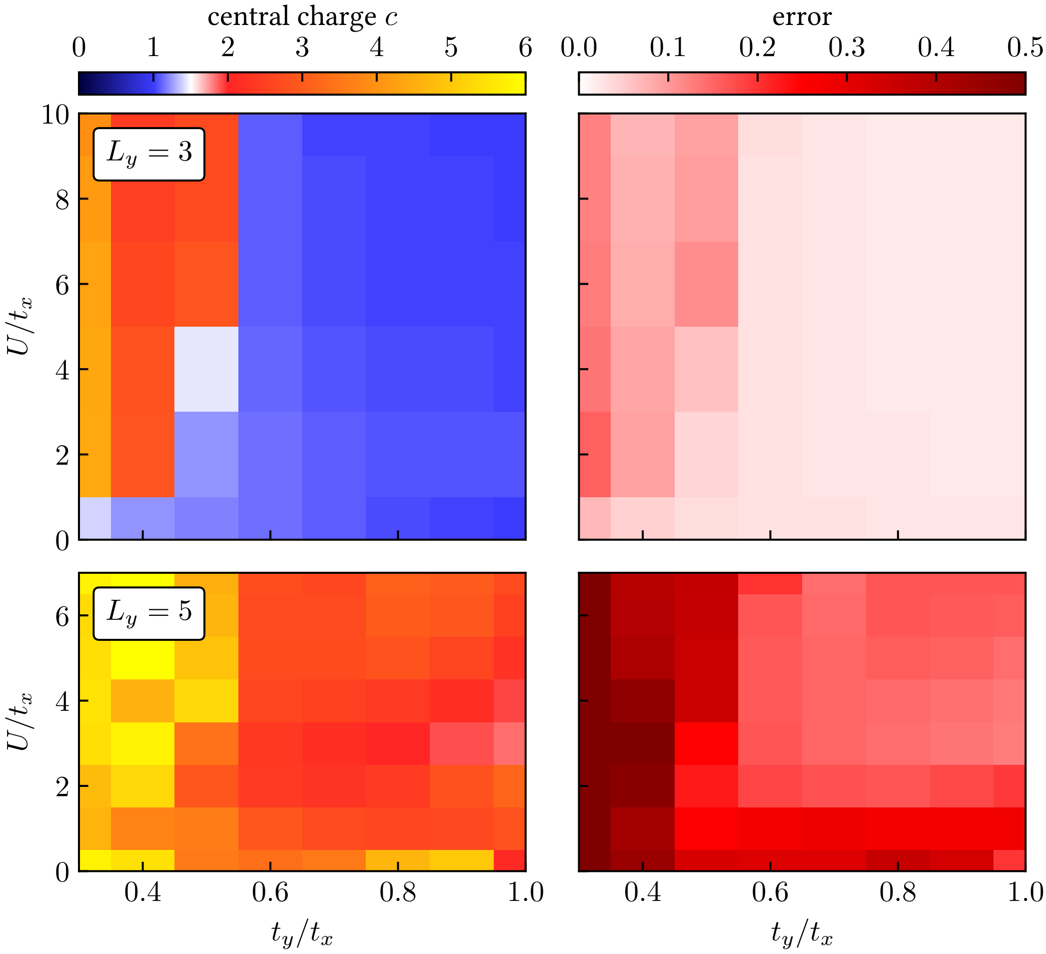

Fig. 3.30. Central charge c as extracted from the bipartite entanglement entropy using a scaling collapse. For $L_y = 3$ (upper row) we only find a state with $c \approx c_{\text{SP}} = 1$, but not the bilayer phase at $c_{\text{B}} = 2$. In contrast, for $L_y = 5$ (lower row) we find a large region with central charge $c = 2$ even for small interaction strengths, which is interpreted as the bilayer phase. For smaller t_y/t_x, we find an increase of the central charge close to the predicted value $c(t_y = 0) = L_y$ in the limit of decoupled chains.

Preliminary Conclusions and Outlook

We conclude our discussion of arrays of coupled chains at $\nu = 1$ by briefly summarizing our results. For systems of $L_y = 4$ chains we found clear evidence for at least three distinct phases. In the limit of weak inter-chain coupling we find a topologically trivial Luttinger liquid-like phase. Upon increasing the inter-chain hopping the system undergoes transitions towards topological phases with chiral edge modes. At weak interactions we find the strong pairing phase most prominently characterized by its central charge $c_{\mathrm{SP}} = 2$, whereas at stronger repulsion we find the bilayer phase with central charge $c_{\mathrm{B}} = 2$. Note that we did not find evidence for the emergence of the Pfaffian state, $c_{\mathrm{Pf}} = 3/2$, in our analysis.

All three states found in our numerics show clear signatures in the momentum distributions along the edge. The topological states also show a characteristic exponential decay of correlations along the chain in the bulk. At $t_y/t_x = 1$, the correlation length of this decay shows a first sign of a divergence as the interaction strength approaches the critical value U_c for the transition between strong pairing and bilayer phase, hence hinting towards the phase transition being continuous.

At sufficiently weak interactions we also observe a transient regime where a first analysis hints towards another state with central charge $c = 3$. The nature of this state could not be resolved completely yet and we cannot exclude finite size effects at this point.

A first analysis of arrays of $L_y = 3$ and 5 chains shows a qualitatively different behavior of the ground state. Most prominently, the bilayer phase seems to be absent for interactions up to $U/t_x = 10$ on three chains. In contrast, the strong pairing phase at small U/t_x does not emerge for any repulsive interaction in a system consisting of five chains. While we could not resolve this dependence on system size yet, we consider it an interesting feature to be in reach for an experimental study using existing cold atom platforms.

The analysis of the $\nu = 1$ case is still work-in-progress. Not surprisingly, various questions are still open and deserve a more detailed analysis. Most strikingly, the aparent absence of the Pfaffian state in systems with open boundary conditions studied here poses an interesting challenge. Apart from our study of a related system on a cylinder discussed above [1], also exact diagonalization studies of tori found the Pfaffian state at sufficiently weak Hubbard repulsion [165]. We believe that studying the particle entanglement spectrum of the states found here might give further insight into this discrepancy [50, 165]. Furthermore, a dependence on the topology of the underlying space (strip, cylinder, or torus) is worth exploring in light of the varying capabilities of different experimental platforms to realize these topologies.

Connecting the strips studied here to extended cylinders also allows for additional numerical insight: An adiabatic flux insertion protocol similar to that used above in the Laughlin case might reveal differences in the Hall response of the various phases found here. Furthermore, spatial bipartitions along the cylinder axis would allow for an extraction of the momentum resolved spatial entanglement spectrum of the edge and hence a classification of the edge states.

Finally, finding a mechanism to stabilize the Pfaffian state on strips is of prime importance to near-future cold atom experiments. Also, developing novel protocols to couple to and probe the emergent Majorana edge mode would be a highly worthwhile endeavor building on our recent progress [196].

3.4. Summary and Outlook

Our extensive numerical studies of the anisotropically coupled Hofstadter-Bose-Hubbard system found a variety of ground state phases. In particular, we found that tuning the hopping anisotropy can induce phase transitions from weakly coupled Luttinger liquid-like states to topologically ordered states close to the isotropic limit.

For the case of magnetic filling factor $\nu = 1/2$ we found a transition to the bosonic Laughlin state at strong but finite repulsive interactions. Numerically, the topological nature of the state at isotropic coupling is evident from a sharp drop of the central charge from $c = L_y$ in the trivial phase to $c = 1$ in the Laughlin phase. An explicit evaluation of the many-body Chern number provides additional evidence for the topological phase transition. Experimentally, the central charge on both sides of the phase transition can be estimated using Fock basis snapshots by approximating the entanglement entropy by the particle number entropy. Also more conservative observables like the suppression of two-particle on-site correlations or the finite momentum of its chiral edge modes allow for a detection of the topologically ordered Laughlin state. The system studied here, consisting of tunably coupled chains, provides a promising route towards the adiabatic preparation, detection and characterization of interacting topological states of matter using existing experimental techniques. Measuring the entanglement entropy using more than one basis has been proposed [197, 198] and might give further insight into similar systems.

Increasing the magnetic filling factor to $\nu = 1$, we find even more exotic topological phases. While we did not find evidence of the celebrated Pfaffian state, we found evidence for a strong pairing phase and a bilayer phase, depending on the strength of the on-site repulsion. The transition between these phases manifests in significant changes of the central charge, the correlation length, and the momentum distribution in the edge. The preliminary results of our study of this system raise many interesting questions which will be addressed in future studies: How does the strip geometry connect to cylinders and tori? Is it possible to stabilize the Pfaffian state on open strips? And what are realistic detection schemes for the various topological phases in cold atom experiments?

4 Towards Large Systems: Coupling Fractional Chern Insulators

4.1. Introduction and Outline

Having access to large fractional Chern insulators (FCIs) of many particles is desirable, especially from a conceptual point of view. This reduces finite size effects and allows for a reliable extrapolation to the thermodynamic limit. Apart from this technical point, studies involving quasiparticles and especially their braiding behavior require system sizes significantly larger than the magnetic length. At the same time, cold atom experiments studying FCIs are still limited to small particle numbers, with a recent first realization of a $\nu = 1/2$ Laughlin state of two atoms on 4×4 sites [25]. While in the thermodynamic limit topologically ordered states are separated from trivial ones by a gap closing, small systems exhibit a significant finite size gap. Therefore, small systems are advantageous for the adiabatic preparation of topologically ordered states from trivial states.

However, experiments ultimately aim for true many-body states in large systems. Among the main goals of cold atom experiments on FCIs is the direct observation of (non-Abelian) anyon braiding, which necessarily requires enough particles to realize quasiparticle or quasihole states as well as large enough systems to move the particles around each other in real space. Other objectives also require extended systems, for example the direct measurement of the central charge as those proposed in the previous chapter [2, 5]. Therefore, it is of prime importance to develop protocols taking the existing experiments to their true potential by growing large systems.

In this chapter we propose to couple existing Laughlin states of two bosons on 4×4 sites to achieve this goal. We analyze different promising protocols, varying local hopping amplitudes and potential barriers, to first connect two patches to grow a Laughlin state of four bosons in Sec. 4.2. Afterwards, in Sec. 4.3 we extend our protocol to grow extended chains of up to five patches hosting ten particles in total, thus ending up with a total system size of 20×4 sites. We compare different protocols for tuning the hopping amplitudes and provide first evidence for the scalability of a particularly simple approach. Finally, in Sec. 4.4 four patches are connected in a square geometry of 9×9 sites hosting eight bosons, allowing for the direct preparation of a large Laughlin state in a geometry which is promising for future braiding experiments. This chapter is based on preliminary results which are yet to be published [6].

We study the Hofstadter-Bose-Hubbard model in the Landau gauge on a square lattice of dimensions $L_x \times L_y$:

$$\hat{\mathcal{H}}_{L_x \times L_y} = -t \sum_{x,y} \left(\hat{a}^\dagger_{x+1,y} \hat{a}_{x,y} + \mathrm{e}^{2\pi i \alpha x} \hat{a}^\dagger_{x,y+1} \hat{a}_{x,y} + \mathrm{H.c.} \right) + \frac{U}{2} \sum_{x,y} \hat{n}_{x,y} \left(\hat{n}_{x,y} - 1 \right) . \quad (4.1)$$

Here, $\hat{a}^{(\dagger)}_{x,y}$ annihilates (creates) a boson at site (x, y) and $\hat{n}_{x,y} = \hat{a}^\dagger_{x,y} \hat{a}_{x,y}$ is the particle number operator. We consider strong but finite Hubbard repulsion realistic for cold atom experiments,

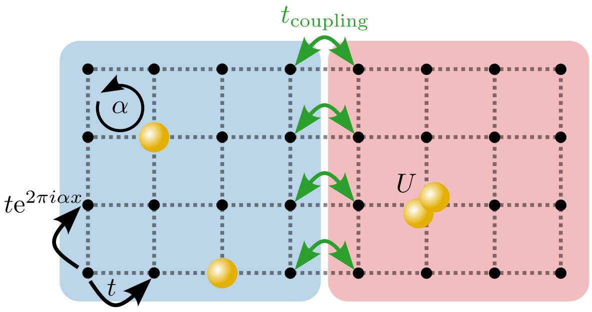

Fig. 4.1. *Hopping protocol*: Coupling two 4×4 Hofstadter-Bose-Hubbard patches with $N = 2$ particles in each half of the system, indicated by the blue and red shading respectively. The parameter t_{coupling} is dynamically adjusted to connect the initially decoupled patches into one extended system.

$U/t = 8$, and infinitely strong Hubbard repulsion, $U/t = \infty$. While we will comment on the differences between the two cases below, we already mention that the exact value of the (strong) Hubbard repulsion does not affect the results significantly.

In our simulations, we make use of exact diagonalization for small systems and tensor network methods for larger systems. In particular, we use the SyTen toolkit [138] to perform density matrix renormalization group (DMRG) [135–137] simulations for static properties and its implementation of the time-dependent variational principle (TDVP) [199, 200] for dynamical calculations.

4.2. Coupling Two 4×4-Patches

While the details of the experimental protocol might differ between realizations, we envision two closely related approaches to grow extended FCIs from existing patches. On the one hand, we will consider completely decoupled patches which are then connected by turning on a local hopping t_{coupling} between the two patches. On the other hand, we will start from a system of 9×4 sites with a strong potential barrier V_{barrier} on the center column, splitting the system into two 4×4-patches. Turning off the potential barrier we can grow an extended FCI state in the enlarged system.

4.2.1. Hopping Protocol: Turning on Local Hoppings

We start our study by discussing the "*hopping protocol*" for which we begin with two decoupled 4×4-patches which are then coupled by a local hopping at the edge connecting the patches, see Fig. 4.1. To this end, we consider the modified Hamiltonian

$$\hat{\mathcal{H}}_{2p}(t_{\text{coupling}}) = \hat{\mathcal{H}}^{(1)}_{4\times 4} + \hat{\mathcal{H}}^{(2)}_{4\times 4} - t_{\text{coupling}} \sum_{y=1}^{4} \left(\hat{a}^{\dagger}_{5,y} \hat{a}_{4,y} + \text{H.c.} \right), \tag{4.2}$$

where the first two terms describe the two decoupled patches, while the last term describes the coupling between the two patches.

Static Properties

To gain some intuition for the time and energy scales involved in an adiabatic coupling of the two patches, we determine the many-body gap Δ between the ground state and the first

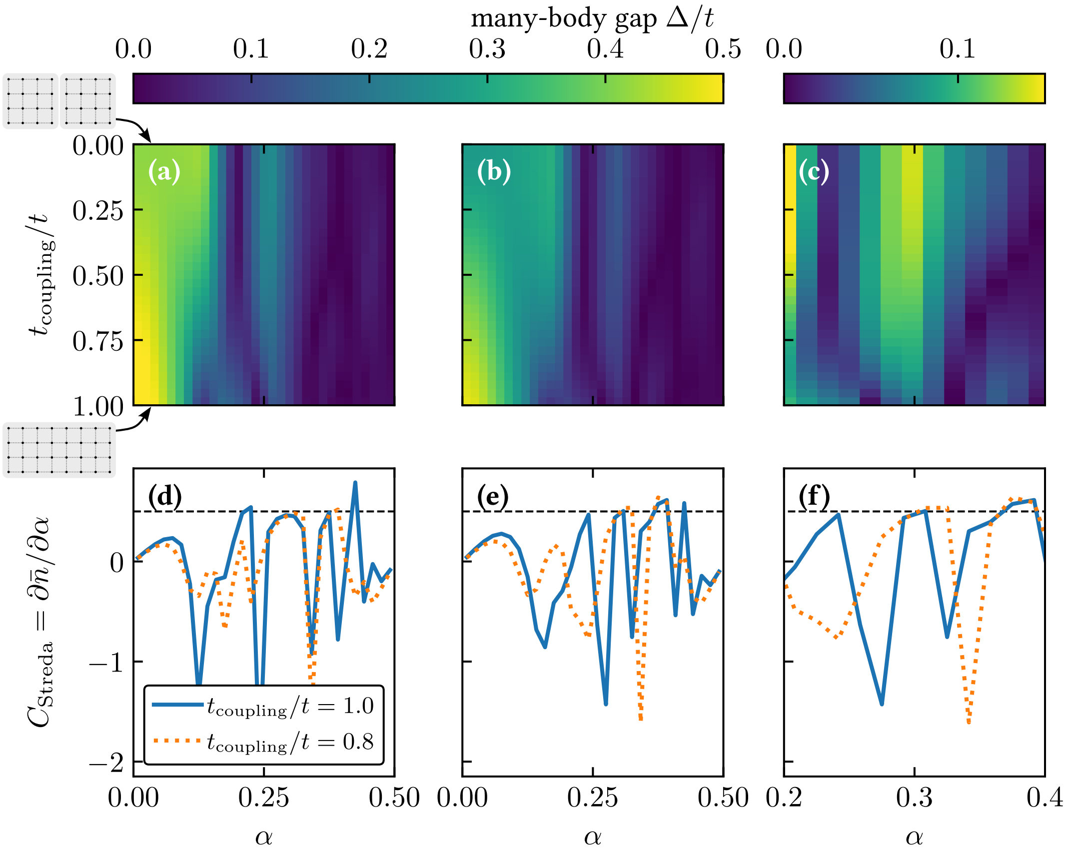

Fig. 4.2. *Hopping protocol*: **(a-c)** Many-body gap Δ obtained from the exact diagonalization of a system of two coupled 4×4-patches for **(a)** $U/t = \infty$ and **(b, c)** $U/t = 8$. We tune both the flux per plaquette α and the coupling strength t_{coupling} between the two patches. Panel **(c)** is a zoom-in of **(b)** focusing on the regime relevant to the $\nu = 1/2$ Laughlin state, characterized by the opening of the many-body gap in the decoupled patches at $\alpha \approx 0.25$. Note that in this regime the gap remains open for all t_{coupling} and therefore provides a promising path for adiabatic state preparation. **(d-f)** Many-body Chern number C_{Streda} obtained using Středa's formula. In the gapped region discussed before we find $C_{\text{Streda}} = 1/2$ as expected for the $\nu = 1/2$ Laughlin state.

excited state. To this end, we perform an exact diagonalization of the full Hamiltonian for varying coupling strength t_{coupling} and flux α. The results given in Fig. 4.2 indicate the possibility to grow a larger Laughlin state from two decoupled Laughlin states by slowly increasing the inter-patch coupling t_{coupling} at fixed flux $\alpha \approx 0.3$. In particular, we note that this result holds true for both hard-core bosons ($U/t = \infty$) and for finite Hubbard repulsion ($U/t = 8$).

To further confirm the topological nature of the ground state, we extract the many-body Chern number using Středa's formula [201, 202],

$$C_{\text{Streda}} = 2\pi \frac{\partial \bar{n}}{\partial \varphi} = \frac{\partial \bar{n}}{\partial \alpha}, \tag{4.3}$$

where $\bar{n}$ is the bulk density of the system. We consider the central 4×2 sites to form the bulk of the sample and find the Chern number in the gapped phase around $\alpha \approx 0.3$ to be $C = 1/2$, see Fig. 4.2. This agrees with the expectation for the continuum Laughlin state at $\nu = 1/2$, so that we conclude that the homogeneously coupled system at $t_{\text{coupling}} = t$ indeed hosts a lattice analog of this topologically ordered target-state.

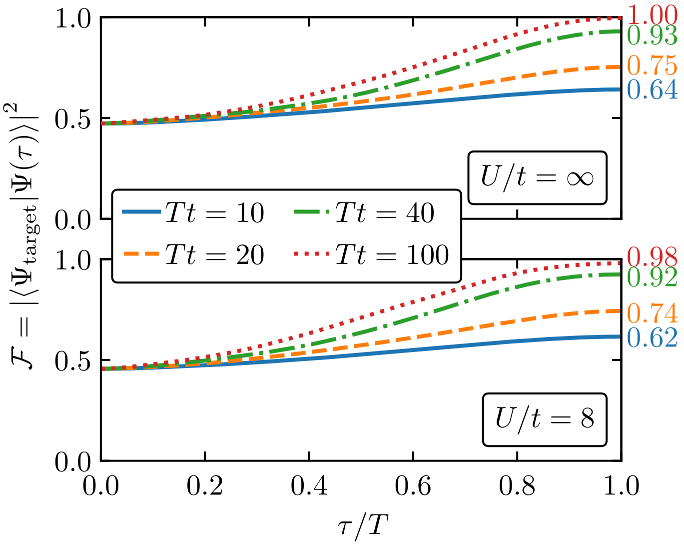

Fig. 4.3. *Hopping protocol*: Target-state fidelity of the time-evolved state $|\Psi(\tau)\rangle$ for various preparation times T upon linearly coupling two patches.

Time-Evolution

Motivated by these findings, we consider a simple preparation protocol, where the hopping amplitude between the two patches is increased linearly over time τ during a finite preparation time T,

$$t_{\text{coupling}}(\tau) = \frac{\tau}{T}\,t, \tag{4.4}$$

while the magnetic flux per plaquette is kept fixed, $\alpha = 0.3$. Integrating the time-dependent Schrödinger equation we calculate the time-evolution of the initial product state

$$|\Psi_{\text{initial}}\rangle = |\Psi(\tau = 0)\rangle = |\Psi_0^{(1)}\rangle \otimes |\Psi_0^{(2)}\rangle\,, \tag{4.5}$$

where $|\Psi_0^{(k)}\rangle$ is the ground state in the initially decoupled 4×4-patches labeled by k. Our target-state $|\Psi_{\text{target}}\rangle$ is the ground state of the large 8×4-system. We determine the target-state fidelity of the time-evolved state $|\Psi(\tau)\rangle$, which is defined as

$$\mathcal{F}(\tau) = |\,\langle\Psi_{\text{target}}|\Psi(\tau)\rangle\,|^2. \tag{4.6}$$

Already without any further optimization of the preparation path, we find a final fidelity $\mathcal{F}_{\text{final}} = \mathcal{F}(T) > 0.9$ for preparation times $Tt \geq 40$, see Fig. 4.3. In our simulations, we considered a path along which the minimal many-body gap is $\Delta_{\text{min}} \approx 0.09t$. Note, however, that for most of the ramp the many-body gap is significantly larger, so that an improved, potentially non-linear, ramp of the coupling is expected to result in shorter preparation times with comparable target-state overlap.

Entanglement Growth

While the initial state is a product state for which the entanglement entropy between the patches vanishes, $S(\tau = 0) = 0$, the target-state is clearly an entangled state, $S(\tau = T) > 0$. Next, we will probe this behavior and provide additional insight into the build-up of entanglement.

Matrix product states (MPS) allow for a particularly simple extraction of the bipartite entanglement entropy between spatial subsystems. Therefore, we perform time-evolution simulations

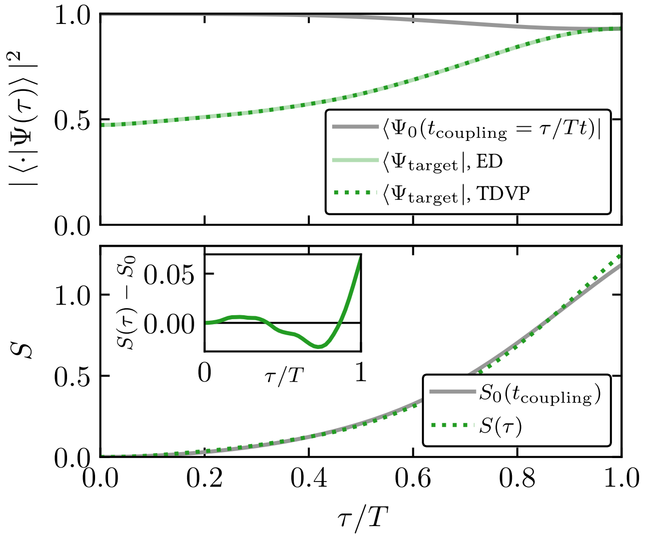

Fig. 4.4. *Hopping protocol*: In the upper panel, the target-state fidelity of the state obtained performing the time-evolution via TDVP for an MPS (green dotted line) and exact diagonalization (shaded green line) are in excellent agreement. We find a large overlap of the time-evolved state with the instantaneous ground state at all times (gray line). Furthermore, we observe the expected entanglement growth (lower panel) as the two patches are coupled both for the time-evolved state (green) and the instantaneous ground state (gray). Inset: The excess entropy in the time-evolved state at $\tau/T=1$ is attributed to a small population of excited states. Data is given for $U/t=\infty$, $Tt=40$ and $N_{\text{Trotter}}=40$.

using the time-dependent variational principle (TDVP) method for MPS and track the entanglement entropy $S(\tau)$ between the two 4×4 subsystems. To this end, we perform a Trotterization of the time-evolution operator,

$$\hat{\mathcal{U}}=\mathcal{T}\int_0^T \mathrm{d}\tau\ \mathrm{e}^{-i\tau\hat{\mathcal{H}}_{2p}(\tau)}\approx\prod_{n=0}^{N_{\text{Trotter}}}\mathrm{e}^{-i\delta\tau\hat{\mathcal{H}}_{2p}(\tau_n)}, \tag{4.7}$$

where $\delta\tau=T/N_{\text{Trotter}}$, $\tau_n=n\delta\tau$, and $\hat{\mathcal{H}}_{2p}(\tau)=\hat{\mathcal{H}}_{2p}(t_{\text{coupling}}(\tau))$. In particular, we consider a preparation time of $Tt=40$ and achieve convergence in the Trotter step size for $N_{\text{Trotter}}=40$.

In our time-evolution simulation, we find the expected growth of entanglement as the patches are connected, see Fig. 4.4. In particular, the final entanglement entropy is slightly higher than in the instantaneous ground state of the 8×4 system, $S_0(t_{\text{coupling}})$, see also the inset in Fig. 4.4. We attribute this to excitations to higher states as we connect the patches.

Conclusions

Based on the static many-body gap and our time-evolution simulations, we conclude that it is in principle possible to prepare an extended Laughlin state in cold atom experiments by connecting two originally independent patches of 2 particles on 4×4 sites. We find that target-state fidelities of $\mathcal{F}_{\text{final}}>0.9$ can be achieved for preparation times on the order $Tt\gtrsim 40$, even without further optimization of the preparation path. We consider this a (numerical) proof-of-principle for the adiabatic preparation of large Laughlin states from 4×4-patches.

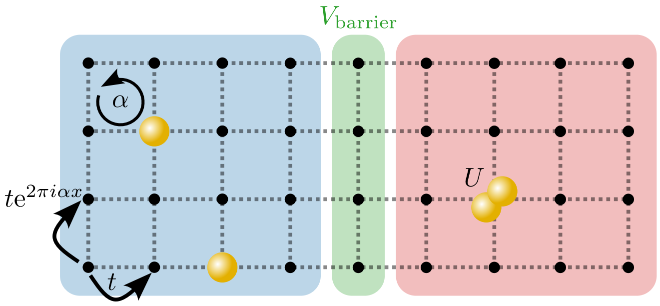

Fig. 4.5. *Barrier protocol*: Coupling two 4×4 Hofstadter-Bose-Hubbard patches with $N = 2$ particles in each half of the system, indicated by the blue and red shading respectively. The patches are separated by a local potential barrier (green region), which is dynamically lowered to connect the patches into one extended 9×4 system.

4.2.2. Barrier Protocol: Turning off a Potential Barrier

Reassured by this proof-of-principle, we next turn to an alternative preparation protocol. Here, we propose to start from a system of size 9×4, initially split into two halves by a tunable potential barrier. The Hamiltonian for such a system, using what we call the "*barrier protocol*", reads

$$\hat{\mathcal{H}}_{2p}(V_{\text{barrier}}) = \hat{\mathcal{H}}_{9\times4} + V_{\text{barrier}} \sum_{y=1}^{4} \hat{n}_{5,y}, \tag{4.8}$$

where V_{barrier}/t is the height of the potential barrier, see Fig. 4.5.

Static Properties

Again, we diagonalize the Hamiltonian exactly for hard-core bosons ($U/t = \infty$) and finite Hubbard repulsion ($U/t = 8$) and find an adiabatic path from the decoupled regime to the fully coupled system without any barrier, see Fig. 4.6. In particular, we note that already relatively weak local potentials, $V_{\text{barrier}}/t \approx 1$, provide a sufficient barrier to split the system into two parts. Note however, that while the excitation gap is almost constant above $V_{\text{barrier}}/t = 0.5$, the microscopic structure might still differ from the completely decoupled limit. We will encounter this behavior below in the analysis of our time-evolution simulations.

Calculating the Chern number using Středa's formula as above, we again find evidence for a topologically non-trivial state in the gapped regime. Furthermore, the extracted Chern number $C_{\text{Streda}} \approx 1/2$ agrees with the expectation for the $1/2$-Laughlin state. We attribute the deviations from the exactly quantized value to the small size (3×2) of the central bulk region used.

Time-Evolution: Linear Ramp

Performing a similar time-evolution protocol as above, we again calculate the overlap of the time-evolved product state with the target-state for a time dependent potential barrier of the form

$$V_{\text{barrier}}(\tau) = V_0 \left(1 - \frac{\tau}{T}\right), \tag{4.9}$$

where we fix the initial potential barrier $V_0 = 5t$ in our time-evolution calculations. Our simulations are done for constant flux per plaquette $\alpha = 0.3$. We find that, as for the hopping protocol, the target-state fidelity is already substantial ($\mathcal{F}_{\text{final}} \approx 0.6$) for relatively short ramp times ($Tt \approx 20$), see Fig. 4.7. However, the simple linear ramp of the barrier does in general not give as good target-state overlap as a direct coupling of the two patches discussed before.

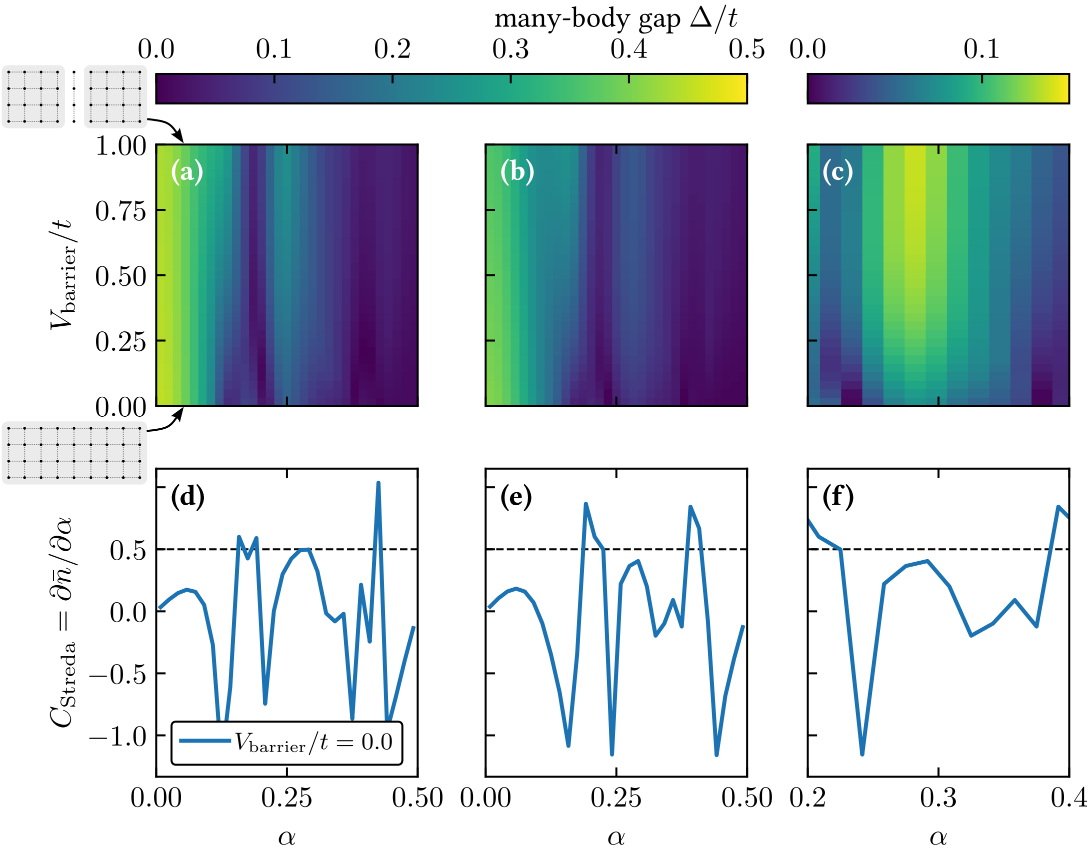

Fig. 4.6. *Barrier protocol*: **(a-c)** Many-body gap Δ obtained from the exact diagonalization of a system of two coupled 4×4-patches for **(a)** $U/t = \infty$ and **(b, c)** $U/t = 8$. We tune both the flux per plaquette α and the height of the potential barrier V_{barrier} between the two patches. Panel **(c)** is a zoom-in of **(b)** focusing on the regime relevant to the $\nu = {}^1\!/_2$ Laughlin state, characterized by the opening of the many-body gap in the decoupled patches at $\alpha \approx 0.25$. Note that in this regime the gap remains open for all V_{barrier} and therefore provides a promising path for adiabatic state preparation. **(d-f)** Many-body Chern number C_{Streda} obtained using Středa's formula. In the gapped region discussed before we find $C_{\text{Streda}} \approx {}^1\!/_2$ as expected for the $\nu = {}^1\!/_2$ Laughlin state.

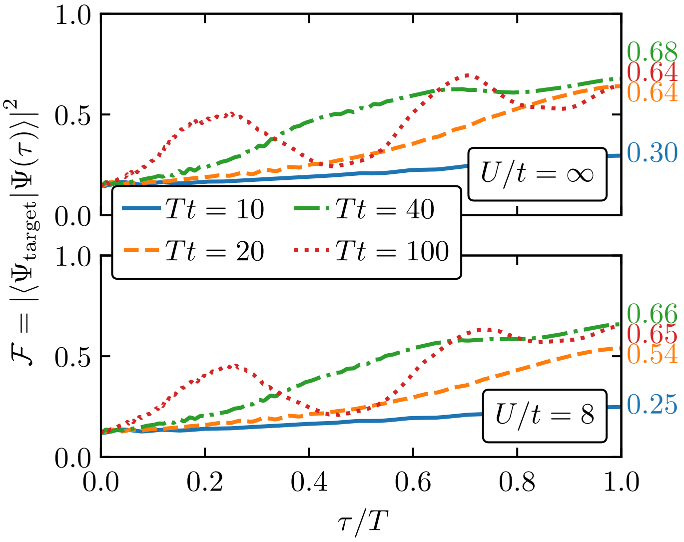

Fig. 4.7. *Barrier protocol*: Target-state fidelity of the time-evolved state $|\Psi(\tau)\rangle$ for varying preparation times T upon linearly turning off the potential barrier, starting from $V_{\text{barrier}}(\tau = 0) = V_0 = 5t$. The target-state overlaps are significantly smaller than for the hopping protocol discussed above.

Time-Evolution: Two-step Ramp

Next, we modify the protocol by splitting up the turn-off of the potential barrier into two parts. Specifically, we reduce the barrier from $V_{\text{barrier}}(0) = V_0 = 5t$ to $V_{\text{barrier}}(T_1) = t$ over a time $T_1 < T$. Then, we slowly turn off the barrier completely during a second time $T - T_1$. We can write this piecewise linear function as

$$V_{\text{barrier}}(\tau) = \begin{cases} \frac{T_1-\tau}{T_1}\, V_0 + \frac{\tau}{T_1}\, t & \text{for } \tau \leq T_1, \\ \frac{T-\tau}{T-T_1}\, t & \text{for } \tau \geq T_1. \end{cases} \tag{4.10}$$

The two parts of the modified ramp can be intuitively understood as follows: The first part, $\tau \leq T_1$, takes the system from the essentially decoupled regime to a point closer to the coupled case. The non-trivial evolution from an (approximate) product state of decoupled patches to the correlated state in the fully coupled limit is performed in the second part, $\tau \geq T_1$. Instead of performing the entire time-evolution at the same ramp speed, the region of smaller many-body gaps (i.e. small V_{barrier}/t) is traversed slower compared to the simple linear ramp.

Unsurprisingly, the modified ramp performs better at reaching high fidelity with the target-state at fixed total ramp time, see Fig. 4.8. We also monitor the entanglement entropy for both barrier protocols, where we clearly see the quenched nature of the time evolution as a jump of the entanglement entropy from $S(\tau = 0) = 0$ (initial product state) to $(\tau > 0) > 0$, see Fig. 4.9. This is again a consequence of the initial state not being an exact eigenstate of the time-dependent Hamiltonian already at $\tau = 0$.

Here, we only perform some exemplifying time-evolution simulations to show the general advantage of piecewise linear ramps over a simple linear ramp. We believe further improvement to be possible by using more complicated ramp profiles which can be optimized using, for example, machine learning techniques.

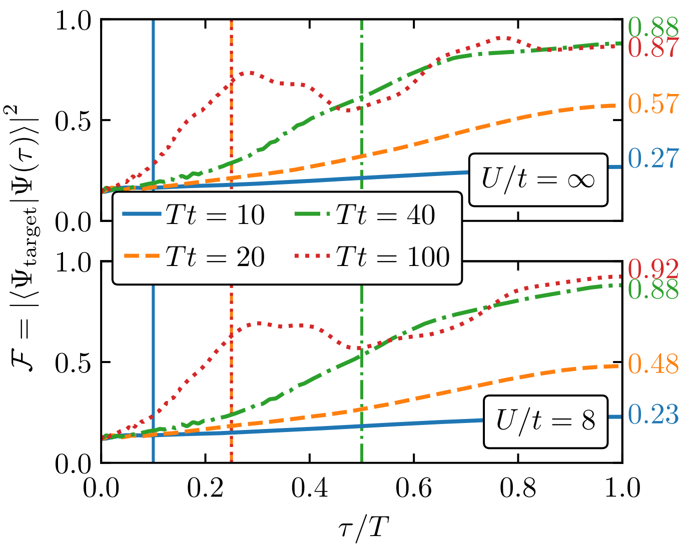

Fig. 4.8. *Two-step barrier protocol*: Target-state fidelity of the time-evolved state for varying preparation times T upon turning off the potential barrier in two linear steps, starting from $V_{\text{barrier}}(\tau = 0) = V_0 = 5t$. We vary the intermediate time T_1 at which the piecewise linear ramp passes through $V_{\text{barrier}}(\tau) = t$ (indicated by vertical lines).

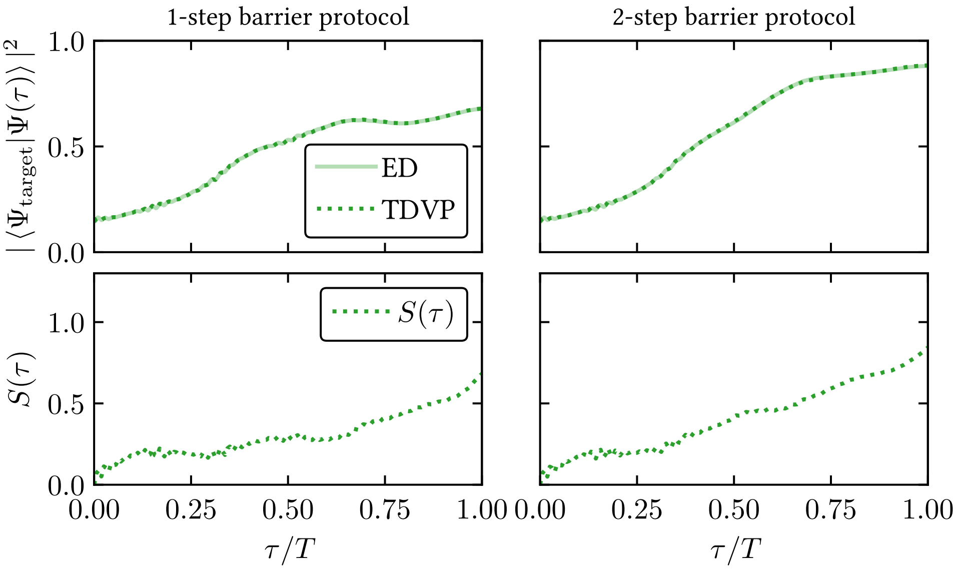

Fig. 4.9. *Barrier protocol* (left column) and *two-step barrier protocol* (right column): In the upper row , the target-state fidelity of the state obtained performing the time-evolution via TDVP for an MPS (green dotted lines) and exact diagonalization (shaded green lines) are in excellent agreement. Furthermore, we observe the expected entanglement growth (lower row) as the two patches are coupled both for the time-evolved state (green) and the instantaneous ground state (gray). Note the jump from $S(\tau = 0) = 0$ to $S(\tau > 0) > 0$ due to the quench-like time evolution. Data is given for $U/t = \infty$, $Tt = 40$ and $N_{\text{Trotter}} = 1600$.

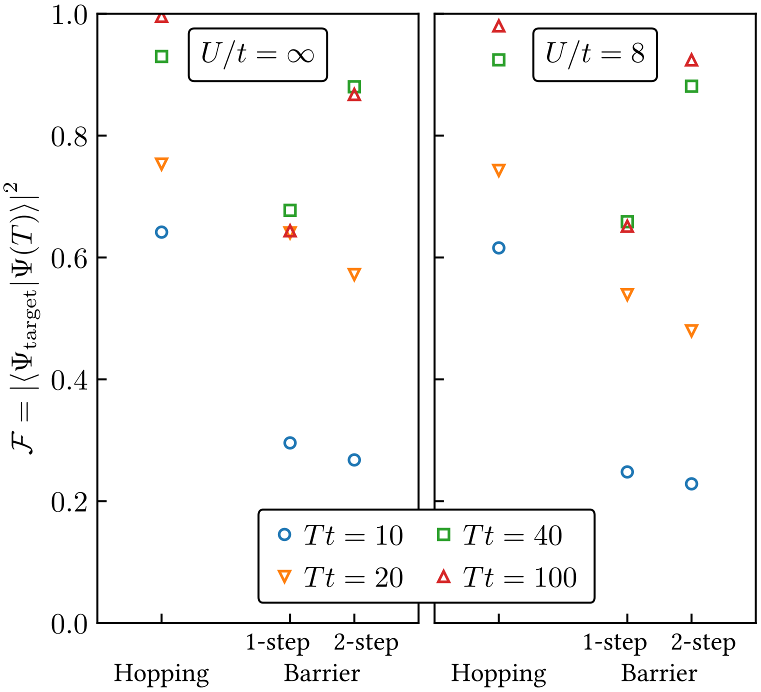

Fig. 4.10. Target-state fidelity of the final time-evolved state $|\Psi(\tau = T)\rangle$ for the preparation protocols discussed above. We find good performance of all protocols for sufficiently slow ramps with the hopping protocol out-performing both the one- and two-step barrier protocols.

Conclusions

We conclude from our simulations that the barrier protocol provides an alternative route for growing extended Laughlin states in optical lattices. The results of our study are summarized in Fig. 4.10. While linearly turning off the barrier results in low target-state fidelities, optimizing the ramp allows for fidelities comparable to the hopping protocol.

4.3. Super-Chains: Coupling More Patches

Our earlier numerical studies [2] found extended chains to provide interesting new insights involving the edge theory of FCI states. Here, we explore the possibility to couple more than two patches in an elongated system which we will call a super-chain. The Hamiltonian describing such a super-chain reads

$$\hat{\mathcal{H}}_{\text{chain}}\left(\left\{t^{(k)}_{\text{coupling}}\right\}\right) = \sum_{k=1}^{N_{\text{patches}}} \hat{\mathcal{H}}^{(k)}_{4\times 4} - \sum_{k=1}^{N_{\text{patches}}-1} t^{(k)}_{\text{coupling}} \sum_{y=1}^{4} \left(\hat{a}^{\dagger}_{4k+1,y}\hat{a}_{4k,y} + \text{H.c.}\right). \quad (4.11)$$

The couplings between the different patches may be adjusted independently. As systems of $N_{\text{patches}} = 3, 4, 5$ patches become too large to be treated with exact diagonalization, we turn to simulations based on matrix product states (MPS) to first find the low-lying states of the system and afterwards perform time-evolution.

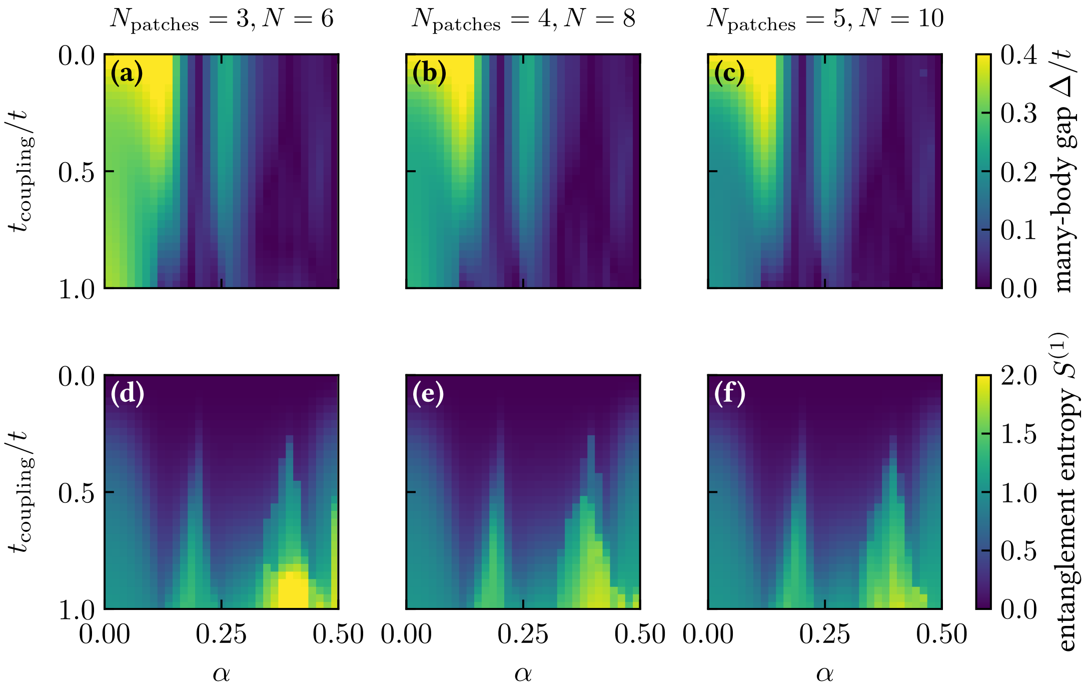

Fig. 4.11. *Super-chains*: Coupling $N_{\mathrm{patches}} = 3, 4$ or 5 patches into a super-chain results in essentially unchanged behavior for the many-body gap Δ/t **(a-c)** and the entanglement entropy between the first patch and the remaining system **(d-f)**. While the gaps are quantitatively smaller than for the case of $N_{\mathrm{patches}} = 2$ (see Fig. 4.2), the relatively large gap related to the Laughlin state on a single patch remains clearly visible in all cases.

Static Properties

We start with a system of homogeneous couplings, $t^{(1)}_{\mathrm{coupling}} = \ldots = t^{(N_{\mathrm{patches}}-1)}_{\mathrm{coupling}} = t_{\mathrm{coupling}}$, and restrict our analysis to the case $U/t = \infty$. Given our earlier findings we do not expect qualitative changes in the case of finite Hubbard repulsion.

We calculate the many-body gap Δ using DMRG searches for the ground state and the first excited state. Furthermore, we extract the entanglement entropy $S^{(1)}$ between the first patch and the rest of the system from the ground state MPS.

Irrespective of the number of patches, we find a gapped state connected to the Laughlin state at $\alpha \approx 0.3$ on a single patch, see Fig. 4.11. The gap around $\alpha \approx 0.3$ persists for all values of the coupling between the patches, so that we believe an adiabatic preparation of elongated systems from smaller patches to be realistic. At the same time, the entanglement between the first patch and the remaining system remains relatively small compared to the gapless states at larger and smaller flux per plaquette α. We interpret this as additional indication for the Laughlin state extending to large systems, as the Laughlin state is known to exhibit weak (long-range) entanglement.

Time-Evolution

As for the two-patch systems above, we perform time-evolution simulations starting from a product state

$$|\Psi_{\mathrm{initial}}\rangle = \bigotimes_{k=1}^{N_{\mathrm{patches}}} |\Psi_0^{(k)}\rangle \,. \tag{4.12}$$

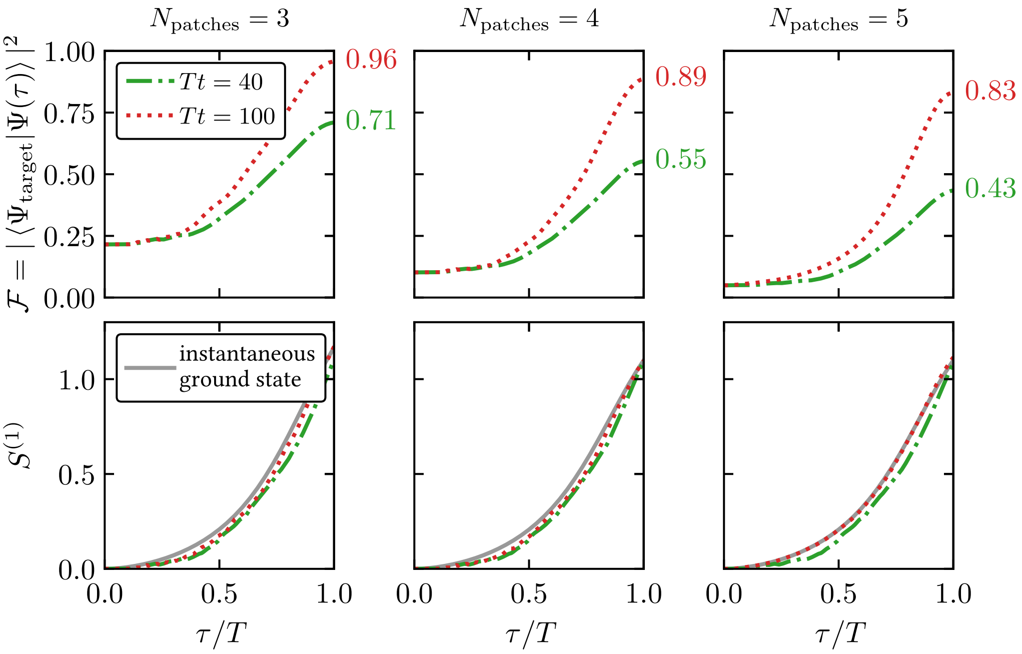

Fig. 4.12. *Super-chains*: Target-state fidelity $\mathcal{F}$ and entanglement entropy $S^{(1)}$ of the first patch upon linearly coupling all patches simultaneously.

We employ the time-dependent variational principle (TDVP) to evolve the MPS representing the initial state. We evolve the state with the time-dependent form of the Hamiltonian in Eq. (4.11), where the time-dependence enters via the change of the hopping amplitudes $t^{(k)}_\text{coupling}(\tau)$. In all our simulations we keep the flux per plaquette fixed to $\alpha = 0.3$.

Coupling All Patches at Once

In a first attempt to grow extended systems in the Laughlin regime, we couple all patches simultaneously, see Fig. 4.12. This first simple protocol provides target-state fidelities of $\mathcal{F} > 0.8$ for $Tt = 100$. However, the target-state overlap at the end of the ramp clearly decreases as more patches are added. While this limits the scalability beyond a certain system size, we are confident that extended systems similar to those studied in Chapter 3 are within reach. Nevertheless, we next study two alternative protocols to grow extended systems from originally decoupled patches to see whether we can reach even higher target-state fidelities in large systems.

Iteratively Coupling Pairs of Patches

For an even number of patches it might be favorable to first couple them in pairs of two patches before coupling the pairs among each other. We investigate this concept for a set of $N_\text{patches} = 4$ patches. In particular, we split the preparation time T in equal intervals, such that we first couple two patches each to form two pairs ($\tau \leq T/2$) and then connect the pairs ($\tau > T/2$).

For $Tt = 40$ and 100 we find that this protocol yields target-state fidelities which are significantly *lower* than those from a simultaneous coupling of all patches, see Fig. 4.13. Furthermore, the time-evolved state exhibits larger entanglement entropy than the target-state.

The protocol under study leads to a large fraction of the state being excited to higher states. We attribute this to the relatively fast ramp in the first half of the preparation, when connecting pairs of two patches. Extending this time period might result in higher overlaps at the end of the

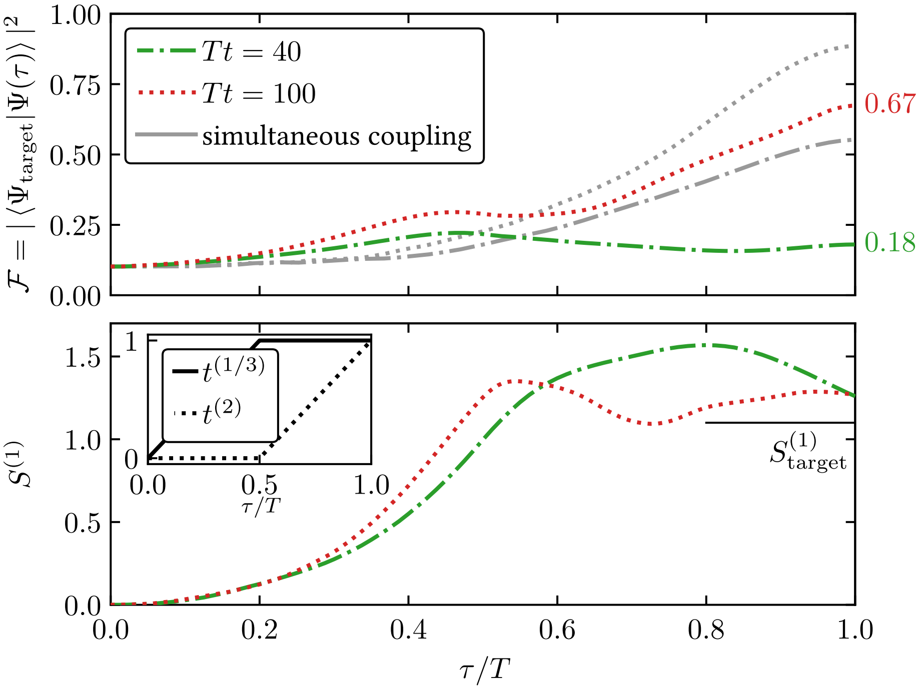

Fig. 4.13. *Super-chains*: Target-state fidelity $\mathcal{F}$ and entanglement entropy $S^{(1)}$ of the first patch upon first growing two pairs of patches ($\tau/T < 0.5$) and afterwards connecting the pairs ($\tau/T \geq 0.5$). The gray lines in the upper panel indicate the overlap achieved when all hoppings are ramped up simultaneously. The inset in the lower panel visualizes the different intra- ($t^{(1)} = t^{(3)}$) and inter-pair ($t^{(2)}$) coupling strengths.

complete ramp.

Attaching One Patch at a Time

We conclude our analysis of the super-chain setup by studying a protocol where the patches are attached one after the other. In particular, we linearly ramp up the couplings $t^{(k)}_{\text{coupling}}$, $k = 1, \dots N_{\text{patches}} - 1$, between the patches consecutively:

$$t^{(k)}_{\text{coupling}}(\tau)/t = \begin{cases} 0 & \text{for } \frac{\tau}{T} < \frac{k-1}{N_{\text{patches}}-1} \\ \frac{\tau}{T}\,(N_{\text{patches}}-1)-(k-1) & \text{for } \frac{k-1}{N_{\text{patches}}-1} \leq \frac{\tau}{T} \leq \frac{k}{N_{\text{patches}}-1} \\ 1 & \text{for } \frac{\tau}{T} > \frac{k}{N_{\text{patches}}-1} \end{cases}. \tag{4.13}$$

As before, we calculate the target-state fidelity as a function of time as well as the entanglement entropy between the first patch and the rest of the system. While we find large target-state overlaps for the slowest ramps considered here ($Tt = 100$), we do not find as good overlaps for a faster ramp, see Fig. 4.14. Furthermore, we find a significant increase in the entanglement entropy compared to that of the target-state. Again, we attribute the enhanced excitation to higher energy states to the reduced time taken to attach each individual patch.

Conclusions

Based on these results, we conclude that it is possible to grow extended Laughlin states in long chains similar to those studied in Chapter 3. We believe this approach to be scalable to system sizes relevant for experimental measurements of the central charge. In our analysis it turned out most promising to simultaneously couple all patches, as this allows for relatively short overall

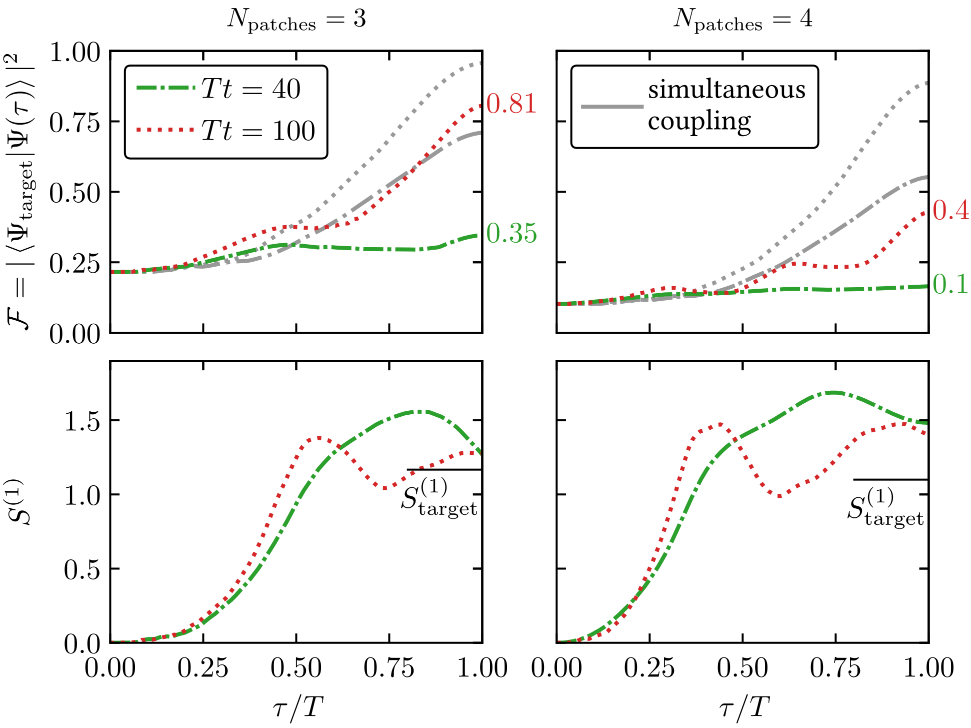

Fig. 4.14. *Super-chains*: Target-state fidelity $\mathcal{F}$ and entanglement entropy $S^{(1)}$ of the first patch upon consecutively connecting the patches. The gray lines in the upper row indicate the overlap achieved when all hoppings are ramped up simultaneously.

preparation times while still changing the local couplings sufficiently slowly. For such a protocol we achieved target-state fidelities of $\mathcal{F} > 0.8$ for up to five patches and $Tt = 100$.

In contrast, first coupling pairs of patches and afterwards connecting the pairs did not reach similar fidelities in our analysis. We note, however, that such a protocol might show its full potential only once even longer systems are studied. Similarly, we did not find it advantageous to couple the patches consecutively.

4.4. Large Square: Coupling Four Patches

Finally, we try to grow another large system by coupling four patches to obtain a large square. We focus on a barrier protocol, where a 9×9-system of eight atoms is split into four 4×4-patches by a local potential, see Fig. 4.15. This system is described by the Hamiltonian

$$\hat{\mathcal{H}}_{\text{square}}(V_{\text{barrier}}) = \hat{\mathcal{H}}_{9\times 9} + V_{\text{barrier}} \left(\sum_{y=1}^{9} \hat{n}_{5,y} + \sum_{x=1}^{9} \hat{n}_{x,5} - \hat{n}_{5,5} \right) . \tag{4.14}$$

Static Properties

As before, we perform DMRG simulations to determine the ground state and the lowest excited state, and determine the many-body gap for the case of hard-core bosons ($U/t = \infty$) and finite Hubbard repulsion ($U/t = 8$), where in the latter case we truncate the local Hilbert space to at most four bosons per site ($N_{\max} = 4$). We again find an adiabatic connection from a product

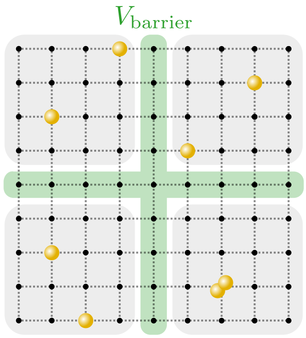

Fig. 4.15. Coupling four 4×4-patches (gray squares) with $N = 2$ particles each by turning off a potential barrier of height V_{barrier} (green cross).

state of four Laughlin states to a large Laughlin state in the homogeneously coupled system, see Fig. 4.16. Note, however, that close to the homogeneously coupled limit, $V_{\text{barrier}} = 0$, the many-body gap is reduced as a result of the extended system size. Nevertheless, we expect an adiabatic growing scheme to be applicable as the low-energy excitations are expected to be localized at the edge.

Time-Evolution

Once again, we start from a product state of four two-particle Laughlin states,

$$|\Psi_{\text{initial}}\rangle = \bigotimes_{k=1}^{4} |\Psi_0^{(k)}\rangle \,, \tag{4.15}$$

and use the TDVP method to perform a time-evolution simulation for a simple preparation protocol where we linearly reduce the height of the potential barrier,

$$V_{\text{barrier}}(\tau) = V_0 \left(1 - \frac{\tau}{T}\right) . \tag{4.16}$$

In particular, we consider the case $V_0/t = 1$, $\alpha = 0.25$, and $Tt = 40$ and 100. We furthermore restrict our time-evolution simulations to the hard-core bosonic case, $U/t = \infty$.

We monitor the target-state fidelity $\mathcal{F}$ along the preparation path as well as the entanglement entropy between the left two patches and the rest of the system, see Fig. 4.17. While for a sufficiently slow ramp, $Tt = 100$, we reach a final target-state fidelity of $\mathcal{F} = 0.35$, a faster ramp resulted in a significantly lower target-state fidelity. Furthermore, we find a similar oscillatory behavior of the fidelity as for the two-patch barrier protocol discussed above. Therefore, it might be favorable to stop the slow turn-off of the barrier discussed here once the maximum fidelity is reached and instead turn off the barrier suddenly at that point. Additionally, we believe that further optimization of the ramp protocol - similar to that for the earlier barrier protocol - might result in larger target state fidelity and hence more accurate state preparation. Therefore, we are confident that it is possible to grow extended Laughlin states even in the square geometry with sufficiently high fidelity.

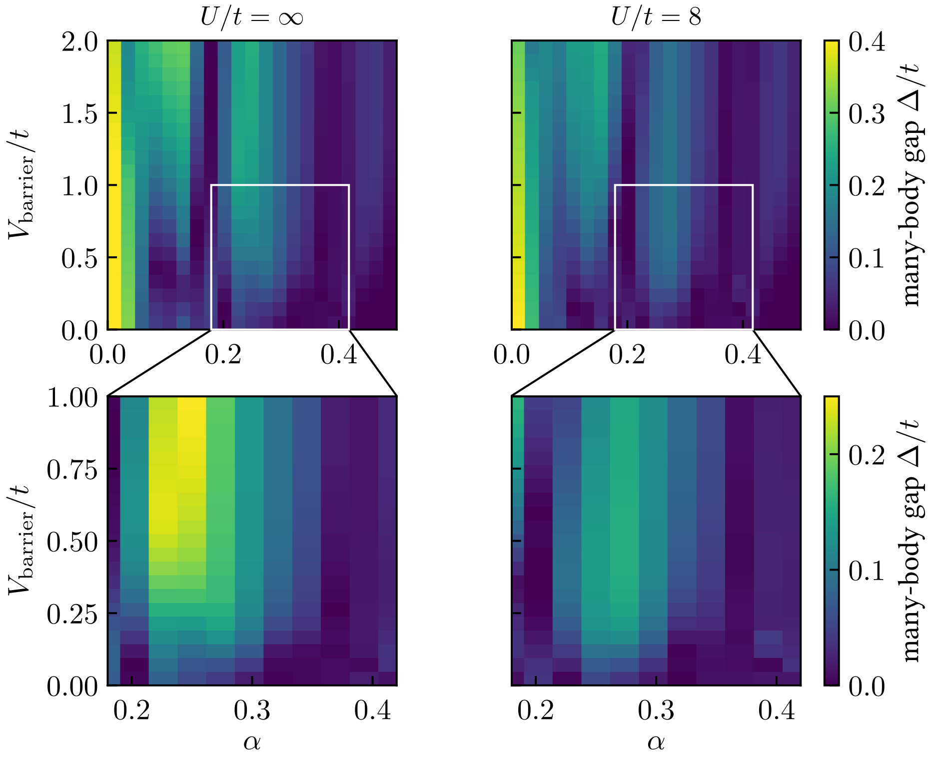

Fig. 4.16. *Large square*: Many-body gap Δ obtained using DMRG simulations of a system of four coupled 4×4-patches. Panels in the lower row show a zoomed-in version of data in the upper row. We tune both the flux per plaquette α and the barrier height V_{barrier} between the patches. The gap of the Laughlin state at $\alpha \approx 0.25$ remains finite in all cases, even though it significantly decreases as the system gets larger.

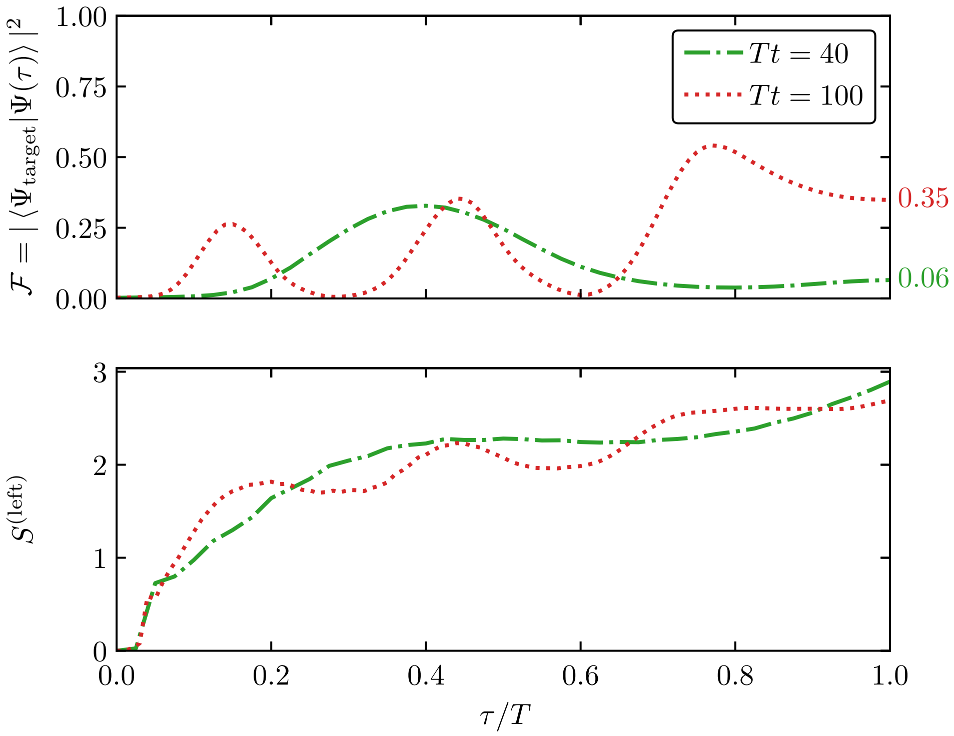

Fig. 4.17. *Large square*: Target-state fidelity $\mathcal{F}$ and entanglement entropy $S^{(\text{left})}$ of the left two patches for a linearly decreasing barrier height $V_{\text{barrier}}/t = 1 - \tau/T$ at constant flux per plaquette $\alpha = 0.25$. Similar to the barrier protocol for only two patches (Fig. 4.7) we find some oscillatory behavior. The target state fidelity reached at the end of the preparation protocol might be improved further by modifying the ramp similar to the barrier protocol discussed above.

4.5. Summary and Outlook

We found evidence that various different preparation protocols are well-suited to prepare extended Laughlin states by gluing together copies of the recently realized two-particle state on 4×4 sites. In particular, time-evolution simulations found target-state fidelities above 80 % for connecting two patches for preparation times of 40 tunneling times. Extended chains of up to 20×4 sites could be grown with similar fidelities by simultaneously turning on couplings between neighboring patches over a time of 100 tunneling times. Alternative protocols investigated here did not yield higher fidelity, but we believe further optimization of the ramp to be worthwhile in the future. Finally, we investigated the possibility to couple four patches in a square geometry by linearly turning off an initial potential barrier.

While these results show the scalability of a modular approach, further questions remain. On the one hand, it is always desirable to reach even higher fidelities at shorter ramp times. Especially in the case of many patches we believe an optimization of the different couplings to be profitable in the future. Here, state-of-the-art machine learning techniques might be useful to find particularly efficient paths in parameter space [203–205]. Such an approach might even take into account experimental details which are difficult to investigate on an abstract level.

On the other hand, new opportunities unique to cold atom quantum simulators become available as larger systems are now within reach. For example, growing long chains will allow for direct measurements of the central charge, thus providing direct evidence of the topological nature of the state. Furthermore, access to large systems in a square geometry might give the opportunity to directly probe braiding properties of quasiparticles and quasiholes of the Laughlin state. In particular, it might be possible to directly grow a quasihole state using a slight variation of the protocol discussed above by adding a local repulsive potential. In conclusion, building on the latest milestone of realizing a two-atom Laughlin state, exciting new directions are just opening up based on this modular approach.

5 Quantum Hall Ferromagnetism: Spinful Interacting Chern Insulators

5.1. Introduction and Outline

While the earlier chapters of this dissertation focused on bosonic systems, we will now discuss a lattice analog of the *fermionic* quantum Hall (QH) problem. In particular, we consider a close relative of the paradigmatic Fermi-Hubbard model in two dimensions with an additional perpendicular magnetic field. Extensive numerical studies have found many different phases of the doped Fermi-Hubbard model [206, 207], and an additional magnetic field provides the interesting possibility to further enhance interaction effects in flat, topological bands.

Generally speaking, strongly interacting fermionic systems host a variety of interesting quantum many-body states with exotic excitations. In particular, the emergence of ferromagnetism in strongly correlated systems is a phenomenon well-known in condensed matter physics and subject of ongoing research. For instance, the interplay of strong interactions and the Pauli exclusion principle can lead to Stoner ferromagnetism, the fate of which remains unclear when kinetic terms are added. While in many lattice models the fermions' dispersion results in delocalization of the particles and destabilization of the ferromagnet, flat bands can restore strong interaction effects and ferromagnetic correlations. Due to their flat bands, QH systems provide a powerful platform to study this mechanism.

Indeed, at magnetic filling factor $\nu = 1$, the ground state of the two-dimensional electron gas in the continuum was predicted to be ferromagnetically ordered [208, 209]. Furthermore, the low-lying charged excitations around this QH ferromagnet have been predicted to exhibit exotic spin textures known as skyrmions. These are characterized by local ferromagnetic correlations while being in an overall spin-singlet state [160, 210–216].

The QH ferromagnet and its skyrmionic excitations were observed in solid state experiments [217–223]. Recently, they attracted considerable attention in the context of twisted bilayer graphene [224–227] and related synthetic bilayer systems [228]. However, such experiments mainly use transport and spectroscopic measurements and therefore do not provide detailed microscopic insights. In contrast, quantum simulation allows for a better microscopic understanding, in particular of density and spin structures, and may provide direct coherent control over individual excitations, therefore allowing for a systematic study of their interactions.

Cold atoms in optical lattices have already enabled extensive studies of the Fermi-Hubbard model [206, 229–231], and implementations of artificial gauge fields in optical lattices exist [18–22]. Combining both achievements allows to study ferromagnetism in the strongly doped Hubbard model and explore its relation to phenomena known to arise in high-T_c superconductors.

While textbook calculations predict Stoner ferromagnetism even without a magnetic field and analytical considerations for flat-band Hubbard models found ferromagnetic ground states in specific cases [232], we demonstrate that the tunability of synthetic magnetic fields in cold atoms [22] enables a systematic search for the onset of Stoner-type QH ferromagnetism, the associated topological excitations and their interactions.

In particular, we propose to study the Hofstadter-Fermi-Hubbard model using ultracold atoms. We demonstrate, by performing large-scale DMRG simulations, that for magnetic filling factor $\nu \leq 1$ the ground state is fully spin polarized for a wide range of parameters, realizing a lattice version of the QH ferromagnet. We reveal the nature of the low-energy spin-singlet states around $\nu \approx 1$ and find that they host quasiparticles and quasiholes exhibiting spin-spin correlations reminiscent of skyrmions. Finally, for large magnetic flux per plaquette as well as for lower doping, we predict the breakdown of Stoner ferromagnetism and observe ground states with local spin anti-alignment.

This chapter is based on the results from Ref. [3], the text and figures of which were rearranged, adapted, and extended here. We start with a brief review of quantum Hall physics at $\nu = 1$ in Sec. 5.2, focusing on the role of the electron spin. In particular, we discuss the emergence of QH ferromagnetism and the related skyrmion quasiparticles and -holes. Afterwards, we present our numerical results for similar effects in the Hofstadter-Fermi-Hubbard model in Sec. 5.3, before summarizing our findings and briefly discussing open questions in Sec. 5.4.

5.2. Quantum Hall Physics at $\nu = 1$

The quantization of the Hall conductance was first observed by von Klitzing *et al.* [10] in electronic systems for integer filling factors ν. In this section we will discuss the corresponding state at $\nu = 1$, before extending our review from the integer quantum Hall state to states with interaction induced ferromagnetism.

5.2.1. Spin Polarized Systems: Integer Quantum Hall Effect

The two-dimensional electron gas can be described by the first quantized Hamiltonian

$$\hat{\mathcal{H}} = \sum_{j=1}^{N} \frac{1}{2m_b} \left(\hat{\mathbf{p}}_j + \frac{e}{c} \mathbf{A} \left(\hat{\mathbf{r}}_j \right) \right)^2 + \sum_{j<k=1}^{N} U \left(|\hat{\mathbf{r}}_j - \hat{\mathbf{r}}_k| \right) + g\mu \sum_{j=1}^{N} \mathbf{B} \cdot \hat{\mathbf{s}}_j, \tag{5.1}$$

where we introduced the spin operator $\hat{\mathbf{s}}_j$ for the j-th particle and the band mass m_b of the electrons. The first term contains the kinetic energy in the presence of a perpendicular magnetic field $\mathbf{B} = \nabla \times \mathbf{A} = B\mathbf{e}_z$, where $\mathbf{A}$ is the vector potential, the second term contains the pairwise Coulomb interaction among the particles, and the last term gives the Zeeman energy for the electronic spins in the external magnetic field.

We start our discussion by giving some typical energy scales of the system following arguments in Ref. [57]. The natural length scale of a system in a magnetic field of flux density B is the magnetic length, $\ell_B = \sqrt{\hbar c / eB}$. Equipped with this length scale, we can introduce the typical Coulomb energy of two electrons at distance ℓ_B, $U_\mathrm{C} = e^2/\epsilon \ell_B$, where ϵ is the material-dependent dielectric constant. We note that the typical Coulomb energy scales as $U \propto \sqrt{B}$.

Similarly, we can analyze the kinetic term. The non-interacting problem exhibits flat Landau levels at energies $E_n = \hbar\omega_c \left(n + 1/2\right)$, where we defined the cyclotron frequency $\omega_c = \frac{eB}{m_b c} \propto B$. Note that in our convention the Landau level is by itself agnostic to spin[1], so that a spin-$1/2$ system hosts one independent copy of Landau levels for each spin.

The Zeeman term splits the degeneracy between the two Landau level copies. In particular, the Zeeman energy scales linearly with the magnetic flux density and so does the spacing ΔE_Z

---

[1] It is possible to include the contribution of the Zeeman term in the Landau levels, however we do not do this here, but separate these two contributions.

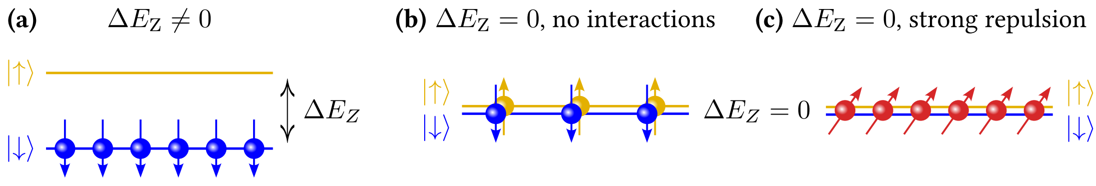

Fig. 5.1. Schematic level structure for a two-dimensional electron gas subject to a strong perpendicular magnetic field at $\nu = 1$. **(a)** In the non-interacting case and for a finite Zeeman splitting ΔE_Z the ground state is a spin polarized integer quantum Hall state. **(b)** For vanishing Zeeman splitting the spinful Landau levels become degenerate. In the absence of interactions, a hugely degenerate state forms which evades a simple interpretation. **(c)** In contrast, strong local repulsion results in a unique ground state which is spontaneously spin-polarized to exploit the Pauli principle. This state is known as a *quantum Hall ferromagnet.*

between the spin-dependent Landau levels.

From these arguments we conclude that for strong magnetic fields the effect of the Coulomb repulsion becomes negligible, while the Zeeman term and the kinetic energy are the dominant contributions. In particular, because of the Zeeman term it is favorable for the spins to align anti-parallel to the magnetic field, hence resulting in a spin polarized ground state. At the same time, in the absence of interactions, a spin polarized system at filling factor $\nu = 1$ is well described by a single Slater determinant of lowest Landau level orbitals, see Fig. 5.1**(a)**. This state is the celebrated integer quantum Hall state at $\nu = 1$, which is incompressible and exhibits a quantized Hall response [10, 57].

Charged Excitations

We briefly comment on the low-lying charged excitations of the integer quantum Hall state at $\nu = 1$. Removing a single particle results in a reduction of the total spin by $\Delta S = -1/2$, see Fig. 5.2**(a)**, while the spin polarization remains unchanged,

$$P_S = \left|\frac{N_\uparrow - N_\downarrow}{N_\uparrow + N_\downarrow}\right| = \left|\frac{0 - (N-1)}{0 + (N-1)}\right| = 1. \tag{5.2}$$

Similarly, adding a single particle decreases the total spin by $\Delta S = -1/2$ as the additional particle necessarily has to occupy a state in the lowest Landau level of the opposite spin.[2] However, the spin polarization decreases in this case, see Fig. 5.2**(b)**,

$$P_S = \left|\frac{1 - N}{1 + N}\right| < 1, \tag{5.3}$$

and decreases further as more particles are added.

In summary, the spin of the system changes by $\Delta S = -1/2$ both for the hole and electron doped case. In contrast, the spin polarization decreases only for $\nu > 1$, while the quasihole regime for $\nu < 1$ remains spin polarized in the non-interacting case. We will see shortly that the situation changes drastically in the presence of interactions.

5.2.2. Vanishing Zeeman Shift: Emergence of Quantum Hall Ferromagnetism

Another insightful limit of the Hamiltonian in Eq. (5.1) is reached if the Zeeman term vanishes, $\Delta E_Z = 0$. In this case, the SU(2) spin-rotational symmetry of the model is restored and the spin-dependent Landau levels become degenerate.

---

[2] Here we assumed that the cyclotron gap $\hbar\omega_c$ is significantly larger than the Zeeman splitting ΔE_Z.

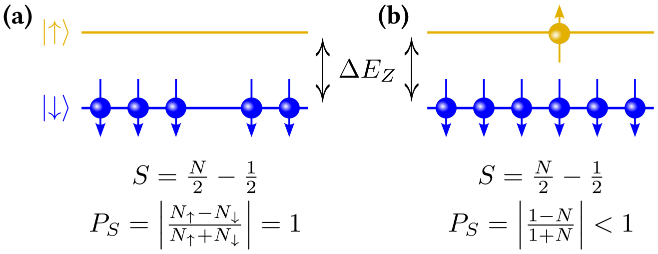

Fig. 5.2. Low-lying charged excitations of the integer quantum Hall state at $\nu = 1$ in the non-interacting limit. **(a)** Removing a single electron results in a system of spin $S = {}^{(N-1)}/_2$ which remains completely spin polarized, $P_S = 1$. **(b)** In contrast, adding an electron reduces the spin polarization, $P_S < 1$, while again giving a state of total spin $S = {}^{(N-1)}/_2$.

Neglecting interaction effects, the ground state becomes highly degenerate, with essentially arbitrary total spin S, see Fig. 5.1**(b)**. Similar to the paradigm of fractional quantum Hall physics, where interactions lift the extensive degeneracy of the partially filled Landau level, interactions can favor a unique ground state also at integer filling factors. For simplicity we consider the case of on-site interactions in the following argument, however the results also carry over to Coulomb-interacting particles [208, 209].

For a system with strong on-site repulsion it is desirable to avoid particles at the same position. A simple, yet effective way to achieve this is by exploiting the Pauli exclusion principle, stating that no two fermions can occupy the same single-particle quantum state. While particles of opposite spin could still occupy the same position, this is not the case for particles of equal spin. Therefore, a spin polarized state with total spin $S = {}^{N}/_2$ necessarily has vanishing on-site interaction energy and hence is a promising ground state candidate, see Fig. 5.1**(c)**. Note, however, that the SU(2) spin-rotational symmetry is not broken explicitly by the magnetic field, but in contrast is broken spontaneously by the spin alignment of the electrons. This interaction induced spin polarized state is commonly referred to as a *quantum Hall ferromagnet*.

While the assumption of vanishing Zeeman splitting might seem unphysical at first, small Zeeman shifts can in fact be reached experimentally in solid state systems for example by tilting the sample, changing the electron density, or applying pressure to the system [57]. Furthermore, the behavior described here is robust to those small, but finite Zeeman energies, achievable in existing experiments. Consequently, QH ferromagnetism at $\nu = 1$ and its accompanying low-lying excitations were by now observed in various solid state experiments [217–223]. Similar physics was also explored in the context of bilayer systems [208, 209, 228], with a particular emphasis on twisted bilayer graphene [224–227].

5.2.3. Topological Spin Textures: Skyrmions as Low-Lying Excitations

In the case of the non-interacting integer quantum Hall state, the total spin of the ground state was found to change by only $\Delta S = -{}^{1}/_2$ upon adding or removing electrons relative to $\nu = 1$. In contrast, the ground state of the interacting system behaves very differently. In early exact diagonalization studies, Rezayi found that adding or removing a single electron from the QH ferromagnet results in a macroscopic change of the ground state spin, resulting in a total spin-singlet, $S = 0$ [210, 212]. Furthermore, the corresponding quasihole and quasiparticle states were identified with certain topological spin textures known as (anti-)skyrmions [211, 213–216].

A detailed understanding and description of the skyrmions and their effective theory is rooted in a topological quantum field theory related to non-linear sigma models and Chern-Simons theory, the discussion of which is beyond the scope of this thesis. Nevertheless, an intuitive physical picture of the skyrmions is given here, following the line of thought of Ref. [233].

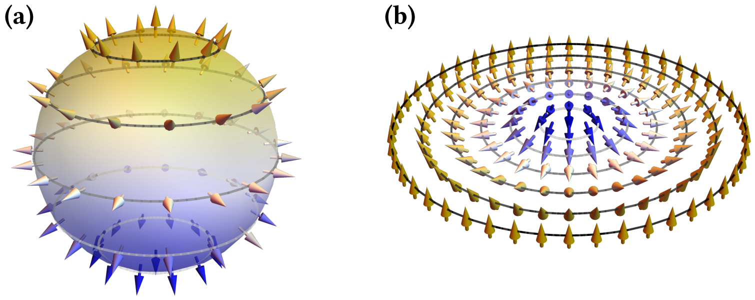

Fig. 5.3. **(a)** The hedgehog spin configuration is described by the order parameter $\mathbf{m}(\mathbf{r})$ pointing out of a sphere, hence wrapping around the sphere once. Therefore, it has topological charge $\mathcal{Q} = 1$. **(b)** Upon stereographic projection to the plane, a non-trivial spin texture is obtained which is known as the *hedgehog skyrmion*. Note that while locally the spin is almost perfectly aligned, at large distances the spin is anti-aligned.

Consider a 3-component order parameter $\mathbf{m}(\mathbf{r})$ satisfying the constraint $|\mathbf{m}(\mathbf{r})|^2 = 1$ for all $\mathbf{r}$. The infinitely extended plane $\mathbb{R}^2$ can be identified with the two-dimensional sphere $\mathbb{S}^2$ using the appropriate boundary conditions for the order parameter,

$$\lim_{|\mathbf{r}|\to\infty} \mathbf{m}(\mathbf{r}) = \mathbf{m}_0. \tag{5.4}$$

In conclusion, the order parameter is a smooth map $\mathbf{m} : \mathbb{S}^2 \to \mathbb{S}^2$ describing a spin configuration on the sphere. Such maps can be classified using the second homotopy group of the 2-sphere, $\pi_2(\mathbb{S}^2) = \mathbb{Z}$. In particular, the topological invariant associated with such a spin configuration is integer valued and given by the topological charge (or Pontryagin index),

$$\mathcal{Q} = \frac{1}{8\pi} \int \mathrm{d}^2 x \, \epsilon_{ij} \mathbf{m} \cdot (\partial_i \mathbf{m} \times \partial_j \mathbf{m}) \, . \tag{5.5}$$

Physically speaking, the topological charge counts how often the spin configuration wraps around the sphere $\mathbb{S}^2$.

The Hedgehog Skyrmion

A particularly insightful example of a *classical* skyrmion involves a spin texture where the order parameter points out of the sphere at every point, i.e. $\mathbf{m}(\mathbf{r}) = \hat{\mathbf{e}}_r$ in spherical coordinates, so that the spin is aligned almost perfectly locally. This spin configuration is also known as the hedgehog configuration. In particular, the spin wraps around the sphere once, thus the topological charge is $\mathcal{Q} = 1$.

Using the stereographic projection from the sphere to the two-dimensional plane, it becomes evident that the spin infinitely far away from the origin is perfectly anti-aligned with the spin at the origin, i.e.

$$\mathbf{m}(|\mathbf{r}| = 0) = -\mathbf{m}(|\mathbf{r}| = \infty). \tag{5.6}$$

The resulting projected spin configuration is commonly referred to as the *hedgehog skyrmion*, see Fig. 5.3.

A similar construction for a quantum mechanical spin allows for an SU(2) symmetric spin-singlet state with topological charge $\mathcal{Q} = \pm 1$. Such a (quantum) skyrmion is believed to describe the low-lying quasiparticle and quasihole excitations of the QH ferromagnet around $\nu \approx 1$. While finite Zeeman shifts and related effects affect the size of the skyrmion and the total spin of the ground state, accurate theoretical calculations are in excellent agreement with experimental measurements [213, 214]. In particular, signatures of skyrmion excitations have been observed using various methods [217–223].

However, typical solid state experiments do not allow for a direct microscopic observation of the spin texture, but rely on spectroscopic and transport measurements. In contrast, single site resolution in combination with spin resolved measurements in cold atom quantum simulators may allow for such microscopic insights. Therefore, we propose to realize QH ferromagnetism and the accompanying skyrmionic excitations in the fermionic Hofstadter-Hubbard model with ultracold atoms. In the remainder of this chapter, we will explore this possibility using extensive numerical simulations.

5.3. Hofstadter-Fermi-Hubbard Model: Ferromagnetism on a Lattice

Discretizing the continuum quantum Hall problem, we study spin-$1/2$ fermions subject to a magnetic field on a two-dimensional square lattice of size $L_x \times L_y$. Choosing the Landau gauge along the y-direction, the Hamiltonian reads

$$\hat{\mathcal{H}} = -t \sum_{x,y,\sigma} \left(\hat{c}^{\dagger}_{x+1,y,\sigma} \hat{c}_{x,y,\sigma} + \mathrm{e}^{2\pi i \alpha x} \hat{c}^{\dagger}_{x,y+1,\sigma} \hat{c}_{x,y,\sigma} + \mathrm{H.c.} \right) + \frac{U}{2} \sum_{x,y} \hat{n}_{x,y,\uparrow} \hat{n}_{x,y,\downarrow}, \tag{5.7}$$

where $\hat{c}^{(\dagger)}_{x,y,\sigma}$ is the annihilation (creation) operator for a spin-σ fermion at site (x, y) and $\hat{n}_{x,y,\sigma}$ is the corresponding number operator. The first term of the Hamiltonian describes hopping on the lattice. Upon hopping around a single plaquette, the fermions pick up a phase $2\pi\alpha$, corresponding to α flux quanta per plaquette. The second term describes the Hubbard interaction of strength U on doubly occupied sites. We emphasize the absence of a Zeeman term in our study, hence preserving the $\mathrm{SU}(2)$ spin-rotational symmetry of the Hamiltonian.

We study the model on a cylinder by imposing open boundary conditions in x-direction and periodic boundary conditions in y-direction. Furthermore, we choose strong repulsive Hubbard interactions, $U/t = 8$, which includes Landau level mixing effects and is realistically achievable in state-of-the-art cold atom experiments. However, we believe our results to extend to other values of the interaction strength exceeding the bandwidth. For a system of N particles we define the density $n = N/(L_x L_y)$ and the hole concentration δ away from half-filling, such that $n = 1 - \delta$. Furthermore, we define the magnetic filling factor $\nu = N/N_\phi$, where $N_\phi = \alpha\,(L_x - 1)\,L_y$ is the total number of flux quanta.

In the limit of vanishing flux, $\alpha = 0$, the model reduces to the 2D Hubbard model with its various quantum phases [206, 207]. Upon adding a magnetic field, α, the single-particle Bloch bands split up into flat magnetic subbands resembling the Landau levels known from the continuum [63]. The formation of flat magnetic bands is expected to enhance interaction effects and leads to QH physics, in particular the potential emergence of QH ferromagnetism at filling factor $\nu = 1$. For small flux α and density n, lattice effects are negligible and we expect our results to connect to known continuum results [170]. Increasing the flux per plaquette, lattice effects become more dominant and the continuum description breaks down.

To study lattice effects, we perform single-site DMRG simulations [135–139]. We exploit the $\mathrm{U}(1)$ symmetry associated with particle number conservation and the $\mathrm{SU}(2)$ spin-rotational symmetry of the model. This allows us to calculate the variational ground state in the sectors of minimal ($S = 0$) and maximal total spin ($S = S_{\max} = N/2$) on cylinders of size $L_x \times L_y = 31 \times 4$ and 33×5 while varying both the magnetic flux per plaquette and the density.

Quantum Hall Ferromagnetism at $\nu \leq 1$

First, we focus on systems with magnetic filling factor $\nu \approx 1$. Close to the continuum limit, where the flux per plaquette α and the particle density $n = 1 - \delta$ are small, we expect the ground state to exhibit QH ferromagnetism for $\nu = 1$ [170]. In particular, the ground state is expected to be magnetically ordered for $\nu \leq 1$ with an incompressible QH state at $\nu = 1$.

This is confirmed by our DMRG simulations where we find the ground state to be spin polarized, see Fig. 5.4. Furthermore, this behavior extends significantly to larger flux α where lattice effects become increasingly relevant. This clearly shows the emergence of QH ferromagnetism in the Hofstadter-Fermi-Hubbard model. However, above some large critical flux $\alpha_c \approx 0.35$ per plaquette the QH ferromagnetism at $\nu \lesssim 1$ breaks down and we find that the ground state is a spin-singlet.

While we did not perform a systematic finite size extrapolation to the thermodynamic limit, we note that the results presented here are not affected by the circumference of the cylinder significantly. In combination with the long extent of the cylinders along their axis in comparison to the magnetic length, we expect our results to extrapolate to the thermodynamic limit.

Incompressibility of the QH Ferromagnet

In the continuum, the QH state at $\nu = 1$ is known to be incompressible. To verify that also the state found in our lattice studies shares this behavior, we calculate the energy cost $\mu_{N,+} = E_{N+1} - E_N$ to add a particle in the spin polarized sector as function of the filling factor. Ideally, for an incompressible state we expect this energy cost to have a discontinuity. In the finite systems studied here, this discontinuity will be smeared out, but we still expect a sharp increase at $\nu = 1$. Indeed, using our DMRG results for the energy in the spin polarized sector we find such a jump, see Fig. 5.5**(a,b)**. While most simulations in this chapter were done at even particle numbers to allow for states with total spin $S = 0$, our incompressibility analysis explicitly used *all* numbers of particles within a certain range.

Another signature of incompressibility is a finite charge gap in the thermodynamic limit. To probe this feature, we calculate the charge gap $\Delta\mu_N = E_{N+1} + E_{N-1} - 2E_N$ in the spin polarized sector. We find a large charge gap, $\Delta\mu_{\nu=1} \gtrsim 0.5t$, at filling factor $\nu = 1$, while the gap essentially closes away from this filling factor, see Fig. 5.5**(c,d)**. Given the weak dependence of the charge gap on the cylinder circumference, we believe the gap to remain open also in the thermodynamic limit, hence providing further evidence for the incompressible QH ferromagnet at $\nu = 1$.

Comparison with Trial States

Before deepening our understanding of the DMRG results, we introduce two paradigmatic trial states describing the spin polarized and unpolarized sector, respectively. Since the two states feature different short-range correlations, comparing their variational energies provides insights into the underlying magnetic order.

For the spin polarized case our trial state $|\Psi^{\text{trial}}_{S=S_{\text{max}}}\rangle$ is the exact eigenstate of the non-interacting Hofstadter model with energy $E^{\text{trial}}_{S=S_{\text{max}}}$ constituted by a Fermi sea of N identical fermions.

For the spin-singlet sector we make a resonating valence bond (RVB) ansatz [234]. We start from a state consisting of $N/2$ up- and down-spin fermions each forming separate Fermi seas, $|\Psi^{\uparrow/\downarrow}\rangle$. To account for the strong Hubbard repulsion, we perform a Gutzwiller projection [235]

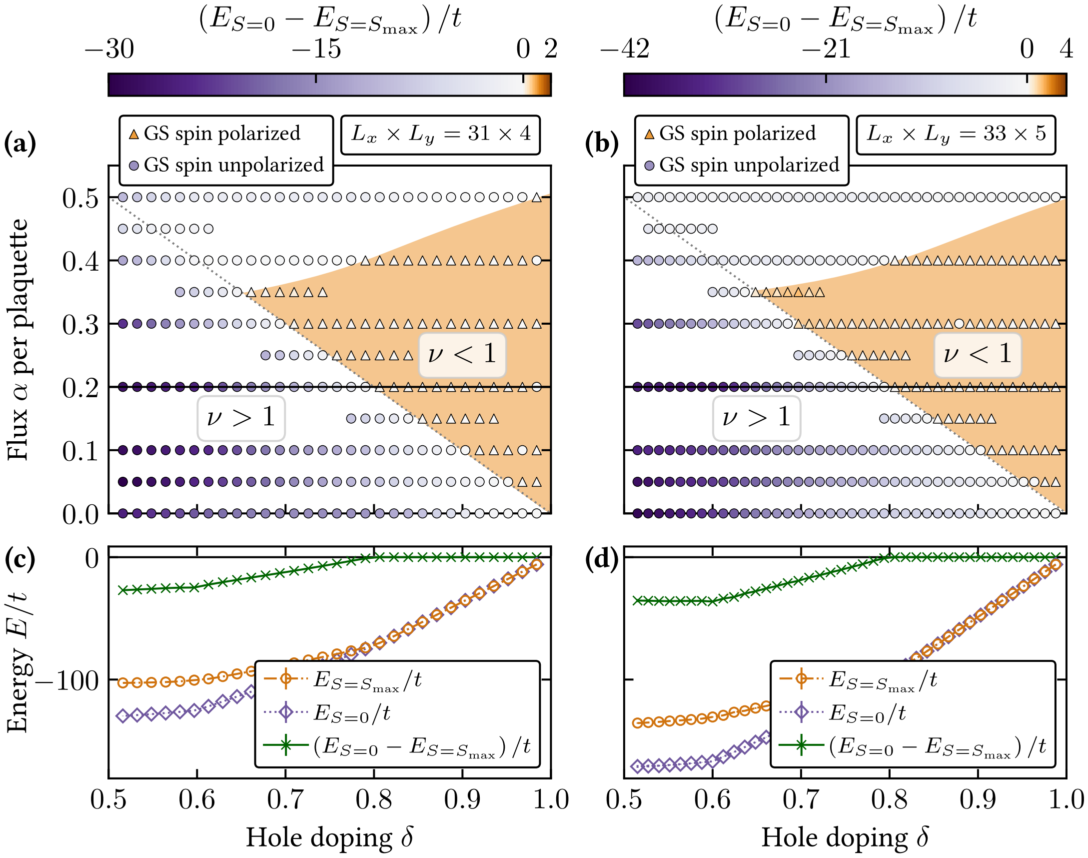

Fig. 5.4. **(a, b)** Energy difference between the lowest energy states found in DMRG for the $S = S_{\max}$ and the $S = 0$ sectors as function of magnetic flux per plaquette α and doping level δ. The gray dotted line indicates $\nu = 1$. For $\alpha \lesssim 0.35$ and $\nu \leq 1$ (shaded region) the ground state is spin polarized with an almost degenerate spin-singlet excited state (see also **(c, d)**). In contrast, for $\nu > 1$ the spin-singlet is energetically favored significantly. At large flux, $\alpha \gtrsim \alpha_c \approx 0.35$, the QH ferromagnetism breaks down and we find the ground state to be unpolarized even for $\nu < 1$. **(c, d)** Ground state energies in both sectors at $\alpha = 0.2$ (solid line in **(a, b)**), where errorbars are smaller than the symbols. Data is given for systems of size $L_x \times L_y = 31 \times 4$ **(a, c)** and 33×5 **(b, d)**.

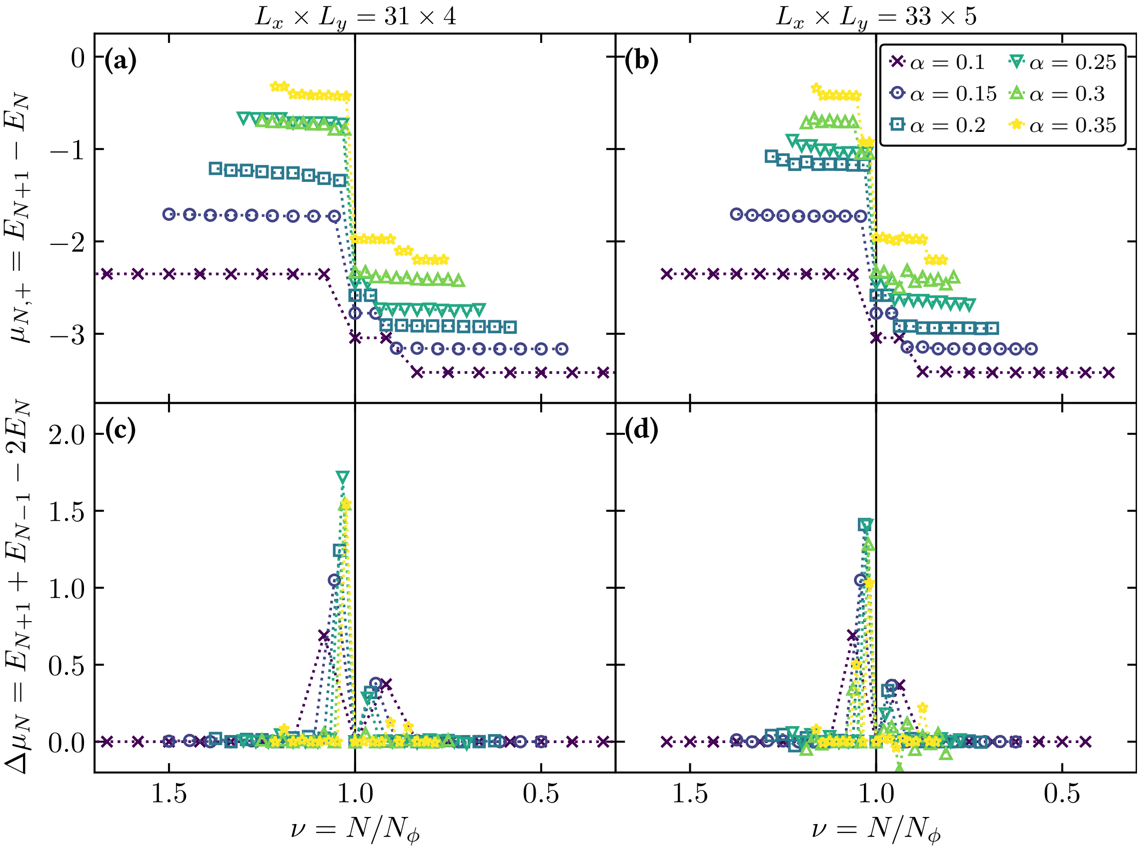

Fig. 5.5. **(a, b)** Energy cost $\mu_{N,+}$ for adding a particle and **(c, d)** charge gap $\Delta\mu_N$ in the spin polarized sector as function of the filling factor ν and varying flux α. We find a clear jump of $\mu_{N,+}$ at $\nu = 1$ indicating the incompressibility of the spin polarized state. Correspondingly, we observe a large charge gap $\Delta\mu_{\nu=1} \gtrsim 0.5t$ at this filling. This is in agreement with the spin polarized state at $\nu = 1$ being a lattice analog of the QH ferromagnet. Data shown for systems of sizes $L_x \times L_y = 31 \times 4$ **(a, c)** and 33×5 **(b, d)**.

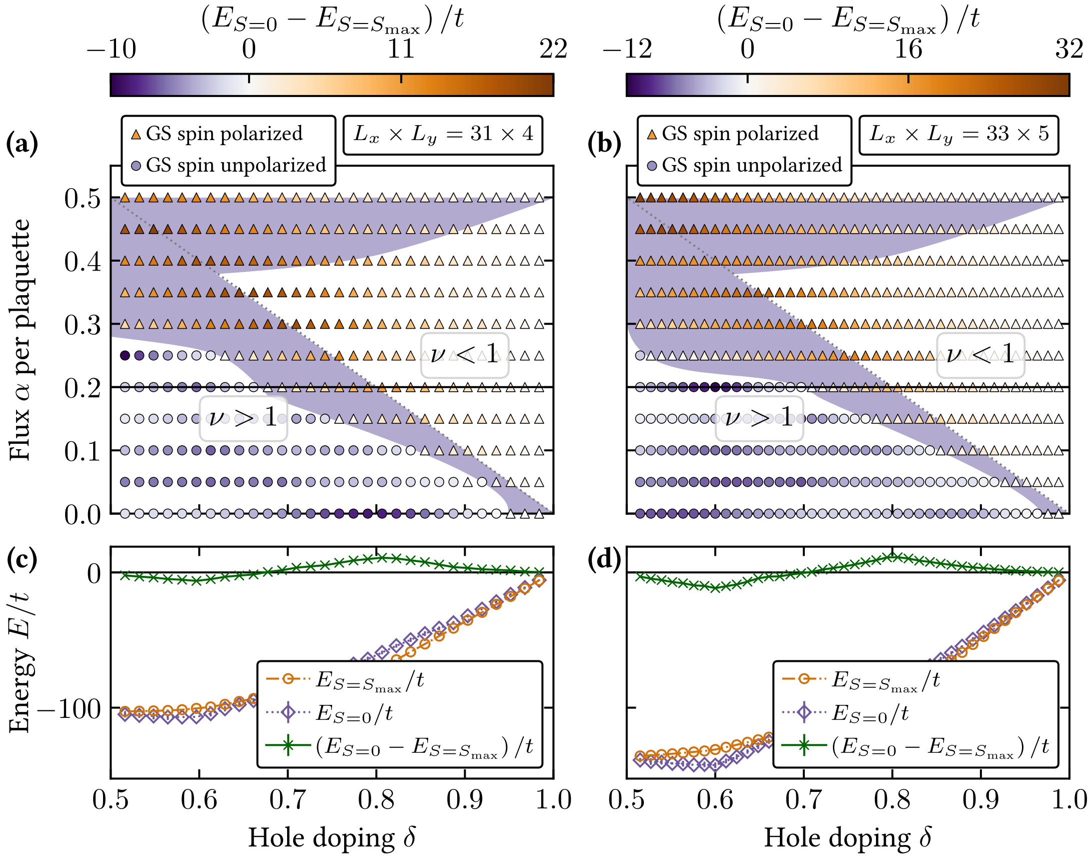

Fig. 5.6. **(a, b)** Energy difference between the trial energies for the $S = S_{\max}$ and the $S = 0$ sectors. The gray dotted line indicates $\nu = 1$ and the shaded area indicates the regime where the DMRG finds the ground state in the spin-singlet sector, while the trial states predict ferromagnetic order. **(c, d)** Trial state energies in both sectors at $\alpha = 0.2$ (solid line in **(a, b)**), where errorbars are smaller than the symbols. Data is given for systems of size $L_x \times L_y = 31 \times 4$ **(a, c)** and 33×5 **(b, d)**.

to project out doubly occupied sites and obtain the trial state

$$|\Psi^{\text{trial}}_{S=0}\rangle = \hat{\mathcal{P}}_{\text{G}} \left(|\Psi^{\uparrow}\rangle \otimes |\Psi^{\downarrow}\rangle \right), \qquad \hat{\mathcal{P}}_{\text{G}} = \prod_{x,y} \left(1 - \hat{n}_{x,y,\uparrow}\hat{n}_{x,y,\downarrow}\right). \tag{5.8}$$

We determine the variational energy $E^{\text{trial}}_{S=0}$ of this state using Metropolis Monte Carlo sampling of $N_{\text{MC}} = 1000$ snapshots.

As previously for the DMRG energies, we compare the trial energies in the different spin sectors in Fig. 5.6. The trial states predict correctly the existence of QH ferromagnetism revealed earlier by DMRG. For large α and some fillings $\nu \gtrsim 1$, however, we find a region (shading in Fig. 5.6) where QH ferromagnetism is predicted, but DMRG revealed a spin-singlet ground state.

This can be understood from the qualitatively different local structure of the trial states. In particular, the variational energy is only sensitive to local correlations. Hence the extended range of QH ferromagnetism predicted by the trial states provides a first indication that non-trivial spin textures may lead to the formation of spin-singlet ground states while retaining local spin alignment: this is a hallmark of skyrmion formation.

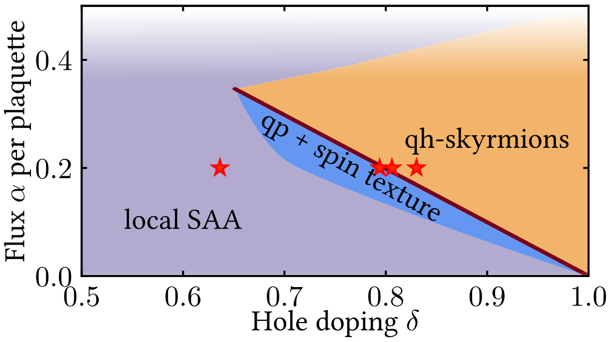

Fig. 5.7. Schematic phase diagram for the $S = 0$ sector. We find quasihole (qh) skyrmion states, quasiparticle (qp) states carrying interesting spin textures, as well as states exhibiting local spin anti-alignment (SAA). While the qh-skyrmion state is a low-lying excitation of the QH ferromagnet, the other states constitute the global ground state of the model across all spin sectors. The stars indicate the points studied in Fig. 5.8.

Skyrmions at $\nu \approx 1$

We now turn to the low-energy spin-singlet states competing with the QH ferromagnet. In the regime we have just identified using the trial states, where local ferromagnetic correlations play an important role, we expect the spin-singlet states to exhibit interesting spin correlations evolving from short-range spin alignment into long-range anti-alignment. A general overview of the resulting phase diagram for the $S = 0$ sector is given in Fig. 5.7.

To identify and understand the different phases, we consider the local density,

$$n(x) = \sum_{y=1}^{L_y} \langle \hat{n}_{x,y} \rangle / L_y, \tag{5.9}$$

and the normalized spin-spin correlations,

$$C_{x_0}(x) = \frac{1}{L_y} \sum_{y=1}^{L_y} \left\langle \hat{\mathbf{S}}_{x0,y} \cdot \hat{\mathbf{S}}_{x,y} \right\rangle \Big/ \left\langle \hat{n}_{x0,y} \hat{n}_{x,y} \right\rangle, \tag{5.10}$$

relative to a position x_0 in the bulk of the system. On-site, we expect this spin-spin correlation function to be $C_{x_0}(x_0) = 3/4$ for spin-$1/2$ fermions.

At filling factor $\nu = 1$, the low-energy spin-singlet excitation (above the spin-polarized ground state) shows local ferromagnetic correlations, which at long distances continuously evolve into anti-aligned correlations, see Fig. 5.8**(a)**. Similar to the continuum case [211, 213], this indicates the existence of skyrmion states in lattice systems.

Upon removing fermions from the spin-singlet $\nu = 1$ state, the local density develops localized drops, see Fig. 5.8**(b)**. We interpret these as quasiholes of charge $q_{\mathrm{qh}} = -1$ derived from the $\nu = 1$ state. The charge of these quasiholes is consistent with the prediction for skyrmions in the continuum QH system [213]. Considering spin-spin correlations relative to a reference site in the center of the system, we find spin textures reminiscent of domain walls at the locations of the quasiholes. In contrast, relative to the center of the quasiholes, the spin-spin correlations are again consistent with localized skyrmion excitations. In particular, we find indication of local ferromagnetic correlations, while at larger distances from the quasihole the spins are anti-aligned. We note, however, that the degree of spin (anti-)alignment is suppressed compared to the skyrmionic excitation at $\nu = 1$.

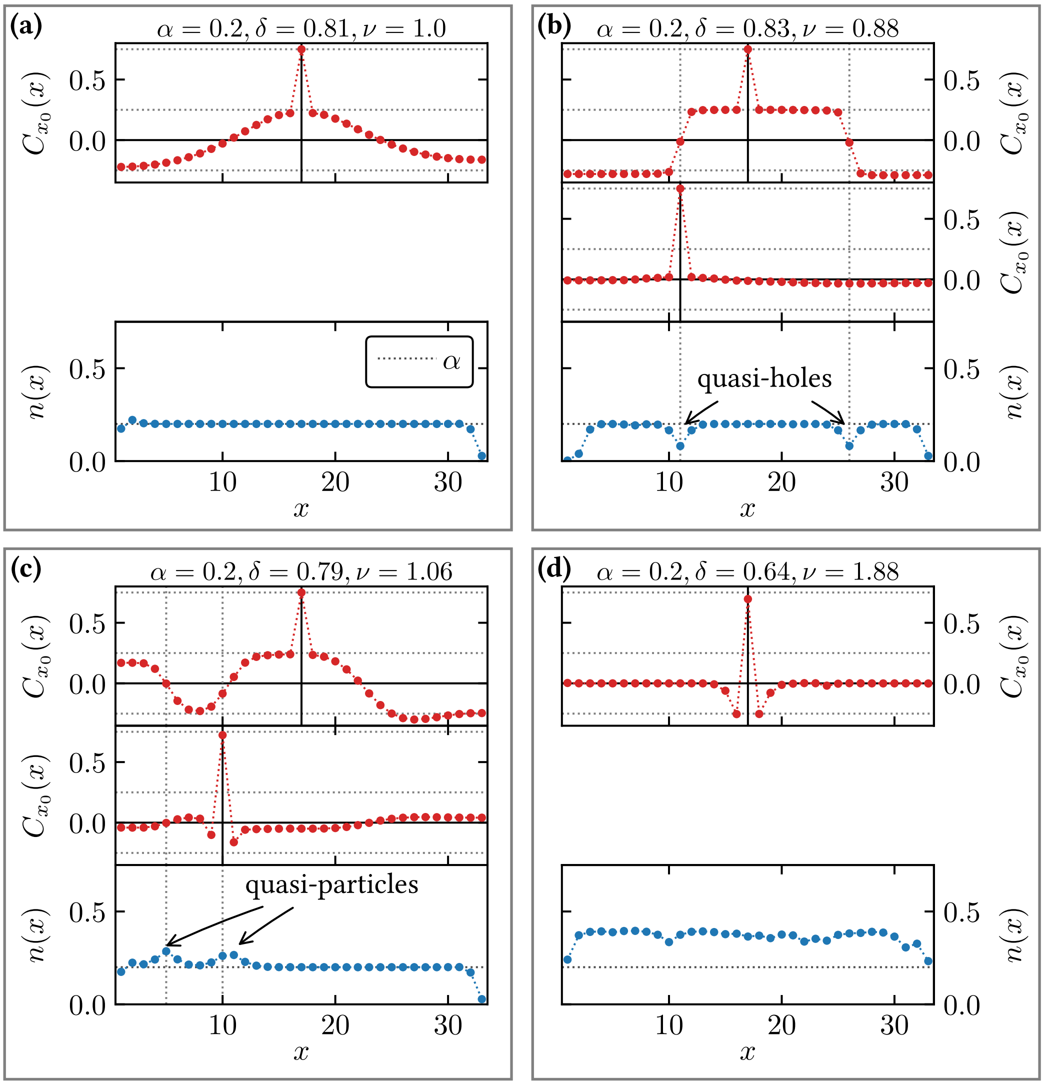

Fig. 5.8. Low-energy $S = 0$ state at $\alpha = 0.2$ with signatures of skyrmion states in **(a-c)**. **(a)** $\nu = 1$: Spin-spin correlations resembling the characteristic behavior of skyrmions. **(b)** $\nu < 1$: Quasihole (qh) skyrmion state descending from the $\nu = 1$ state. **(c)** $\nu > 1$: Quasiparticle (qp) skyrmion excitation of the $\nu = 1$ state. **(d)** $\nu \gg 1$: State exhibiting local spin anti-alignment (SAA). The reference site for the spin-spin correlations is indicated by the vertical black line. For the qh and qp states, we compare the correlations relative to both a site in the density structure and a distant site in the bulk. Data is given for a system of size $L_x \times L_y = 33 \times 5$ and the parameters indicated by stars in Fig. 5.7.

We interpret the low-lying excitations of the QH ferromagnet at filling factor $\nu < 1$ as quasihole skyrmions. In particular, we note that the number of quasihole skyrmions hosted by the system increases as the particle density is reduced. We stress again that the overall ground state in this regime is spin polarized, while the spin-singlet states just discussed are low-energy excitations.

In contrast, for filling factors $\nu > 1$, as additional fermions are added to the system, we always find the ground state to be in the $S = 0$ sector independent of α. Furthermore, we find that the ground state hosts localized quasiparticles of charge $q_{\mathrm{qp}} = 1$. Similar to the quasihole case, we find a characteristic change of the spin-spin correlations around the quasiparticles as visualized in Fig. 5.8**(c)**. While we could clearly identify these as quasihole skyrmions in the former case, the situation is less clear for the quasiparticles. We attribute this to the larger size of the quasiparticle and the Pauli correlation hole. Around the quasiparticle the spins seem to be anti-aligned on a short length scale. Nevertheless, at intermediate length scales, we find light signatures of spin alignment, with spin anti-alignment further away, reminiscent of skyrmionic spin textures. For a reference site in the center of the system we again find a behavior similar to that of domain walls related to the quasiparticles. We note however, that compared to the quasihole case the domain walls are less sharp in this case and extend over a finite range.

In conclusion, we interpret these quasiparticles as being dressed by non-trivial spin textures, which may be related to skyrmions or constitute a precursor of stripe formation. We note that the parameter regime where these exotic spin structures are observed is also part of the regime where our trial states predict the ground state to be ferromagnetically ordered globally. In the ground states obtained using DMRG, this global order is replaced by local ferromagnetic correlations, while non-trivial spin textures lead to the formation of a global spin-singlet.

Spin Textures at Large Flux and Low Density

For large flux per plaquette, $\alpha > \alpha_c \approx 0.35$, we found the ground state at $\nu = 1$ to be a spin-singlet state, see Fig. 5.4. However, upon reducing the particle number and hence the filling factor, we again find spin polarized ground states in the extremely dilute regime. In particular, for some cases close to the transition between spin polarized and spin-singlet ground states we even observe spin correlations reminiscent of the skyrmion textures close to $\nu = 1$ for $\alpha \lesssim \alpha_c$ discussed above, see Fig. 5.9.

Furthermore, in the dilute regime at large magnetic flux we also find significant density modulations, see Fig. 5.9. While we could not fully resolve their origin yet, these oscillations might be a result of the interplay of strong magnetic fields and diluteness, reminiscent of the emergence of Wigner crystals in the continuum [236].

Non-skyrmion Ground States

So far, the states discussed were significantly influenced by the local spin alignment underlying the $\nu = 1$ QH ferromagnet. Now, we turn to a first explorative analysis of the phase diagram in regimes where the influence of the QH ferromagnetism essentially disappears.

Upon increasing the particle number such that $\nu \gg 1$, we find the ground state to be a spin-singlet characterized by local spin anti-alignment with essentially uncorrelated spins on large length scales, see Fig. 5.8**(d)**. This is in clear contrast to the skyrmion states which exhibit local ferromagnetism as one of their main features. The local spin anti-alignment is reminiscent of free fermions exhibiting a Pauli exclusion hole [237].

Such a state is the ground state for a broad range of parameters and might host other more complicated structures, some of which might be related to the myriads of phases known from the doped Hubbard model. Furthermore, earlier studies [238] using renormalized mean-field theory

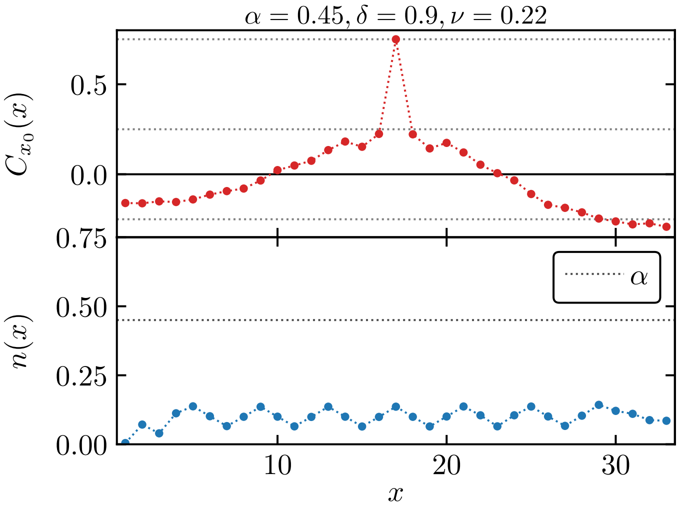

Fig. 5.9. Spin-spin correlations $C_{x_0}(x)$ (upper panel) and local density $n(x)$ (lower panel) for large magnetic flux $\alpha = 0.45 > \alpha_c$ and small filling factor, where the ground state is spin polarized. The overall behavior is reminiscent of the skyrmion textures discussed close to filling factor $\nu = 1$ at smaller magnetic fields $\alpha \leq \alpha_c$. Data is given for a system of size $L_x \times L_y = 33 \times 5$ and $x_0 = 17$.

and exact diagonalization also found phases with enlarged unit cells in this regime, which we can neither confirm nor completely exclude in our finite-size simulations. Note that in this regime of large particle numbers the numerical simulations are particularly challenging and we believe the density to be not fully converged yet.

Finally, we return to the regime $\nu \lesssim 1$. Upon increasing the flux per plaquette, we find a qualitative change of the behavior. For large flux per plaquette, $\alpha > \alpha_c \approx 0.35$, the QH ferromagnetism breaks down and also the ground state at $\nu \lesssim 1$ is a spin-singlet. Furthermore, for some values of the filling factor, this spin-singlet state does no longer exhibit neither skyrmionic correlations nor local spin anti-alignment, but instead some oscillatory behavior of the spin correlations, see Fig. 5.10. At the same time, in the very dilute regime, $\nu \ll 1$, the ground state is again spin polarized even for large flux, as discussed at the end of the last section.

5.4. Summary and Outlook

Summarizing our study of the fermionic Hofstadter-Hubbard model, we have found evidence for QH ferromagnetism to emerge at magnetic filling factor $\nu = 1$. Additionally, we have identified a skyrmion-like behavior of the low-energy spin-singlet states. In particular, the local density and the spin-spin correlations reveal quasihole skyrmions and quasiparticles dressed by spin textures for filling factor $\nu \approx 1$. For large flux per plaquette $\alpha \gtrsim 0.35$, we have observed a breakdown of QH ferromagnetism in favor of a spin-singlet ground state. The microscopic nature of this state and its origin deserve a more detailed analysis and should be addressed in the future.

Our work paves the way for future investigations of many interacting skyrmions, in particular at very low fermion densities. Furthermore, varying the Hubbard interaction strength U/t might give insight into the stability of the QH ferromagnet against Landau level mixing or allow to explore doped chiral quantum spin liquids [239]. More broadly, connections to high-T_c superconductivity can be explored by going to the small-flux limit. Extending the model to bilayer systems or finite temperatures will lead to further interesting questions for future research. Fur-

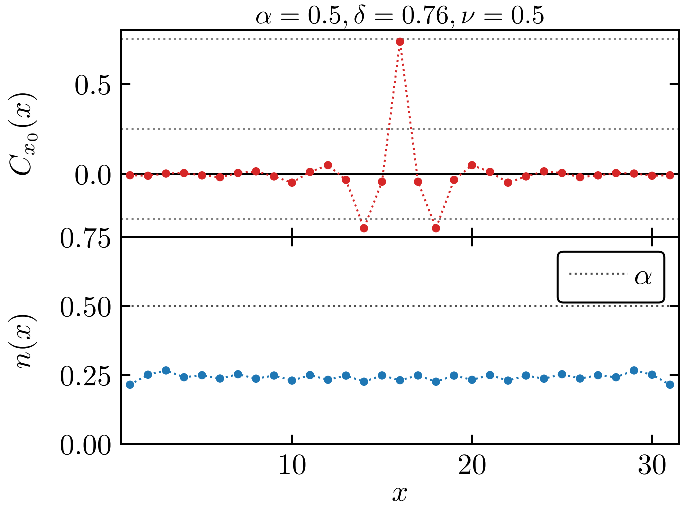

Fig. 5.10. Spin-spin correlations $C_{x_0}(x)$ (upper panel) and local density $n(x)$ (lower panel) for large magnetic flux $\alpha = 0.5 > \alpha_c$ and filling factor $\nu = 0.5$, where the spin-singlet state constitutes the ground state of the system. We find oscillations in the spin-spin correlations significantly different from the correlations found in other regions of parameter space. Data is given for a system of size $L_x \times L_y = 31 \times 4$ and $x_0 = 16$.

thermore, different lattice geometries exhibiting topological flat bands might allow for similar effects, even in the absence of a net magnetic field.

The model studied here can be realized with ultracold fermions in optical lattices, which provide simultaneous spin and charge resolution down to individual lattice sites. In particular, specific spin sectors can be experimentally addressed using adiabatic preparation schemes [170]. This type of system would also allow to add further-range dipolar interactions, which can be used to address the fractional QH regime where we expect similar skyrmion excitations to exist [240–243].

6 Analytical Considerations: Trial Wave Functions on a Lattice

6.1. Introduction and Outline

While the previous parts of this thesis mainly considered numerical studies, we now turn towards some analytical insights regarding fractional Chern insulators. In particular, we generalize the continuum composite fermion theory to lattice systems and propose variational trial states.

Existing approaches to derive lattice analogs of familiar fractional quantum Hall (FQH) states are often based on conformal field theory [244–250]. In these cases, one tries to realize a given FQH state on a lattice and constructs the state without initially referring to a specific lattice Hamiltonian. Ultimately, a parent Hamiltonian for the resulting lattice state is constructed *a posteriori*.

Here, we follow a conceptually different approach. Motivated by the possibility to study FQH physics in optical lattice experiments realizing the Hofstadter-Bose-Hubbard model, we derive a trial state for the ground state of this specific Hamiltonian. This philosophy is similar to the approaches pursued in the early days of FQH physics to find trial states for the observed plateaus in the Hall resistance, starting from a well-known Hamiltonian and ending up with an approximate ground state wave function for this Hamiltonian, most prominently realized in Laughlin's wave functions at $\nu = {}^1\!/\!{}_m$ [26].

A particularly fruitful source of continuum trial wave functions has been Jain's composite fermion construction, where $m \in \mathbb{Z}$ flux quanta are attached to the original particles, turning them into composite fermions (CFs) in an effective magnetic field [60]. By using CFs, it is not only possible to recover the familiar Laughlin states at $\nu = {}^1\!/\!{}_m$, but also many other states, including hierarchy states [61] at $\nu = {}^p\!/\!{}_{(mp\pm1)}$ with $p \in \mathbb{N}$, and, by forming bound states of CFs, even more exotic states like Moore and Read's Pfaffian state [62] or Read and Rezayi's parafermion states [169]. CF trial states not only give an intuitive understanding of the microscopic nature of various FQH states, but also provide extraordinarily reliable predictions to compare them to exact ground states in numerical simulations [57].

Inspired by the successes of the continuum CF approach, we perform a similar construction on the square lattice, noting that our approach could be generalized to other lattice geometries as well. In particular, we turn hard-core bosons into composite fermions by attaching a single flux quantum to the bosons and derive an effective Hamiltonian for the composite fermions coupled to a dynamical gauge field. To benchmark our findings, we compare different variational ansätze and their variational energies to (quasi-)exact numerical results. We anticipate the preliminary results presented here to provide a promising starting point for further variational studies and related investigations of lattice analogs of FQH systems.

This chapter is structured as follows: In Sec. 6.2 we briefly review the continuum CF construction with a special emphasis on the flux attachment procedure. Afterwards, in Sec. 6.3, we adapt this approach to the square lattice, for which we also propose several trial states and benchmark their variational energies. In Sec. 6.4 we summarize our findings and discuss potential next steps for improving and using the trial states found here.

6.2. Composite Fermion Theory in the Continuum

Historically, the observation of the FQH effect by Tsui *et al.* [13] marked the beginning of a new era in the study of strongly correlated many-body systems. While the integer quantum Hall effect can be understood in terms of essentially non-interacting fermions, the situation is more involved at fractional filling factors. Early on, it has become clear that interactions have to play a crucial role in understanding the FQH effect. However, the paradigm of using weakly interacting emergent degrees of freedom to describe interacting many-body systems is ubiquitous in condensed matter physics and there is reason to believe that such a description also exists for the FQH problem.

Indeed, among a few other approaches, Jain developed what is now known as the composite fermion (CF) picture of the (electronic) FQH effect [60], based on earlier ideas by Read [251] and Zhang, Hansson, and Kivelson [252]. The scheme was later extended further to also describe bosonic systems [101, 102].

We will discuss the foundations of the CF picture below, closely following the presentation in Refs. [57, 60].

6.2.1. Qualitative Picture of the Composite Fermion Theory

Consider particles subject to a magnetic field with flux density B, such that the magnetic filling factor is $\nu = {}^{\rho}\!/\!_{(B/\phi_0)}$, where ρ is the particle density and $\phi_0 = {}^{hc}\!/\!_{e}$ is the magnetic flux quantum.[1] An integer number m of flux quanta from the original flux B is attached to the particles such that the composite particles obey fermionic statistics, i.e. for bosons (fermions) m has to be odd (even). While the details are not fully resolved yet, the flux attachment is believed to be a result of the repulsive interaction between the particles, and the composita are the anticipated composite fermions, ^{m}CFs. Next, the remaining magnetic flux is adiabatically spread out over the entire system, which is *assumed* to not close the gap along the process.[2] The ^{m}CFs experience a reduced magnetic flux $B^\star = B - m\phi_0\rho$ and hence exhibit magnetic filling factor $\nu^\star = {}^{\rho}\!/\!_{(B^\star/\phi_0)}$. For certain choices of ν and m the magnetic filling factor of the CFs takes integer values, $\nu^\star = p \in \mathbb{N}$, such that the CFs form an integer quantum Hall state. For these choices, the filling factor of the *original* particles is given by

$$\nu = \frac{\rho}{{}^{B}\!/\!_{\phi_0}} = \frac{\rho}{{}^{B^\star}\!/\!_{\phi_0} + m\rho} = \frac{\nu^\star}{1 + m\nu^\star} = \frac{p}{mp+1}, \tag{6.1}$$

which is commonly known as the *Jain sequence* of quantum Hall fractions.

Note that for fermions with even m the denominator of this fraction is always odd. Moreover, for $p = 1$ we recover the fractions $\nu = {}^{1}\!/\!_{m}$ of the Laughlin states.

To summarize, the qualitative picture behind the composite fermion approach is as follows:

1. The original particles experience a strong magnetic field such that the magnetic filling factor is $\nu = \frac{p}{mp+1}$ (Fig. 6.1**(a)**).

---

[1] From now on, we will use natural units where $\hbar = c = e = 1$.

[2] Note that this is indeed a non-trivial assumption! The energy spectrum will certainly change during the spreading of the flux, the necessary assumption is that the ground state remains gapped.

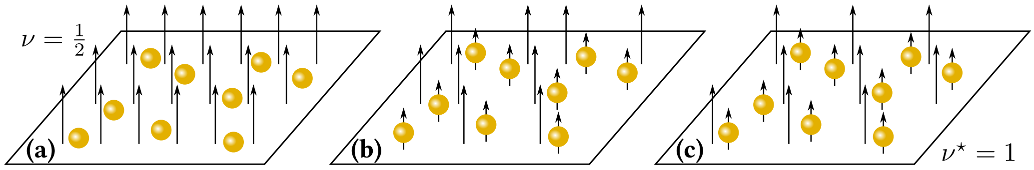

Fig. 6.1. Visualization of the composite fermion construction for the case of bosons at $\nu = 1/2$ **(a)**. In this case, one flux quantum is attached to each boson, resulting at first in an inhomogeneous magnetic field from the remaining flux quanta **(b)**. This magnetic field is smeared out, resulting in composite fermions at $\nu^\star = 1$, which can now form an integer quantum Hall state **(c)**.

2. Repulsive interactions lead to the attachment of m flux quanta to the original particles, resulting in weakly interacting ^{m}CFs (Fig. 6.1**(b)**).
3. The remaining magnetic flux is smeared out over the entire system such that the CFs experience a homogeneous reduced magnetic flux $B^\star = B - m\phi_0\rho$, resulting in an integer quantum Hall state of the CFs at filling factor $\nu^\star = p$ (Fig. 6.1**(c)**).

An important, yet non-trivial, step in this model is the smearing out of the remaining flux after attaching some of the flux quanta, which can be understood as a type of mean-field approximation.

6.2.2. Constructing Trial Wave Functions with the Composite Fermion Theory

Having introduced the general philosophy of the CF theory, we will now use it to motivate certain wave functions from the CF picture. We would like to stress that this is not a rigorous derivation. On the contrary, we *postulate* trial wave functions for the FQH state based on physical intuition about the CFs. These trial wave functions have been used in the literature extensively and many of the resulting predictions have been verified numerically. For further details we refer the interested reader to Chapter 6 of Jain's book on composite fermions [57].

Consider ^{m}CFs experiencing a uniform magnetic field $B^\star$. The vector potential describing the attached flux quanta is given by

$$\mathbf{a}(\mathbf{r}_k) = \frac{m\phi_0}{2\pi}\sum_{j\neq k}\nabla_{\mathbf{r}_k}\theta_{kj} \qquad \text{with} \qquad \theta_{jk} = i\log\frac{z_j - z_k}{|z_j - z_k|} = -\arg\left(z_j - z_k\right), \tag{6.2}$$

where j, k label the particles. Therefore, the first-quantized Hamiltonian for the underlying particles after neglecting the interactions[3] reads

$$\hat{\mathcal{H}} = \frac{1}{2M}\sum_i\left(\hat{\mathbf{p}}_i + \mathbf{A}^\star\left(\hat{\mathbf{r}}_i\right) + \mathbf{a}\left(\hat{\mathbf{r}}_i\right)\right)^2, \tag{6.3}$$

where $\mathbf{A}^\star$ generates the magnetic field $B^\star$ and M is the mass of the particles. Our goal is to find the ground state Ψ of this Hamiltonian and its ground state energy E_0,

$$\hat{\mathcal{H}}\Psi = E_0\Psi. \tag{6.4}$$

We eliminate the attached flux by performing the singular gauge transformation

$$\Psi = \Phi^{\mathrm{CF}}\mathrm{e}^{-im\sum_{j<k}\theta_{jk}} = \Phi^{\mathrm{CF}}\prod_{j<k}\left(\frac{z_j - z_k}{|z_j - z_k|}\right)^m, \tag{6.5}$$

---

[3] Here, we assumed that the main effect of the interactions is to realize the flux attachment and therefore neglect them once we have achieved this.

and end up with the Schrödinger equation for non-interacting composite fermions at $\nu^\star = p \in \mathbb{N}$,

$$\frac{1}{2M}\sum_i \left(\hat{\mathbf{p}}_i + \mathbf{A}^\star\left(\hat{\mathbf{r}}_i\right)\right)^2 \Phi^{\mathrm{CF}} = E\Phi^{\mathrm{CF}}, \tag{6.6}$$

the solution to which are the familiar integer quantum Hall states Φ_p^{CF}. Therefore, we arrive at the trial state

$$\Psi_\nu(B) = \Phi_p^{\mathrm{CF}}(B^\star)\prod_{j<k}\left(\frac{z_j - z_k}{|z_j - z_k|}\right)^m. \tag{6.7}$$

While hinting in the right direction, this trial wave function is not a good candidate yet as it has the same probability amplitude as the uncorrelated Φ_p^{CF} and does not encode the correlations which make the FQH states exciting. Furthermore, our trial state does not match the very successful Laughlin wave functions at $\nu = {}^1/_{(m+1)}$,

$$\Psi_{\mathrm{LN}}(B) = \Phi_1(B)\prod_{j<k}\left(z_j - z_k\right)^m. \tag{6.8}$$

However, this provides us with the necessary guidance to arrive at a promising candidate, where we remove the denominators $|z_j - z_k|$ and evaluate the integer quantum Hall wave function at B instead of $B^\star$. Thus, we end up with the final trial wave function

$$\Psi_\nu(B) = \Phi_p(B)\prod_{j<k}\left(z_j - z_k\right)^m, \tag{6.9}$$

which can be improved further by projecting it to the lowest Landau level [60].

Before concluding our discussion of the continuum CF theory, we would like to briefly comment on the *ad hoc* change to the wave function done here. The original trial state includes factors of $\prod_{j<k}\left(\frac{z_j - z_k}{|z_j - z_k|}\right)^m$, which correspond to the attachment of m *flux tubes* to each electron. In contrast, the Jastrow factor $\prod_{j<k}\left(z_j - z_k\right)^m$ describes a state where each particles sees m *vortices* on all other particles. Physically speaking, we assume that during the adiabatic spreading of the magnetic flux the attached flux tubes are transformed into vortices. This at the same time makes it necessary to change the magnetic field entering the non-interacting $\Phi_1(B)$.

6.3. Composite Fermion Theory on a Lattice

We now turn towards lattice systems and try to adapt the CF construction accordingly. We consider hard-core bosons on a two-dimensional square lattice subject to a perpendicular magnetic field. Instead of assuming a static magnetic field as in the earlier chapters of this thesis, we promote it to a dynamical degree of freedom, thus ending up with the Hamiltonian

$$\hat{\mathcal{H}} = -t\sum_{\langle ij\rangle}\hat{a}_i^\dagger \mathrm{e}^{i\hat{\varphi}_{\langle ij\rangle}}\hat{a}_j + \mathrm{H.c.}, \tag{6.10}$$

where $\hat{a}_i^{(\dagger)}$ annihilates (creates) a boson at lattice site i, $\hat{\varphi}_{\langle ij\rangle}$ denotes the dynamical gauge degree of freedom on the *directed* link connecting the sites i and j, and the sum is over links between nearest neighboring sites.[4]

---

[4] We remark that Eq. (6.10) is a $\mathrm{U}(1)$ lattice gauge theory, however we will not go into further detail regarding this exciting field of research here.

6.3.1. Lattice Composite Fermions

Similar to earlier constructions for lattice anyons [253, 254], we define new operators

$$\hat{f}_i := \mathrm{e}^{i\hat{\phi}_i}\hat{a}_i, \qquad \hat{\phi}_i = \pi \sum_{l \neq i} \Theta(i, p_l)\hat{n}_l, \tag{6.11}$$

where $\hat{n}_l = \hat{a}_l^\dagger \hat{a}_l = \hat{f}_l^\dagger \hat{f}_l$ is the number operator at site l, p_l denotes the plaquette to the upper right of l, and $\Theta(i, p_l)$ is an arbitrary, real function of a lattice site and a plaquette. For a generic function Θ, the prefactor $\mathrm{e}^{i\hat{\phi}_i}$ acts on all lattice sites except the site i and is in particular *not* local in the usual sense. For different sites $i \neq j$, we use the identity

$$\mathrm{e}^{i\hat{\phi}_i}\hat{a}_j^\dagger = \mathrm{e}^{i\pi\Theta(i,p_j)}\hat{a}_j^\dagger \mathrm{e}^{i\hat{\phi}_i} \tag{6.12}$$

to obtain the commutation properties of the $\hat{f}$-operators,

$$\hat{f}_i\hat{f}_j^\dagger = \delta_{ij}\left(1 - 2\hat{n}_i\right) + \mathrm{e}^{i\pi(\Theta(i,p_j) - \Theta(j,p_i))}\hat{f}_j^\dagger \hat{f}_i \qquad \forall i, j, \tag{6.13}$$

where the first term is a result of the hard-core bosonic commutation relation

$$\left[\hat{a}_i, \hat{a}_j^\dagger\right] = \delta_{ij}\left(1 - 2\hat{n}_i\right). \tag{6.14}$$

We require the function Θ to satisfy the constraint

$$\Theta(i, p_j) - \Theta(j, p_i) = 1 \mod 2 \qquad \forall i \neq j \tag{6.15}$$

and arrive at the identity

$$\hat{f}_i\hat{f}_j^\dagger = \begin{cases} 1 - \hat{f}_i^\dagger \hat{f}_i & \text{for } i = j, \\ -\hat{f}_j^\dagger \hat{f}_i & \text{for } i \neq j \end{cases} \qquad \Leftrightarrow \qquad \left\{\hat{f}_i, \hat{f}_j^\dagger\right\} = \delta_{ij}. \tag{6.16}$$

Furthermore, using the hard-core property of the initial bosons $\hat{a}_i$ we find

$$\left\{\hat{f}_i, \hat{f}_j\right\} = \left\{\hat{f}_i^\dagger, \hat{f}_j^\dagger\right\} = 0, \tag{6.17}$$

which complete the fermionic anti-commutation algebra. Therefore, we interpret the f-particles as lattice composite fermions from now on, taking the role of the composite fermions in the continuum. In particular, the operator $\hat{\phi}_i$ can be interpreted as creating a flux solenoid which is attached to an original boson to create a CF. Other composite particles can be obtained by generalizing Eq. (6.11) to

$$\hat{f}_i^{(m)} := \mathrm{e}^{i\hat{\phi}_i^{(m)}}\hat{a}_i, \qquad \hat{\phi}_i^{(m)} = \pi m \sum_{l \neq i} \Theta(i, p_l)\hat{n}_l, \tag{6.18}$$

resulting in m flux quanta being attached to the initial particles and the f-particles having statistical angle πm. In particular, even (odd) m results in the f-particles being composite bosons (fermions) as in the continuum CF construction. Note that in all cases the attached flux explicitly depends on the density everywhere else on the lattice and hence this construction is clearly non-local.

Equipped with these results we can now rewrite the bosonic Hamiltonian in Eq. (6.10) in terms of the new fermionic operators. As the phase operators $\hat{\varphi}$ commute with the bosonic operators, they also commute with the fermionic operators and we can write

$$\hat{\mathcal{H}} = -t \sum_{\langle ij \rangle} \hat{f}_i^\dagger \mathrm{e}^{i\left(\hat{\varphi}_{\langle ij \rangle} + \delta\hat{\varphi}_{\langle ij \rangle}\right)} \hat{f}_j + \text{H.c.}, \tag{6.19}$$

where we defined

$$\delta\hat{\varphi}_{\langle ij\rangle} \coloneqq \hat{\phi}_i - \hat{\phi}_j = \pi \sum_{l\neq i,j} \left(\Theta\left(i,p_l\right) - \Theta\left(j,p_l\right)\right)\hat{n}_l + \pi\Theta(i,p_j)\hat{n}_j - \pi\Theta(j,p_i)\hat{n}_i. \tag{6.20}$$

For the hard-core particles at hand, we can drop the last two terms in this expression as they do not contribute to the Hamiltonian on the physical Hilbert space. Therefore, we end up with the somewhat simpler expression

$$\delta\hat{\varphi}_{\langle ij\rangle} \coloneqq \hat{\phi}_i - \hat{\phi}_j = \pi \sum_{l\neq i,j} \left(\Theta\left(i,p_l\right) - \Theta\left(j,p_l\right)\right)\hat{n}_l. \tag{6.21}$$

Next, we choose an arbitrary reference axis on the lattice and denote the position of the lattice site j by $z_j = x_j + iy_j$. Furthermore, we choose the function Θ to be

$$\Theta(i,p_j) = \frac{1}{\pi}\arg(z_i - z_j), \tag{6.22}$$

which is consistent with the assumption

$$\Theta(i,p_j) - \Theta(j,p_i) = \frac{1}{\pi}\left(\arg(z_i - z_j) - \arg(z_j - z_i)\right) = 1 \mod 2 \tag{6.23}$$

made above. Thus, we arrive at

$$\hat{f}_i = \mathrm{e}^{i\hat{\phi}_i}\hat{a}_i, \qquad \hat{\phi}_i = \sum_{l\neq i} \arg\left(z_i - z_l\right)\hat{n}_l, \tag{6.24}$$

which can be rewritten as

$$\hat{f}_i = \mathrm{e}^{\sum_{l\neq i}\log\left(\frac{z_i - z_l}{|z_i - z_l|}\right)\hat{n}_l}\hat{a}_i = \left(\prod_{l\neq i}\left(\frac{z_i - z_l}{|z_i - z_l|}\right)^{\hat{n}_l}\right)\hat{a}_i = \left(\prod_{l}\left(\frac{z_i - z_l}{|z_i - z_l|}\right)^{\hat{n}_l}\right)\hat{a}_i. \tag{6.25}$$

This form proves useful when studying correlations between the composite fermions and related composite particles [7]. For our current purposes, we do not follow this line of research further, but instead investigate the Hamiltonian in Eq. (6.10) and its ground state properties. To this end, we next rewrite the Hamiltonian as

$$\hat{\mathcal{H}} = -t\sum_{\langle ij\rangle} \hat{f}_i^\dagger \mathrm{e}^{i\left(\hat{\varphi}_{\langle ij\rangle} + \delta\hat{\varphi}_{\langle ij\rangle}\right)}\hat{f}_j + \mathrm{H.c.}, \quad \text{with} \quad \delta\hat{\varphi}_{\langle ij\rangle} = \sum_{l\neq i,j}\arg\left(\frac{z_i - z_l}{z_j - z_l}\right)\hat{n}_l, \tag{6.26}$$

6.3.2. Coupling the Gauge and Matter Sectors

So far, we focused on the matter sector and transmuted the hard-core bosons into composite fermions. However, to obtain non-trivial correlations between the matter sector and the gauge field we may perform another unitary transformation which acts on both sectors. To this end, we first introduce bosonic ladder operators $\hat{b}^{(\dagger)}_{\langle ij\rangle}$ for the gauge degrees of freedom satisfying

$$\hat{\varphi}_{\langle ij\rangle} = \hat{b}^\dagger_{\langle ij\rangle} + \hat{b}_{\langle ij\rangle}. \tag{6.27}$$

Next, we define a set of link-*dependent* transformations

$$\hat{U}_{\langle ij\rangle} = \exp\left[\frac{\delta\hat{\varphi}_{\langle ij\rangle}}{2}\left(\hat{b}^\dagger_{\langle ij\rangle} - \hat{b}_{\langle ij\rangle}\right)\right] \tag{6.28}$$

acting on the gauge fields as

$$\hat{U}^\dagger_{\langle ij\rangle}\hat{\varphi}_{\langle ij\rangle}\hat{U}_{\langle ij\rangle} = \hat{\varphi}_{\langle ij\rangle} + \delta\hat{\varphi}_{\langle ij\rangle}, \tag{6.29}$$

where the last term depends on the densities $\hat{n}_k$ and hence connects the gauge field and the matter. Multiplying all the commuting, link-dependent transformations we can define the link-*independent* unitary transformation

$$\hat{\mathcal{U}} := \prod_{\langle ij\rangle} \hat{U}_{\langle ij\rangle}, \tag{6.30}$$

still resulting in

$$\hat{\mathcal{U}}^\dagger\hat{\varphi}_{\langle ij\rangle}\hat{\mathcal{U}} = \hat{\varphi}_{\langle ij\rangle} + \delta\hat{\varphi}_{\langle ij\rangle}. \tag{6.31}$$

Thus, we can rewrite the Hamiltonian in Eq. (6.26) as

$$\hat{\mathcal{H}} = -t\sum_{\langle ij\rangle} \hat{f}^\dagger_i\hat{\mathcal{U}}^\dagger \mathrm{e}^{i\hat{\varphi}_{\langle ij\rangle}}\hat{\mathcal{U}}\hat{f}_j + \text{H.c.}. \tag{6.32}$$

We denote links on the lattice by Greek letters ($\mu = \langle\mu_1\mu_2\rangle$) and define anti-Hermitian operators

$$\hat{\mathcal{A}}_i := -\frac{1}{2}\sum_{\mu\not\ni i} \arg\left(\frac{z_{\mu_1}-z_i}{z_{\mu_2}-z_i}\right)\left(\hat{b}^\dagger_\mu - \hat{b}_\mu\right). \tag{6.33}$$

We find

$$\hat{\mathcal{U}}\hat{f}_j = \mathrm{e}^{\hat{\mathcal{A}}_j}\hat{f}_j\hat{\mathcal{U}} \qquad \text{and} \qquad \hat{f}^\dagger_i\hat{\mathcal{U}}^\dagger = \hat{\mathcal{U}}^\dagger\hat{f}^\dagger_i\mathrm{e}^{-\hat{\mathcal{A}}_i}, \tag{6.34}$$

which we use to rewrite the fermionic Hamiltonian as

$$\hat{\mathcal{H}} = \hat{\mathcal{U}}^\dagger\hat{\hat{\mathcal{H}}}\hat{\mathcal{U}} \quad \text{with} \quad \hat{\hat{\mathcal{H}}} = -t\sum_{\langle ij\rangle}\hat{f}^\dagger_i\mathrm{e}^{-\hat{\mathcal{A}}_i}\mathrm{e}^{i\hat{\varphi}_{\langle ij\rangle}}\mathrm{e}^{\hat{\mathcal{A}}_j}\hat{f}_j + \text{H.c.}. \tag{6.35}$$

This transformed version of the original hard-core bosonic Hamiltonian in Eq. (6.10) serves as our starting point for a variational analysis of the ground state.

Effective Magnetic Flux

Having found an amenable Hamiltonian for the fermionic degrees of freedom, we briefly discuss the (effective) magnetic flux experienced by the CFs. We consider a CF hopping around a plaquette p, described by the expression

$$\hat{f}^\dagger_1\mathrm{e}^{-\hat{\mathcal{A}}_1}\mathrm{e}^{i\hat{\varphi}_{\langle 14\rangle}}\mathrm{e}^{\hat{\mathcal{A}}_4}\hat{f}_4\hat{f}^\dagger_4\mathrm{e}^{-\hat{\mathcal{A}}_4}\mathrm{e}^{i\hat{\varphi}_{\langle 43\rangle}}\mathrm{e}^{\hat{\mathcal{A}}_3}\hat{f}_3\hat{f}^\dagger_3\mathrm{e}^{-\hat{\mathcal{A}}_3}\mathrm{e}^{i\hat{\varphi}_{\langle 32\rangle}}\mathrm{e}^{\hat{\mathcal{A}}_2}\hat{f}_2\hat{f}^\dagger_2\mathrm{e}^{-\hat{\mathcal{A}}_2}\mathrm{e}^{i\hat{\varphi}_{\langle 21\rangle}}\mathrm{e}^{\hat{\mathcal{A}}_1}\hat{f}_1, \tag{6.36}$$

where $1,\ldots,4$ denote the lattice sites around the plaquette in counter-clockwise manner. Introducing the notation

$$\delta(k\notin\lambda) = \begin{cases} 1 & \text{for } k\notin\lambda \\ 0 & \text{for } k\in\lambda \end{cases} \tag{6.37}$$

and using the commutator

$$\left[\hat{\varphi}_\lambda, \hat{\mathcal{A}}_k\right] = -\delta(k\notin\lambda)\arg\left(\frac{z_{\lambda_1}-z_k}{z_{\lambda_2}-z_k}\right), \tag{6.38}$$

we find that this expression is equivalent to the more compact

$$\hat{f}^\dagger_1\hat{f}_2\hat{f}^\dagger_2\hat{f}_3\hat{f}^\dagger_3\hat{f}_4\hat{f}^\dagger_4\hat{f}_1\mathrm{e}^{i\left(\sum_{\mu\in\partial p}\hat{\varphi}_\mu - \arg\left(\frac{z_2-z_1}{z_3-z_1}\right) - \arg\left(\frac{z_3-z_1}{z_4-z_1}\right)\right)}. \tag{6.39}$$

Next, we use the discrete rotational and translational symmetries of the model to simplify the $\arg$-term and abbreviate the terms in the exponentials to find for the hopping around a plaquette

$$\hat{f}_1^\dagger \dots \hat{f}_1 \mathrm{e}^{i\left(\sum_{\mu\in\partial p}\hat{\varphi}_\mu + \frac{\pi}{2}\right)}. \tag{6.40}$$

We conclude that the effective magnetic flux per plaquette experienced by the CFs is given by $\sum_{\mu\in\partial p}\hat{\varphi}_\mu + \frac{\pi}{2}$. Intuitively speaking, the CF not only feels the magnetic flux from the original gauge field ($\sum_\mu \hat{\varphi}_\mu$) but also an additional quarter flux quantum ($+\frac{\pi}{2}$). This additional flux quantum is exactly the one carried by the CF itself: As the flux pierces the system through the plaquettes, the “flux tube” attached to the original boson at a specific site is spread out over the four plaquettes around this site. Therefore, a composite fermion hopping around a plaquette effectively experiences an additional quarter flux quantum through the encircled plaquette.

Shifting the Attached Flux Quanta

In order to avoid the contribution from the flux carried by a CF itself, we may perform an additional (singular) gauge transformation such that the entire flux quantum pierces one single plaquette. To this end, we define the unitary transformation

$$\hat{\mathcal{V}} := \mathrm{e}^{\sum_i \hat{n}_i \sum_{\mu\ni i}\vartheta_{i,\mu}\left(\hat{b}_\mu^\dagger - \hat{b}_\mu\right)} \tag{6.41}$$

and apply it to the gauge field,

$$\hat{\mathcal{V}}^\dagger \hat{\varphi}_{\langle ij\rangle}\hat{\mathcal{V}} = \hat{\varphi}_{\langle ij\rangle} - 2\sum_{k=i,j}\hat{n}_k\vartheta_{k,\langle ij\rangle} \quad\Leftrightarrow\quad \hat{\varphi}_{\langle ij\rangle} = \hat{\mathcal{V}}^\dagger \hat{\varphi}_{\langle ij\rangle}\hat{\mathcal{V}} + 2\sum_{k=i,j}\hat{n}_k\vartheta_{k,\langle ij\rangle}. \tag{6.42}$$

Therefore, we can rewrite the Hamiltonian in Eq. (6.35) as

$$\begin{aligned}
\hat{\hat{\mathcal{H}}} &= -t\sum_{\langle ij\rangle}\hat{f}_i^\dagger \mathrm{e}^{-\hat{\mathcal{A}}_i}\hat{\mathcal{V}}^\dagger \mathrm{e}^{i\hat{\varphi}_{\langle ij\rangle}+2i\sum_{k=i,j}\hat{n}_k\vartheta_{k,\langle ij\rangle}}\hat{\mathcal{V}}\mathrm{e}^{\hat{\mathcal{A}}_j}\hat{f}_j + \text{H.c.} \\
&= -t\sum_{\langle ij\rangle}\hat{f}_i^\dagger \hat{\mathcal{V}}^\dagger \mathrm{e}^{-\hat{\mathcal{A}}_i}\mathrm{e}^{i\hat{\varphi}_{\langle ij\rangle}+2i\sum_{k=i,j}\hat{n}_k\vartheta_{k,\langle ij\rangle}}\mathrm{e}^{\hat{\mathcal{A}}_j}\hat{\mathcal{V}}\hat{f}_j + \text{H.c.} \\
&= -t\sum_{\langle ij\rangle}\hat{\mathcal{V}}^\dagger \hat{f}_i^\dagger \mathrm{e}^{-\hat{\hat{\mathcal{A}}}_i}\mathrm{e}^{i\hat{\hat{\varphi}}_{\langle ij\rangle}}\mathrm{e}^{\hat{\hat{\mathcal{A}}}_j}\hat{f}_j\hat{\mathcal{V}} + \text{H.c.},
\end{aligned} \tag{6.43}$$

where we used

$$\hat{\mathcal{V}}\hat{f}_k = \mathrm{e}^{-\sum_{\mu\ni k}\vartheta_{k,\mu}\left(\hat{b}_\mu^\dagger - \hat{b}_\mu\right)}\hat{f}_k\hat{\mathcal{V}} \tag{6.44}$$

and defined

$$\hat{\hat{\mathcal{A}}}_k = \hat{\mathcal{A}}_k - \sum_{\mu\ni k}\vartheta_{k,\mu}\left(\hat{b}_\mu^\dagger - \hat{b}_\mu\right) \qquad \text{and} \qquad \hat{\hat{\varphi}}_\mu = \hat{\varphi}_\mu + 2\sum_{k\in\mu}\hat{n}_k\vartheta_{k,\mu}. \tag{6.45}$$

We remark that for physical states ($\hat{n}_j = 0, 1$) the density-dependent contribution to the phase $\hat{\hat{\varphi}}_{\langle ij\rangle}$ in the Hamiltonian drops out and therefore we arrive at the transformed Hamiltonian

$$\hat{\mathcal{H}}_{\mathcal{UV}} := -t\sum_{\langle ij\rangle}\hat{f}_i^\dagger \mathrm{e}^{-\hat{\hat{\mathcal{A}}}_i}\mathrm{e}^{i\hat{\varphi}_{\langle ij\rangle}}\mathrm{e}^{\hat{\hat{\mathcal{A}}}_j}\hat{f}_j + \text{H.c. such that } \hat{\mathcal{H}} = \hat{\mathcal{U}}^\dagger\hat{\hat{\mathcal{H}}}\hat{\mathcal{U}} = \left(\hat{\mathcal{U}}\hat{\mathcal{V}}\right)^\dagger \hat{\mathcal{H}}_{\mathcal{UV}}\left(\hat{\mathcal{U}}\hat{\mathcal{V}}\right). \tag{6.46}$$

Next, we perform a similar calculation as above to find the effective magnetic flux experienced by the fermions after this additional transformation. In particular, we use

$$\left[\hat{\varphi}_\lambda, \hat{\hat{\mathcal{A}}}_k\right] = -\delta(k\notin\lambda)\arg\left(\frac{z_{\lambda_1}-z_k}{z_{\lambda_2}-z_k}\right) - 2\delta(k\in\lambda)\vartheta_{k,\lambda} \tag{6.47}$$

to obtain

$$\begin{aligned}
&\hat{f}_1^\dagger \mathrm{e}^{-\hat{\tilde{\mathcal{A}}}_1} \mathrm{e}^{i\hat{\varphi}_{\langle 14\rangle}} \mathrm{e}^{\hat{\tilde{\mathcal{A}}}_4} \hat{f}_4 \hat{f}_4^\dagger \mathrm{e}^{-\hat{\tilde{\mathcal{A}}}_4} \mathrm{e}^{i\hat{\varphi}_{\langle 43\rangle}} \mathrm{e}^{\hat{\tilde{\mathcal{A}}}_3} \hat{f}_3 \hat{f}_3^\dagger \mathrm{e}^{-\hat{\tilde{\mathcal{A}}}_3} \mathrm{e}^{i\hat{\varphi}_{\langle 32\rangle}} \mathrm{e}^{\hat{\tilde{\mathcal{A}}}_2} \hat{f}_2 \hat{f}_2^\dagger \mathrm{e}^{-\hat{\tilde{\mathcal{A}}}_2} \mathrm{e}^{i\hat{\varphi}_{\langle 21\rangle}} \mathrm{e}^{\hat{\tilde{\mathcal{A}}}_1} \hat{f}_1 \\
&= \hat{f}_1^\dagger \dots \hat{f}_1 \mathrm{e}^{i\left(\sum_{\mu\in\partial p} \hat{\varphi}_\mu + \sum_{\mu\in\partial p}\left(-\delta(1\notin\mu)\arg\left(\frac{z_{\mu_1}-z_1}{z_{\mu_2}-z_1}\right) - 2\delta(1\in\mu)\vartheta_{1,\mu}\right)\right)} \qquad (6.48) \\
&= \hat{f}_1^\dagger \dots \hat{f}_1 \mathrm{e}^{i\left(\sum_{\mu\in\partial p} \hat{\varphi}_\mu + \frac{\pi}{2} - 2\vartheta_{1,\langle 12\rangle} - 2\vartheta_{1,\langle 41\rangle}\right)}.
\end{aligned}$$

We conclude that after the additional gauge transformation the effective flux experienced by the composite fermions is given by the expression

$$\hat{\tilde{\Phi}} = \sum_{\mu\in\partial p} \hat{\varphi}_\mu + \frac{\pi}{2} - 2\vartheta_{1,\langle 12\rangle} - 2\vartheta_{1,\langle 41\rangle}. \tag{6.49}$$

The main advantage of this expression over the one without the transformation $\hat{\mathcal{V}}$ is that it allows us to adjust the parameters $\vartheta_{i,\mu}$ as desired. We use this freedom to choose a specific set of parameters:

$$\vartheta_{i,\mu} = \begin{cases} -\frac{3\pi}{8} & \text{for } \mu = \langle i, i+x\rangle \\ -\frac{5\pi}{8} & \text{for } \mu = \langle i, i+y\rangle \\ \frac{7\pi}{8} & \text{for } \mu = \langle i-x, i\rangle \\ \frac{\pi}{8} & \text{for } \mu = \langle i-y, i\rangle \\ 0 & \text{otherwise} \end{cases} \qquad \text{and} \qquad \vartheta_{i,\langle\mu_1,\mu_2\rangle} = -\vartheta_{i,\langle\mu_2,\mu_1\rangle}. \tag{6.50}$$

With this choice, the effective flux reads

$$\hat{\tilde{\Phi}} = \sum_{\mu\in\partial p} \hat{\varphi}_\mu \mod 2\pi, \tag{6.51}$$

independent of the starting site for the hopping process around the plaquette. While our choice of $\vartheta_{i,\mu}$ breaks the translational invariance of the model, will find the particularly simple form of the effective flux in this gauge to be useful below.

6.3.3. Reduced Magnetic Flux for the Composite Fermions on Mean-Field Level

So far, all manipulations were exact and no approximations were made. To proceed further, we will use a variational mean-field approach based on a product ansatz in the transformed basis. To this end, we transform the (unknown) exact ground state $|\Psi\rangle$ of the fermionic Hamiltonian in Eq. (6.46) to a new basis, $|\tilde{\Psi}\rangle = \hat{\mathcal{V}}\hat{\mathcal{U}}\,|\Psi\rangle$. In this basis, we assume the state to be a product state of the fermionic and the bosonic degrees of freedom, i.e.

$$|\tilde{\Psi}\rangle = |\tilde{\psi}_f\rangle \otimes |\tilde{\varphi}_b\rangle\,. \tag{6.52}$$

Later on, this product form will allow us to treat the fermionic sector separately, in analogy with the continuum CF approach. Choosing specific ansätze for the two sectors we may then perform a variational minimization of the energy functional

$$E\left[\tilde{\psi}_f, \tilde{\varphi}_b\right] := \frac{\langle\Psi|\,\hat{\mathcal{H}}\,|\Psi\rangle}{\langle\Psi|\Psi\rangle} = \frac{\langle\tilde{\Psi}|\,\hat{\mathcal{H}}_{\mathcal{U}\mathcal{V}}\,|\tilde{\Psi}\rangle}{\langle\tilde{\Psi}|\tilde{\Psi}\rangle}. \tag{6.53}$$

Inspired by the external magnetic field with flux $2\pi\alpha$ per plaquette in similar calculations, we enforce a mean-field level flux constraint,

$$2\pi\alpha \overset{!}{=} \langle\Psi|\sum_{\mu\in\partial p}\hat{\varphi}_\mu|\Psi\rangle \qquad \forall p, \tag{6.54}$$

to obtain

$$\begin{aligned}
2\pi\alpha &\overset{!}{=} \sum_{\mu\in\partial p} \langle\tilde{\Psi}|\hat{\mathcal{V}}\hat{\mathcal{U}}\hat{\varphi}_\mu\hat{\mathcal{U}}^\dagger\hat{\mathcal{V}}^\dagger|\tilde{\Psi}\rangle \\
&= \sum_{\mu\in\partial p} \langle\tilde{\Psi}|\left(\hat{\mathcal{V}}\hat{\varphi}_\mu\hat{\mathcal{V}}^\dagger - \delta\hat{\varphi}_\mu\right)|\tilde{\Psi}\rangle \\
&= \sum_{\mu\in\partial p} \langle\tilde{\Psi}|\left(\hat{\varphi}_\mu + 2\sum_{k\in\mu}\hat{n}_k\vartheta_{k,\mu} - \delta\hat{\varphi}_\mu\right)|\tilde{\Psi}\rangle \\
&= \langle\tilde{\Psi}|\hat{\tilde{\Phi}}|\tilde{\Psi}\rangle + 2\sum_{\mu\in\partial p}\sum_{k\in\mu}\langle\tilde{\Psi}|\hat{n}_k|\tilde{\Psi}\rangle\,\vartheta_{k,\mu} - \sum_{\mu\in\partial p}\sum_{k\notin\mu}\arg\left(\frac{z_{\mu_1}-z_k}{z_{\mu_2}-z_k}\right)\langle\tilde{\Psi}|\hat{n}_k|\tilde{\Psi}\rangle\,.
\end{aligned} \tag{6.55}$$

Assuming a homogeneous mean-field density $\bar{n} = \langle\tilde{\Psi}|\hat{n}_k|\tilde{\Psi}\rangle$ for the fermions (and equivalently for the initial hard-core bosons) this equation can be rewritten as

$$2\pi\alpha = \langle\tilde{\Psi}|\hat{\tilde{\Phi}}|\tilde{\Psi}\rangle + 2\bar{n}\sum_{\mu\in\partial p}\sum_{k\in\mu}\vartheta_{k,\mu} - \bar{n}\sum_{\mu\in\partial p}\sum_{k\notin\mu}\arg\left(\frac{z_{\mu_1}-z_k}{z_{\mu_2}-z_k}\right). \tag{6.56}$$

The first term on the right hand side is the mean-field value of the effective flux $2\pi\alpha^\star$ experienced by the composite fermions, which we can now write as

$$2\pi\alpha^\star = 2\pi\alpha - 2\bar{n}\sum_{\mu\in\partial p}\sum_{k\in\mu}\vartheta_{k,\mu} + \bar{n}\sum_{\mu\in\partial p}\sum_{k\notin\mu}\arg\left(\frac{z_{\mu_1}-z_k}{z_{\mu_2}-z_k}\right). \tag{6.57}$$

For our choice of $\vartheta_{i,\mu}$ we find that $\vartheta_{\mu_1,\mu} + \vartheta_{\mu_2,\mu} = \pm\frac{\pi}{2}$ for μ parallel to $\pm\hat{\mathrm{e}}_x$ $(\mp\hat{\mathrm{e}}_y)$, respectively. Therefore, going around an entire plaquette, the contribution from the second term vanishes.

Also the last term on the right hand side can be simplified further. As the sum only depends on the relative positions of the lattice sites among each other, we can exploit the translational and rotational symmetries of the model and consider the plaquette enclosed by the sites $\{0, 1, 1+i, i\}$

in complex coordinates. We obtain

$$
\begin{aligned}
&\sum_{\mu\in\partial p}\sum_{k\notin\mu}\arg\left(\frac{z_{\mu_1}-z_k}{z_{\mu_2}-z_k}\right)\\
&=\sum_{z_k\neq 0,1}\arg\left(\frac{0-z_k}{1-z_k}\right)+\sum_{z_k\neq 1,1+i}\arg\left(\frac{1-z_k}{1+i-z_k}\right)\\
&\quad+\sum_{z_k\neq 1+i,i}\arg\left(\frac{1+i-z_k}{i-z_k}\right)+\sum_{z_k\neq i,0}\arg\left(\frac{i-z_k}{0-z_k}\right)\\
&=\sum_{k\notin\{0,1,1+i,i\}}\underbrace{\left(\arg\left(\frac{0-z_k}{1-z_k}\right)+\arg\left(\frac{1-z_k}{1+i-z_k}\right)+\arg\left(\frac{1+i-z_k}{i-z_k}\right)+\arg\left(\frac{i-z_k}{0-z_k}\right)\right)}_{=0}\\
&\quad+\arg\left(\frac{0-1-i}{1-1-i}\right)+\arg\left(\frac{0-i}{1-i}\right)+\arg\left(\frac{1-0}{1+i-0}\right)+\arg\left(\frac{1-i}{1+i-i}\right)\\
&\quad+\arg\left(\frac{1+i-0}{i-0}\right)+\arg\left(\frac{1+i-1}{i-1}\right)+\arg\left(\frac{i-1}{0-1}\right)+\arg\left(\frac{i-1-i}{0-1-i}\right)\\
&=\arg\left(1-i\right)+\arg\left(\frac{1}{1+i}\right)+\arg\left(\frac{1}{1+i}\right)+\arg\left(1-i\right)\\
&\quad+\arg\left(1-i\right)+\arg\left(\frac{1}{1+i}\right)+\arg\left(1-i\right)+\arg\left(\frac{1}{1+i}\right)\\
&=4\left(-\arg(1+i)+\arg(1-i)\right)=-2\pi.
\end{aligned}
\tag{6.58}
$$

We conclude that the effective magnetic flux experienced by the CFs on mean-field level is given by the strikingly simple expression

$$
2\pi\alpha^\star=2\pi\alpha-2\pi\bar{n}\qquad\Leftrightarrow\qquad\alpha^\star=\alpha-\bar{n}.\tag{6.59}
$$

As in the continuum approach [60], the effective magnetic flux experienced by the CFs is reduced compared to the external magnetic flux. Furthermore, this flux reduction is proportional to the density of the CFs and, equivalently, the original bosons. Therefore, we can express the magnetic filling factor ν of the original bosonic model in terms of the effective filling factor $\nu^\star=\bar{n}/\alpha^\star$ for the CFs,

$$
\nu=\frac{\bar{n}}{\alpha}=\frac{\bar{n}}{\alpha^\star+\bar{n}}=\frac{\nu^\star}{1+\nu^\star}\qquad\text{or conversely,}\qquad\nu^\star=\frac{\bar{n}}{\alpha^\star}=\frac{\bar{n}}{\alpha-\bar{n}}=\frac{\nu}{1-\nu}.\tag{6.60}
$$

This result agrees with the simplest bosonic Jain sequence in the continuum fractional quantum Hall effect [60]. In particular, bosons at filling factor $\nu=1/2$ result in CFs at $\nu^\star=1$, which might form an integer quantum Hall state if the effective Hamiltonian $\hat{\mathcal{H}}_{\mathcal{UV}}$ exhibits a topological lowest band.

Before studying some paradigmatic trial states, we briefly comment on the mean-field value of the bosonic degrees of freedom $|\tilde{\varphi}_b\rangle$ after applying the transformation $\mathcal{UV}$. To this end, we evaluate the expression $\langle\tilde{\tilde{\Psi}}|\hat{\hat{\Phi}}|\tilde{\Psi}\rangle$ to define the mean-field constraint

$$
2\pi\alpha^\star\overset{!}{=}\langle\tilde{\Psi}|\hat{\hat{\Phi}}|\tilde{\Psi}\rangle=\langle\tilde{\Psi}|\sum_{\mu\in\partial p}\hat{\varphi}_\mu|\tilde{\Psi}\rangle=\sum_{\mu\in\partial p}\langle\tilde{\varphi}_b|\hat{\varphi}_\mu|\tilde{\varphi}_b\rangle\tag{6.61}
$$

for the transformed gauge degrees of freedom.

6.3.4. Variational Trial States

Next, we use the general product ansatz in Eq. (6.52) for the ground state trial wave function to determine variational ground state energies for analytical trial states. In general, the variational ground state energy is given by

$$\begin{aligned} E\left[\tilde{\psi}_f, \tilde{\varphi}_b\right] &= \frac{\langle\tilde{\Psi}|\, \hat{\mathcal{H}}_{\mathcal{UV}}\, |\tilde{\Psi}\rangle}{\langle\tilde{\Psi}|\tilde{\Psi}\rangle} \\ &= -t \sum_{\langle ij\rangle} \frac{\langle\tilde{\Psi}|\, \hat{f}_i^\dagger \mathrm{e}^{-\hat{\tilde{\mathcal{A}}}_i} \mathrm{e}^{i\hat{\varphi}_{\langle ij\rangle}} \mathrm{e}^{\hat{\tilde{\mathcal{A}}}_j} \hat{f}_j\, |\tilde{\Psi}\rangle}{\langle\tilde{\Psi}|\tilde{\Psi}\rangle} + \text{c.c.} \\ &= -t \sum_{\langle ij\rangle} \frac{\langle\tilde{\psi}_f|\, \hat{f}_i^\dagger \hat{f}_j\, |\tilde{\psi}_f\rangle}{\langle\tilde{\psi}_f|\tilde{\psi}_f\rangle} \frac{\langle\tilde{\varphi}_b|\, \mathrm{e}^{-\hat{\tilde{\mathcal{A}}}_i} \mathrm{e}^{i\hat{\varphi}_{\langle ij\rangle}} \mathrm{e}^{\hat{\tilde{\mathcal{A}}}_j}\, |\tilde{\varphi}_b\rangle}{\langle\tilde{\varphi}_b|\tilde{\varphi}_b\rangle} + \text{c.c..} \end{aligned} \tag{6.62}$$

Below, we will consider specific ansätze to obtain variational energies.

Coherent State Ansatz

First, we consider a coherent state ansatz for the bosonic degrees of freedom,

$$|\tilde{\varphi}_b\rangle = \prod_\mu |\beta_\mu\rangle \qquad \text{with} \qquad \hat{b}_\mu\, |\beta_\mu\rangle = \beta_\mu\, |\beta_\mu\rangle\,, \tag{6.63}$$

where we assume real-valued $\beta_\mu \in \mathbb{R}$. The operators $\mathrm{e}^{\hat{\tilde{\mathcal{A}}}_k}$ act as displacement operators on the coherent states $|\beta_\mu\rangle$. Therefore, we can evaluate the bosonic expectation value analytically,

$$\begin{aligned} &\langle\tilde{\varphi}_b|\, \mathrm{e}^{-\hat{\tilde{\mathcal{A}}}_i} \mathrm{e}^{i\hat{\varphi}_{\langle ij\rangle}} \mathrm{e}^{\hat{\tilde{\mathcal{A}}}_j}\, |\tilde{\varphi}_b\rangle \\ &= \left(\left(\prod_\mu \langle\beta_\mu|\right) \mathrm{e}^{-\hat{\tilde{\mathcal{A}}}_i}\right) \mathrm{e}^{i\hat{\varphi}_{\langle ij\rangle}} \left(\mathrm{e}^{\hat{\tilde{\mathcal{A}}}_j} \left(\prod_\nu |\beta_\nu\rangle\right)\right) \\ &= \left(\prod_\mu \langle\beta_\mu - \delta\beta_\mu^{(i)}|\right) \mathrm{e}^{i\hat{\varphi}_{\langle ij\rangle}} \left(\prod_\nu |\beta_\nu - \delta\beta_\nu^{(j)}\rangle\right) \\ &= \left(\prod_{\mu\neq\langle ij\rangle} \langle\beta_\mu - \delta\beta_\mu^{(i)}|\beta_\mu - \delta\beta_\mu^{(j)}\rangle\right) \langle\beta_{\langle ij\rangle} - \delta\beta_{\langle ij\rangle}^{(i)}|\mathrm{e}^{i\hat{\varphi}_{\langle ij\rangle}}|\beta_{\langle ij\rangle} - \delta\beta_{\langle ij\rangle}^{(j)}\rangle\,, \end{aligned} \tag{6.64}$$

where we defined

$$\delta\beta_\eta^{(k)} := \frac{1}{2}\left(\delta(k \notin \eta) \arg\left(\frac{z_{\eta_1} - z_k}{z_{\eta_2} - z_k}\right) + 2\delta(k \in \eta)\vartheta_{k,\eta}\right). \tag{6.65}$$

Simplifying the coherent state overlaps further, we arrive at

$$\begin{aligned} \langle\tilde{\varphi}_b|\, \mathrm{e}^{-\hat{\tilde{\mathcal{A}}}_i} \mathrm{e}^{i\hat{\varphi}_{\langle ij\rangle}} \mathrm{e}^{\hat{\tilde{\mathcal{A}}}_j}\, |\tilde{\varphi}_b\rangle &= \mathrm{e}^{-\frac{1}{2}\left(1+\sum_\mu \left(\delta\beta_\mu^{(i)} - \delta\beta_\mu^{(j)}\right)^2\right)} \mathrm{e}^{i\left(2\beta_{\langle ij\rangle} - \left(\delta\beta_{\langle ij\rangle}^{(i)} + \delta\beta_{\langle ij\rangle}^{(j)}\right)\right)} \\ &= \mathrm{e}^{-\frac{1}{2}\left(1+\sum_\mu \left(\delta\beta_\mu^{(i)} - \delta\beta_\mu^{(j)}\right)^2\right)} \mathrm{e}^{i\left(2\beta_{\langle ij\rangle} - \vartheta_{i,\langle ij\rangle} - \vartheta_{j,\langle ij\rangle}\right)} \end{aligned} \tag{6.66}$$

and therefore the effective (free) fermion Hamiltonian

$$\hat{\mathcal{H}}_{\text{eff}}^{\text{cs}} = -\sum_{\langle ij\rangle} \tilde{t}_{\langle ij\rangle}^{\text{cs}} \mathrm{e}^{2i\beta_{\langle ij\rangle} - i\left(\vartheta_{i,\langle ij\rangle} + \vartheta_{j,\langle ij\rangle}\right)} \hat{f}_i^\dagger \hat{f}_j + \text{H.c.} \tag{6.67}$$

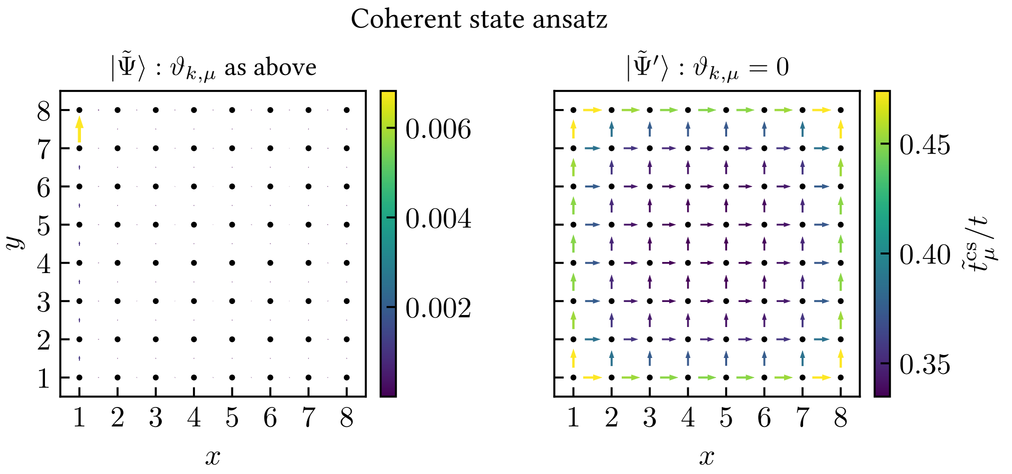

Fig. 6.2. Hopping amplitudes $\tilde{t}^{\text{cs}}_{\mu}$ in an 8×8-system for two choices of $\vartheta_{k,\mu}$ from the coherent state ansatz. Using the choice in Eq. (6.50) and hence the ansatz $|\tilde{\Psi}\rangle$, most of the hopping amplitudes essentially vanish and the remaining contribution is highly inhomogeneous (left panel). For vanishing $\vartheta_{k,\mu} = 0$, i.e. the variational ansatz $|\tilde{\Psi}'\rangle = \hat{\mathcal{V}}^\dagger\,|\tilde{\Psi}\rangle$, the hopping amplitudes are slightly increased towards the edge of the system while being almost constant in the bulk (right panel). The color, width, and length of the arrows indicate the hopping amplitude. Width and length are increased by a factor of 100 in the left panel for better visibility.

for the CFs, where we defined the effective hopping amplitudes

$$\tilde{t}^{\text{cs}}_{\langle ij\rangle} = t\mathrm{e}^{-\frac{1}{2}\left(1+\sum_{\mu}\left(\delta\beta_{\mu}^{(i)}-\delta\beta_{\mu}^{(j)}\right)^{2}\right)}. \tag{6.68}$$

In particular, we find that the CFs experience a reduced hopping amplitude $\tilde{t}^{\text{cs}}_{\langle ij\rangle}/t < 1$, independent of the choice of $\vartheta_{k,\mu}$. However, the exact value of the hopping amplitudes, is affected by the choice of $\vartheta_{k,\mu}$, where the choice in Eq. (6.50) results in essentially vanishing hopping amplitudes, see Fig. 6.2. Furthermore, in a finite system the hopping amplitudes become inhomogeneous. In any case, for a fermion hopping around a plaquette p the additional phases due to the $\vartheta_{k,\mu}$-terms in the Hamiltonian cancel, such that the composite fermion experiences a magnetic flux $2\sum_{\mu\in\partial p}\beta_\mu$ per plaquette. This can be avoided by considering the variational ansatz $|\tilde{\Psi}'\rangle = \mathcal{V}^\dagger\,|\tilde{\Psi}\rangle$, which removes the additional phases $\vartheta_{k,\mu}$ in the variational energy and the hopping elements.

While in principle an optimization of the coherent state ansatz $|\tilde{\varphi}_b\rangle = \prod_\mu |\beta_\mu\rangle$ could be undertaken numerically, we choose an approach relying on our physical intuition. On mean-field level the composite fermions experience the reduced magnetic flux $\alpha^\star = \alpha - \bar{n}$ per plaquette, see Eq. (6.61). We make a Landau gauge ansatz for the coherent states $|\beta_\mu\rangle$ by assuming

$$\beta_{\langle ij\rangle} = \begin{cases} 0 & \text{for } \langle ij\rangle = \mathbf{e}_x, \\ \pi\alpha^\star x_i & \text{for } \langle ij\rangle = \mathbf{e}_y. \end{cases} \tag{6.69}$$

Then the lowest energy state is the exactly known ground state of the non-interacting effective Hamiltonian

$$\hat{\mathcal{H}}^{\text{cs}}_{\text{eff}} = -\sum_{\langle ij\rangle}\tilde{t}^{\text{cs}}_{\langle ij\rangle}\mathrm{e}^{2i\beta_{\langle ij\rangle}-i\left(\vartheta_{i,\langle ij\rangle}+\vartheta_{j,\langle ij\rangle}\right)}\hat{f}_i^\dagger\hat{f}_j + \text{H.c.}. \tag{6.70}$$

The single-particle spectrum of this Hamiltonian is given in Fig. 6.3 for two choices of $\vartheta_{k,\mu}$. Accordingly, the variational energy of the N-particle state is given by the sum of the lowest

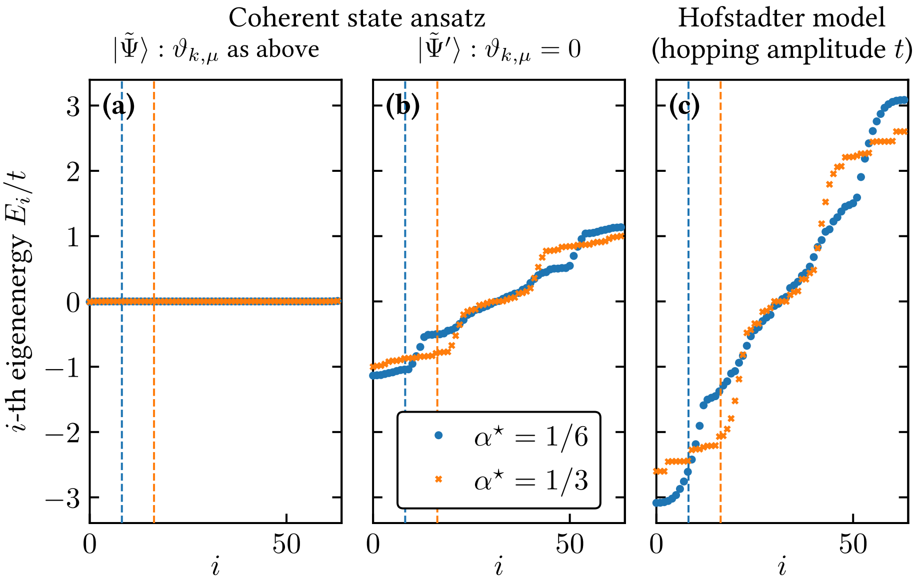

Fig. 6.3. Single-particle energy levels E_i of the effective composite fermion Hamiltonian $\hat{\mathcal{H}}_{\text{eff}}^{\text{cs}}$ Eq. (6.70) from the coherent state ansatz for different choices of $\vartheta_{k,\mu}$ **(a,b)** and a vanilla Hofstadter model at hopping amplitude t **(c)** for $L_x \times L_y = 10 \times 10$. The effective Hamiltonian for $\vartheta_{k,\mu} = 0$ exhibits separated flat bands similar to the Hofstadter spectrum. The dashed vertical lines separate the first $N_\phi = \alpha^\star (L_x - 1)(L_y - 1)$ states from the rest of the spectrum.

N single-particle energies. Here, we evaluate the variational energy for $N = 3$ particles on 6×6 sites and compare it to exact ground state energies of the Hofstadter-Bose-Hubbard model obtained via exact diagonalization. To this end, we consider the Hamiltonian in Eq. (6.10) and fix the link phases $\varphi_{\langle ij \rangle}$ according to the Landau gauge with phases in y-direction, i.e.

$$\varphi_{\langle ij \rangle} = \begin{cases} 0 & \text{for } \langle ij \rangle = \mathbf{e}_x, \\ 2\pi\alpha x_i & \text{for } \langle ij \rangle = \mathbf{e}_y. \end{cases} \tag{6.71}$$

We also perform analogous, quasi-exact density matrix renormalization group (DMRG) simulations for systems of $L_x = L_y = 6, 8, 10$ sites and $N = 3, 6, 10$ particles.

The variational energies obtained from this ansatz as well as the (quasi-)exact ground state energies are given in Fig. 6.4. We find the variational energies to be significantly higher than the energies obtained using ED and DMRG. While the ansatz state $|\tilde{\Psi}'\rangle = \hat{\mathcal{V}}^\dagger |\tilde{\Psi}\rangle$, i.e. $\vartheta_{k,\mu} = 0$, gives significantly better results than $|\tilde{\Psi}\rangle$, it is still desirable to improve the variational ansatz to find lower and hence more accurate variational energies.

Compact Coherent State Ansatz

Next, we consider a modified coherent state ansatz for the bosonic degrees of freedom,

$$|\tilde{\varphi}_b\rangle = \prod_\mu |\overline{\beta_\mu}\rangle \quad \text{with} \quad |\overline{\beta_\mu}\rangle = \sum_{n=-\infty}^{\infty} |\beta_\mu + 2\pi n\rangle \quad \text{and} \quad \hat{b}_\mu |\beta_\mu\rangle = \beta_\mu |\beta_\mu\rangle, \tag{6.72}$$

where we assume real-valued $\beta_\mu \in \mathbb{R}$. The modified coherent states $|\overline{\beta_\mu}\rangle$ are 2π-periodic, which seems a natural assumption for the compact gauge degree of freedom. We call this ansatz the *compact coherent state ansatz.*

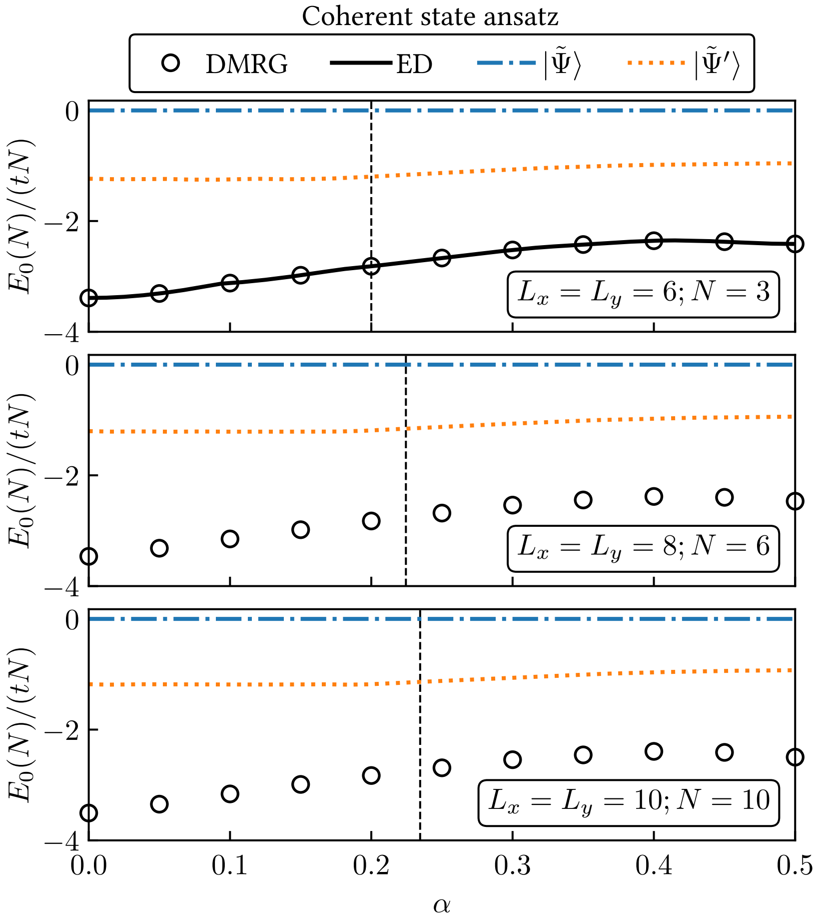

Fig. 6.4. Ground state energy for the Hofstadter-Bose-Hubbard model (black) and two variational ansätze (blue and orange) for different system sizes and particle numbers. The black line (upper panel) indicates the results obtained by exact diagonalization, while the circles are the quasi-exact energies from DMRG. The blue dash-dotted line is the variational energy obtained from the coherent state ansatz $|\tilde{\Psi}\rangle$, whereas the orange dotted line is for the modified ansatz $|\tilde{\Psi}'\rangle = \hat{\mathcal{V}}^{\dagger} |\tilde{\Psi}\rangle$ which gives significantly lower energies. Both trial states, however, deviate significantly from the ground state energy. The vertical dashed lines indicate the flux per plaquette $\alpha = (2N-1)/((L_x-1)(L_y-1))$ where the 1/2-Laughlin state is expected for open boundary conditions.

As mentioned before, the operators $\mathrm{e}^{\hat{\tilde{\mathcal{A}}}_k}$ act as displacement operators on the usual coherent states $|\beta_\mu\rangle$ and hence also on the modified states,

$$\mathrm{e}^{\hat{\tilde{\mathcal{A}}}_k}\, \overline{|\beta_\mu\rangle} = \overline{|\beta_\mu - \delta\beta_\mu^{(k)}\rangle}\,, \tag{6.73}$$

where we used

$$\delta\beta_\eta^{(k)} := \frac{1}{2}\left(\delta(k \notin \eta)\arg\left(\frac{z_{\eta_1} - z_k}{z_{\eta_2} - z_k}\right) + 2\delta(k \in \eta)\vartheta_{k,\eta}\right). \tag{6.74}$$

Therefore, we can calculate the bosonic expectation value,

$$\begin{aligned} &\langle\tilde{\varphi}_b|\, \mathrm{e}^{-\hat{\tilde{\mathcal{A}}}_i}\mathrm{e}^{i\hat{\varphi}_{\langle ij\rangle}}\mathrm{e}^{\hat{\tilde{\mathcal{A}}}_j}\, |\tilde{\varphi}_b\rangle \\ &= \left(\prod_{\mu\neq\langle ij\rangle} \overline{\langle\beta_\mu - \delta\beta_\mu^{(i)}}\,\overline{|\beta_\mu - \delta\beta_\mu^{(j)}\rangle}\right) \overline{\langle\beta_{\langle ij\rangle} - \delta\beta_{\langle ij\rangle}^{(i)}}|\mathrm{e}^{i\hat{\varphi}_{\langle ij\rangle}}\,\overline{|\beta_{\langle ij\rangle} - \delta\beta_{\langle ij\rangle}^{(j)}\rangle}\,. \end{aligned} \tag{6.75}$$

The overlaps of the states $\overline{|\beta_\mu\rangle}$ can be evaluated analytically,

$$\begin{aligned} \overline{\langle\beta_\mu - \delta\beta_\mu^{(i)}}\,\overline{|\beta_\mu - \delta\beta_\mu^{(j)}\rangle} &= \sum_{k,m=-\infty}^{\infty} \exp\left[-\frac{1}{2}\left(\delta\beta_\mu^{(i)} - \delta\beta_\mu^{(j)} + 2\pi m\right)^2\right] \\ &= \left(\sum_{k=-\infty}^{\infty}\right)\vartheta_3\left(\frac{\delta\beta_\mu^{(i)} - \delta\beta_\mu^{(j)}}{2}, \mathrm{e}^{-1/2}\right)/\sqrt{2\pi}, \end{aligned} \tag{6.76}$$

where we introduced the Jacobi theta function $\vartheta_3\left(u,q\right) = 1 + 2\sum_{n=1}^{\infty} q^{n^2}\cos(2nu)$. The apparent problem of this overlap being divergent will be cured when calculating observables as we always normalize these by the norm of the ansatz state.

With these results at hand, we arrive at

$$\frac{\langle\tilde{\varphi}_b|\, \mathrm{e}^{-\hat{\tilde{\mathcal{A}}}_i}\mathrm{e}^{i\hat{\varphi}_{\langle ij\rangle}}\mathrm{e}^{\hat{\tilde{\mathcal{A}}}_j}\, |\tilde{\varphi}_b\rangle}{\langle\tilde{\varphi}_b|\tilde{\varphi}_b\rangle} = \mathrm{e}^{-\frac{1}{2}+i\left(2\beta_{\langle ij\rangle}-2\left(\vartheta_{i,\langle ij\rangle}-\vartheta_{j,\langle ij\rangle}\right)\right)}\prod_\mu \frac{\vartheta_3\left(\frac{\delta\beta_\mu^{(i)}-\delta\beta_\mu^{(j)}}{2}, \mathrm{e}^{-1/2}\right)}{\vartheta_3\left(0, \mathrm{e}^{-1/2}\right)} \tag{6.77}$$

and therefore the effective Hamiltonian

$$\hat{\mathcal{H}}_{\text{eff}}^{\text{ccs}} = -\sum_{\langle ij\rangle}\tilde{t}_{\langle ij\rangle}^{\text{ccs}}\mathrm{e}^{2i\beta_{\langle ij\rangle}-i\left(\vartheta_{i,\langle ij\rangle}+\vartheta_{j,\langle ij\rangle}\right)}\hat{f}_i^\dagger\hat{f}_j + \text{H.c.} \tag{6.78}$$

for the composite fermions, where we defined the effective hopping amplitudes

$$\tilde{t}_{\langle ij\rangle}^{\text{ccs}} = t\mathrm{e}^{-1/2}\prod_\mu \frac{\vartheta_3\left(\frac{\delta\beta_\mu^{(i)}-\delta\beta_\mu^{(j)}}{2}, \mathrm{e}^{-1/2}\right)}{\vartheta_3\left(0, \mathrm{e}^{-1/2}\right)}. \tag{6.79}$$

These hopping amplitudes can be evaluated accurately and are illustrated in Fig. 6.5. They show a qualitatively similar behavior as the hopping amplitudes obtained for the usual coherent state ansatz. In particular, the strength of the hopping amplitudes for states such that $\vartheta_{k,\mu} = 0$ is essentially the same for the usual coherent state ansatz and the modified ansatz. This is also evident from the analytical structure of the hopping amplitudes, as

$$\begin{aligned} \frac{\vartheta_3\left(\frac{\Delta_\mu^{(ij)}}{2}, \mathrm{e}^{-1/2}\right)}{\vartheta_3\left(0, \mathrm{e}^{-1/2}\right)} &= \frac{\sum_{m=-\infty}^{\infty}\exp\left[-\frac{1}{2}\left(\delta\beta_\mu^{(i)} - \delta\beta_\mu^{(j)} + 2\pi m\right)^2\right]}{\sum_{m=-\infty}^{\infty}\exp\left[-2\pi^2 m^2\right]} \\ &\approx \exp\left[-\frac{1}{2}\left(\left(\delta\beta_\mu^{(i)} - \delta\beta_\mu^{(j)}\right) \mod 2\pi\right)^2\right], \end{aligned} \tag{6.80}$$

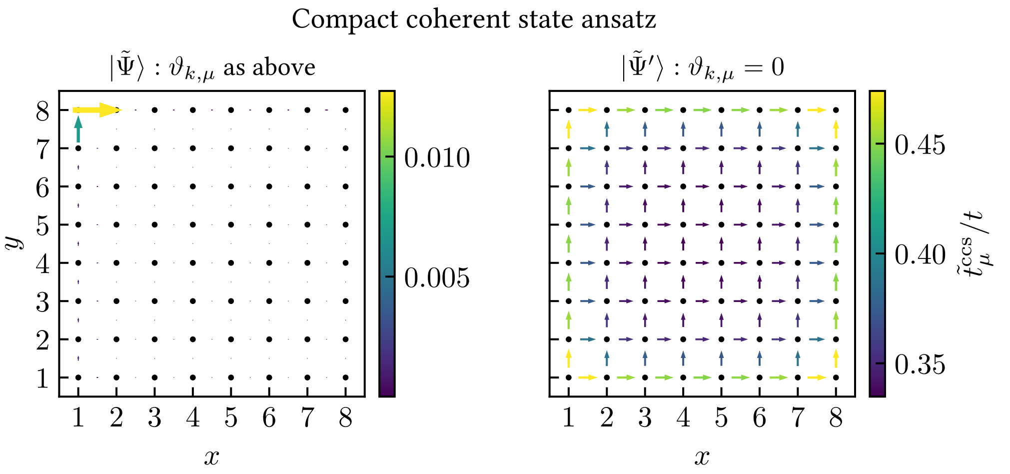

Fig. 6.5. Hopping amplitudes $\tilde{t}_\mu^{\mathrm{ccs}}$ in an 8×8-system for two choices of $\vartheta_{k,\mu}$ from the *compact* coherent state ansatz. As for the usual coherent states, for vanishing $\vartheta_{k,\mu} = 0$ the hopping amplitudes are slightly increased towards the edge of the system while being almost constant in the bulk, while using the choice in Eq. (6.50) most of the hopping amplitudes essentially vanish and the remaining contribution is highly inhomogeneous. The color, width, and length of the arrows indicate the hopping amplitude. Width and length are increased by a factor of 100 in the left panel for better visibility.

which under the assumption that $\left|\delta\beta_\mu^{(i)} - \delta\beta_\mu^{(j)}\right| < \pi$ agrees very well with the expression from the usual coherent state ansatz.

As for the usual coherent state ansatz, we diagonalize the fermionic Hamiltonian in Eq. (6.78), calculate the single particle spectrum, see Fig. 6.6, and evaluate the variational energy. The results of this diagonalization are presented in Fig. 6.7. Both the variational energies and their qualitative features agree very well for the compact coherent state ansatz and its non-compact relative. In particular, there are no signatures of a qualitative change of behavior in the Laughlin regime.

Vortex Ansatz

In the continuum, the best trial state from the CF construction is not the one obtained by attaching flux tubes to the particles but the one with vortices attached. A similar ansatz can also be made on the lattice,

$$|\tilde{\psi}_f\rangle = \mathrm{e}^{m\sum_{i<j}\log(z_i-z_j)\hat{n}_i\hat{n}_j}\,|\Phi(N)\rangle = \prod_{i<j}(z_i - z_j)^{m\hat{n}_i\hat{n}_j}\,|\Phi(N)\rangle\,, \tag{6.81}$$

where $|\Phi(N)\rangle$ is the N-particle ground state of the non-interacting Hofstadter model at flux α per plaquette. The bosonic ansatz is again chosen to be a product of (conventional) coherent states $|\beta_{\langle ij\rangle}\rangle$,

$$\beta_{\langle ij\rangle} = \begin{cases} 0 & \text{for } \langle ij\rangle = \mathbf{e}_x, \\ \pi\alpha x_i & \text{for } \langle ij\rangle = \mathbf{e}_y, \end{cases} \tag{6.82}$$

which is then transformed using $\hat{\mathcal{U}}\hat{\mathcal{V}}$, where we choose $\vartheta_{k,\mu} = 0$.

The wave function $|\tilde{\psi}_f\rangle$ can be expanded in the Fock states $|\{n_k\}\rangle$ such that

$$|\tilde{\psi}_f\rangle = \sum_{\{n_k\}} \left(\prod_{i<j}(z_i - z_j)^{mn_in_j}\right) |\{n_k\}\rangle\, \underbrace{\langle\{n_k\}\,|\Phi(N)\rangle}_{=:c(\{n_k\})}\,. \tag{6.83}$$

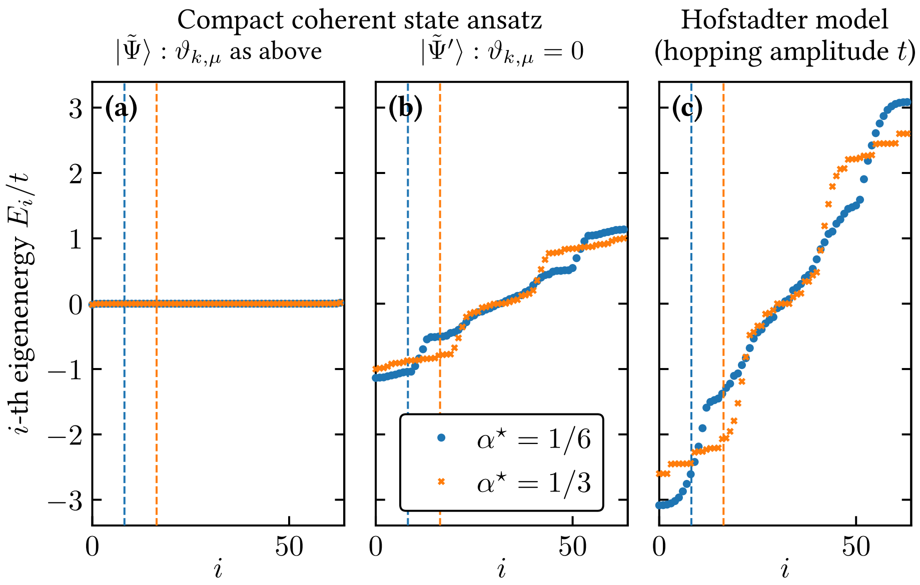

Fig. 6.6. Single-particle energy levels E_i of the effective composite fermion Hamiltonian $\hat{\mathcal{H}}^{\text{ccs}}_{\text{eff}}$ Eq. (6.78) from the *compact* coherent state ansatz for different choices of $\vartheta_{k,\mu}$ **(a,b)** and a vanilla Hofstadter model at hopping amplitude t **(c)** for $L_x \times L_y = 10 \times 10$. For $\vartheta_{k,\mu} = 0$ the band structure of the effective Hamiltonian is essentially unchanged compared to the usual coherent state ansatz (see Fig. 6.3). The dashed vertical lines separate the first $N_\phi = \alpha^\star(L_x - 1)(L_y - 1)$ states from the rest of the spectrum.

The variational energy can be rewritten as

$$E = \frac{\langle\tilde{\psi}_f|\hat{\mathcal{H}}^{\text{CF}}_{\text{eff}}|\tilde{\psi}_f\rangle}{\langle\tilde{\psi}_f|\tilde{\psi}_f\rangle} = \frac{\langle\tilde{\psi}_f|\hat{\mathcal{H}}^{\text{CF}}_{\text{eff}}|\tilde{\psi}_f\rangle \,/\, \langle\Phi(N)|\Phi(N)\rangle}{\langle\tilde{\psi}_f|\tilde{\psi}_f\rangle \,/\, \langle\Phi(N)|\Phi(N)\rangle}, \tag{6.84}$$

where both numerator and denominator can be evaluated using Monte-Carlo sampling of the wave function $|\Phi(N)\rangle$ and evaluating the expressions

$$\begin{aligned} h(\{n_k\}) &= \sum_{\{n'_l\}} \langle\{n'_l\}\,|\hat{\mathcal{H}}^{\text{CF}}_{\text{eff}}|\,\{n_k\}\rangle \left(\prod_{i<j}(\bar{z}_i - \bar{z}_j)^{mn'_i n'_j}(z_i - z_j)^{mn_i n_j}\right)\frac{\overline{c(\{n_l\})}}{\overline{c(\{n_k\})}}, \\ \mathcal{N}(\{n_k\}) &= \prod_{i<j}|z_i - z_j|^{2mn_i n_j} \end{aligned} \tag{6.85}$$

for each snapshot. Thus, we arrive at our final expression for the variational energy,

$$E = \frac{\sum_{|\text{snapshot}\rangle} h(|\text{snapshot}\rangle)}{\sum_{|\text{snapshot}\rangle} \mathcal{N}(|\text{snapshot}\rangle)}. \tag{6.86}$$

We generate $N_{\text{MC}} = 20.000$ snapshots for different values of the flux per plaquette α and evaluate the variational energy using the "*vortex state*". We find that the energies are slightly higher than those obtained from the coherent state ansätze, see Fig. 6.8. However, while the fermionic density distribution in those cases tends to exhibits a charge accumulation at the edge because of the inhomogeneous hopping amplitudes, the vortex state qualitatively resembles the droplet in the center of the system typical for Hall states, see Fig. 6.9.

We therefore believe that modifications of the vortex state investigated here deserve particular attention in the future when studying more sophisticated ansätze.

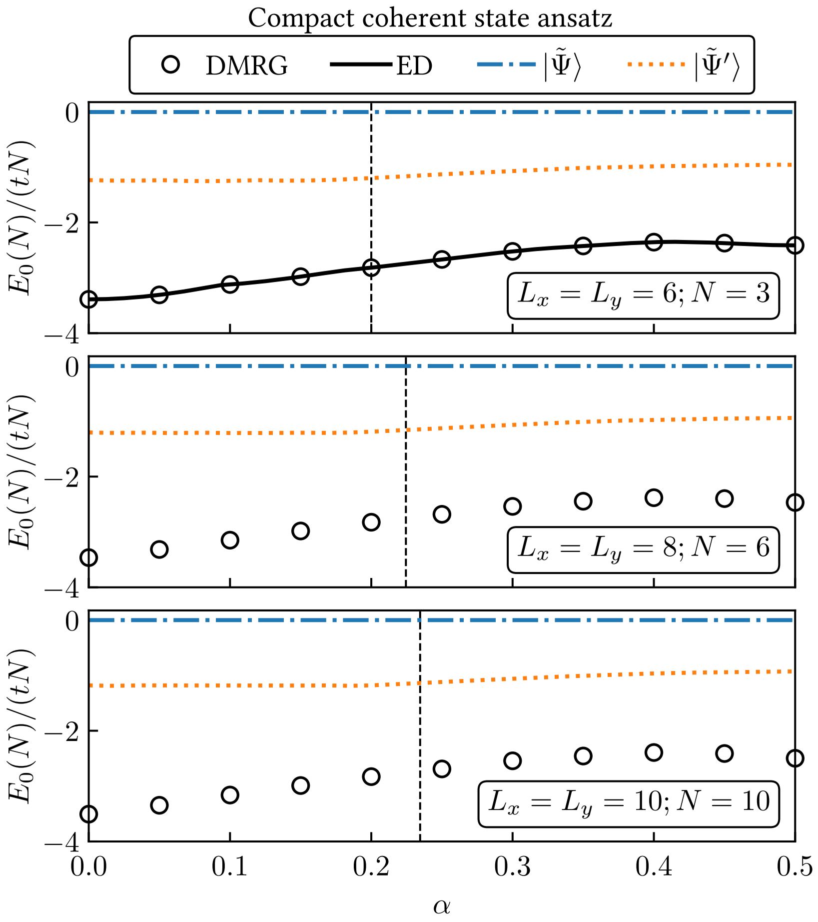

Fig. 6.7. Ground state energy for the Hofstadter-Bose-Hubbard model (black) and two variational ansätze (blue and orange) for different system sizes and particle numbers. The black line (upper panel) indicates the results obtained by exact diagonalization, while the circles are the quasi-exact energies from DMRG. The blue dash-dotted line is the variational energy obtained from the *compact* coherent state ansatz $|\tilde{\Psi}\rangle$, whereas the orange dotted line is for the ansatz $|\tilde{\Psi}'\rangle = \hat{\mathcal{V}}^\dagger |\tilde{\Psi}\rangle$ which gives significantly lower energies. Both trial states, deviate significantly from the ground state energy and are less successful than the usual coherent state ansatz in Fig. 6.4. The vertical dashed lines indicate the flux per plaquette $\alpha = (2N-1)/((L_x-1)(L_y-1))$ where the $^1/_2$-Laughlin state is expected for open boundary conditions.

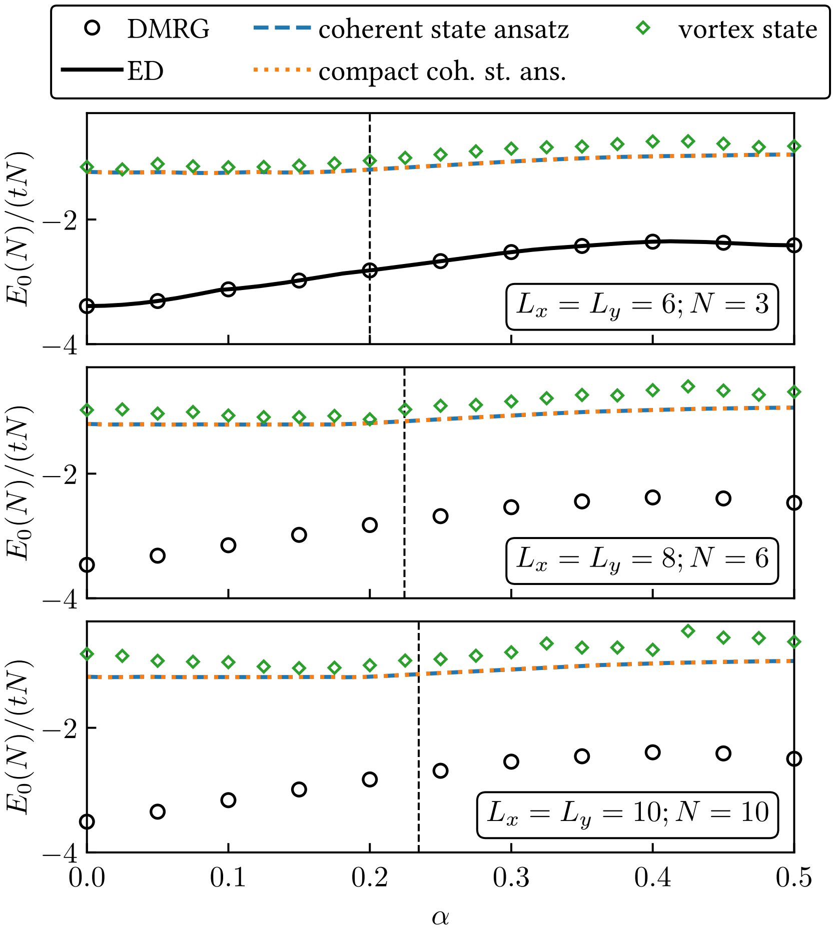

Fig. 6.8. Variational energies from coherent state ansätze (blue and orange), the vortex state ansatz (green) and (quasi-)exact ground state energies (black) of the Hofstadter-Bose-Hubbard model as discussed above. We find that none of the variational states considered gives variational energies which are in good agreement with the exact energy.

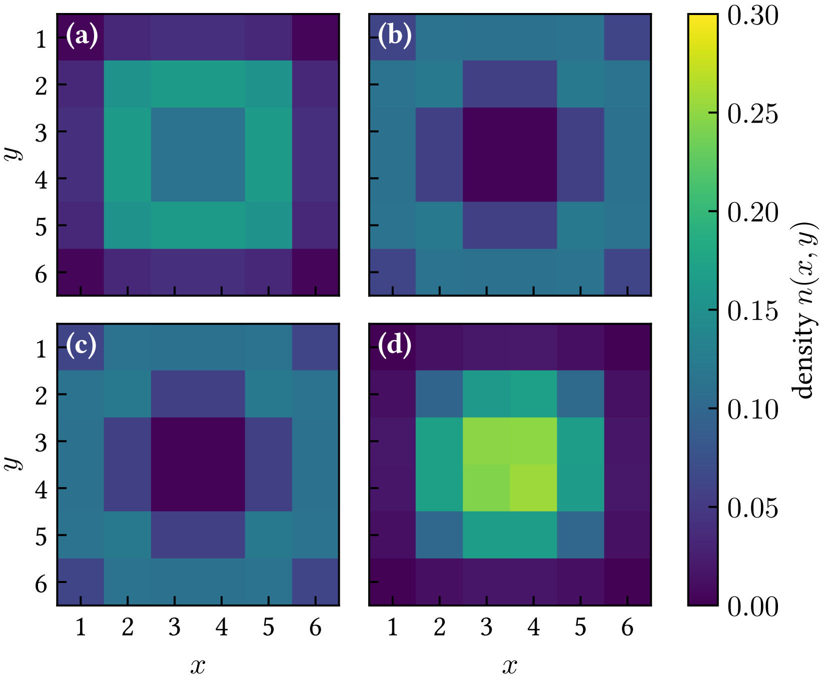

Fig. 6.9. Local densities $n(x, y)$ as obtained from **(a)** exact diagonalization of the Hofstadter-Bose-Hubbard model, **(b)** the variational coherent state ansatz and **(c)** its compactified variant, and **(d)** the vortex ansatz. For the coherent ansätze, we choose the variant $|\tilde{\Psi}'\rangle$ with $\vartheta_{k,\mu} = 0$. All data shown is for $N = 3$ particles on 6×6 sites at $\alpha = 0.25$. While the coherent state ansätze accumulate density at the edge of the system due to the inhomogeneous hopping amplitudes, the vortex ansatz overestimates the density in the center, but qualitatively captures the formation of a bulk region.

Outlook: Projected trial state

A possible approach to improve the accuracy of the trial state is to project our earlier ansätze to the physical Hilbert space defined by the constraint

$$\begin{aligned}
&\left(2\pi\alpha - \sum_{\mu\in\partial p} \hat{\varphi}_\mu\right) |\Psi\rangle = 0 \\
\Leftrightarrow \quad & \hat{\mathcal{V}}\hat{\mathcal{U}} \left(2\pi\alpha - \sum_{\mu\in\partial p} \hat{\varphi}_\mu\right) \hat{\mathcal{U}}^\dagger \hat{\mathcal{V}}^\dagger |\tilde{\Psi}\rangle = \left(2\pi\alpha - \sum_{\mu\in\partial p} \hat{\mathcal{V}}\hat{\mathcal{U}}\hat{\varphi}_\mu \hat{\mathcal{U}}^\dagger \hat{\mathcal{V}}^\dagger\right) |\tilde{\Psi}\rangle \qquad (6.87) \\
&= \left(2\pi\alpha - \sum_{\mu\in\partial p} \left(\hat{\varphi}_\mu - \delta\hat{\varphi}_\mu\right) + 2\sum_{k\in\mu} \hat{n}_k \vartheta_{k,\mu}\right) |\tilde{\Psi}\rangle = 0.
\end{aligned}$$

Such a projection manifestly encodes the flux attachment procedure locally and therefore might result in a more accurate treatment of the composite fermions beyond mean-field effects. While we remark that this is in stark contrast to the continuum CF construction, where the mean-field approximation for the magnetic field is explicitly performed, such a treatment might be favorable in the presence of an additional length scale set by the lattice length.

In order to find the variational energy for a projected ansatz, one might perform Metropolis Monte Carlo sampling in the physical Hilbert space. In particular, it seems promising to perform the sampling for the bosonic degrees of freedom in the eigenbasis of the link operators $\hat{\varphi}_\mu$ and in the real-space Fock basis for the fermions. While we do not perform this sampling here, we believe this approach to be a promising route for future studies of variational trial states for fractional Chern insulators.

6.4. Summary and Outlook

Using a construction similar to Fradkin's lattice anyon approach [253, 254], we derived a composite fermion representation of hard-core bosons in the presence of a dynamical gauge field. We intertwined the gauge and matter degrees of freedom using a unitary transformation acting on both sectors and derive an effective theory for the composite fermions in the presence of the gauge field. On mean-field level the magnetic flux experienced by the composite fermions agrees with the continuum prediction for the Jain sequence states.

We performed a mean-field decoupling, where the gauge degrees of freedom are modeled by different types of coherent states consistent with the mean-field flux per plaquette, resulting in an effective free Hamiltonian for the composite fermions. Using these trial states, we obtained variational energies, which are, however, still significantly higher than ground state energies obtained from ED and DMRG simulations of the Hofstadter-Bose-Hubbard model at the corresponding static magnetic field. Inspired by the construction of continuum trial states using composite fermion theory, we constructed a similar "vortex state" reminiscent of the continuum Laughlin wave function. While the variational energies of this state are slightly higher than those of our earlier trial states, the vortex state is expected to provide a closer analogy to the continuum CF theory and therefore might prove useful in future applications.

Given the deviations of our variational energies from the exact ground state energies, further investigations are necessary to find a reliable trial state. One particularly promising approach to achieve this is by projecting the trial wave functions into the proper physical Hilbert space, where the flux attachment condition is fulfilled exactly. While the mean-field treatment presented here seems favorable in the light of the continuum analogy, it is very well possible that lattice effects render such a mean-field description inaccurate in the presence of strong lattice effects. This again highlights the importance of accurate trial wave functions taking into account lattice effects and connecting to the continuum limit, $\alpha \to 0$ in dilute systems.

The potential applications of accurate trial wave functions are manifold. We would like to emphasize three aspects which are particularly promising in our opinion. Firstly, trial wave functions of the form proposed here are easy to evaluate even in large systems, where conventional numerical methods become unfeasible. Secondly, such trial wave functions allow for efficient time-evolution simulations and studies at finite temperatures. While we did not study excited states so far, such an extension is in principle easily possible. Finally, composite fermion approaches are only one particular proposal to describe Hall systems. We expect trial states like ours to shed light on questions around the competition of lattice effects, in particular at large flux and higher particle number densities, where the analogy with the continuum limit is expected to break down. Having another powerful theoretical tool available is expected to open up new avenues in the study of fractional Chern insulators and competing states.

Conclusion and Outlook

In this thesis, we employed variational methods to explore (fractional) quantum Hall states on a lattice, with a focus on the Hofstadter-Hubbard model that can be simulated using cold atom quantum simulators.

Chapter 1 provided background on topological order and the quantum Hall effect, presented key concepts of quantum simulation, and introduced the numerical methods used in this work. In Chapter 2, we examined non-Abelian fractional quantum Hall states, finding compelling evidence for the Pfaffian state as the ground state of the Hofstadter-Bose-Hubbard model. Chapter 3 proposed elongated systems as a means to probe topological order using the central charge, discussing the paradigmatic filling factors $\nu = 1/2$ and 1. Inspired by recent experiments, we investigated the feasibility of a modular approach to grow extended Laughlin states from small patches in Chapter 4. In Chapter 5, we complemented our analyses with a study of fermionic quantum Hall ferromagnetism and examined its stability in a lattice model, finding evidence for skyrmion-like excitations in the spinless sector. Finally, Chapter 6 explored analytical trial states by generalizing the composite fermion approach to lattice systems, deriving an effective Hamiltonian, and presenting variational ansätze.

The field of cold atom quantum simulation of fractional Chern insulators (FCIs) is rapidly advancing and experimental studies are now within reach. In particular, the recent realization of a two-boson Laughlin state [25] has shown great promise in realizing and probing FCIs in cold atom systems. The extension of these experiments to larger systems, such as elongated chains, will allow for measurements of the central charge and braiding properties. Our work addressed the need for adiabatic preparation schemes employing a scalable, modular approach.

Increasing the particle number, studies of more exotic states, such as the bosonic Pfaffian state at $\nu = 1$, become possible. We provided evidence for a lattice Pfaffian state in the Hofstadter-Bose-Hubbard model on cylinders with only two-body repulsion. Interestingly, finite system sizes play a crucial role in the emergence of competing states, as exemplified by the different topological ground states for $L_y = 3, 4$, and 5 coupled chains, neither of which could be identified as the Pfaffian state found on cylinders. We observed a similar behavior for $\nu = 1/2$, where the Laughlin state only constitutes the ground state in systems of more than two chains. This dependence on system size, i.e. system geometry, as well as the effects of boundary conditions, i.e. system topology, should be explored further in future (numerical) studies. Experiments have the unique opportunity to realize various interesting correlated states in this system and can help to clarify the phase diagram.

Similar physics is also at play in fermionic systems, where quantum Hall ferromagnetism can be studied in lattice systems. In experiments, skyrmionic excitations can be probed directly using spin-resolved measurements. The variant of the Hubbard model considered here is also of interest for the broad community studying such models more generally. The effect of the external magnetic field is not fully understood yet and it will be insightful to investigate further which states are favored and destroyed under these conditions.

While numerical approaches to study lattice systems are well established, analytical approaches starting from the Hamiltonian are less developed, in contrast to the continuum, where composite fermions and field theory methods are commonly used. In our work, we laid the foundation to develop variational trial states in lattice systems based on the composite fermion approach to the fractional quantum Hall problem.

In summary, the work presented in this thesis has contributed to the exploration of topologically ordered states, the development of adiabatic preparation schemes, the study of quantum Hall ferromagnetism in lattice systems, and the development of analytical approaches to study related systems.

Outlook

Following up on the work presented in this thesis, several avenues for future research open up. Special emphasis is on cold atom quantum simulation, which is expected to prove fruitful in understanding the correlated nature of fractional Chern insulators. One potential direction is to investigate the Hall response [82, 83, 87, 172] in exotic states of matter like the Pfaffian state and to study its excitations in more detail [39, 84, 88, 89, 196]. To this end, it is necessary to clarify the role of boundary conditions and understand how the Pfaffian state can best be realized in cold atom experiments. In particular, it is still an open question whether the Pfaffian state can be realized in the Hofstadter-Bose-Hubbard model with open boundary conditions and, if not, which modifications are necessary to achieve this long-standing goal.

Related to the ambiguity of the ground state in open boundary conditions, it is necessary to find a way to ultimately prove that potential candidates are in fact in the topological universality class of the Pfaffian state. Here, combining abstract results from the classification of topological orders [27, 255–257] with current cold atom experiments can lead to novel yet realistic detection schemes.

Up to now, realizing and controlling large systems remains challenging for experiments. Employing machine learning techniques to reach higher fidelities might improve modular approaches like the one presented above [203–205]. In the light of future anyon braiding experiments, it is desirable to realize systems hosting quasiholes, which might be realizable via adiabatic state preparation. Once having created the anyons, they have to be braided without perturbing the underlying system. With respect to topological quantum computation applications it is of high interest to probe the non-Abelian braiding directly [55].

Realistic systems always operate at finite temperatures, which is likely to further complicate the situation. Understanding the effect of finite temperatures on (signatures of) the topological order of FCIs is necessary to make such systems useful for applications.

Especially the last two points might be addressed using for example analytical trial states in cases where existing numerical techniques break down. Such trial states can also guide future investigations of the reality of composite fermions and alike in lattice systems. In particular, the speculated existence of hidden off-diagonal long-range order [195, 251] could be investigated using similar ideas, as well as the p-wave nature of the pairing in the Pfaffian state [62].

Finally, connections to other phenomena in condensed matter physics, like high-temperature superconductivity or chiral spin liquids, might deepen our understanding of correlated many-body systems further. The advent of more sophisticated interactions in cold atom experiments will keep such platforms relevant in these endeavors in the future.

Bibliography

[1] F. A. Palm, M. Buser, J. Léonard, M. Aidelsburger, U. Schollwöck, and F. Grusdt. Bosonic Pfaffian state in the Hofstadter-Bose-Hubbard model. *Physical Review B*, **103**(16), L161101, 2021.

[2] F. A. Palm, S. Mardazad, A. Bohrdt, U. Schollwöck, and F. Grusdt. Snapshot-based detection of $\nu = \frac{1}{2}$ Laughlin states: Coupled chains and central charge. *Physical Review B*, **106**(8), L081108, 2022.

[3] F. A. Palm, M. Kurttutan, A. Bohrdt, U. Schollwöck, and F. Grusdt. Ferromagnetism and skyrmions in the Hofstadter-Fermi-Hubbard model. *New Journal of Physics*, **25**, 023021, 2023.

[4] R. H. Wilke, T. Köhler, F. A. Palm, and S. Paeckel. Symmetry-protected Bose-Einstein condensation of interacting hardcore Bosons, arXiv:2110.15770, 2021.

[5] F. A. Palm, C. Repellin, N. Goldman, and F. Grusdt. Interacting Topological States on Coupled Chains at Filling Factor $\nu = 1$. in preparation.

[6] F. A. Palm, N. Goldman, and F. Grusdt. Growing Fractional Chern Insulators in a Quantum Gas Microscope. in preparation.

[7] F. Pauw, F. A. Palm, A. Bohrdt, S. Paeckel, and F. Grusdt. Detecting Hidden Order in Fractional Chern Insulators. in preparation.

[8] K. von Klitzing. The quantized Hall effect. *Reviews of Modern Physics*, **58**(3), 519–531, 1986.

[9] Nobel Prize Outreach AB. The Nobel Prize in Physics 1985. `https://www.nobelprize.org/prizes/physics/1985/summary/`, 1985.

[10] K. v. Klitzing, G. Dorda, and M. Pepper. New Method for High-Accuracy Determination of the Fine-Structure Constant Based on Quantized Hall Resistance. *Physical Review Letters*, **45**(6), 494–497, 1980.

[11] D. J. Thouless, M. Kohmoto, M. P. Nightingale, and M. den Nijs. Quantized Hall Conductance in a Two-Dimensional Periodic Potential. *Physical Review Letters*, **49**(6), 405–408, 1982.

[12] Y. Choquet-Bruhat, C. DeWitt-Morette, and M. Dillard-Bleick. *Analysis, manifolds, and physics.* North-Holland Pub. Co., 1982.

[13] D. C. Tsui, H. L. Stormer, and A. C. Gossard. Two-Dimensional Magnetotransport in the Extreme Quantum Limit. *Physical Review Letters*, **48**(22), 1559–1562, 1982.

[14] Q. Niu, D. J. Thouless, and Y.-S. Wu. Quantized Hall conductance as a topological invariant. *Physical Review B*, **31**(6), 3372–3377, 1985.

[15] B. I. Halperin. Statistics of Quasiparticles and the Hierarchy of Fractional Quantized Hall States. *Physical Review Letters*, **52**(18), 1583–1586, 1984.

[16] D. Arovas, J. R. Schrieffer, and F. Wilczek. Fractional Statistics and the Quantum Hall Effect. *Physical Review Letters*, **53**, 722–723, 1984.

[17] A. Y. Kitaev. Fault-tolerant quantum computation by anyons. *Annals of Physics*, **303**(1), 2–30, 2003.

[18] N. Goldman, J. C. Budich, and P. Zoller. Topological quantum matter with ultracold gases in optical lattices. *Nature Physics*, **12**(7), 639–645, 2016.

[19] M. Aidelsburger, S. Nascimbene, and N. Goldman. Artificial gauge fields in materials and engineered systems. *Comptes Rendus Physique*, **19**, 394–432, 2018.

[20] M. Aidelsburger, M. Atala, M. Lohse, J. T. Barreiro, B. Paredes, and I. Bloch. Realization of the Hofstadter Hamiltonian with Ultracold Atoms in Optical Lattices. *Physical Review Letters*, **111**(18), 185301, 2013.

[21] H. Miyake, G. A. Siviloglou, C. J. Kennedy, W. C. Burton, and W. Ketterle. Realizing the Harper Hamiltonian with Laser-Assisted Tunneling in Optical Lattices. *Physical Review Letters*, **111**(18), 185302, 2013.

[22] M. E. Tai, A. Lukin, M. Rispoli, R. Schittko, T. Menke, D. Borgnia, P. M. Preiss, F. Grusdt, A. M. Kaufman, and M. Greiner. Microscopy of the interacting Harper–Hofstadter model in the two-body limit. *Nature*, **546**(7659), 519–523, 2017.

[23] N. Gemelke, E. Sarajlic, and S. Chu. Rotating Few-body Atomic Systems in the Fractional Quantum Hall Regime, arXiv:1007.2677, 2010.

[24] L. W. Clark, N. Schine, C. Baum, N. Jia, and J. Simon. Observation of Laughlin states made of light. *Nature*, **582**(7810), 41–45, 2020.

[25] J. Léonard, S. Kim, J. Kwan, P. Segura, F. Grusdt, C. Repellin, N. Goldman, and M. Greiner. Realization of a fractional quantum Hall state with ultracold atoms. , 2022.

[26] R. B. Laughlin. Anomalous Quantum Hall Effect: An Incompressible Quantum Fluid with Fractionally Charged Excitations. *Physical Review Letters*, **50**(18), 1395–1398, 1983.

[27] X. Chen, Z.-C. Gu, and X.-G. Wen. Local unitary transformation, long-range quantum entanglement, wave function renormalization, and topological order. *Physical Review B*, **82**, 155138, 2010.

[28] S. Bravyi, M. B. Hastings, and S. Michalakis. Topological quantum order: Stability under local perturbations. *Journal of Mathematical Physics*, **51**(9), 093512, 2010.

[29] M. B. Hastings and S. Michalakis. Quantization of Hall Conductance for Interacting Electrons on a Torus. *Communications in Mathematical Physics*, **334**(1), 433–471, 2015.

[30] F. Grusdt. Lecture Notes on “Strongly crrelated quantum systems”, 2020.

[31] C.-K. Chiu, J. C. Y. Teo, A. P. Schnyder, and S. Ryu. Classification of topological quantum matter with symmetries. *Reviews of Modern Physics*, **88**(3), 035005, 2016.

[32] A. Hatcher. *Algebraic Topology.* Cambridge University Press, 2002.

[33] N. R. Cooper, J. Dalibard, and I. B. Spielman. Topological bands for ultracold atoms. *Reviews of Modern Physics*, **91**(1), 015005, 2019.

[34] M. Kohmoto. Topological invariant and the quantization of the Hall conductance. *Annals of Physics*, **160**(2), 343–354, 1985.

[35] V. J. Goldman and B. Su. Resonant Tunneling in the Quantum Hall Regime: Measurement of Fractional Charge. *Science*, **267**(5200), 1010–1012, 1995.

[36] R. de Picciotto, M. Reznikov, M. Heiblum, V. Umansky, G. Bunin, and D. Mahalu. Direct observation of a fractional charge. *Nature*, **389**(6647), 162–164, 1997.

[37] L. Saminadayar, D. C. Glattli, Y. Jin, and B. Etienne. Observation of the e/3 Fractionally Charged Laughlin Quasiparticle. *Physical Review Letters*, **79**(13), 2526–2529, 1997.

[38] F. Wilczek. Quantum Mechanics of Fractional-Spin Particles. *Physical Review Letters*, **49**(14), 957–959, 1982.

[39] J. Nakamura, S. Liang, G. C. Gardner, and M. J. Manfra. Direct observation of anyonic braiding statistics. *Nature Physics*, **16**(9), 931–936, 2020.

[40] H. Bartolomei, M. Kumar, R. Bisognin, A. Marguerite, J.-M. Berroir, E. Bocquillon, B. Plaçais, A. Cavanna, Q. Dong, U. Gennser, Y. Jin, and G. Fève. Fractional statistics in anyon collisions. *Science*, **368**(6487), 173–177, 2020.

[41] A. Kitaev. Anyons in an exactly solved model and beyond. *Annals of Physics*, **321**(1), 2–111, 2006.

[42] X. G. Wen and Q. Niu. Ground-state degeneracy of the fractional quantum Hall states in the presence of a random potential and on high-genus Riemann surfaces. *Physical Review B*, **41**(13), 9377–9396, 1990.

[43] Y. Hatsugai. Topological aspects of the quantum Hall effect. *Journal of Physics: Condensed Matter*, **9**(12), 2507–2549, 1997.

[44] A. M. Essin and V. Gurarie. Bulk-boundary correspondence of topological insulators from their respective Green's functions. *Physical Review B*, **84**(12), 125132, 2011.

[45] B. I. Halperin. Quantized Hall conductance, current-carrying edge states, and the existence of extended states in a two-dimensional disordered potential. *Physical Review B*, **25**(4), 2185–2190, 1982.

[46] X. G. Wen. Chiral Luttinger liquid and the edge excitations in the fractional quantum Hall states. *Physical Review B*, **41**(18), 12838–12844, 1990.

[47] Y. Hatsugai. Chern number and edge states in the integer quantum Hall effect. *Physical Review Letters*, **71**(22), 3697–3700, 1993.

[48] Y. Hatsugai. Edge states in the integer quantum Hall effect and the Riemann surface of the Bloch function. *Physical Review B*, **48**(16), 11851–11862, 1993.

[49] P. Calabrese and J. Cardy. Entanglement entropy and quantum field theory. *Journal of Statistical Mechanics: Theory and Experiment*, **2004**(06), P06002, 2004.

[50] H. Li and F. D. M. Haldane. Entanglement Spectrum as a Generalization of Entanglement Entropy: Identification of Topological Order in Non-Abelian Fractional Quantum Hall Effect States. *Physical Review Letters*, **101**(1), 010504, 2008.

[51] M. Haque, O. Zozulya, and K. Schoutens. Entanglement Entropy in Fermionic Laughlin States. *Physical Review Letters*, **98**(6), 060401, 2007.

[52] O. S. Zozulya, M. Haque, K. Schoutens, and E. H. Rezayi. Bipartite entanglement entropy in fractional quantum Hall states. *Physical Review B*, **76**(12), 125310, 2007.

[53] A. Sterdyniak, N. Regnault, and B. A. Bernevig. Extracting Excitations from Model State Entanglement. *Physical Review Letters*, **106**(10), 100405, 2011.

[54] M. Levin and X.-G. Wen. Detecting Topological Order in a Ground State Wave Function. *Physical Review Letters*, **96**(11), 110405, 2006.

[55] A. Kitaev and J. Preskill. Topological Entanglement Entropy. *Physical Review Letters*, **96**(11), 110404, 2006.

[56] R. E. Prange and S. M. Girvin, editors. *The Quantum Hall Effect.* Springer US, 1987.

[57] J. K. Jain. *Composite Fermions.* Cambridge University Press, Cambridge, 2007.

[58] H. L. Stormer. Nobel Lecture: The fractional quantum Hall effect. *Reviews of Modern Physics*, **71**(4), 875–889, 1999.

[59] V. W. Scarola, K. Park, and J. K. Jain. Cooper instability of composite fermions. *Nature*, **406**(6798), 863–865, 2000.

[60] J. K. Jain. Composite-fermion approach for the fractional quantum Hall effect. *Physical Review Letters*, **63**(2), 199–202, 1989.

[61] F. D. M. Haldane. Fractional Quantization of the Hall Effect: A Hierarchy of Incompressible Quantum Fluid States. *Physical Review Letters*, **51**(7), 605–608, 1983.

[62] G. Moore and N. Read. Nonabelions in the fractional quantum hall effect. *Nuclear Physics B*, **360**(2-3), 362–396, 1991.

[63] D. R. Hofstadter. Energy levels and wave functions of Bloch electrons in rational and irrational magnetic fields. *Physical Review B*, **14**(6), 2239–2249, 1976.

[64] A. Kol and N. Read. Fractional quantum Hall effect in a periodic potential. *Physical Review B*, **48**(12), 8890–8898, 1993.

[65] A. S. Sørensen, E. Demler, and M. D. Lukin. Fractional Quantum Hall States of Atoms in Optical Lattices. *Physical Review Letters*, **94**(8), 086803, 2005.

[66] M. Hafezi, A. S. Sørensen, E. Demler, and M. D. Lukin. Fractional quantum Hall effect in optical lattices. *Physical Review A*, **76**(2), 023613, 2007.

[67] R. N. Palmer and D. Jaksch. High-Field Fractional Quantum Hall Effect in Optical Lattices. *Physical Review Letters*, **96**(18), 180407, 2006.

[68] M. Hafezi, A. S. Sørensen, M. D. Lukin, and E. Demler. Characterization of topological states on a lattice with Chern number. *Europhysics Letters (EPL)*, **81**(1), 10005, 2007.

[69] L. Hormozi, G. Möller, and S. H. Simon. Fractional Quantum Hall Effect of Lattice Bosons Near Commensurate Flux. *Physical Review Letters*, **108**(25), 256809, 2012.

[70] F. Grusdt and M. Höning. Realization of fractional Chern insulators in the thin-torus limit with ultracold bosons. *Physical Review A*, **90**(5), 053623, 2014.

[71] G. Möller and N. R. Cooper. Fractional Chern Insulators in Harper-Hofstadter Bands with Higher Chern Number. *Physical Review Letters*, **115**(12), 126401, 2015.

[72] M. Gerster, M. Rizzi, P. Silvi, M. Dalmonte, and S. Montangero. Fractional quantum Hall effect in the interacting Hofstadter model via tensor networks. *Physical Review B*, **96**(19), 195123, 2017.

[73] A. Hudomal, N. Regnault, and I. Vasić. Bosonic fractional quantum Hall states in driven optical lattices. *Physical Review A*, **100**(5), 053624, 2019.

[74] J. Boesl, R. Dilip, F. Pollmann, and M. Knap. Characterizing fractional topological phases of lattice bosons near the first Mott lobe. *Physical Review B*, **105**(7), 075135, 2022.

[75] L. Stenzel, A. L. C. Hayward, U. Schollwöck, and F. Heidrich-Meisner. Topological phases in the Fermi-Hofstadter-Hubbard model on hybrid-space ladders. *Physical Review A*, **102**(2), 023315, 2020.

[76] M. Popp, B. Paredes, and J. I. Cirac. Adiabatic path to fractional quantum Hall states of a few bosonic atoms. *Physical Review A*, **70**(5), 053612, 2004.

[77] F. Grusdt, F. Letscher, M. Hafezi, and M. Fleischhauer. Topological Growing of Laughlin States in Synthetic Gauge Fields. *Physical Review Letters*, **113**(15), 155301, 2014.

[78] M. Barkeshli, N. Y. Yao, and C. R. Laumann. Continuous Preparation of a Fractional Chern Insulator. *Physical Review Letters*, **115**(2), 026802, 2015.

[79] Y.-C. He, F. Grusdt, A. Kaufman, M. Greiner, and A. Vishwanath. Realizing and adiabatically preparing bosonic integer and fractional quantum Hall states in optical lattices. *Physical Review B*, **96**(20), 201103(R), 2017.

[80] J. Motruk and F. Pollmann. Phase transitions and adiabatic preparation of a fractional Chern insulator in a boson cold-atom model. *Physical Review B*, **96**(16), 165107, 2017.

[81] Z. Liu, E. J. Bergholtz, and J. C. Budich. Dissipative preparation of fractional Chern insulators. *Physical Review Research*, **3**(4), 043119, 2021.

[82] C. Repellin, J. Léonard, and N. Goldman. Fractional Chern insulators of few bosons in a box: Hall plateaus from center-of-mass drifts and density profiles. *Physical Review A*, **102**(6), 063316, 2020.

[83] J. Motruk and I. Na. Detecting Fractional Chern Insulators in Optical Lattices Through Quantized Displacement. *Physical Review Letters*, **125**(23), 236401, 2020.

[84] F. Grusdt, N. Y. Yao, D. Abanin, M. Fleischhauer, and E. Demler. Interferometric measurements of many-body topological invariants using mobile impurities. *Nature Communications*, **7**(1), 11994, 2016.

[85] Z.-P. Cian, H. Dehghani, A. Elben, B. Vermersch, G. Zhu, M. Barkeshli, P. Zoller, and M. Hafezi. Many-Body Chern Number from Statistical Correlations of Randomized Measurements. *Physical Review Letters*, **126**(5), 050501, 2021.

[86] D. T. Tran, A. Dauphin, A. G. Grushin, P. Zoller, and N. Goldman. Probing topology by "heating": Quantized circular dichroism in ultracold atoms. *Science Advances*, **3**(8), e1701207, 2017.

[87] C. Repellin and N. Goldman. Detecting Fractional Chern Insulators through Circular Dichroism. *Physical Review Letters*, **122**(16), 166801, 2019.

[88] R. Umucalılar, E. Macaluso, T. Comparin, and I. Carusotto. Time-of-Flight Measurements as a Possible Method to Observe Anyonic Statistics. *Physical Review Letters*, **120**(23), 230403, 2018.

[89] R. O. Umucalılar. Real-space probe for lattice quasiholes. *Physical Review A*, **98**(6), 063629, 2018.

[90] X.-Y. Dong, A. G. Grushin, J. Motruk, and F. Pollmann. Charge Excitation Dynamics in Bosonic Fractional Chern Insulators. *Physical Review Letters*, **121**(8), 086401, 2018.

[91] B. Wang, X. Dong, and A. Eckardt. Measurable signatures of bosonic fractional Chern insulator states and their fractional excitations in a quantum-gas microscope. *SciPost Physics*, **12**(3), 095, 2022.

[92] M. Račiūnas, F. N. Ünal, E. Anisimovas, and A. Eckardt. Creating, probing, and manipulating fractionally charged excitations of fractional Chern insulators in optical lattices. *Physical Review A*, **98**(6), 063621, 2018.

[93] E. Macaluso, T. Comparin, R. O. Umucalılar, M. Gerster, S. Montangero, M. Rizzi, and I. Carusotto. Charge and statistics of lattice quasiholes from density measurements: A tree tensor network study. *Physical Review Research*, **2**(1), 013145, 2020.

[94] J. A. Kjäll and J. E. Moore. Edge excitations of bosonic fractional quantum Hall phases in optical lattices. *Physical Review B*, **85**(23), 235137, 2012.

[95] F. D. M. Haldane. Model for a Quantum Hall Effect without Landau Levels: Condensed-Matter Realization of the "Parity Anomaly". *Physical Review Letters*, **61**(18), 2015–2018, 1988.

[96] Z. Liu and E. J. Bergholtz. Recent Developments in Fractional Chern Insulators, arXiv:2208.08449, 2022.

[97] J. R. Abo-Shaeer, C. Raman, J. M. Vogels, and W. Ketterle. Observation of Vortex Lattices in Bose-Einstein Condensates. *Science*, **292**(5516), 476–479, 2001.

[98] V. Schweikhard, I. Coddington, P. Engels, V. P. Mogendorff, and E. A. Cornell. Rapidly Rotating Bose-Einstein Condensates in and near the Lowest Landau Level. *Physical Review Letters*, **92**(4), 040404, 2004.

[99] R. J. Fletcher, A. Shaffer, C. C. Wilson, P. B. Patel, Z. Yan, V. Crépel, B. Mukherjee, and M. W. Zwierlein. Geometric squeezing into the lowest Landau level. *Science*, **372**(6548), 1318–1322, 2021.

[100] R. Yao, S. Chi, B. Mukherjee, A. Shaffer, M. Zwierlein, and R. J. Fletcher. Observation of chiral edge transport in a rapidly-rotating quantum gas, arXiv:2304.10468, 2023.

[101] N. R. Cooper and N. K. Wilkin. Composite fermion description of rotating Bose-Einstein condensates. *Physical Review B*, **60**(24), R16279–R16282, 1999.

[102] N. K. Wilkin and J. M. F. Gunn. Condensation of "Composite Bosons" in a Rotating BEC. *Physical Review Letters*, **84**(1), 6–9, 2000.

[103] N. Regnault and T. Jolicoeur. Quantum Hall Fractions in Rotating Bose-Einstein Condensates. *Physical Review Letters*, **91**(3), 030402, 2003.

[104] N. Regnault and T. Jolicoeur. Quantum Hall fractions for spinless bosons. *Physical Review B*, **69**(23), 235309, 2004.

[105] B. Paredes, P. Fedichev, J. I. Cirac, and P. Zoller. $\frac{1}{2}$-Anyons in Small Atomic Bose-Einstein Condensates. *Physical Review Letters*, **87**(1), 010402, 2001.

[106] M. Roncaglia, M. Rizzi, and J. Dalibard. From rotating atomic rings to quantum Hall states. *Scientific Reports*, **1**, 43, 2011.

[107] J. Zhang, J. Beugnon, and S. Nascimbene. Creating fractional quantum Hall states with atomic clusters using light-assisted insertion of angular momentum. *Physical Review A*, **94**(4), 043610, 2016.

[108] N. R. Cooper. Rapidly rotating atomic gases. *Advances in Physics*, **57**(6), 539–616, 2008.

[109] W. S. Bakr, J. I. Gillen, A. Peng, S. Fölling, and M. Greiner. A quantum gas microscope for detecting single atoms in a Hubbard-regime optical lattice. *Nature*, **462**, 74–77, 2009.

[110] J. F. Sherson, C. Weitenberg, M. Endres, M. Cheneau, I. Bloch, and S. Kuhr. Single-atom-resolved fluorescence imaging of an atomic Mott insulator. *Nature*, **467**, 68–72, 2010.

[111] P. M. Preiss, R. Ma, M. E. Tai, J. Simon, and M. Greiner. Quantum gas microscopy with spin, atom-number, and multilayer readout. *Physical Review A*, **91**(4), 041602(R), 2015.

[112] A. Bergschneider, V. M. Klinkhamer, J. H. Becher, R. Klemt, G. Zürn, P. M. Preiss, and S. Jochim. Spin-resolved single-atom imaging of ^{6}Li in free space. *Physical Review A*, **97**, 063613, 2018.

[113] M. Atala, M. Aidelsburger, J. T. Barreiro, D. Abanin, T. Kitagawa, E. Demler, and I. Bloch. Direct measurement of the Zak phase in topological Bloch bands. *Nature Physics*, **9**, 795–800, 2013.

[114] L. Duca, T. Li, M. Reitter, I. Bloch, M. Schleier-Smith, and U. Schneider. An Aharonov-Bohm interferometer for determining Bloch band topology. *Science*, **347**(6219), 288–292, 2014.

[115] B. K. Stuhl, H.-I. Lu, L. M. Aycock, D. Genkina, and I. B. Spielman. Visualizing edge states with an atomic Bose gas in the quantum Hall regime. *Science*, **349**(6255), 1514–1518, 2015.

[116] M. Mancini, G. Pagano, G. Cappellini, L. Livi, M. Rider, J. Catani, C. Sias, P. Zoller, M. Inguscio, M. Dalmonte, and L. Fallani. Observation of chiral edge states with neutral fermions in synthetic Hall ribbons. *Science*, **349**(6255), 1510–1513, 2015.

[117] J. Cho, D. G. Angelakis, and S. Bose. Fractional Quantum Hall State in Coupled Cavities. *Physical Review Letters*, **101**(24), 246809, 2008.

[118] R. O. Umucalılar and I. Carusotto. Artificial gauge field for photons in coupled cavity arrays. *Physical Review A*, **84**(4), 043804, 2011.

[119] A. L. C. Hayward, A. M. Martin, and A. D. Greentree. Fractional Quantum Hall Physics in Jaynes-Cummings-Hubbard Lattices. *Physical Review Letters*, **108**(22), 223602, 2012.

[120] M. Hafezi, M. D. Lukin, and J. M. Taylor. Non-equilibrium fractional quantum Hall state of light. *New Journal of Physics*, **15**(6), 063001, 2013.

[121] I. Carusotto and C. Ciuti. Quantum fluids of light. *Reviews of Modern Physics*, **85**(1), 299–366, 2013.

[122] N. R. Cooper and J. Dalibard. Reaching Fractional Quantum Hall States with Optical Flux Lattices. *Physical Review Letters*, **110**(18), 185301, 2013.

[123] N. Y. Yao, A. V. Gorshkov, C. R. Laumann, A. M. Läuchli, J. Ye, and M. D. Lukin. Realizing Fractional Chern Insulators in Dipolar Spin Systems. *Physical Review Letters*, **110**(18), 185302, 2013.

[124] E. Kapit, M. Hafezi, and S. H. Simon. Induced Self-Stabilization in Fractional Quantum Hall States of Light. *Physical Review X*, **4**(3), 031039, 2014.

[125] A. Sterdyniak, B. A. Bernevig, N. R. Cooper, and N. Regnault. Interacting bosons in topological optical flux lattices. *Physical Review B*, **91**(3), 035115, 2015.

[126] T. Ozawa, H. M. Price, A. Amo, N. Goldman, M. Hafezi, L. Lu, M. C. Rechtsman, D. Schuster, J. Simon, O. Zilberberg, and I. Carusotto. Topological photonics. *Reviews of Modern Physics*, **91**(1), 015006, 2019.

[127] F. Grusdt and M. Fleischhauer. Fractional quantum Hall physics with ultracold Rydberg gases in artificial gauge fields. *Physical Review A*, **87**(4), 043628, 2013.

[128] S. Weber, R. Bai, N. Makki, J. Mögerle, T. Lahaye, A. Browaeys, M. Daghofer, N. Lang, and H. P. Büchler. Experimentally Accessible Scheme for a Fractional Chern Insulator in Rydberg Atoms. *PRX Quantum*, **3**(3), 030302, 2022.

[129] T.-H. Yang, B.-Z. Wang, X.-C. Zhou, and X.-J. Liu. Quantum Hall states for Rydberg arrays with laser-assisted dipole-dipole interactions. *Physical Review A*, **106**(2), L021101, 2022.

[130] V. Kalmeyer and R. B. Laughlin. Equivalence of the resonating-valence-bond and fractional quantum Hall states. *Physical Review Letters*, **59**(18), 2095–2098, 1987.

[131] F. Becca and S. Sorella. *Quantum Monte Carlo Approaches for Correlated Systems*. Cambridge University Press, 2017.

[132] G. Carleo and M. Troyer. Solving the quantum many-body problem with artificial neural networks. *Science*, **355**(6325), 602–606, 2017.

[133] R. Orús. Tensor networks for complex quantum systems. *Nature Reviews Physics*, **1**(9), 538–550, 2019.

[134] M. C. Bañuls. Tensor Network Algorithms: a Route Map. *Annual Review of Condensed Matter Physics*, **14**(1), 173–191, 2023.

[135] U. Schollwöck. The density-matrix renormalization group in the age of matrix product states. *Annals of Physics*, **326**(1), 96–192, 2011.

[136] S. R. White. Density matrix formulation for quantum renormalization groups. *Physical Review Letters*, **69**(19), 2863–2866, 1992.

[137] U. Schollwöck. The density-matrix renormalization group. *Reviews of Modern Physics*, **77**(1), 259–315, 2005.

[138] C. Hubig, F. Lachenmaier, N.-O. Linden, T. Reinhard, L. Stenzel, A. Swoboda, M. Grundner, and S. Mardazad. The SyTen toolkit.

[139] C. Hubig, I. P. McCulloch, U. Schollwöck, and F. A. Wolf. Strictly single-site DMRG algorithm with subspace expansion. *Physical Review B*, **91**(15), 155115, 2015.

[140] C. Gros. Physics of projected wavefunctions. *Annals of Physics*, **189**(1), 53–88, 1989.

[141] N. Metropolis, A. W. Rosenbluth, M. N. Rosenbluth, A. H. Teller, and E. Teller. Equation of State Calculations by Fast Computing Machines. *The Journal of Chemical Physics*, **21**(6), 1087–1092, 1953.

[142] W. K. Hastings. Monte Carlo sampling methods using Markov chains and their applications. *Biometrika*, **57**(1), 97–109, 1970.

[143] B. Dalla Piazza. *Theories of Experimentally Observed Excitation Spectra of Square Lattice Antiferromagnets.* PhD thesis, École Polytechnique Fédérale de Lausanne, 2014.

[144] C. Nayak, S. H. Simon, A. Stern, M. Freedman, and S. D. Sarma. Non-Abelian anyons and topological quantum computation. *Reviews of Modern Physics*, **80**(3), 1083–1159, 2008.

[145] A. J. Park, E. McKay, D. Lu, and R. Laflamme. Simulation of anyonic statistics and its topological path independence using a seven-qubit quantum simulator. *New Journal of Physics*, **18**(4), 043043, 2016.

[146] H.-N. Dai, B. Yang, A. Reingruber, H. Sun, X.-F. Xu, Y.-A. Chen, Z.-S. Yuan, and J.-W. Pan. Four-body ring-exchange interactions and anyonic statistics within a minimal toric-code Hamiltonian. *Nature Physics*, **13**(12), 1195–1200, 2017.

[147] C. Song, D. Xu, P. Zhang, J. Wang, Q. Guo, W. Liu, K. Xu, H. Deng, K. Huang, D. Zheng, S.-B. Zheng, H. Wang, X. Zhu, C.-Y. Lu, and J.-W. Pan. Demonstration of Topological Robustness of Anyonic Braiding Statistics with a Superconducting Quantum Circuit. *Physical Review Letters*, **121**(3), 030502, 2018.

[148] P. Bonderson, K. Shtengel, and J. K. Slingerland. Probing Non-Abelian Statistics with Quasiparticle Interferometry. *Physical Review Letters*, **97**, 016401, 2006.

[149] J. M. Leinaas and J. Myrheim. On the theory of identical particles. *Il Nuovo Cimento B Series 11*, **37**(1), 1–23, 1977.

[150] F. Wilczek. Magnetic Flux, Angular Momentum, and Statistics. *Physical Review Letters*, **48**(17), 1144–1146, 1982.

[151] J. S. Birman. *Braids, links, and mapping class groups.* Princeton University Press, 1974.

[152] R. Willett, J. P. Eisenstein, H. L. Störmer, D. C. Tsui, A. C. Gossard, and J. H. English. Observation of an even-denominator quantum number in the fractional quantum Hall effect. *Physical Review Letters*, **59**(15), 1776–1779, 1987.

[153] W. Pan, R. R. Du, H. L. Stormer, D. C. Tsui, L. N. Pfeiffer, K. W. Baldwin, and K. W. West. Strongly Anisotropic Electronic Transport at Landau Level Filling Factor $\nu = 9/2$ and $\nu = 5/2$ under a Tilted Magnetic Field. *Physical Review Letters*, **83**(4), 820–823, 1999.

[154] J. S. Xia, W. Pan, C. L. Vicente, E. D. Adams, N. S. Sullivan, H. L. Stormer, D. C. Tsui, L. N. Pfeiffer, K. W. Baldwin, and K. W. West. Electron Correlation in the Second Landau Level: A Competition Between Many Nearly Degenerate Quantum Phases. *Physical Review Letters*, **93**(17), 176809, 2004.

[155] M. Greiter, X.-G. Wen, and F. Wilczek. Paired Hall state at half filling. *Physical Review Letters*, **66**(24), 3205–3208, 1991.

[156] M. Greiter, X. G. Wen, and F. Wilczek. Paired Hall states. *Nuclear Physics B*, **374**(3), 567–614, 1992.

[157] M. Greiter and R. Thomale. Non-Abelian Statistics in a Quantum Antiferromagnet. *Physical Review Letters*, **102**(20), 207203, 2009.

[158] M. Greiter, D. F. Schroeter, and R. Thomale. Parent Hamiltonian for the non-Abelian chiral spin liquid. *Physical Review B*, **89**(16), 165125, 2014.

[159] Y.-F. Wang, H. Yao, Z.-C. Gu, C.-D. Gong, and D. N. Sheng. Non-Abelian Quantum Hall Effect in Topological Flat Bands. *Physical Review Letters*, **108**(12), 126805, 2012.

[160] F. D. M. Haldane and E. H. Rezayi. Spin-singlet wave function for the half-integral quantum Hall effect. *Physical Review Letters*, **60**(10), 956–959, 1988.

[161] R. H. Morf. Transition from Quantum Hall to Compressible States in the Second Landau Level: New Light on the $\nu = 5/2$ Enigma. *Physical Review Letters*, **80**(7), 1505–1508, 1998.

[162] E. H. Rezayi and F. D. M. Haldane. Incompressible Paired Hall State, Stripe Order, and the Composite Fermion Liquid Phase in Half-Filled Landau Levels. *Physical Review Letters*, **84**(20), 4685–4688, 2000.

[163] R. L. Willett. The quantum Hall effect at 5/2 filling factor. *Reports on Progress in Physics*, **76**(7), 076501, 2013.

[164] N. R. Cooper, N. K. Wilkin, and J. M. F. Gunn. Quantum Phases of Vortices in Rotating Bose-Einstein Condensates. *Physical Review Letters*, **87**(12), 120405, 2001.

[165] A. Sterdyniak, N. Regnault, and G. Möller. Particle entanglement spectra for quantum Hall states on lattices. *Physical Review B*, **86**(16), 165314, 2012.

[166] E. H. Rezayi and F. D. M. Haldane. Laughlin state on stretched and squeezed cylinders and edge excitations in the quantum Hall effect. *Physical Review B*, **50**(23), 17199–17207, 1994.

[167] E. J. Bergholtz, J. Kailasvuori, E. Wikberg, T. H. Hansson, and A. Karlhede. Pfaffian quantum Hall state made simple: Multiple vacua and domain walls on a thin torus. *Physical Review B*, **74**, 081308(R), 2006.

[168] A. Seidel and D.-H. Lee. Abelian and Non-Abelian Hall Liquids and Charge-Density Wave: Quantum Number Fractionalization in One and Two Dimensions. *Physical Review Letters*, **97**(5), 056804, 2006.

[169] N. Read and E. Rezayi. Beyond paired quantum Hall states: Parafermions and incompressible states in the first excited Landau level. *Physical Review B*, **59**(12), 8084–8092, 1999.

[170] L. Palm, F. Grusdt, and P. M. Preiss. Skyrmion ground states of rapidly rotating few-fermion systems. *New Journal of Physics*, **22**(8), 083037, 2020.

[171] B. Andrade, V. Kasper, M. Lewenstein, C. Weitenberg, and T. Graß. Preparation of the 1/2 Laughlin state with atoms in a rotating trap. *Physical Review A*, **103**(6), 063325, 2021.

[172] M. Buser, S. Greschner, U. Schollwöck, and T. Giamarchi. Probing the Hall Voltage in Synthetic Quantum Systems. *Physical Review Letters*, **126**, 030501, 2021.

[173] C. L. Kane, R. Mukhopadhyay, and T. C. Lubensky. Fractional Quantum Hall Effect in an Array of Quantum Wires. *Physical Review Letters*, **88**(3), 036401, 2002.

[174] J. C. Y. Teo and C. L. Kane. From Luttinger liquid to non-Abelian quantum Hall states. *Physical Review B*, **89**(8), 085101, 2014.

[175] Y. Fuji and A. Furusaki. Quantum Hall hierarchy from coupled wires. *Physical Review B*, **99**(3), 035130, 2019.

[176] B. Michen, C. Repellin, and J. C. Budich. Adiabatic preparation of fractional Chern insulators from an effective thin-torus limit, arXiv:2212.11294, 2022.

[177] T. Giamarchi. *Quantum Physics in One Dimension*. Oxford University Press, 2003.

[178] X. G. Wen. Gapless boundary excitations in the quantum Hall states and in the chiral spin states. *Physical Review B*, **43**(13), 11025–11036, 1991.

[179] A. Petrescu and K. Le Hur. Chiral Mott insulators, Meissner effect, and Laughlin states in quantum ladders. *Physical Review B*, **91**(5), 054520, 2015.

[180] M. Calvanese Strinati, E. Cornfeld, D. Rossini, S. Barbarino, M. Dalmonte, R. Fazio, E. Sela, and L. Mazza. Laughlin-like States in Bosonic and Fermionic Atomic Synthetic Ladders. *Physical Review X*, **7**(2), 021033, 2017.

[181] A. Petrescu, M. Piraud, G. Roux, I. P. McCulloch, and K. Le Hur. Precursor of the Laughlin state of hard-core bosons on a two-leg ladder. *Physical Review B*, **96**(1), 014524, 2017.

[182] M. Calvanese Strinati, S. Sahoo, K. Shtengel, and E. Sela. Pretopological fractional excitations in the two-leg flux ladder. *Physical Review B*, **99**(24), 245101, 2019.

[183] A. J. Ferris and G. Vidal. Perfect sampling with unitary tensor networks. *Physical Review B*, **85**(16), 165146, 2012.

[184] M. Buser, U. Schollwöck, and F. Grusdt. Snapshot-based characterization of particle currents and the Hall response in synthetic flux lattices. *Physical Review A*, **105**(3), 033303, 2022.

[185] A. Lukin, M. Rispoli, R. Schittko, M. E. Tai, A. M. Kaufman, S. Choi, V. Khemani, J. Léonard, and M. Greiner. Probing entanglement in a many-body–localized system. *Science*, **364**(6437), 256–260, 2019.

[186] A. Petrescu, H. F. Song, S. Rachel, Z. Ristivojevic, C. Flindt, N. Laflorencie, I. Klich, N. Regnault, and K. Le Hur. Fluctuations and entanglement spectrum in quantum Hall states. *Journal of Statistical Mechanics: Theory and Experiment*, **2014**(10), P10005, 2014.

[187] E. H. Lieb and W. Liniger. Exact Analysis of an Interacting Bose Gas. I. The General Solution and the Ground State. *Physical Review*, **130**(4), 1605–1616, 1963.

[188] E. H. Lieb. Exact Analysis of an Interacting Bose Gas. II. The Excitation Spectrum. *Physical Review*, **130**(4), 1616–1624, 1963.

[189] T. Cheon and T. Shigehara. Fermion-Boson Duality of One-Dimensional Quantum Particles with Generalized Contact Interactions. *Physical Review Letters*, **82**(12), 2536–2539, 1999.

[190] H. Dehghani, Z.-P. Cian, M. Hafezi, and M. Barkeshli. Extraction of the many-body Chern number from a single wave function. *Physical Review B*, **103**(7), 075102, 2021.

[191] D. Hügel and B. Paredes. Chiral ladders and the edges of quantum Hall insulators. *Physical Review A*, **89**(2), 023619, 2014.

[192] M. Piraud, F. Heidrich-Meisner, I. P. McCulloch, S. Greschner, T. Vekua, and U. Schollwöck. Vortex and Meissner phases of strongly interacting bosons on a two-leg ladder. *Physical Review B*, **91**(14), 140406(R), 2015.

[193] M. Di Dio, S. De Palo, E. Orignac, R. Citro, and M.-L. Chiofalo. Persisting Meissner state and incommensurate phases of hard-core boson ladders in a flux. *Physical Review B*, **92**(6), 060506(R), 2015.

[194] M. Buser, C. Hubig, U. Schollwöck, L. Tarruell, and F. Heidrich-Meisner. Interacting bosonic flux ladders with a synthetic dimension: Ground-state phases and quantum quench dynamics. *Physical Review A*, **102**, 053314, 2020.

[195] S. M. Girvin and A. H. MacDonald. Off-diagonal long-range order, oblique confinement, and the fractional quantum Hall effect. *Physical Review Letters*, **58**(12), 1252–1255, 1987.

[196] B.-Y. Sun, N. Goldman, M. Aidelsburger, and M. Bukov. Engineering and probing non-Abelian chiral spin liquids using periodically driven ultracold atoms, arXiv:2211.09777, 2022.

[197] B. Bergh and M. Gärttner. Experimentally Accessible Bounds on Distillable Entanglement from Entropic Uncertainty Relations. *Physical Review Letters*, **126**(19), 190503, 2021.

[198] B. Bergh and M. Gärttner. Entanglement detection in quantum many-body systems using entropic uncertainty relations. *Physical Review A*, **103**(5), 052412, 2021.

[199] J. Haegeman, J. I. Cirac, T. J. Osborne, I. Pižorn, H. Verschelde, and F. Verstraete. Time-Dependent Variational Principle for Quantum Lattices. *Physical Review Letters*, **107**(7), 070601, 2011.

[200] J. Haegeman, C. Lubich, I. Oseledets, B. Vandereycken, and F. Verstraete. Unifying time evolution and optimization with matrix product states. *Physical Review B*, **94**(16), 165116, 2016.

[201] P. Středa. Theory of quantised Hall conductivity in two dimensions. *Journal of Physics C: Solid State Physics*, **15**(22), L717–L721, 1982.

[202] P. Středa. Quantised Hall effect in a two-dimensional periodic potential. *Journal of Physics C: Solid State Physics*, **15**(36), L1299–L1303, 1982.

[203] P. B. Wigley, P. J. Everitt, A. van den Hengel, J. W. Bastian, M. A. Sooriyabandara, G. D. McDonald, K. S. Hardman, C. D. Quinlivan, P. Manju, C. C. N. Kuhn, I. R. Petersen, A. N. Luiten, J. J. Hope, N. P. Robins, and M. R. Hush. Fast machine-learning online optimization of ultra-cold-atom experiments. *Scientific Reports*, **6**, 28632, 2016.

[204] Z. Vendeiro, J. Ramette, A. Rudelis, M. Chong, J. Sinclair, L. Stewart, A. Urvoy, and V. Vuletić. Machine-learning-accelerated Bose-Einstein condensation. *Physical Review Research*, **4**(4), 043216, 2022.

[205] Y.-J. Xie, H.-N. Dai, Z.-S. Yuan, Y. Deng, X. Li, Y.-A. Chen, and J.-W. Pan. Bayesian learning for optimal control of quantum many-body states in optical lattices. *Physical Review A*, **106**(1), 013316, 2022.

[206] A. Bohrdt, E. Demler, and F. Grusdt. Rotational Resonances and Regge-like Trajectories in Lightly Doped Antiferromagnets. *Physical Review Letters*, **127**(19), 197004, 2021.

[207] D. P. Arovas, E. Berg, S. Kivelson, and S. Raghu. The Hubbard Model. *Annual Review of Condensed Matter Physics*, **13**(1), 239–274, 2022.

[208] K. Yang, K. Moon, L. Zheng, A. H. MacDonald, S. M. Girvin, D. Yoshioka, and S.-C. Zhang. Quantum ferromagnetism and phase transitions in double-layer quantum Hall systems. *Physical Review Letters*, **72**(5), 732–735, 1994.

[209] Z. F. Ezawa and G. Tsitsishvili. Quantum Hall ferromagnets. *Reports on Progress in Physics*, **72**(8), 086502, 2009.

[210] E. H. Rezayi. Reversed-spin excitations of the fractionally quantized Hall effect from finite-size calculations. *Physical Review B*, **36**(10), 5454–5457, 1987.

[211] D.-H. Lee and C. L. Kane. Boson-vortex-Skyrmion duality, spin-singlet fractional quantum Hall effect, and spin-1/2 anyon superconductivity. *Physical Review Letters*, **64**(12), 1313–1317, 1990.

[212] E. H. Rezayi. Wave functions and other properties of spin-reversed quasiparticles at ν=1/m Landau-level occupation. *Physical Review B*, **43**(7), 5944–5949, 1991.

[213] S. L. Sondhi, A. Karlhede, S. A. Kivelson, and E. H. Rezayi. Skyrmions and the crossover from the integer to fractional quantum Hall effect at small Zeeman energies. *Physical Review B*, **47**(24), 16419–16426, 1993.

[214] H. A. Fertig, L. Brey, R. Côté, and A. H. MacDonald. Charged spin-texture excitations and the Hartree-Fock approximation in the quantum Hall effect. *Physical Review B*, **50**(15), 11018–11021, 1994.

[215] K. Moon, H. Mori, K. Yang, S. M. Girvin, A. H. MacDonald, L. Zheng, D. Yoshioka, and S.-C. Zhang. Spontaneous interlayer coherence in double-layer quantum Hall systems: Charged vortices and Kosterlitz-Thouless phase transitions. *Physical Review B*, **51**(8), 5138–5170, 1995.

[216] A. H. MacDonald, H. A. Fertig, and L. Brey. Skyrmions without Sigma Models in Quantum Hall Ferromagnets. *Physical Review Letters*, **76**(12), 2153–2156, 1996.

[217] S. E. Barrett, G. Dabbagh, L. N. Pfeiffer, K. W. West, and R. Tycko. Optically Pumped NMR Evidence for Finite-Size Skyrmions in GaAs Quantum Wells near Landau Level Filling ν=1. *Physical Review Letters*, **74**(25), 5112–5115, 1995.

[218] A. Schmeller, J. P. Eisenstein, L. N. Pfeiffer, and K. W. West. Evidence for Skyrmions and Single Spin Flips in the Integer Quantized Hall Effect. *Physical Review Letters*, **75**(23), 4290–4293, 1995.

[219] E. H. Aifer, B. B. Goldberg, and D. A. Broido. Evidence of Skyrmion Excitations about ν=1 in n-Modulation-Doped Single Quantum Wells by Interband Optical Transmission. *Physical Review Letters*, **76**(4), 680–683, 1996.

[220] M. J. Manfra, B. B. Goldberg, L. Pfeiffer, and K. West. Optical determination of the spin polarization of a quantum Hall ferromagnet. *Physica E: Low-dimensional Systems and Nanostructures*, **1**(1-4), 28–35, 1997.

[221] C. M. Townsley, R. Chughtai, R. J. Nicholas, and M. Henini. Observation of skyrmions in a two-dimensional hole system. *Physical Review B*, **71**(7), 073303, 2005.

[222] L. Bryja, A. Wójs, and M. Potemski. Quantum Hall skyrmions in a hole gas with a large spin gap. *Physical Review B*, **73**(24), 241302(R), 2006.

[223] M. Lupatini, P. Knüppel, S. Faelt, R. Winkler, M. Shayegan, A. Imamoglu, and W. Wegscheider. Spin Reversal of a Quantum Hall Ferromagnet at a Landau Level Crossing. *Physical Review Letters*, **125**(6), 067404, 2020.

[224] E. Khalaf, S. Chatterjee, N. Bultinck, M. P. Zaletel, and A. Vishwanath. Charged skyrmions and topological origin of superconductivity in magic-angle graphene. *Science Advances*, **7**(19), 2021.

[225] E. Khalaf and A. Vishwanath. Baby skyrmions in Chern ferromagnets and topological mechanism for spin-polaron formation in twisted bilayer graphene. *Nature Communications*, **13**, 6245, 2022.

[226] S. Chatterjee, M. Ippoliti, and M. P. Zaletel. Skyrmion superconductivity: DMRG evidence for a topological route to superconductivity. *Physical Review B*, **106**(3), 035421, 2022.

[227] P. Mai, E. W. Huang, J. Yu, B. E. Feldman, and P. W. Phillips. Interaction-driven spontaneous ferromagnetic insulating states with odd Chern numbers. *npj Quantum Materials*, **8**, 14, 2023.

[228] Z.-P. Cian, T. Grass, A. Vaezi, Z. Liu, and M. Hafezi. Engineering quantum Hall phases in a synthetic bilayer graphene system. *Physical Review B*, **102**(8), 085430, 2020.

[229] R. Jördens, N. Strohmaier, K. Günter, H. Moritz, and T. Esslinger. A Mott insulator of fermionic atoms in an optical lattice. *Nature*, **455**, 204–207, 2008.

[230] T. Esslinger. Fermi-Hubbard Physics with Atoms in an Optical Lattice. *Annual Review of Condensed Matter Physics*, **1**(1), 129–152, 2010.

[231] L. Tarruell and L. Sanchez-Palencia. Quantum simulation of the Hubbard model with ultracold fermions in optical lattices. *Comptes Rendus Physique*, **19**(6), 365–393, 2018.

[232] H. Katsura, I. Maruyama, A. Tanaka, and H. Tasaki. Ferromagnetism in the Hubbard model with topological/non-topological flat bands. *EPL (Europhysics Letters)*, **91**(5), 57007, 2010.

[233] E. Fradkin. *Field theories of condensed matter physics*. Cambridge University Press, Cambridge, 2013.

[234] P. W. Anderson. The Resonating Valence Bond State in La_2CuO_4 and Superconductivity. *Science*, **235**(4793), 1196–1198, 1987.

[235] M. C. Gutzwiller. Effect of Correlation on the Ferromagnetism of Transition Metals. *Physical Review Letters*, **10**(5), 159–162, 1963.

[236] E. Wigner. On the Interaction of Electrons in Metals. *Phys. Rev.*, **46**, 1002–1011, 1934.

[237] J. Koepsell, D. Bourgund, P. Sompet, S. Hirthe, A. Bohrdt, Y. Wang, F. Grusdt, E. Demler, G. Salomon, C. Gross, and I. Bloch. Microscopic evolution of doped Mott insulators from polaronic metal to Fermi liquid. *Science*, **374**(6563), 82–86, 2021.

[238] W.-L. Tu, F. Schindler, T. Neupert, and D. Poilblanc. Competing orders in the Hofstadter t–J model. *Physical Review B*, **97**(3), 035154, 2018.

[239] A. Szasz, J. Motruk, M. P. Zaletel, and J. E. Moore. Chiral Spin Liquid Phase of the Triangular Lattice Hubbard Model: A Density Matrix Renormalization Group Study. *Physical Review X*, **10**(2), 021042, 2020.

[240] R. K. Kamilla, X. G. Wu, and J. K. Jain. Skyrmions in the fractional quantum Hall effect. *Solid State Communications*, **99**(4), 289–293, 1996.

[241] A. Wójs and J. J. Quinn. Spin excitation spectra of integral and fractional quantum Hall systems. *Physical Review B*, **66**(4), 045323, 2002.

[242] R. L. Doretto, M. O. Goerbig, P. Lederer, A. O. Caldeira, and C. Morais Smith. Spin-excitations of the quantum Hall ferromagnet of composite fermions. *Physical Review B*, **72**(3), 035341, 2005.

[243] A. C. Balram, U. Wurstbauer, A. Wójs, A. Pinczuk, and J. K. Jain. Fractionally charged skyrmions in fractional quantum Hall effect. *Nature Communications*, **6**, 8981, 2015.

[244] H.-H. Tu, A. E. B. Nielsen, J. I. Cirac, and G. Sierra. Lattice Laughlin states of bosons and fermions at filling fractions 1/q. *New Journal of Physics*, **16**(3), 033025, 2014.

[245] I. Glasser, J. I. Cirac, G. Sierra, and A. E. B. Nielsen. Exact parent Hamiltonians of bosonic and fermionic Moore-Read states on lattices and local models. *New Journal of Physics*, **17**(8), 082001, 2015.

[246] I. Glasser, J. I. Cirac, G. Sierra, and A. E. B. Nielsen. Lattice effects on Laughlin wave functions and parent Hamiltonians. *Physical Review B*, **94**(24), 245104, 2016.

[247] S. Manna, J. Wildeboer, G. Sierra, and A. E. B. Nielsen. Non-Abelian quasiholes in lattice Moore-Read states and parent Hamiltonians. *Physical Review B*, **98**(16), 165147, 2018.

[248] A. E. B. Nielsen, I. Glasser, and I. D. Rodríguez. Quasielectrons as inverse quasiholes in lattice fractional quantum Hall models. *New Journal of Physics*, **20**(3), 033029, 2018.

[249] B. Jaworowski, N. Regnault, and Z. Liu. Characterization of quasiholes in two-component fractional quantum Hall states and fractional Chern insulators in $|C| = 2$ flat bands. *Physical Review B*, **99**(4), 045136, 2019.

[250] B. Jaworowski and A. E. B. Nielsen. Model wave functions for an interface between lattice Laughlin and Moore-Read states. *Physical Review B*, **103**(20), 205149, 2021.

[251] N. Read. Order Parameter and Ginzburg-Landau Theory for the Fractional Quantum Hall Effect. *Physical Review Letters*, **62**(1), 86–89, 1989.

[252] S. C. Zhang, T. H. Hansson, and S. Kivelson. Effective-Field-Theory Model for the Fractional Quantum Hall Effect. *Physical Review Letters*, **62**(1), 82–85, 1989.

[253] E. Fradkin. Jordan-Wigner transformation for quantum-spin systems in two dimensions and fractional statistics. *Physical Review Letters*, **63**(3), 322–325, 1989.

[254] E. Fradkin. Superfluidity of the lattice anyon gas and topological invariance. *Physical Review B*, **42**(1), 570–586, 1990.

[255] X. G. Wen. Topological Orders in Rigid States. *International Journal of Modern Physics B*, **04**(02), 239–271, 1990.

[256] T. Lan, L. Kong, and X.-G. Wen. Theory of (2+1)-dimensional fermionic topological orders and fermionic/bosonic topological orders with symmetries. *Physical Review B*, **94**(15), 155113, 2016.

[257] X.-G. Wen. Colloquium: Zoo of quantum-topological phases of matter. *Reviews of Modern Physics*, **89**(4), 041004, 2017.